HAL
open science

Mechanical behavior of rammed earth walls under Pushover tests

Ranime El Nabouch

To cite this version:

Ranime El Nabouch. Mechanical behavior of rammed earth walls under Pushover tests. Civil Engineering. Université Grenoble Alpes, 2017. English. NNT : 2017GREAA014 . tel-01707009

HAL Id: tel-01707009

https://theses.hal.science/tel-01707009v1

Submitted on 12 Feb 2018

HAL is a multi-disciplinary open access archive for the deposit and dissemination of scientific research documents, whether they are published or not. The documents may come from teaching and research institutions in France or abroad, or from public or private research centers.

L'archive ouverte pluridisciplinaire **HAL**, est destinée au dépôt et à la diffusion de documents scientifiques de niveau recherche, publiés ou non, émanant des établissements d'enseignement et de recherche français ou étrangers, des laboratoires publics ou privés.

Communauté UNIVERSITÉ Grenoble Alpes

THÈSE

Pour obtenir le grade de

DOCTEUR DE LA COMMUNAUTE UNIVERSITE GRENOBLE ALPES

Spécialité : **Génie civil et sciences de l'habitat**

Arrêté ministériel : 25 mai 2016

Présentée par

Ranime EL NABOUCH

Thèse dirigée par **Olivier PLÉ**
co-dirigée par **Pascal PERROTIN**
encadrée par **Quoc-Bao BUI**

préparée au sein du **LOCIE**
dans **l'École Doctorale SISEO**

Mechanical behavior of rammed earth walls under Pushover tests

Comportement mécanique des murs en Pisé soumis à la poussée progressive

Thèse soutenue publiquement le **8 juin 2017**,
devant le jury composé de :

Jean Claude MOREL
Professeur, Coventry University, Rapporteur
Evelyne TOUSSAINT
Professeur, Université Clermont Auvergne, Rapporteur
Sofiane AMZIANE
Professeur, Université Clermont Auvergne, Président
Antonin FABBRI
Chargé de Recherche, Ecole Nationale des Travaux Publics de l'Etat, Examinateur
Yannick SIEFFERT
Maître de conférences HDR, Université Grenoble Alpes, Examinateur
Olivier PLE
Professeur, Université Savoie Mont Blanc, Directeur de thèse
Pascal, PERROTIN
Maître de conférences HDR, Université Savoie Mont Blanc, Codirecteur de thèse
Quoc-Bao, BUI
Maître de conférences, Université Savoie Mont Blanc, Encadrant

Acknowledgments

First of all, I would like to thank my director Olivier Plé, for his continuous support, his enthusiasm and his confidence in me. His guidance helped me in all the time of research and writing of this thesis.

I would like also to thank my advisor Pascal Perrotin for all the motivating discussion we had, for the brilliant ideas and the positiveness that he transmitted to me during the most difficult times. His advice on both research as well as on my career have been invaluable.

Likewise, I thank my advisor Quoc-Bao Bui who introduced me to the world of "rammed earth" and who was always willing to share his experience and expertise through these three years. He taught me how to be a researcher and I will always be grateful for this.

My thesis committee also had a great role in making this work more valuable. In particular, I would like to thank my thesis referees, Jean-Claude Morel and Evelyne Toussaint for the time they allocated to read my manuscript and for their precious reviews and comments. Also, thanks to Sofiane Amziane, president of the jury, Antonin Fabbri and Yannick Sieffert for being part of my thesis committee.

This PhD was carried out in the LOCIE laboratory at the University of Savoie Mont Blanc. I, therefore, thank its director Monika Woloszyn for offering me the perfect work conditions. I gratefully acknowledge the funding received towards my PhD from National Research Agency (ANR) through the PRIMATERRE project.

In the LOCIE, I wish to thank Jean-Patrick and Néomie for the interesting discussions we exchanged during my PhD and also for their help during my teaching experience. I would like also to express my gratitude to Professor Joseph Pastor. It has been a great honor for me to have his participation on my PhD topic.

I warmly thank the technical staff for their help during these three years. A special thanks goes to Thierry who put all his effort and patience to help me in all my experiments. I thank Cedric for his help in the execution of the experimental program. I also want to thank the administrative staff Martine, Isabelle and Elisabeth for their help in all the different procedures.

In my work I have also received enormous help from different scientists, and experts on my issues. For that, I thank Pierre Vacher who answered all my questions concerning the digital image correlation. And Nicolas Meunier, for all the interesting experimental advice that he provided me concerning the construction of the walls.

I dedicate this part to thank all my colleagues and friends who helped and supported me during all these years. A special acknowledgment goes to my dear colleague Julien Berger who never got bored of hearing the repetition of my presentation and who gave me great advises before my defense. Special thanks to the very good people and friends I met in Chambery: Gaelle, Nolwenn, Bastian, Marie, Ioannis, Sara, Clément, Léa, Patricia, Suelen and of course my old friends: Caroline, Jana, Karine, Diala, and Maria. Thanks to my special cousin Farah and for her assistance before submitting my thesis and for my room-mate Lama for her support before my thesis defense.

Lastly, I would like to thank my family for all their love and encouragement. I am deeply grateful to my mother Maha and my sister Dima for having always believed in and encouraged me. Finally, I thank my husband Rabih for his strong support during these three years and for his unconditional love. I could not have completed this work without you. *Thank you.*

Abstract

Determining the mechanical behavior of rammed earth walls is a highly important feature giving that there is a renewed interest in the use of the natural material in building construction. On one hand, it contributes to finding suitable and appropriate ways for the conservation and restoration of these building and on another hand, it draws new recommendations for the conception of new rammed earth structures with respect to new building regulations (earthquake building guideline, new thermal regulation).

In this context, this thesis investigates the behavior of rammed earth walls subjected to lateral loading. Four unstabilized rammed earth walls were tested under a combination of vertical and monotonic pushover tests up to failure. The shear behavior of these walls is studied along with the failure modes by means of digital image correlation. Results showed that the response of the rammed earth is characterized by significant non-linear behavior with a remarkable ductility. In general, the walls experienced a shear failure due to the failure of diagonal struts. Cracks at the interface between the bottom layers were also observed.

The performance of these walls was assessed based on the pushover methodology. The experimental work was completed with the determination of the mechanical characteristics of rammed earth in compression and an investigation of the shear components: cohesion and friction angle of the rammed earth through shear box tests on a different scale. Finally, the relevance of these parameters was tested by performing a numerical model that aims to simulate the experimental tests done on the scale of the walls.

Keywords*: Rammed earth, pushover tests, in-plane behavior, numerical simulation, application to Standard Eurocode 8.*

Résumé

La détermination des comportements mécaniques des murs en pisé est d'une importance capitale dans un contexte où il y a un regain d'intérêt pour l'utilisation de matériaux de construction à très faible impact environnementaux. D'une part, cette étude contribue à trouver des moyens appropriés pour la conservation et la restauration du patrimoine bâti et, d'autre part, permet d'établir de nouvelles recommandations pour la conception de nouvelles structures en pisé dans le respect des règlements de la construction (réglementation thermique et réglementation parasismique).

Dans ce contexte, cette thèse étudie le comportement des murs en pisé soumis à des sollicitations horizontales. Quatre murs de terre en pisé non stabilisés ont été testés sous une combinaison de charge verticale et horizontale monotone (type pushover) jusqu'à la rupture. Le comportement au cisaillement et les modes de ruptures de ces murs sont étudiés à l'aide d'une technique de corrélation d'images à grande échelle. Les résultats ont montré que le pisé est caractérisé par un comportement mécanique non linéaire très significatif et une ductilité remarquable. D'une manière générale, les murs ont subi une rupture de cisaillement due à une fissuration principale au niveau de la bielle de compression. Des fissures à l'interface entre les différentes couches ont également été observées.

L'évaluation de la performance de ces murs a été effectuée sur la base de la méthodologie pushover. Le travail expérimental a été complété avec la détermination des caractéristiques mécaniques du matériau pisé en compression puis une étude en cisaillement directe (cohésion et angle de frottement) à l'aide de deux boites de Casagrande de tailles différentes. Enfin, l'importance de ces paramètres a été analysée en réalisant des simulations numériques à l'échelle du mur.

***Mots clefs**: Pisé, poussée progressive, comportement dans le plan, simulation numérique, application à l'Eurocode 8.*

Table of Contents

Acknowledgments i
Abstract iv
Résumé v
List of Figures xi
List of Tables xviii

Chapter 1. An Overview on Rammed Earth in building materials 1

1.1 Introduction 2
1.2 Background on earth construction 2
1.2.1 Wattle and daub 3
1.2.2 Adobe 4
1.2.3 Cob 4
1.2.4 Compressed earth bricks (CEB) 5
1.3 Rammed earth 6
1.3.1 Historical Background 8
1.3.2 Modern rammed earth 12
1.3.3 Advantages of rammed earth material 15
1.4 Durability, Vulnerabilities of rammed earth 19
1.4.1 Durability of rammed earth structures 19
1.4.2 Vulnerability of rammed earth 20
1.5 Research objectives and methodology 20
1.5.1 Conclusion and problem statement 20
1.5.2 PRIMATERRE research project 21
1.5.3 Thesis objective 21

Chapter 2. Identifying the mechanical parameters for the used earth 23

2.1 Introduction 24
2.2 General comments on the properties of rammed earth material 24
2.2.1 Grain size distribution 24
2.2.2 Dry density 25
2.2.3 Mechanical behavior: Compressive Strength 27
2.3 Properties of the used rammed earth 30
2.3.1 Origin and physical characteristics 30
2.3.2 Manufacturing water content: 33
2.4 Unconfined compression tests on the rammed earth used 35
2.4.1 Specimen preparation 35
2.4.2 Experimental set-up 37
2.4.3 Digital image correlation 38
2.4.4 Results: Compressive strength and Young's Modulus 39
2.4.5 Results of DIC on rammed earth specimens 41
2.5 Identification of cohesion and friction angles by direct shear tests on rammed earth used 48

2.5.1 Bibliography about shear tests applied on rammed earth 49
2.5.2 Principles of the Casagrande shear test 50
2.5.3 Tests on the full-scale shear box 52
2.5.4 Analysis of the results 61
2.5.5 Tests on standard Casagrande box 65
2.6 Discussion 69
2.7 Summary and Conclusions 70

Chapter 3. In-plane behavior of rammed earth walls under static loading: experimental testing 73

3.1 Introduction 74
3.2 Experimental laboratory tests found in literature 74
3.3 In-plane failure modes: Referring to masonry walls 79
3.4 Experimental Program of Pushover tests 81
3.4.1 Specimen manufacturing 81
3.4.2 Experimental Setup 85
3.4.3 Process of an experiment 88
3.4.4 Comparison of measurement with M3 90
3.4.5 Results of the walls tested 92
3.4.6 Visualizing the crack propagation 97
3.4.7 Summary of the failure modes obtained for rammed earth walls 110
3.4.8 Finale state of the walls 110
3.5 Conclusion 112

Chapter 4. Identifying the parameters for numerical modeling of rammed earth walls 115

4.1 A review from the literature 116
4.2 Modeling rammed earth walls by using Drucker-Prager criterion 119
4.2.1 Description of nonlinear constitute law 119
4.2.2 Homogenous model: application on a diagonal shear test 120
4.3 Validation of Drucker-Prager on Pushover tests 122
4.3.1 Presentation of the model: 122
4.3.2 Influence of the parameters: cohesion and friction angle 125
4.4 Parametric study 128
4.5 Conclusion and recommendation 131

Chapter 5. Assessing the seismic performance of rammed earth walls by pushover tests 133

5.1 Introduction 134
5.1.1 Vulnerability of earth buildings to earthquakes 135
5.1.2 Objective of this chapter 138
5.2 Definition of Limit state of rammed earth walls 139
5.3 Pushover analysis in the seismic assessment: Explanation of the method 145
5.3.1 The Eurocode elastic response spectra 146
5.3.2 Nonlinear Static Analysis Procedure 146

5.3.3 Seismic Demand in acceleration–displacement (S_a-S_d) format 149
5.3.4 Superposition of the capacity spectrum with the demand spectrum 150
5.4 Seismic evaluation of rammed earth house 152
5.4.1 Scale effects 154
5.4.2 Seismic assessment of 1-scale walls: 155
5.5 Conclusion 161

General Conclusion 163

Appendix 167

Synthèse 179

List of publications 185

References 187

List of Figures

Figure 1.1 Earth construction processes classification adapted after Hamard et al. [4], (Wm = manufacture water content, Wop = optimum Proctor water content; WP = water content at plastic limit; WL = water content at liquid limit). 3
Figure 1.2 (a) Building in the central German city of Bad Langensalza made of wattle and daub (Photo: Sebastian Wallroth); (b) House in France, Alsace (Photo: Auroville Earth institute) 3
Figure 1.3 Production of Adobe in Ecuador [6] 4
Figure 1.4 Examples of existing adobe constructions in Aveiro district, Portugal [7] 4
Figure 1.5 (a) Technique of Cob construction; (b) Masmak Castle in Riyadh, Saudi Arabia (Photo: M. Abdulaziz) 5
Figure 1.6 Compressed earth blocks manufactured by means of (a) a manual press [8]; (b) hydraulic press [9] 5
Figure 1.7 Apartments from CEB in Marrakesh, Morocco [10] 6
Figure 1.8 (a) Formwork used in for traditional rammed earth [6]; (b) Rammers used to compact rammed earth [6] 6
Figure 1.9 The use of pneumatic rammer and metallic formwork in modern techniques, (Photo from the laboratory of ENTPE, Lyon) 7
Figure 1.10 Traditionnel house in « Pont de beau voisins », Rhône-Alpes, France 8
Figure 1.11 Visible compacted layers with different thickness of a rammed earth wall constructed in the LOCIE laboratory 8
Figure 1.12 Examples of historical constructions around the world made from rammed earth: (a) Great wall of China; (b) Buildings in Shibam, Yemen (Photo: Auroville earth institute); (c) Alhambra Palace of Granda, Spain [13]; (d) Temple in Japan [12] 9
Figure 1.13 A six stories building in Weilburg, Germany [17] 10
Figure 1.14 Château de Reyrieux, made from rammed earth in France, Reyrieux (Photo: Auroville, earth institute) 10
Figure 1.15 Regions of using rammed earth in France [11] 11
Figure 1.16 Rammed earth house plastered in “Pont de beaux voisins”, Rhône-Alpes, France ... 11
Figure 1.17 Renovation of a part of rammed earth house in “Pont de beaux voisins”, Rhône-Alpes, France 12
Figure 1.18 Stabilized Rammed earth construction in Australia 13
Figure 1.19 Church in Margaret River, Australia made from stabilized earth constructed in 1983 13
Figure 1.20 Stabilized rammed earth in Domaine de la Terre, l’Isle d’Abeau, France (from Auroville, earth institute) 14
Figure 1.21 Pre-fabricated walls being craned into position during construction at Montbrison, Loire (Photo: N. Meunier, 1995) 14
Figure 1.22 Building constructed with 160 pre-fabricated elements [22] 15
Figure 1.23 General view from the south of the walls on the site [49] 19
Figure 2.1 Envelopes for rammed earth construction recommended by Houben and Guillaud [36] 25

Figure 2.2 Relationship between dry density and compressive strength [53] 26
Figure 2.3 Compaction curves and variation of compressive strength with water content and compaction pressure [57] 27
Figure 2.4 The determination of the modulus of elasticity following the ASTM standard 28
Figure 2.5 Variation of compressive strength with water content [63] 30
Figure 2.6 Rammed earth soil origin: farmhouse before and during the demolition, (Photo: N. Meunier) 31
Figure 2.7 Grain size distribution of the earth used 32
Figure 2.8 XRD Patterns of the used soil [66] 33
Figure 2.9 Compaction curves from Proctor tests [68] 33
Figure 2.10 Results obtained with the standard proctor tests using manual and pneumatic rammer 35
Figure 2.11 Prismatic specimens (25 cm × 25 cm × 50 cm) after surfacing 36
Figure 2.12 Polystyrene molds used for the manufacturing cylindrical specimens 36
Figure 2.13 Cylindrical specimen (20-cm diameter, 40-cm height) during the test setup 37
Figure 2.14 (a) Close view of the speckle pattern and the region of interest of a lateral face of a cylindrical specimen (b) and the corresponding histogram of grey level 38
Figure 2.15 (a) Central part used to calculate the Young modulus from the DIC; (b) the vertical displacement fields for the corresponding figure 39
Figure 2.16 State of loading (represented by numbers) corresponding for the calculation of the strain through DIC on Figure 2.16 for specimen (C3) 41
Figure 2.17 The crack pattern and the direction of principal vectors showed by the 7D software for one of the cylindrical specimen (C3) in different states of the loading 44
Figure 2.18 Variation of the density within the layer shown on a rammed earth wall 45
Figure 2.19 The deformation in the direction parallel to the loading for 17 kN state of load for the specimen (C3) 45
Figure 2.20 Failure pattern of the cylindrical specimens (C1) and (C2) 46
Figure 2.21 Crack pattern in the case of two prismatic specimens (P4) and (P5) 47
Figure 2.22 Failure of prismatic specimen 47
Figure 2.23 Effect of the friction in a uniaxial compression test [74] 48
Figure 2.24 Principle of the direct shear test 50
Figure 2.25 Mohr-Coulomb failure envelope 51
Figure 2.26 The model of the large-scale designed shear box 53
Figure 2.27 (a) Manufacturing rammed earth directly in the shear box; (b) Opening two sides of the shear box for evaporation 54
Figure 2.28 The shear box installed on the loading frame 55
Figure 2.29 (a) Plastic film on top of the rammed earth layer; (b) Adding sand on top of the specimen for the surface leveling 55
Figure 2.30 (a) The configuration of the test setup; (b) Positions of the displacement sensors ... 56
Figure 2.31 The horizontal shear force in function of the horizontal displacement of the horizontal actuator 57
Figure 2.32 Unmolding of the upper part of the shear box after the test 58
Figure 2.33 The sheared surface of each specimen with the corresponding value of vertical stress 58

Figure 2.34 Plot of the determination of c and φ for the large shear box inside one layer 59
Figure 2.35 The horizontal shear force in function of the horizontal displacement of the horizontal actuator for the two case tests 60
Figure 2.36 Plot of the determination of c and φ for the large shear box for the two cases 61
Figure 2.37 Variation of the suction in function of soil water content with respect to ENTPE calibration values [87] 62
Figure 2.38 Variation of shear strength with moisture state at test – 30° inclination [88] 63
Figure 2.39 Properties in function of depth for soil normally consolidated: (a) consolidation pressure; (b) undrained cohesion 65
Figure 2.40 (a) A standard direct shear test; (b) the rammed earth specimen inside the box 66
Figure 2.41 Location of the collected samples inside one layer (upper and middle part of earthen layer) 67
Figure 2.42 (a) specimen taken from the upper part; (b) specimen taken from the middle part of an earth layer 67
Figure 2.43 Plot of the determination of c and φ for the standard shear box with the density of each specimen 68
Figure 3.1 (a) Experimental setup of diagonal shear test; (b) Crack pattern at failure of one of the walls, [99] 75
Figure 3.2 Stress-strain curves of the unreinforced rammed earth wallets tested under diagonal compression [99] 75
Figure 3.3 Scheme of the cyclic in-plane shear-compression test [75] 76
Figure 3.4 Crack pattern under a combination of vertical compression and cyclic shear: (a) RE Wall 1, (b) RE Wall 2, (c) and RE Wall3, [75] 76
Figure 3.5 Experimental setup, from the study of [100] 77
Figure 3.6 Failure of unreinforced rammed earth, from the study of [100] 77
Figure 3.7 Horizontal load–displacement response for the wall specimens before and after reinforcement (solid line) [100] 78
Figure 3.8 Failure modes of walls subjected to shear [101] 79
Figure 3.9 Failure mechanism: (a) Sliding on bed joint; (b) Diagonal cracks formation, [102] .. 80
Figure 3.10 Schematic presentation of different types of tests suitable for evaluation of parameters of seismic resistance of masonry wall [104] 81
Figure 3.11 Metallic formwork fixed to the ground before the manufacturing 82
Figure 3.12 Manufacture of the wallet-specimens: (a) preparation of the soil; (b) compaction by the means of a pneumatic rammer; (c) demolding the frameworks; (d) placing the concrete beam on top of the wall 83
Figure 3.13 The four rammed earth specimens before the pushover test 85
Figure 3.14 Test setup on a rammed earth wall (1.5 m × 1.5 m × 0.25 m) 86
Figure 3.15 Vertical tie rod to prevent the beam from rocking 86
Figure 3.16 (a) The position of spot lights and camera; (b) Close-up of a camera and adjustment apparatus 87
Figure 3.17 System placed on top of the beam 88
Figure 3.18 Evolution of the forces applied by the actuators VE1, VE2 and VH and measurement of the sensors M1, M2 and M3 in a function of time for the case of test wall 1 89

Figure 3.19 Horizontal force in function horizontal displacement provided by the hydraulic actuator VH for each of the tested walls. 90
Figure 3.20 Pixels close to the placement of M3 91
Figure 3.21 Comparison between the displacement given by the image correlation and the displacement sensor in function of the horizontal force VH for wall 1 91
Figure 3.22 Displacement vectors of wall 1 during the vertical loading phase 93
Figure 3.23 Vertical deformation at the end of the preloading phase (case of wall 3) 93
Figure 3.24 Horizontal loads on top of the walls in relation to the top horizontal displacements 94
Figure 3.25 Point chosen for the calculation of the top displacement 95
Figure 3.26 Damage of wall 1 after reaching the ultimate load 96
Figure 3.27 Wall 1 just after the manufacturing 96
Figure 3.28 Visualizing less compacted areas in the exterior surface of wall 1 comparing to wall 4 97
Figure 3.29 Strut and tie model: force transfer mechanism from which diagonal shear failure occurs 98
Figure 3.30 In-plane bending failure in a wall 98
Figure 3.31 Crushing on the left side for different walls during the test 99
Figure 3.32 Tensile stresses resulting from compressive strut 100
Figure 3.33 Direction of principal maximal strain vectors that highlight the deformation on the left side of the wall 1 for the ultimate strength 100
Figure 3.34 Visualizing the strut direction through the displacement vector for wall 1 101
Figure 3.35 Expansion of cracking width for wall 1 after attaining the ultimate strength 101
Figure 3.36 Cracking evolution of the wall 1, in function of horizontal displacement 102
Figure 3.37 Crack growth due extension during the pre-loading phase for wall 4 103
Figure 3.38 Crack closure due to compressive stress during the pre-loading phase for wall 4 103
Figure 3.39 Cracking evolution of the wall 4, in function of horizontal displacement for wall 4 104
Figure 3.40 Damage of wall 4 during the horizontal loading for 52 kN of horizontal load (state 2 on Figure 3.39) 104
Figure 3.41 Cracking evolution of the wall 2, in function of horizontal displacement 105
Figure 3.42 Cracking evolution of the wall 3 in function of horizontal displacement 106
Figure 3.43 Losing pixels due to loss of material observed for wall 3. 107
Figure 3.44 Developing of horizontal crack in the first layer and the appearance of local vertical crack near center for wall 2 and 3 108
Figure 3.45 Rocking at the base of wall 3 for 2 (corresponding to 36 kN horizontal loading) 109
Figure 3.46 Rocking at the base of wall 2 (corresponding to 32 kN horizontal loading) 109
Figure 3.47 Summary of all the failure modes of rammed earth walls subjected to shear 110
Figure 3.48 The four walls at the end of the test 111
Figure 3.49 Visualizing interface failure when destroying the walls after each test 112
Figure 4.1 Material models adopted in the numerical modeling: (a) stress-strain relationship in compression; (b) stress-strain relationship in tension; (c) Coulomb friction model used in the interfaces, [76] 117

Figure 4.2 Behaviour of the macro- and micro-model: (a) using the initial parameters; (b) after calibration [76] 117
Figure 4.3 Comparison of the numerical and experimental results for vertical loads [77] 118
Figure 4.4 Comparison of the numerical results in the case of diagonal loading [77] 118
Figure 4.5 Experimental setup of a diagonal compression test [99] 121
Figure 4.6 Numerical model 121
Figure 4.7 (a) Numerical and experimental results of the diagonal compression test; (b) and a zoom at the initial behavior 122
Figure 4.8 Geometry and boundary conditions of the numerical model 124
Figure 4.9 Results of the numerical model with the input parameters of large shear box 126
Figure 4.10 Comparison of the numerical and experimental results 128
Figure 4.11 Comparison of the numerical and experimental results according to the 1st simulation 130
Figure 4.12 Comparison of the numerical and experimental results according to the 2nd simulation 130
Figure 5.1 Distribution of earth construction and high seismic areas in the world [113] 134
Figure 5.2 Earth building map and seismic zones in France [11] 135
Figure 5.3 (a) Fujian Tulou (Hakka rammed earth building) cluster, Fujian province, Southern China; (b) Huanji Tulou wall crack after earthquake, [117] 137
Figure 5.4 Damage of an unreinforced and unstabilised rammed earth building in New Zealand near to Darfield in 2010 [119] 138
Figure 5.5 Damage limit states following drifts proposed by Calvi [126] 140
Figure 5.6 The force-drift ratio for wall 2 and 3 with the evolution of the limit states 142
Figure 5.7 Quantifying the crack width and location with the corresponding limit state 144
Figure 5.8 Suggested limit states for rammed earth walls 145
Figure 5.9 Elastic spectrum from Eurocode 8 146
Figure 5.10 Conceptual explanations for transformation of MDOF to SDOF system 147
Figure 5.11 Bilinear idealization for the equivalent SDOF system [120] 149
Figure 5.12 Demand spectra in S_a-S_d format for constant ductility [132] 150
Figure 5.13 Pushover analysis processing 150
Figure 5.14 Estimation of target displacement from Eurocode method for $T^* > T$ 151
Figure 5.15 Estimation of target displacement from Eurocode method for $T^* < T_c$ 152
Figure 5.16(a) Example of a simple plan of a rammed earth house inspired from (www.architecte-interieur-lyon);(b) The surface of loading calculation corresponding to the internal wall 153
Figure 5.17 The transfer of the loading corresponding to each wall and the equivalent mass of each wall 153
Figure 5.18 Transformation from force-displacement curve to acceleration-displacement curve for case of wall 1 156
Figure 5.19 Idealization of the capacity curves for wall B2 and B3 157
Figure 5.20 Idealization of the capacity curves for wall D1 and D4 157
Figure 5.21 Capacity spectrum for different seismicity zones, soil A 158
Figure 5.22 Capacity spectrum for different seismicity zones, soil B 158

Figure 5.23 Visualizing the intersection points between the elastic spectrum and the capacity curves.....159

List of Tables

Table 1.1 Energy consumption for different type of construction types [28] 16
Table 1.2 Diffusivity of different building material according to [37] and [38] 17
Table 1.3 Recommended design values for rammed earth from several codes 18
Table 2.1 Summary of material properties for rammed earth in the literature 28
Table 2.2 Characteristics of the specimens 37
Table 2.3 Results of the unconfined compression tests (C: Cylindrical specimen, P: Prismatic specimen) 40
Table 2.4 Comparison with other studies in the literature 40
Table 2.5 Moisture content at the testing time depending on the curing time for different type of tests conducted in this thesis 64
Table 2.6 Results of the parameters: large shear box and small shear box 69
Table 2.7 Synthesis of friction angle and cohesion. 70
Table 3.1 A comparison of test results for the wall specimens under in-plane loading from the literature 78
Table 3.2 Characteristics of the wall specimens 84
Table 3.3 Summary of loading system parameters 88
Table 3.4 Young's modulus of the walls 94
Table 3.5 Summary of walls results 95
Table 4.1 Lists of the different parameters required for the different material 124
Table 4.2 Numerical values chosen for the numerical model of rammed earth wall based on the large shear box data 125
Table 4.3 Numerical values chosen for the numerical model of rammed earth wall based on the small shear box data 127
Table 4.4 Parameters considered in the parametric study 129
Table 5.1 Summary of some of the earth buildings inspected after the February 2011 Christchurch Earthquake 137
Table 5.2 Local deformation measures for characterizing different limit states 141
Table 5.3 Scale effect parameters from experiments to the scale of rammed earth wall building 155
Table 5.4 Inter-storey drifts calculated for soil A 160
Table 5.5 Inter-storey drifts calculated for soil B 160
Tableau 6 Résultats des tests de compression non confinés 180
Tableau 7 Résultat de petite et grande boite 181

Chapter 1. An Overview on Rammed Earth in building materials

1.1 Introduction

The objective of this chapter is to present an overview of earth construction and particular on rammed earth structures. The importance of these constructions and the necessity of the conservation of earth heritage are being highlighted along with the importance of enhancing scientific researchers in this domain. Finally, we mention the vulnerabilities of these structures and some of the intervention techniques that are found in the literature.

1.2 Background on earth construction

Since ancient times and from the beginning of civilization, men have used earth to build their houses, monuments, temples etc. Based on an archaeological excavation, the first use of earth goes back to 10 000 BC from the eastern Mediterranean [1]. The earth is widespread worldwide with a large availability, therefore a large number of buildings from earth are found in the world with a great number of earthen heritages.

According to some statics from UNESCO:

- 15 % of the "world cultural heritage" is built with earth
- 25 % of the "world heritage in danger" is built with earth
- 14 % of the "100 most endangered world heritage" is built with earth

Avrami et al. [2] have estimated that more than a half of the world population lives in earth constructions. A great number of these constructions can be found in France, in Germany, in Spain, in North Africa, in Australia, in North and South America and in Asia (China, Japan, …). In some countries, people had no other alternative but to build with earth due to the cost the industrial materials. On the other hand, developing countries look at this material as a new material resource for construction.

The concept of earth construction implies using the local soil. According to [3], there is a wide variety of earth construction techniques that exists which depends on the way of implementation and the soil proportion in clay and water.

These techniques are wattle and daub; cob; rammed earth; earth bricks (adobe) or compressed earth blocks (CEB) assumed to be a popular modern earth technique. The most common techniques are adobe masonry and rammed earth walls. Figure 1.1 shows the distinction between these techniques.

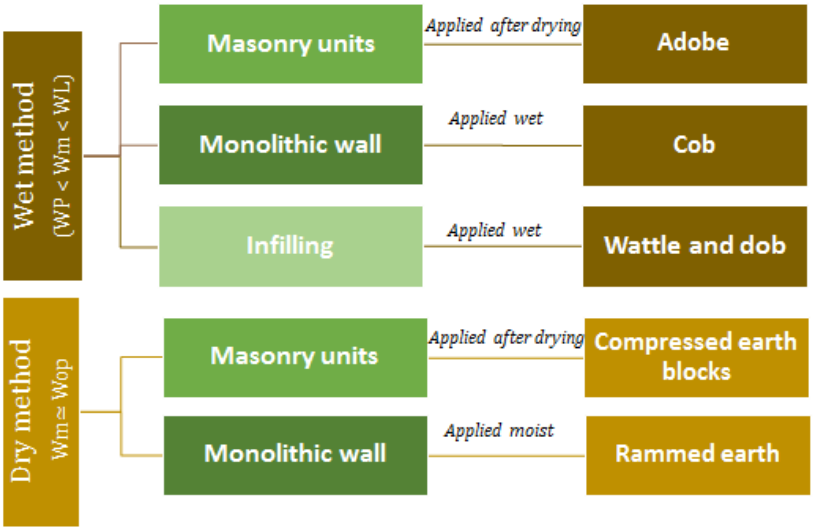

Figure 1.1 Earth construction processes classification adapted after Hamard et al. [4], (Wm = manufacture water content, Wop = optimum Proctor water content; WP = water content at plastic limit; WL = water content at liquid limit)

1.2.1 Wattle and daub

For the wattle and daub, some various techniques exist depending on the region. In the typical technique, the earth is filled against a structure of timber elements. This technique was used for almost 6000 years [5]. The earth, in this case, had no structural function, it can include straw and the mixture is in general very clayey. On the other hand, the timber holds the bearing capacity. This technique is for non-bearing walls and can be used for external and partition walls up to 20 cm thick. Figure 1.2 shows two houses made of wattle and daub in Germany and France, consecutively.

Figure 1.2 (a) Building in the central German city of Bad Langensalza made of wattle and daub (Photo: Sebastian Wallroth); (b) House in France, Alsace (Photo: Auroville Earth institute)

1.2.2 Adobe

Adobe is also an ancient construction technique that consists of filling molds with moist earth to obtain finally the desired shape (Figure 1.3); the adobes are then left in the sun to dry. They are ready to be used as masonry units. The applied mortar is usually made from the same earth used in the production. Many examples can be found for this type of construction in rural and urban buildings as shown in Figure 1.4.

Figure 1.3 Production of Adobe in Ecuador [6]

Figure 1.4 Examples of existing adobe constructions in Aveiro district, Portugal [7]

1.2.3 Cob

As for the cob technique, it consists of mixing clay, sand with organic fibers like straw with the addition of water and the mixture is usually applied by hands without any formwork as in Figure 1.5 (a).

The technique was abundantly used in Europe, where it is termed “Cob” in England and “Bauge” in France; it is similar to the one of the adobes but in some cases it involves the use of more straw fibers mixed in. Many examples also exist as in Saudi Arabia (Figure 1.5 (b)) and the old historical buildings in Shibam, Yemen which involves both rammed earth and cob.

Figure 1.5 (a) Technique of Cob construction; (b) Masmak Castle in Riyadh, Saudi Arabia (Photo: M. Abdulaziz)

1.2.4 Compressed earth bricks (CEB)

Comparing to the traditional earth construction, the CEB (compressed earth bricks) technique is considered to be recent in the earth construction. This method consists of using specific presses to compact earthen materials using molds. The pressure can be applied manually or mechanically (Figure 1.6). This method is considered to be an improvement of the adobes by increasing the mechanical properties (mainly the density). Figure 1.7 shows an example for apartments in Morocco made from CEB blocks.

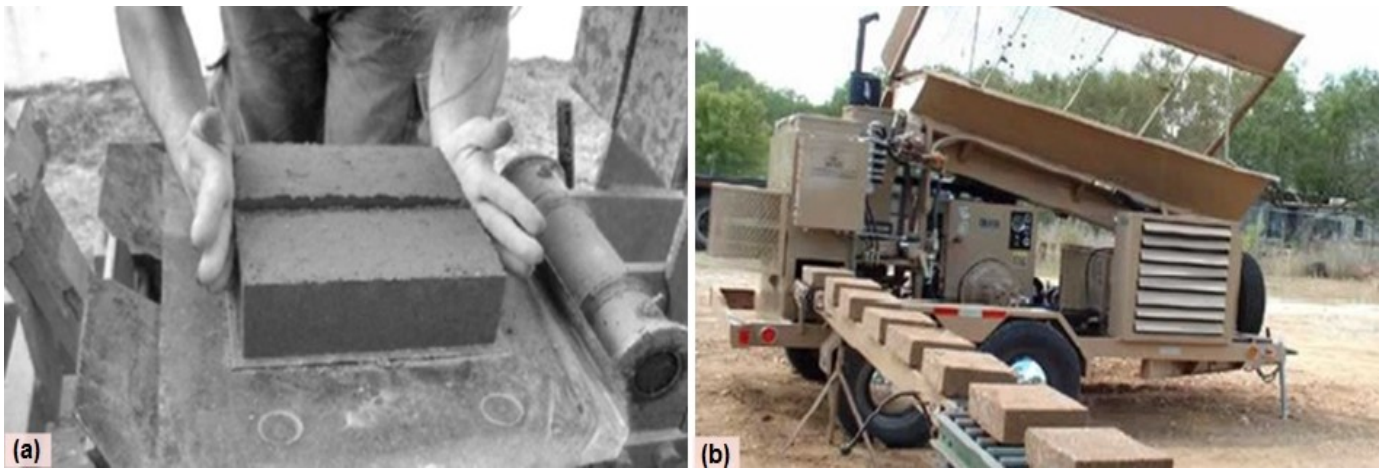

Figure 1.6 Compressed earth blocks manufactured by means of (a) a manual press [8]; (b) hydraulic press [9]

Figure 1.7 Apartments from CEB in Marrakesh, Morocco [10]

1.3 Rammed earth

Rammed earth walls are built by compacting soil between temporary formworks. The formwork usually consists of two parallel surfaces separated and interconnected by spacers as shown in Figure 1.8(a). The principal binder of the grains is the clay. The mixture of the earth is compacted into layers of approximately 15 cm by the use of a rammer. The average thickness of the wall is 50 cm. As each form is filled, another form is placed above it, and the process is carried on until achieving the desired wall height. Forms can be removed directly as soon as the form above is begun.

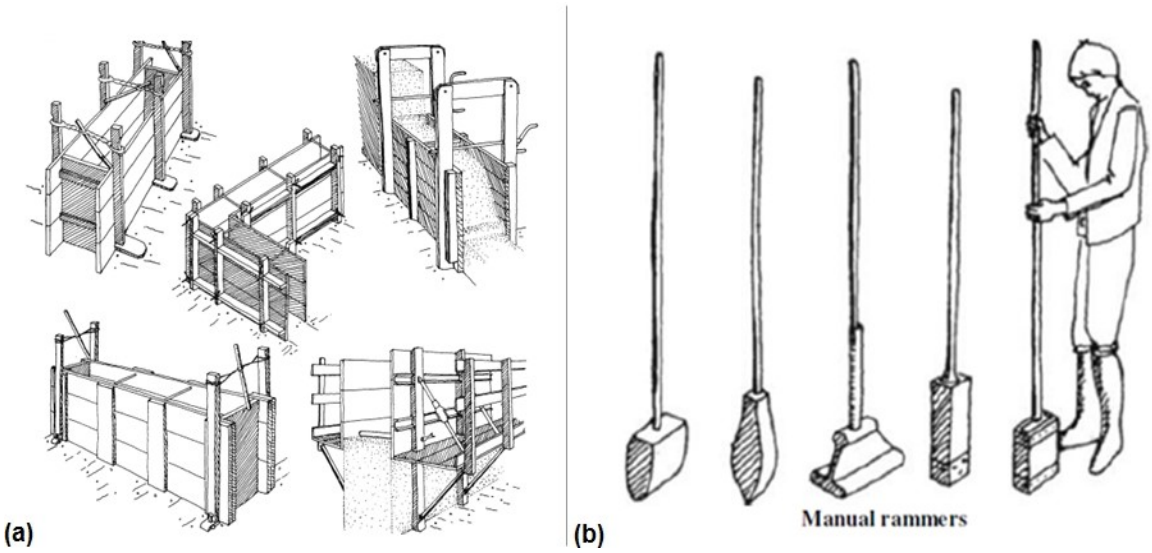

Figure 1.8 (a) Formwork used in for traditional rammed earth; (b) Rammers used to compact rammed earth, [6]

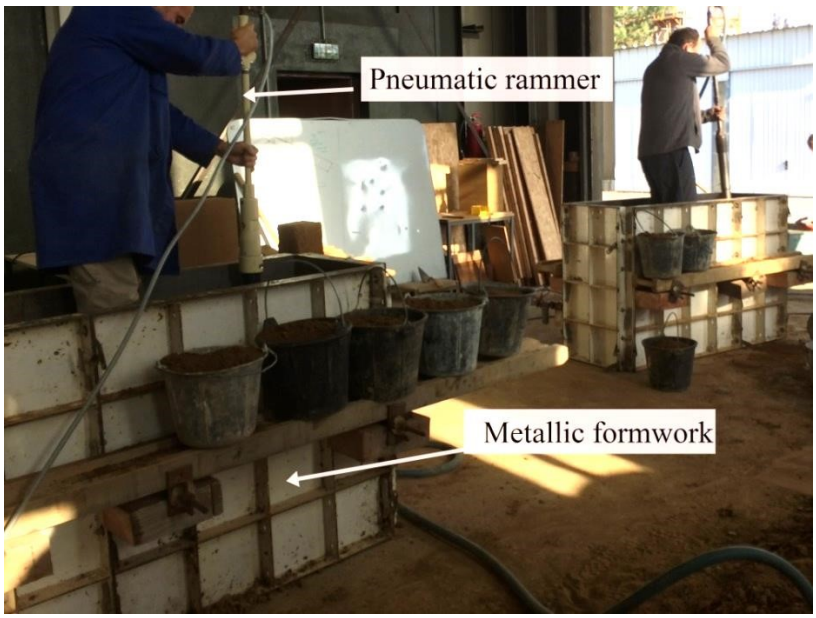

Figure 1.9 The use of pneumatic rammer and metallic formwork in modern techniques, (Photo from the laboratory of ENTPE, Lyon)

The compaction of rammed earth layers is traditionally performed manually using a rammer generally made of wood with different base shape (Figure 1.8 (b)). Nowadays the manual rammer is replaced by a more powerful pneumatic rammer that increases the rapidity of manufacturing and the density of the material (Figure 1.9). Pneumatic rammers are normally powered by compressed air.

In the traditional technique, the formwork is usually made out of wood. Nowadays, metallic shutters are being used instead. The formwork should be well braced in order to assure the stability and preventing any deformation due to the high compressive force induced by the rammer during the compaction process.

The walls take some time to dry completely as the compressive strength increases with the curing time. Figure 1.10 shows a traditional house made of rammed earth in France and Figure 1.11 exhibit the typical earth layers of a test wall in the laboratory of LOCIE, Chambery.

Rammed earth are generally founded on a base built from (stone, pebbles) about 50 cm high [11] to protect the walls from rising damp. In the case of modern construction, this masonry base is usually made from concrete.

Figure 1.10 Traditionnel house in « Pont de beau voisins », Rhône-Alpes, France

Figure 1.11 Visible compacted layers with different thickness of a rammed earth wall constructed in the LOCIE laboratory

1.3.1 Historical Background

From its vernacular use to the monumental impressive construction, rammed earth has left a trace in almost all the continents in the world where some outstanding historical structures can be found.

Some of these historical examples around the world are:

Horuji temple that is Japan's first World Cultural Heritage site [12] built 1300 years ago, the great wall of China one of the largest building-construction, the world heritage site of the Alhambra Palace in Spain constructed around 1238 [13], buildings of Shibam, Yemen made up to 14 stories high [14] that is also declared by UNESCO as world heritage [15] and the most ancient skyscraper city in the world [3]. These constructions are illustrated in Figure 1.12. These

buildings stand out for the possibility of building higher than 2 floors when using rammed earth and represent a good example of the potential durability of the material.

Figure 1.12 Examples of historical constructions around the world made from rammed earth: (a) Great wall of China; (b) Buildings in Shibam, Yemen (Photo: Auroville earth institute); (c) Alhambra Palace of Granda, Spain [13]; (d) Temple in Japan [12]

In Europe:

Rammed earth had been spread from the Mediterranean basin and had been exported to Europe since the 8th century [16]. A great history of earth construction with a wide variety of techniques can be found in Europe. Some of the well-known examples of rammed earth structures that can be found in Europe include a seven-storey load-bearing rammed earth building in Weilburg, Germany (Figure 1.13); the building was constructed in 1828 and is still in use today as well as a rammed earth castle in France that dated to the 17th century (Figure 1.14). These remarkable examples demonstrate once again that with good design and execution the material can meet our various demands of a construction material.

Figure 1.13 A six stories building in Weilburg, Germany [17]

Figure 1.14 Château de Reyrieux, made from rammed earth in France, Reyrieux (Photo: Auroville, earth institute)

Rammed earth in Rhône alpine region, France:

In France, these structures are widespread especially in the Rhône alpine region (as shown in the map by Figure 1.15) where they represent around 40% of rural architectural heritage [18]. A lot of these structures date to more than 300 years and many are still inhabited.

Nowadays, some of these rammed earth houses are plastered for rehabilitation especially for filling existing cracks. The coating can also protect the structure from the effects of weathering.

In the Rhône alpine region, many houses are found coated with plaster and some of them could not even be recognized that they are basically from rammed earth (Figure 1.16, Figure 1.17).

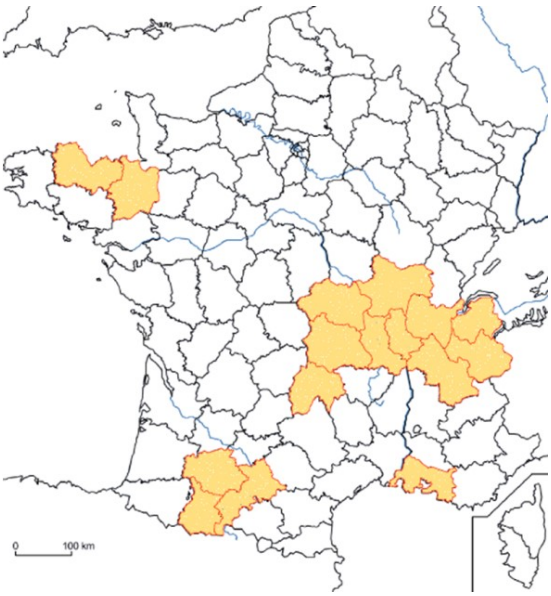

Figure 1.15 Regions of using rammed earth in France [11]

Figure 1.16 Rammed earth house plastered in "Pont de beaux voisins", Rhône-Alpes, France

Figure 1.17 Renovation of a part of rammed earth house in "Pont de beaux voisins", Rhône-Alpes, France

1.3.2 Modern rammed earth

Stabilizing rammed earth:

Today, there are essentially two types of rammed earth: stabilized and non-stabilized rammed. The one made only with clay, is called unstabilized rammed earth as seen earlier in Figure 1.10. Concerning the modern rammed earth, nowadays numerous are stabilized with a hydraulic binder (cement agent) to increase its performances.

In Australia, for example, a large number of modern rammed earth houses (Figure 1.18 and Figure 1.19) were built and estimated to about 25% of new housing [19]. The main reasons for the stabilization are to limit the sensitivity of this material to erosion and to increase its compressive strength. In fact, the sustainability of rammed earth strongly depends on climate and rainfalls. Therefore, the need for stabilization varies from one region to another. Nevertheless, the stabilization of rammed earth greatly increases the cost of construction and the recycling of the material becomes very difficult. Many studies have shown that stabilized rammed earth increases the embodied energy [20], [21]. Some other examples of modern houses in France are illustrated in Figure 1.20 in Isle d'Abeau.

Figure 1.18 Stabilized Rammed earth construction in Australia

Figure 1.19 Church in Margaret River, Australia made from stabilized earth constructed in 1983

Figure 1.20 Stabilized rammed earth in Domaine de la Terre, l'Isle d'Abeau, France (from Auroville, earth institute)

Pre-fabricated rammed earth panels:

Modern rammed earth involves the pre-fabrication of rammed earth panels. The prefabricated earth walls are normally produced in large molds, then lifted by cranes (Figure 1.21) and set on beds of lime mortar. The pre-fabrication of these panels can be produced either on-site or in workshops. An example of a building constructed with pre-fabricated walls is illustrated in Figure 1.22.

Figure 1.21 Pre-fabricated walls being craned into position during construction at Montbrison, Loire (Photo: N. Meunier, 1995)

Figure 1.22 Building constructed with 160 pre-fabricated elements [22]

1.3.3 Advantages of rammed earth material

Towards sustainable development:

The construction sector is one of the most important contributors in energy consumption [23]. In fact, building consumes throughout its life cycle about 20-40% of the total energy use and it has exceeded other sectors [24]. Moreover, it is responsible for high levels of pollution and serious environmental impacts due to the high embodied energy from transformation processing, it also produces a large amount of waste [25]. This industry is considered to be responsible for 30% of carbon dioxide emissions [26].

In world terms the construction industry will keep growing, therefore, it becomes necessary to search for alternative constructive choices that ensure a sustainable development by reducing the construction embodied energy. Choosing a suitable building material can lead to approximately 17% reduction in the energy of a building [27].

Turning to non-industrial materials as local materials can help reduce the energy consumption of the building sector. These materials are extracted directly on the construction site (or near the site) like raw soil and then transformed into construction material with a very low manufacturing energy.

In a study conducted by Morel et al. [28] about the environmental benefits of using local materials, a comparison of the energy consumed between a typical concrete house and a house made of a local material (house made of rammed earth and house made with stone masonry with mortar) was established. The results of this study are summarized in Table 1.1. It was found that the rammed earth house consumes less energy (70 GJ instead of 239) than the concrete house and the house made of masonry (97 GJ instead of 239). Therefore, adopting local materials decrease the amount of energy used in the building and the impact of transportation as well.

Table 1.1 Energy consumption for different type of construction types [28]

	Masonry	Rammed earth	Concrete
Energy (GJ)	97	70	239
Transport (t.km)	1390	1041	6707

The second environmental advantage lies in the demolition phase of the buildings. In fact, the demolition and destruction phase of a material also contributes to the energy consumption of the construction sector [29]. Unstabilized rammed earth is easily recyclable with no need of special treatment or specific storing techniques. The earth can be reused for construction without any environmental impact and therefore no problem of material waste as is the case of conventional materials [30].

Earth construction assumes in this particular context, an environmental advantage through a building life cycle: from construction, operation, maintenance, renovation, and demolition.

Combining thermal comfort with energy efficiency:

Rammed earth walls have a low thermal resistance (*R*-value) [31], in this case, it is expected that they have a poor thermal performance which can contribute for the heat conduction. On the contrary, many researchers have found that the large thermal mass of the rammed earth is capable of improving the thermal characteristic of this material [32], [33] and [29].

In winter, rammed earth serves as thermal mass, the thick walls provide thermal energy storage, absorbing heat from the sun during the day to be released slowly at night when the temperature drops [34].

For a better understanding of this idea, we can have a look at the thermal diffusivity in the material.

In heat transfer analysis, thermal diffusivity is defined as the thermal conductivity divided by density and thermal capacity. It measures the rate of transfer of heat of a material:

$$D = \frac{\lambda}{\rho C_P} \tag{1.1}$$

where

λ is thermal conductivity of the material (W/(m·K))

ρ is density (kg/m³)

C_p is thermal capacity at constant pressure (J/(kg·K)).

Therefore the lower the diffusivity is, the higher is the buffering effect of the material and, as a consequence, there is a time-delay between changes in the external and internal temperatures, referred to as the “thermal lag” [35], [36].

It is, therefore, interesting to have a comparison of the coefficient of diffusivity between different building materials (Table 1.2). According to Table 1.2, earth material (dry or in brick form) offers the lowest values of the material diffusivity which enables to provide thermal comfort during dwelling.

Table 1.2 Diffusivity of different building material according to [37] and [38]

Materials	Density (kg/m^3)	Conductivity (W/ mk)	Diffusivity (m^2/s)
Concrete	2300	1.8	7.8e-7
Dry rammed earth	1730	0.6	5.4e-7
Earth Brick / adobe	1800	0.74	4.1e-7
Stone	2000	1.7	8.5e-7

In the case of hot climate, especially in the summer, the earth walls also contribute to the thermal regulation by absorbing and releasing moisture when necessary, it, therefore, provides a thermal comfort and a more refreshing environment for the occupants. The walls offer the ability to act like a passive air conditioner which will keep ambient conditions inside the building.

With the thermal comfort comes the low energy consumption. In fact, the energy consumption during the occupancy is a major contributor for the energy in the building sector. Having, therefore, a thermal comfort during the dwelling will reduce the energy use for heating or cooling. In this context, rammed earth structure improves the energy efficiency because of their capacity for regulating the temperature and humidity in the indoor air. Some studies were carried out showing a lower energy consumption of the building with rammed earth compared to conventional buildings [39]. Indeed, this is a very desirable aspect to look for in building conception which is promoting for rammed earth constructions.

Earth construction guidelines:

Some countries have already their earth construction standards. Unfortunately, these guidelines are based on conventional materials (e.g. concrete) studies. Consequently, several clauses of these standards need to be improved. This section provides guidelines and codes that exist in the literature. Many countries have set out structural design and structural strengthening of the rammed earth also requirements for formwork, methods of construction, testing and curing of rammed earth. Australia, the New Zealand and Mexico have specific regulations on earth construction.

For example, the Australian Earth Building Handbook was published by [40]. This handbook sets out the principles of good practice and recommended design guidelines, including structural

values or earth-wall design primarily for two-storey building using stabilized and unstabilized earth. Nevertheless, it is basically a consultative document and is yet to be a complete standard.

New Zealand has one of the most advanced legal regulations on modern earth construction. This is structured in three distinct parts:

- NZS 4297 [41] – Engineering design and earth buildings –establishes performance criteria for mechanical strength, shrinkage, durability, and thermal insulation and fire resistance;
- NZS 4298 [42] – Materials and workmanship for earth buildings – defines requirements for materials and workmanship.
- NZS 4299 [43] – Earth buildings not requiring specific design – this part is applicable for buildings with less than 600 m^2 (or 300 m^2 per floor).

The New Mexico code [44] provides some limited information on the soil suitability and moisture content and guidance for construction methods of rammed earth.

Even for countries advanced in rammed earth design, contradictions exist. For example, NZS 4297 code sets a minimal thickness of the wall of 25 cm while the New Mexico code [44] sets two different thicknesses, 45 cm for external wall and 30 cm for internal walls. These codes also reveal some differences concerning the recommended design values as shown in Table 1.3.

Table 1.3 Recommended design values for rammed earth from several codes

Reference	Compressive strength (MPa)	Shear Strength (MPa)	Young's Modulus (MPa)
New Zealand code	0.5	0.035	150
Australian Handbook	0.4 to 0.6	0	500
New Mexico code	2.07	-	-

Some other regulations also exist, like Zimbabwe that have a special regulation for the rammed earth which handles different sections on the materials details, wall design, water absorption and erosion and masonry structural stability which is based on the code practice for rammed earth from Keable [45]. Other known standards are in India [46] and the United States [47].

A lot of uncertainties remain when considering the design methodologies in these standards especially that they are based on rules for unreinforced masonry due to the lack of knowledge and laboratory testing on earth materials.

Most of these recommendations are obtained through extrapolation of experimental results on soils from different parts of the world with different mineralogy and show some contradiction, therefore they cannot be generalized for any type of soil [48].

1.4 Durability, Vulnerabilities of rammed earth

1.4.1 Durability of rammed earth structures

The durability of the material during the lifetime of the structure is an important feature for rammed earth and it concerns normally the resistance to water erosion. Rammed earth is very sensitive to some external effects as rainfall and environmental effects that can contribute to the reduction of wall thickness. Many tests have been used to evaluate the materials for erosions, but unstabilized materials did not succeed these tests. In general, the erosion tests are considered to be severe for earth materials, so they are not appropriate for this material [3].

On the other hand, real structures showed different behavior. Bui et al. [49]evaluated the performance of 104 sections of rammed earth masonry with and without stabilization that was exposed to natural weathering for 20 years (as shown in Figure 1.23) using stereophotogrammetry. The method of stereo-photogrammetry consists on superimposing two photos to obtain the "relief" that appear using a stereoscope. After that, a comparison must be completed between the current relief and the initial one of the wall after the manufacturing to obtain the erosion. More details about this technique can be found in [50].

The study showed that the mean erosion depth was about 0.5% of wall thickness (about 2mm) for stabilized and approximately 1.6% (6.4 mm) for unstabilized materials. The study indicated that rammed earth walls can exceed a life more than 100 years for non-stabilized rammed earth walls. On the other hand, many historical examples of rammed earth structures could represent a good example of the material durability like the temple Japan that was built approximately 1300 years ago. Yet, many uncertainties remain in this field.

Figure 1.23 General view from the south of the walls on the site [49]

1.4.2 Vulnerability of rammed earth

Rammed earth has weak mechanical characteristics and is particularly sensitive to shear, yet most of the rammed earth constructions are predominantly located in seismic zones which make them susceptible to seismic actions and prone to the danger of collapse or failure by physical degradation and cracking (this subject is addressed more in details in chapter 5).Therefore, maintenance and regular repair to withstand all the mentioned effects can be necessary for the conservation of these building.

These problems can be overcome if suitable improvements to the material and strengthening technique were adopted. In general, there is a lack of information on this topic due to the absence of laboratory tests that can validate these methods. Only few laboratory tests had investigated new retrofitting techniques in the case of a seismic action. Some of these techniques like inserting steel bars, and other retrofitting techniques newly found in the literature are presented in appendix A.

The strengthening methods indicate that earth structures may survive under severe physical and mechanical loading (as earthquakes) with moderate damage if properly designed and reinforced, therefore more research development for the study of rammed earth structure must be conducted and proper reinforcement tools should be tested.

However improving the material strength will deteriorate all the other important aspect of rammed earth like the thermal, the hydrothermal performance, the low embodied energy, the reuse potential, the moisture buffering and the cost of the material.

1.5 Research objectives and methodology

1.5.1 Conclusion and problem statement

Earth constructions exist since ancient time, with a large number of earth buildings built more than 1000 years ago and are still standing today. At present, most of the earth building is located in less-developed rural areas, considering the lower cost of the material in comparison to the conventional building materials.

With the growing consciousness for seeking sustainable materials, rammed earth which is one of the most common earth materials used in the past is attracting scientific researchers. The use of rammed earth material reduces the embodied energy coming from extraction, transportation, manufacturing i.e. needed to make a product. Therefore, one of the basics of using this material is creating an environmentally friendly building and expanding the effort to visualize an ecological world.

The durability and strength of rammed earth is an important issue to be addressed. Many examples of historical examples in the world are a clear evidence of the durability of this material if properly designed and maintained.

Obviously, a better understanding of rammed earth from the mechanical and structural point of view will allow us to master its disadvantages and therefore pursuing advanced studies that will permit to protect our earth heritage and to consider its implementation in modern construction as a sustainable building material for the future application.

1.5.2 PRIMATERRE research project

The work presented in this PhD is part of a research project called PRIMATERRE which is funded by the French National Agency of Research (ANR). The main objective of this project is to have recommendation to guide the implementation of rammed earth material by providing means of measurement and guarantying its hypothermal performance and the mechanical and seismic resistance. To achieve these objectives, a global, multi-scale and multi-disciplinary (materials, energy and sociology of innovation, laboratory and in situ, experiment and modelling) research is proposed.

In the end, the project PRIMATERRE should give insights for both on a scientific and practical level, i.e. also realistic in terms of economic and political conditions in the construction sector in France and Europe by proposing recommendation and teaching modules.

It is worth noting that during the work of this thesis, we had the opportunity to use the other insights given by the partners of this project and data obtained through different tests performed on a different scale.

1.5.3 Thesis objective

Due to the fact that heritage of rammed-earth buildings in Europe and in the world needs to be preserved; unstabilized rammed-earth is now the center of several scientific investigations. Concerning the conservation of earthen historic building, for any appropriate repair, it is often substantial to use earth material compatible with the original material. Therefore, it is essential to have a better understanding for unstabilized rammed earth which is the objective of this thesis.

The work in this thesis focuses on the behavior of unstabilized rammed earth at the scale of a wall. The main objective is to provide an accurate knowledge about the mechanical characteristics of this type of construction under in-plane loading. Therefore, walls were built and tested in the laboratory to study their performance.

How would the rammed earth walls fail under in-plane loading? Does the horizontal layer aspect of the structure reduce the overall resistance? What are the main parameters controlling the earthen layers? Are we capable of assessing the seismic behavior of these structures? Is it possible to numerically model such behavior at the scale of a wall?

All these questions are addressed and were answered thanks to an experimental approach of progressive pushover on a wall of rammed with semi-real scale.

Thesis layout:

The thesis is divided into five chapters.

Chapter 1 retraces the history of rammed earth construction and analyses the advantages and limitations of using rammed earth as a construction material. The main objectives of the present project are also outlined.

A review of past studies on the properties of rammed earth is then presented in Chapter 2. It provides a background for the rest of the study on several aspects, such as the characteristic of a rammed earth material, and the experiments that were previously done on this material. In the second part of this chapter the mechanical properties of the rammed earth used in this thesis are determined in order to have the main characteristics such as the compressive and shear strength.

The rammed earth behavior is then investigated at the wall scale in Chapter 3. An experimental study is carried out on several walls with different height/length ratios. The study was carried out by essentially examining the failure modes under in plane loading. The digital image correlation was an important tool that was used in this study.

The Chapter 4 deals with the Finite Element Model of the experiments on the walls described in Chapter 3. The obtained experimental values on the material scale were used in this numerical model to test their reliability. A parametric study was achieved in order to reproduce the experimental results showing the key parameters of this study.

In Chapter 5, the experiments outputs of Chapter 3 were used for the assessment of the seismic performance of the rammed earth walls in different conditions (seismicity zones and soil types).

The last part of the thesis, *General conclusion* presents the conclusions drawn from the thesis and discusses possible directions that can be considered in the future.

Chapter 2. Identifying the mechanical parameters for the used earth

2.1 Introduction

This chapter deals with the assessment of the material used in this thesis by mainly determining the mechanical properties of the rammed earth. The goal of the experiments explored in this chapter is to acquire basic knowledge on the mechanical behavior of the rammed earth used for the manufacturing of the wall. Therefore, uniaxial compression tests and direct shear test were used to investigate some essential mechanical parameters.

In the first part of this chapter, a review of past studies on the properties of rammed earth is presented. In the second part, the compression tests conducted on the used soil are presented where cylindrical and prismatic specimens were used. The experimental program included also using the digital image correlation (DIC) to reveal the locations of the cracks in the specimen during the loading.

This chapter also intends to contribute to the knowledge of shear parameters of the rammed earth using direct shear boxes (section 2.5). The experimental program included using a conventional small-scale shear box and designing a large-scale shear box. This assessment arises from the importance of selecting a representative specimen that reproduces the real scale conditions. A large-scale shear box has never been used to test the shear parameters of rammed earth in previous studies.

2.2 General comments on the properties of rammed earth material

2.2.1 Grain size distribution

The grain size distribution of rammed earth is an important feature when determining the soil suitability for construction. The usual tests used to quantify the proportions of particles consist of performing dry or wet sieving and sedimentation. In general, the rammed earth composition could have a great dispersion but should contain fine gravel and sand with cohesive soils (silt and clay) to act as a binder between the grains [45].

Houben and Guillaud of CRATerre [36] recommend an envelope for a suitable rammed earth particle-size distribution. It is the most well-known and recommended envelopes for rammed earth structure. The particle size distribution chart is illustrated in Figure 2.1. This means that if the soil fits within limit values, the rammed earth will have the required performance and it is suitable for rammed earth constructions.

However, the assessment of the performance of rammed earth based on the soil properties can be misleading based on the wide diversity of existing soil [48]. Therefore, other laboratory tests as compressive strength of specimens are adopted as an indicator of the material performance.

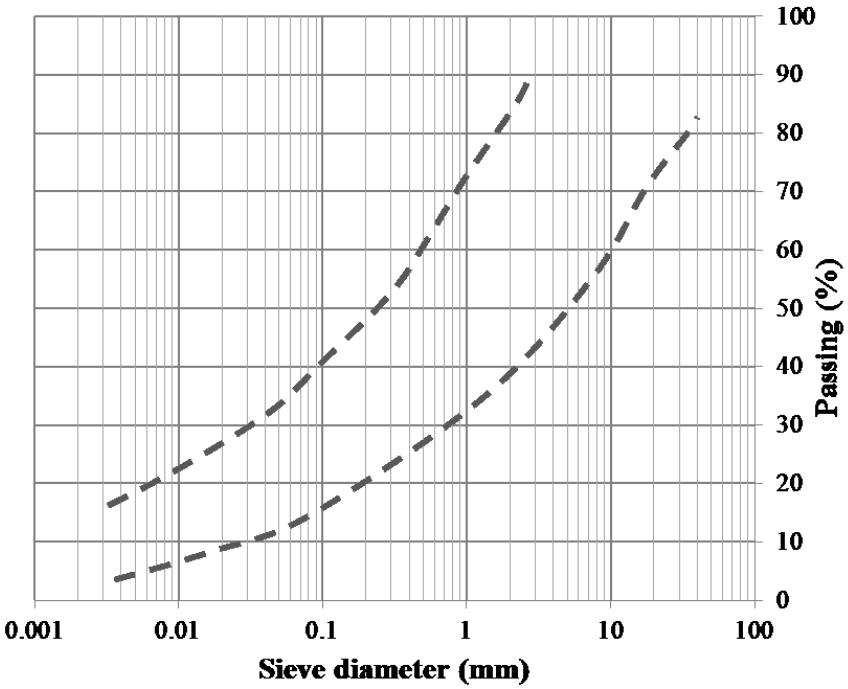

Figure 2.1 Envelopes for rammed earth construction recommended by Houben and Guillaud [36]

2.2.2 Dry density

The dry density of earth material in general and especially of the rammed earth depends on the soil type, the water content during compacting and the manufacturing energy. The maximum dry density gives an indication of the strength of the earthen material. A wide range of dry density values for rammed earth, varying from 1700 kg/m^3 to 2200 kg/m^3 is found in the literature [36], [51] and many others.

The dry density is one of the factors influencing the compressive strength obtained. The resistance to compression of rammed earth is proportional to its dry density as shown by Olivier [52]. A relation between the compressive strength and the dry density achieved in compaction is shown in Figure 2.2 [53].

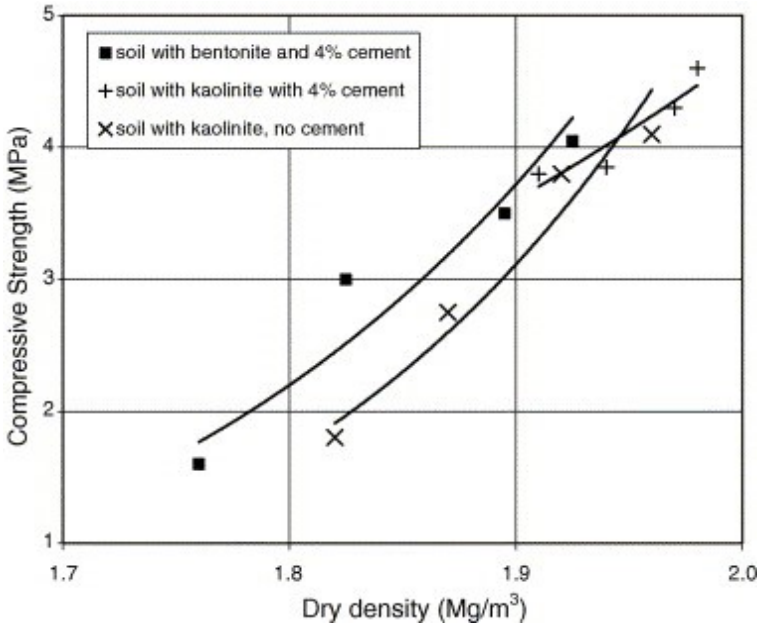

Figure 2.2 Relationship between dry density and compressive strength [53]

Influence of compacting energy:

Many studies were fulfilled to test the influence of the compaction energy on the mechanical properties of earth materials [52], [54]–[56] where it was confirmed that stronger compaction energy increases the dry density of the material and the compressive strength, but the water content must be optimum to obtain the maximum strength.

A study was made by Mesbah et al. [56] on the effect of the compaction energy on the mechanical properties of the "Isle d'Abeau" earth, using cylindrical samples with different pressure levels (from 1.2 MPa to 10 MPa). The optimum water content was determined for the corresponding maximum dry density for each compaction energy. It was found that by using higher energy, the dry density in construction is higher for the same material and the optimum water content becomes lower (as the curves were shifted to the left in Figure 2.3). Results on the compression tests of these samples also confirm that the compressive strength is higher when the density increases.

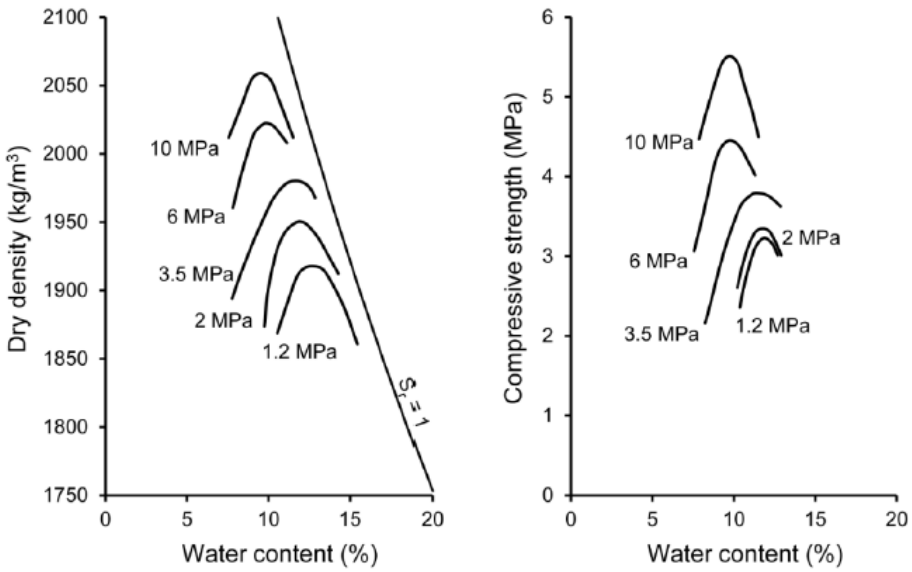

Figure 2.3 Compaction curves and variation of compressive strength with water content and compaction pressure [57]

2.2.3 Mechanical behavior: Compressive Strength

The compressive strength of rammed earth is one of the most important key performance indicators which can be affected by many parameters such as manufacturing moisture content, compaction energy, dry density and sample geometry. Several studies have been carried out recently to analyze its mechanical properties and to characterize its compression strength and elastic modulus.

Summary of some of the material properties of earthen materials found in the (specialized) literature is shown in Table 2.1. In each of these studies, compressive strength and the Young Modulus (E_{tang}) of rammed earth are calculated. The E_{tang} is the conventional young modulus calculated for materials in recent studies in the linear part of the stress – strain curve. This modulus is the slope of the tangent line with the stress-deformation curve. Figure 2.4 illustrates an example of the ASTM standards for the calculation of Young' modulus for the case of thermal insulation material through uniaxial compression tests [58].

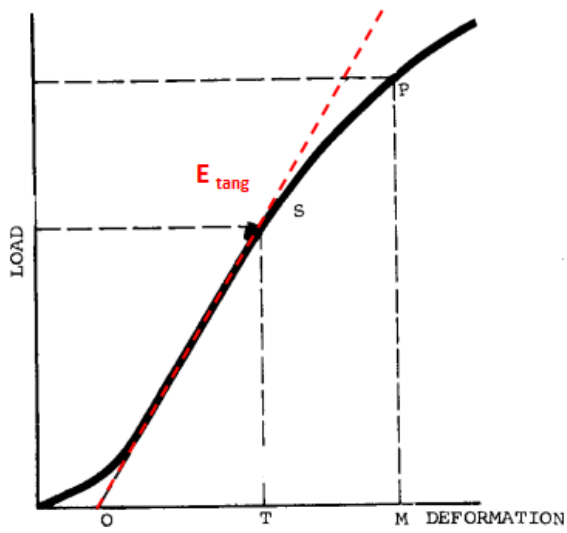

Figure 2.4 The determination of the modulus of elasticity following the ASTM standard

Table 2.1 Summary of material properties for rammed earth in the literature

Specimens	Compressive strength (MPa)	Density (kg/m^3)	Slenderness	E_{tang} (MPa)	Reference
40 × 40 × 65 cm^3	1	1820-1980	1	100	[21]
30 × 30 × 60 cm^3	0.62-0.97	1760-1970	2	160-205	[14]
d=10 cm, h=20 cm	2.46	1850	2	70	[14]
15 × 15 × 15 cm^3	1.8-2	2020-2160	1	-	[59]
10 × 10 × 10 cm^3	0.5-1.3	2020-2160	1	-	[12]

A great dispersion is noted in the materials properties in Table 2.1, particularly for Young's modulus. This is related to many factors as the testing procedures, the workmanship and the type of the soil used. In most of these studies as in [12], [59], the samples are small (10 cm cubes or cylinders 20 cm high ×10 cm in diameter) and are manufactured in the laboratory, hence these samples are not very representative of in-situ material.

Maniatidis and Walker [14] and Bui et al. [60] showed that there is a significant variation in the material performance between small scale samples compared to the samples closer in size to the walls in situ (as shown by the results in Table 2.1). The results of the compressive strength obtained by Maniatidis and Walker, on full-scale prism tests (samples of 60 cm high x 30 cm square prisms) were 50% lower than of the small-scale samples of 20 cm x 10 cm diameter.

Maniatidis and Walker assumed that this variation is due to higher moisture content at the center of the prisms (due to their slower drying rate), and also because of the increase of the gravel content in the full-scale tests. Bui et al. [60] stated that the effect of the compaction energy applied has to be taken into account when manufacturing representative rammed earth samples.

More recent studies are now trying to test the rammed earth having larger scale specimens. Among these studies, Miccoli et al. [61] who investigated the mechanical behavior of earthen materials by comparing three earth materials: earth block masonry, stabilized rammed earth and cob. Compression tests of rammed earth wallets of 50 x 50 x 11 cm^3 were conducted, and it was noted that rammed earth wallets showed the highest compressive strength of all three types of earth constructions, the obtained values of compressive strength is in the range of 3.4 to 4.0 MPa. In another study, Bui et al. [21], gives experimental results on tensile strengths. In this research, local failure was conducted on 100 x 100 x 30 cm^3 walls manufactured in the laboratory and tested under concentrated compression load.

Concerning Young's modulus, several studies were done, showing that the modulus of unstabilized rammed earth can vary from 100 MPa (old walls in the study of Bui and Morel [62] up to 500 MPa (new walls in the study of Bui et al. [60]). However for the stabilized rammed earth, [61] obtained higher values for Young's modulus equal to 4143 MPa, in fact stabilizing the rammed earth have a direct effect on increasing the mechanical performance and thus obtaining higher values for Young's modulus and the compressive strength.

Influence of moisture content on the compressive strength:

One of the problems related to rammed earth material is the water sensibility as in general these materials are very sensitive to water when the surface is exposed to different ambient conditions. With regard to the influence of water on the mechanical properties of rammed earth, Bui et al. [63] studied the effect of moisture content on the mechanical properties of three earthen materials. In this study, different samples with great variation of moisture content from the moment of manufacturing (11–13%) to dry states (1–2%) were tested in unconfined compression at a different state of moisture contents. This study showed that when the moisture content of dry rammed earth walls is below 4% by weight (e.g. due to a change in the RH atmosphere or rainfall) no influence of the wall's strength was detected (Figure 2.5); the variation of compressive strength was not significant. When moisture content was greater than 4%, compressive strength decreases quickly for all tested materials (Figure 2.5).

Subsequently, the stabilization of rammed earth reduces the sensibility to water as seen by the results done for the soil C that showed smaller decreases of the compressive strength compared to the other soils.

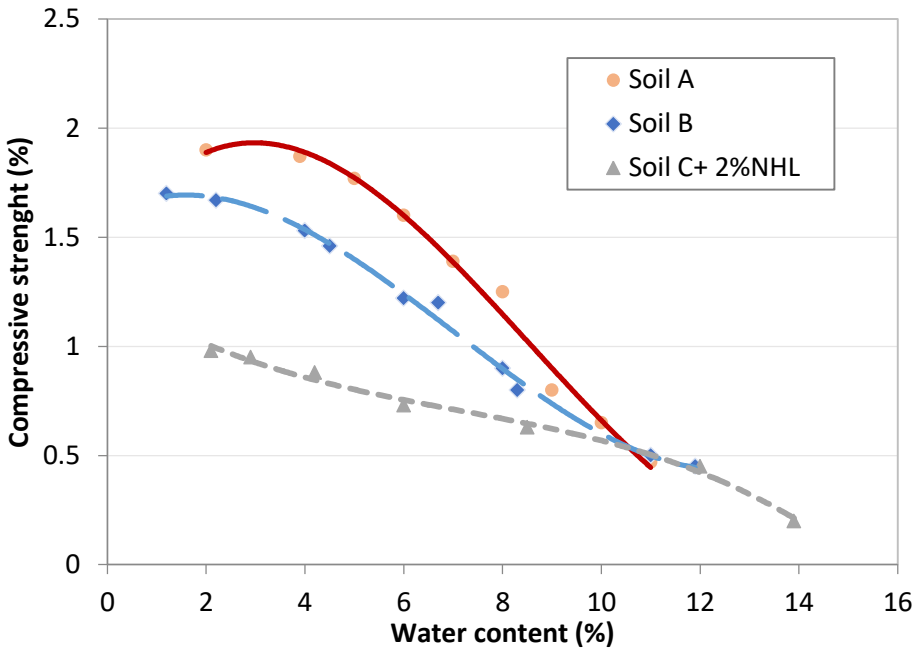

Figure 2.5 Variation of compressive strength with water content [63]

2.3 Properties of the used rammed earth

2.3.1 Origin and physical characteristics

The used earth was provided by a professional rammed earth builder, and it comes from "Dagneux" a village located in the Rhone-Alpes region in the southeast of France, after the demolition of an old farmhouse that was no longer in use (as seen in Figure 2.6). Many existing earth structures are found in this region. Choosing this soil and studying its mechanical behavior is important regarding the conservation and restoration of these building, and for the conception of new earth buildings.

Figure 2.6 Rammed earth soil origin: farmhouse before and during the demolition, (Photo: N. Meunier)

Grain size distribution:

The grain size distribution of the earth has been determined by both wet sieving and sedimentation in accordance with British standard BS1377 [64] and is reported in Figure 2.7.

The earth used is composed of:

- 15% of sand (2 - 0.06 mm)

- 65% of silt (60 - 2 µm)

- 20% of clay (< 2 µm)

The distribution of the grain shows that the soil consists mostly of fine particles (clay and silt) where 50 % of mass was greater than 40 µm in the absence of particles larger than 1mm.

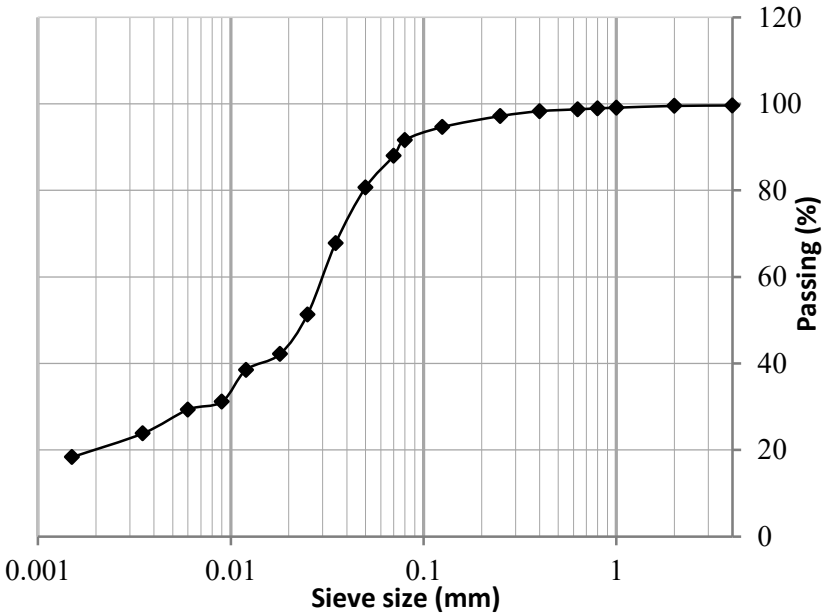

Figure 2.7 Grain size distribution of the earth used

The clay amount in the soil satisfies the limits of clay content proposed in various studies and technical standards [17], [36], [65] where the clay range was varying from 5% (lowest range) to 30% (highest range) which is considered to be acceptable. Nevertheless the particle size distribution does not fit in the area recommended by Houben and Guillaud [17] (Figure 2.1) but as mentioned before this criteria doesn't take into account the great variability of possible soils and techniques; moreover the soil used in this study comes from an existing construction and it is essential to understand the behavior of soil already used in existing structures without any discard to the sustainable aspect of using available local earth [28].

X-ray powder diffraction (XRD) and composition of the soil used:

Analysis through XRD (X-ray powder diffraction) was performed on the same used soil by another research done by Arrigoni et al. [66]. These data were recorded on a small fraction of specimens to identify the clay mineral. The diffraction patterns were recorded with a Bruker D8 advance diffractometer using graphite-monochromated Cu-Kα radiation. The measurement range was 2–50 °2θ and the step was 0.02 °2θ, with a counting time of 1 s/step. The low 2θ range of the patterns, where the reflections of the clay minerals were observed, is reported in Figure 2.8. The analysis reveals the presence of quartz (72.6%), albite (15.1%) and the presence of illite (11%) and traces of vermiculite were identified (1.3%).

The XRD analysis on oriented and glycolate samples shows the absence of expansive clays according to U.S. Geological Survey [67]. These results confirm enough clay content to assure the stiffness of the material, without any expansive clay that can have impacts on swelling and cracking of the material.

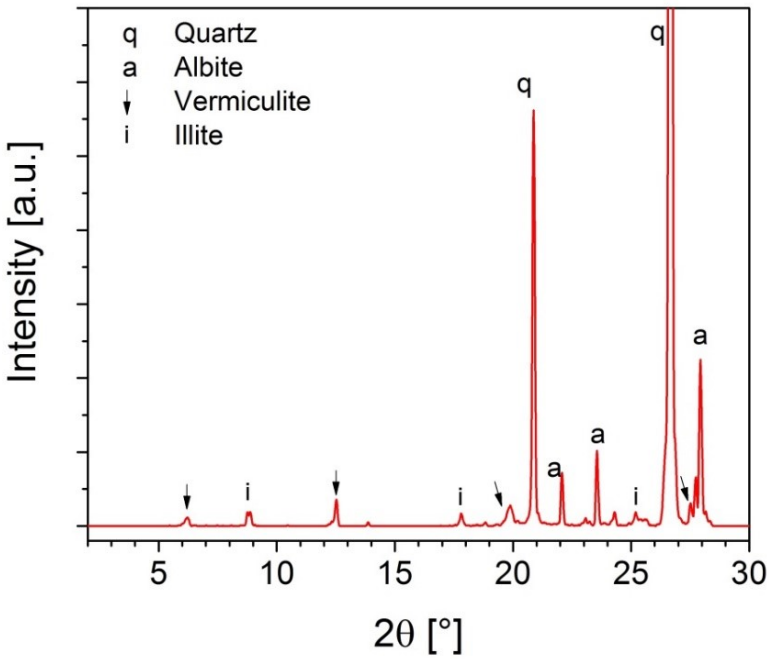

Figure 2.8 XRD Patterns of the used soil [66]

2.3.2 Manufacturing water content:

The optimum water content obtained from usual tests for a selected soil, such as the standard proctor test, can differ from the optimum water content which might be obtained on site for the construction of rammed earth walls. In fact, the standard proctor compaction energy does not apply the same energy of as the one used in earth construction [17], [56]. The compaction energy is low as a result; the optimum moisture content is too high for a pneumatic rammer. Figure 2.9 illustrates more clearly this idea.

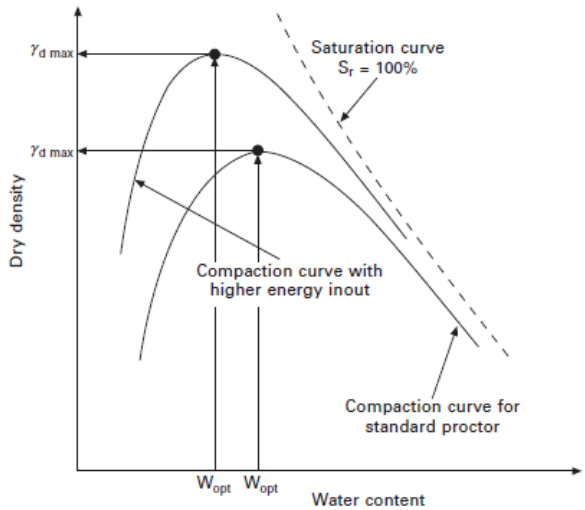

Figure 2.9 Compaction curves from Proctor tests [68]

Therefore the results of a standard proctor are more accurate for the case where a manual rammer is used that implies less compaction energy [69]. Some researchers Maniatidis and Walker [14], Lilley and Robinson [59] and Hall and Djerbib [12] used the modified proctor technique to determine the optimal manufacturing water content of rammed earth without showing the correlation between the results obtained from Proctor with what happens on the site (compaction energy, for example). In fact, a comparison between the compaction effort of Proctor tests and the actual construction method are always difficult. Hence, it is difficult to determine precisely the rammed earth compaction energy because it depends on the rammer, the pressure used and the number of blows for each layer. Basically, it depends greatly on the manufacturer.

None the less, the Proctor compaction method still can be considered as an effective and reliable scientific method to examine the manufacturing water content.

Proctor Test:

In this study, both pneumatic and hand compaction are used to determine the optimum moisture content and maximum dry density of the soil. The samples were manufactured in compliance with the norm NF-P 94093 [70]. The procedure includes compaction of the soil at different water contents. In both pneumatic and manual compaction, the moist soil was compacted in a standard Proctor mold in three layers.

For the manual compaction, each layer was compacted by 25 blows of a 2.49 kg hammer falling from a fixed height of 305 mm. For the pneumatic compaction, the same procedure was adopted, only the rammer was replaced with the pneumatic one in this case. After achieving the final layer, the weight of the compacted soil is measured and the dry density of the soil is calculated. The moisture content of the specimen is determined by calculating the difference in weight of moist and oven dried sample at 105 °C as per NF-P 94-050 [71].

The variation of dry density with the increase in moisture content of the soil at compaction is given in Figure 2.10. The results of the normal Proctor with the standard compactor for the used soil indicate optimum moisture of 14 % and a dry density of 1850 kg/m^3. Regarding the proctor with the pneumatic rammer, it can be seen that the optimum moisture content of the soil decreased to 12.5% and the soil attained higher density (1960 kg/ m^3).

Nevertheless, it is always difficult to specify the proper manufacturing water content of the specimens; moreover, there is still a gap of information about the influence of the manufacturing water content of the specimens on the compressive strength for unstabilized rammed earth. According to the New Zealand earth building standard, the water content of the rammed earth mixture can be within 3 % of the optimum water content obtained. Therefore, the optimum moisture corresponding to the soil used in this study with a pneumatic rammer can be estimated as 2-3% lower than the value obtained with the manual rammer and close to the water content obtained with the pneumatic compactor. For the rest of the specimen preparation, a water content of 12% is adopted.

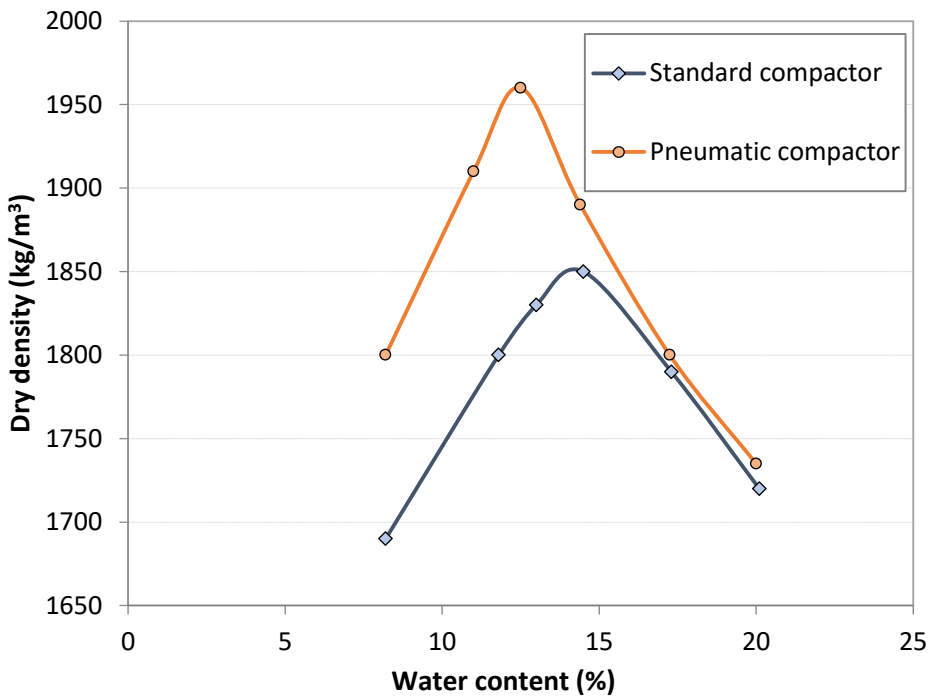

Figure 2.10 Results obtained with the standard proctor tests using manual and pneumatic rammer

2.4 Unconfined compression tests on the rammed earth used

2.4.1 Specimen preparation

To determine the compressive strength and Young's modulus of the earth used for the walls, three prismatic and three cylindrical specimens were manufactured and tested under compression tests. The cylindrical specimens had a 20-cm diameter and 40-cm height and the prismatic specimens measured 25 cm × 25 cm × 50 cm. The dimensions of these specimens were chosen to reproduce compaction energy applied on the walls during manufacturing. All the rectangular prisms are compacted in wooden molds fabricated in the laboratory with the desired shape (Figure 2.11). While for the preparation of cylindrical specimens, the moist soil is poured into polystyrene molds well-tightened as shown in Figure 2.12.

The specimens were compacted in four layers (for the cylindrical specimens) and five layers (for the prismatic specimen), both with the same water content at 12 % and the same wall layer thickness. The mixture was prepared and stored in plastic bags 1 day before the fabrication to assure the homogenization of the water content. The weight of the moist soil required for each layer is calculated in order to have similar layer thickness for the different specimens. Samples were taken each time to check the humidity when manufacturing the specimens. For the cylindrical specimens, a circular piston was used for the pneumatic rammer to facilitate the ramming on a circular section.

The prismatic and cylindrical specimens were unmolded immediately after compaction and then cured in laboratory ambient conditions (20°C and 60% RH) for 2 months. Prior to the unconfined compression tests, the specimens were surfaced with a lime mortar to obtain a flat horizontal surface (Figure 2.11). Surfacing is necessary to ensure a homogeneous distribution of the load executed by the hydraulic actuator. After applying the mortar to ensure a level surfacing, a wood plate is placed over the layer of mortar. The characteristics of the specimens (cylindrical and prismatic) are reported in Table 2.2.

Figure 2.11 Prismatic specimens (25 cm × 25 cm × 50 cm) after surfacing

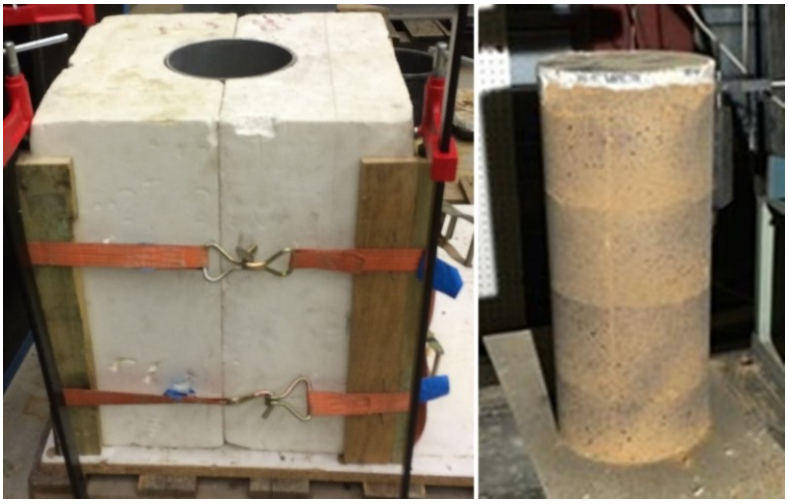

Figure 2.12 Polystyrene molds used for the manufacturing cylindrical specimens

Table 2.2 Characteristics of the specimens

Specimen Number	Specimen Dimension (cm)	Dry Density (kg/m^3)	Water content at test (%)
C1	D=20; h=40	1848	3.2
C2	D=20; h=40	1899	3.9
C3	D=20; h=40	1888	3.2
P4	25 x 25 x 50	1785	2.5
P5	25 x 25 x 50	1798	2.4
P6	25 x 25 x 50	1786	2.7

2.4.2 Experimental set-up

The prismatic and cylindrical specimens were tested in unconfined compression with displacement control of 0.02 mm/s using a hydraulic jack. Figure 2.14 shows a cylindrical specimen during the test setup. The Digital image correlation (DIC) was used as a measurement technique to capture the failure process of rammed earth walls and specimens and to provide all the needed information about the displacement field for the corresponding structure.

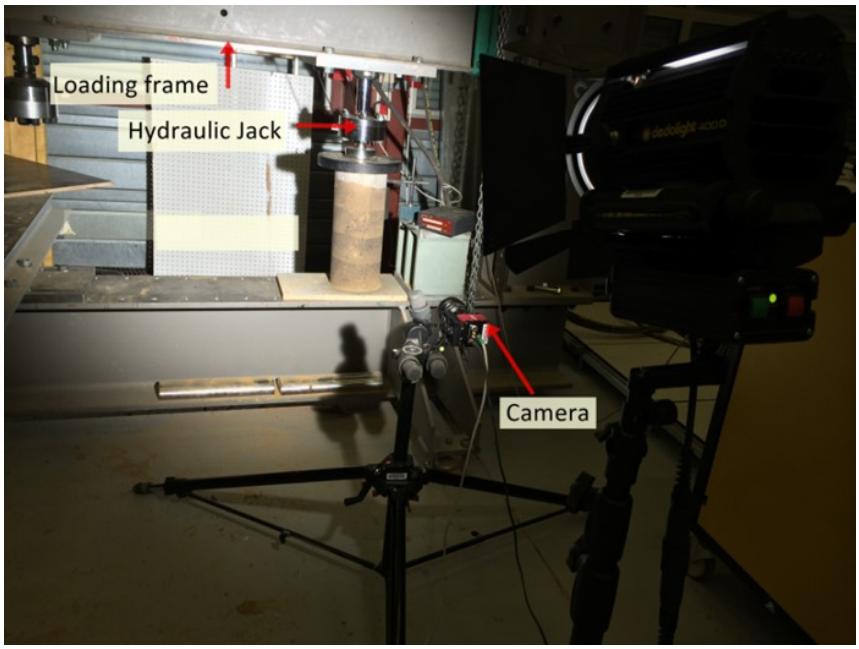

Figure 2.13 Cylindrical specimen (20-cm diameter, 40-cm height) during the test setup

The images for the DIC were recorded using high definition (3248 x 4872) with almost 16 million megapixels white and black camera system. During the tests, a projector was installed. Thus, it is possible to guarantee a constant illumination on the specimen (as seen in Figure 2.14). Random speckle pattern (Figure 2.14 (a)) was applied on the surface of all the specimens and the rammed earth walls using black paint type mat to avoid any reflection of light. The diffusion was done using an airbrush gun where the pressure was controlled with compressors machine, therefore the pressure was regulated while applying the paint in order to give the best pattern. The quality of the random grey level was analyzed in term of histogram. Figure 2.14 (b) presents the histogram of grey level within a region of interest on a rammed earth specimen surface.

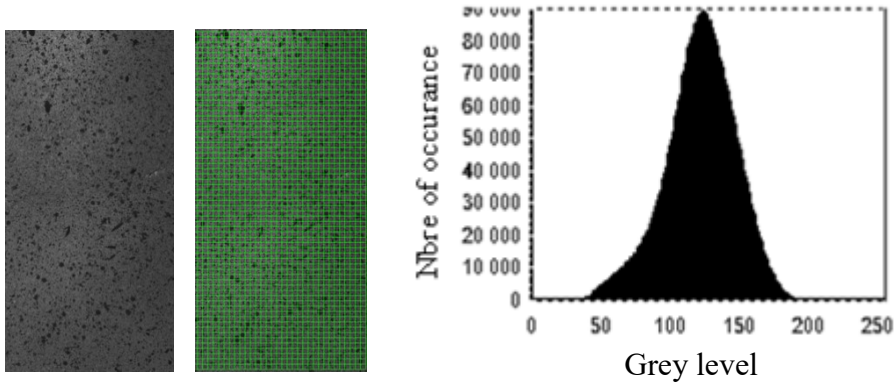

(a) (b)

Figure 2.14 (a) Close view of the speckle pattern and the region of interest of a lateral face of a cylindrical specimen (b) and the corresponding histogram of grey level

2.4.3 Digital image correlation

The DIC is a method capable of calculating the displacement at a surface element. It allows, during solicitations, the measurement of the displacement field at the surface of a specimen by comparing a deformed image to a reference image [72]. The method consists in tracking a random speckle pattern on top of the surface using the recorded images. Different techniques are used to have a random speckle such as spray painting or airbrush, the average spot size must be lower than 20 pixels [73]. The DIC data processing was performed with the 7D software developed by the laboratory SYMME in Annecy-le-Vieux. Appendix B describes more in details the principle of the image correlation technique, including specificities of the 7D software.

It is worth noticing that the 7D software used for DIC processing treats 8-bit images, leading therefore to 256 grey level scaling.

The correlation parameters (defined in appendix B) as the grid step ‘n’ and the correlation pattern ‘p’ chosen in all this study are (n, p) = (20, 20). These parameters are selected in a way to have a good level of correlation for all the images, very close to 100%, which means that the software manages to identify the displacements over the whole area and throughout the test. It is also important to have a grid allowing detailed analysis of the displacements of the studied

surface. As for the precision, the software shows a precision of 0.01 mm for the displacement and a mean standard deviation of 1.1 for the grey level of 2 identical images.

2.4.4 Results: Compressive strength and Young's Modulus

Thanks to the DIC, the displacements during the loading were recorded which enabled to determine Young's modulus of the tested specimens. The Young's modulus was calculated from the displacements of the middle part (following the height) of each specimen as shown in Figure 2.15.

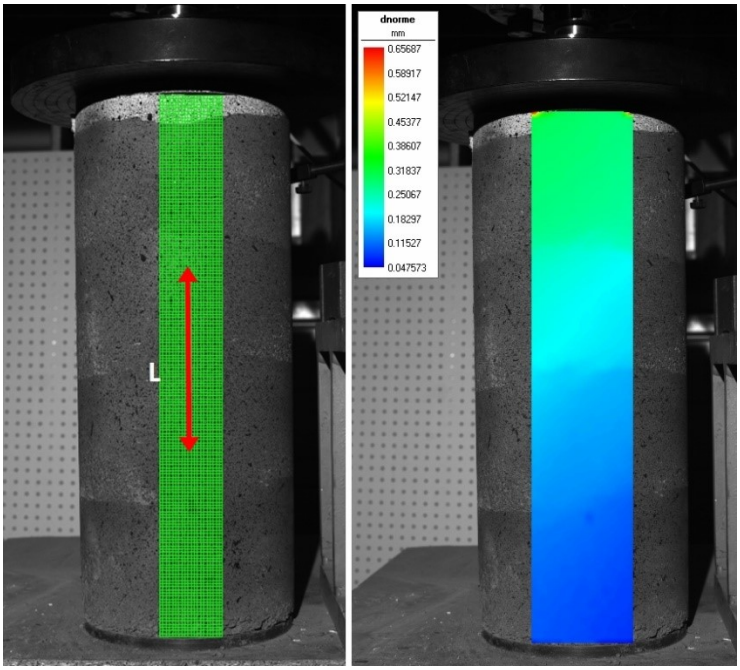

(a) (b)

Figure 2.15 (a) Central part used to calculate the Young modulus from the DIC; (b) the vertical displacement fields for the corresponding figure

$E_{specimen}$ was therefore calculated as follow:

$$E_{specimen} = \frac{\Delta F . L}{S . \Delta L} \tag{2.1}$$

Where F is the difference of the vertical loading applied between two points. L is the length of the specimen, S the surface of the application of the loading, ΔL is the length between the two points at the middle of the specimen. In this study, the distance between two points (one point at the center of a layer and the other point at the center of the upper layer) in the middle of the specimen was calculated.

The results of Young's modulus and compressive strength of the specimens are presented in Table 2.3. A substantial difference in the results of the compressive strength of the prismatic and cylindrical specimens can be observed. Indeed, the influence at the borders (friction during ramming, between the rammed earth and the formwork) was greater in the prismatic specimens

than in the cylindrical ones, especially in the corners of the prismatic specimens. Consequently, cylindrical specimens were better compacted and had better mechanical characteristics.

In the current case of rammed earth house of two stories, walls (50 cm thick) are supposed to be loaded with a normal stress of about 0.3 MPa. In practice, concerning the values obtained of the compressive strength, a structure made with this soil would resist to vertical loads in normal conditions.

Table 2.3 Results of the unconfined compression tests (C: Cylindrical specimen, P: Prismatic specimen)

Specimen Number	Dry Density (kg/m^3)	Compressive Strength (MPa)	Young Modulus (MPa)
C1	1848	1.78	764
C2	1899	2.12	817
C3	1888	2.09	708
P4	1785	0.99	310
P5	1798	0.91	440
P6	1786	1.08	350

This difference in the results for different specimen shapes had already been noted in previous studies in the specialized literature ([14] and [60]). These authors also compared the difference between tests done on cylindrical and prismatic specimens on representative samples. Table 2.4 intend to compare our results with the existing surveys. We could find that the results of these studies do not differ much from ours.

Table 2.4 Comparison with other studies in the literature

Reference	Type of specimen	Dimensions of specimens (cm)	Compressive strength (MPa)	Slenderness
Current study	Prismatic	25 × 25 × 50	1.15	2
	Cylindrical	d=20, h= 40	2	2
[60]	Prismatic	40 x 40 x 64	0.84	1.6
	Cylindrical	d=16, h= 26.5	2.2	1.6
[14]	Prismatic	30 x 30 x 60	0.81	2
	Cylindrical	d=30, h=60	1.9	2

In the study of Maniatidis and Walker [14] where the thickness of the samples was 30 cm (representing rammed earth walls of England where the current thickness is 30 cm), results showed that cylinders of 30 cm diameter do not provide the same values as the prisms which are representative of the walls on site. The same thing was found by [60] on different dimensions of specimens. These findings prove the localized and less effective compaction of the material in the corners of the prisms. It is important to note that Maniatidis and Walker had the same slenderness ratio as the test conducted in our study, unlike the specimen that was done in the study of Bui et al. [60].

2.4.5 Results of DIC on rammed earth specimens

For each test, images were recorded for each second. Through the strain field provided by the 7D software, we are able to understand the general behavior of the specimen during the loading.

The software displays the results of the principal strain that are derived from Green-Lagrange's strain tensor and the maximal strain denoted 'emaxi'. Figure 2.17 displays the principal strain along with the crack pattern (through 'emaxi') for one of the cylindrical specimen and for different states of loading that correspond to Figure 2.16.

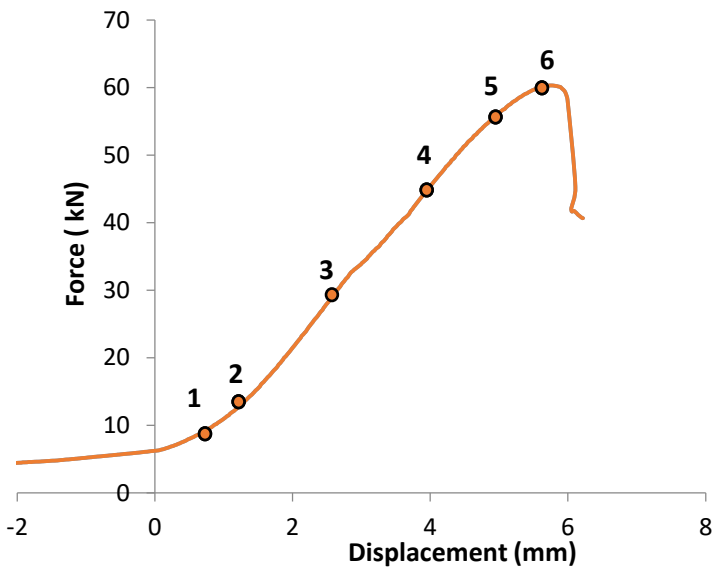

Figure 2.16 State of loading (represented by numbers) corresponding for the calculation of the strain through DIC on Figure 2.16 for specimen (C3)

Force	Principale strain	Values	Crack Pattern	Values of the maximal strain
State 1 8kN	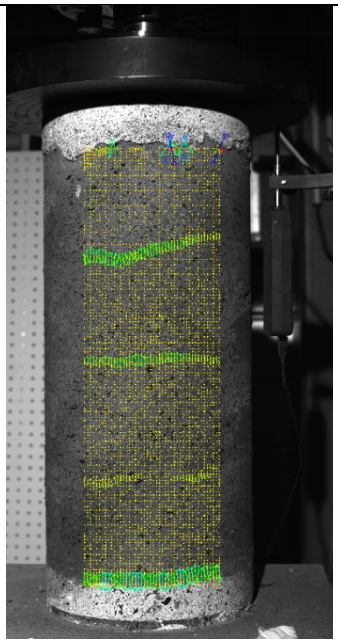	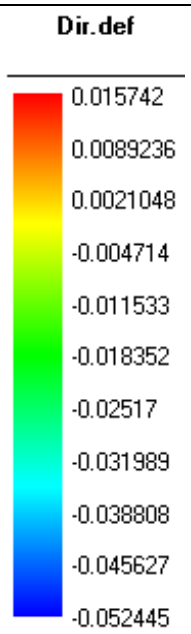	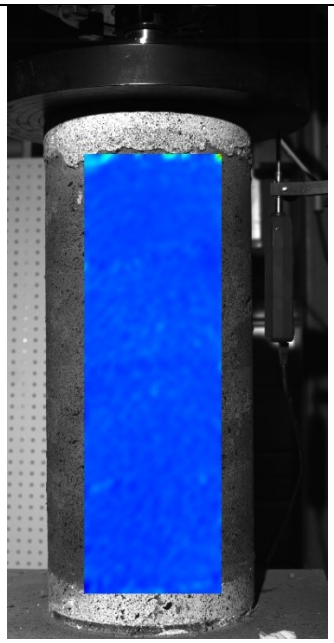	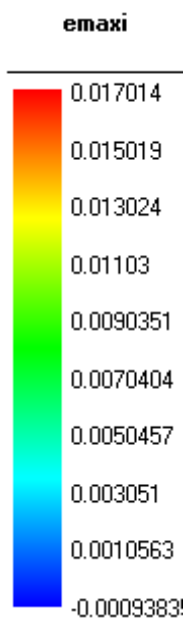
State 2 12.8kN	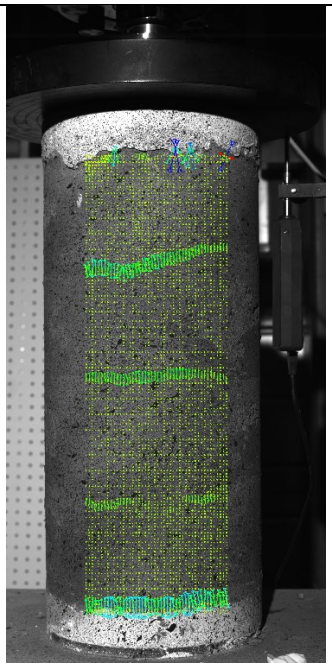		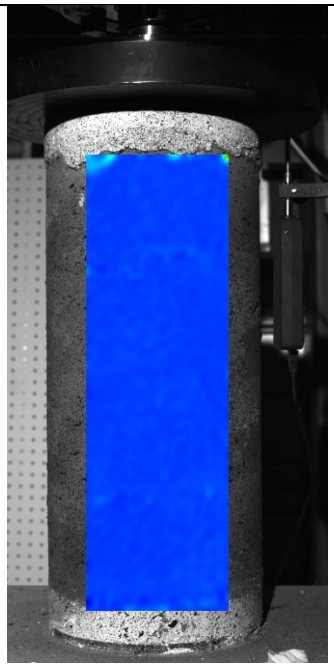	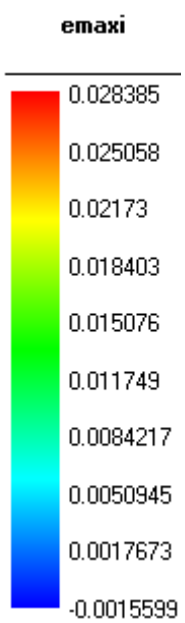

State 3

26.8 kN

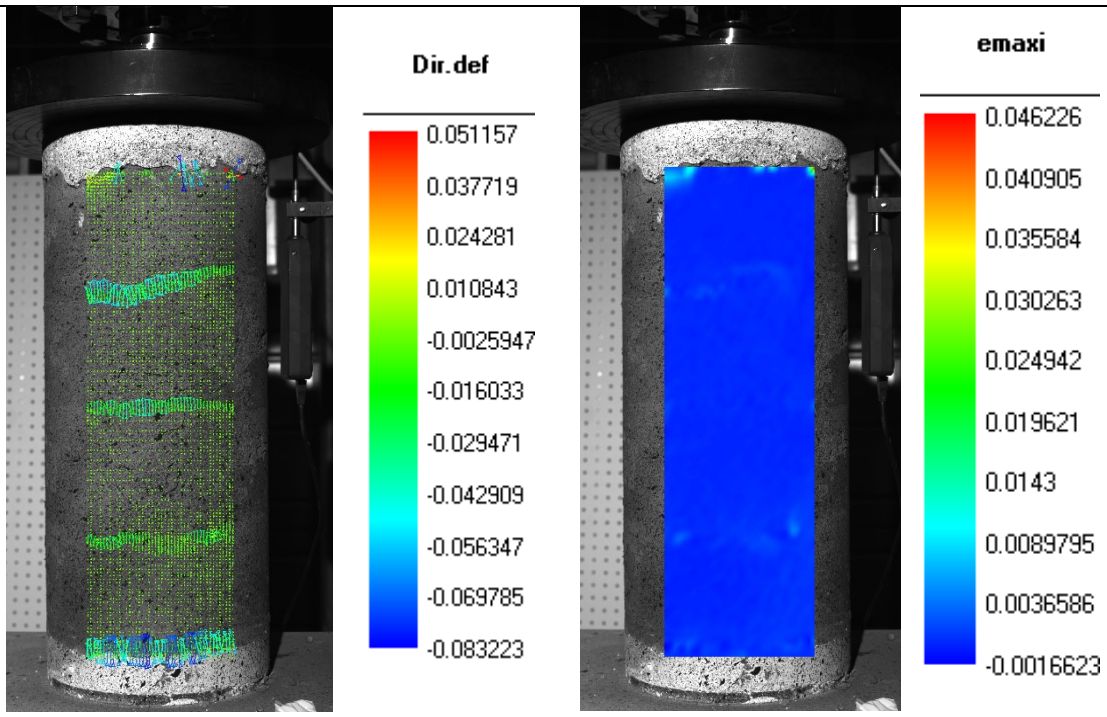

State 4

46 kN

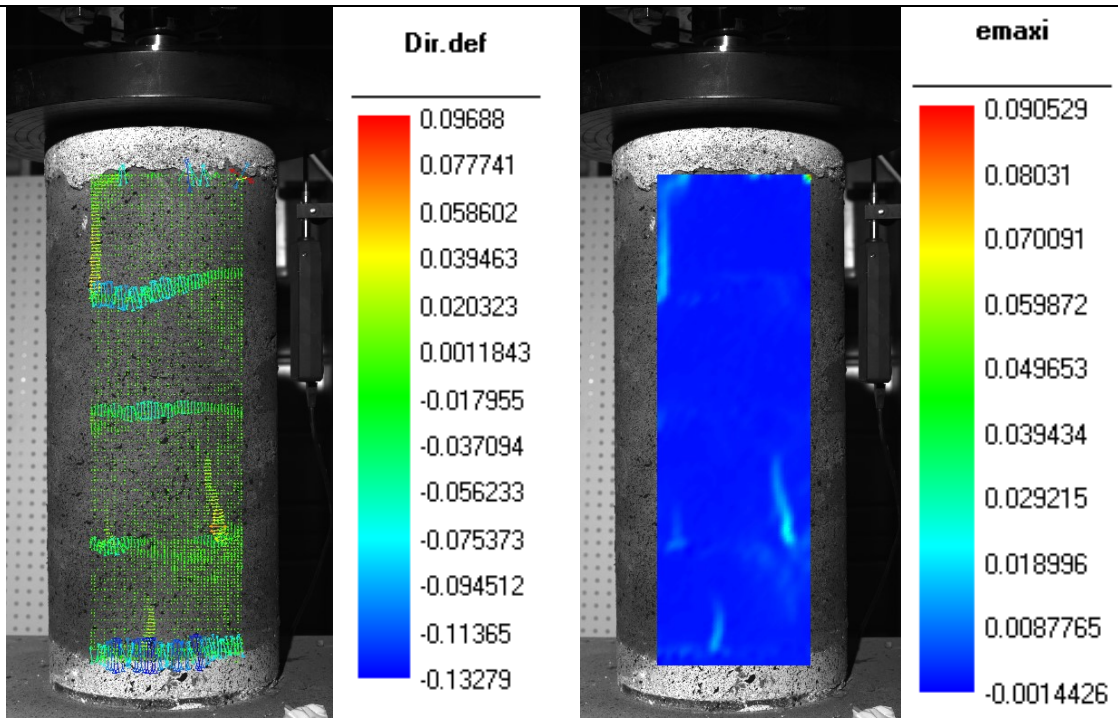

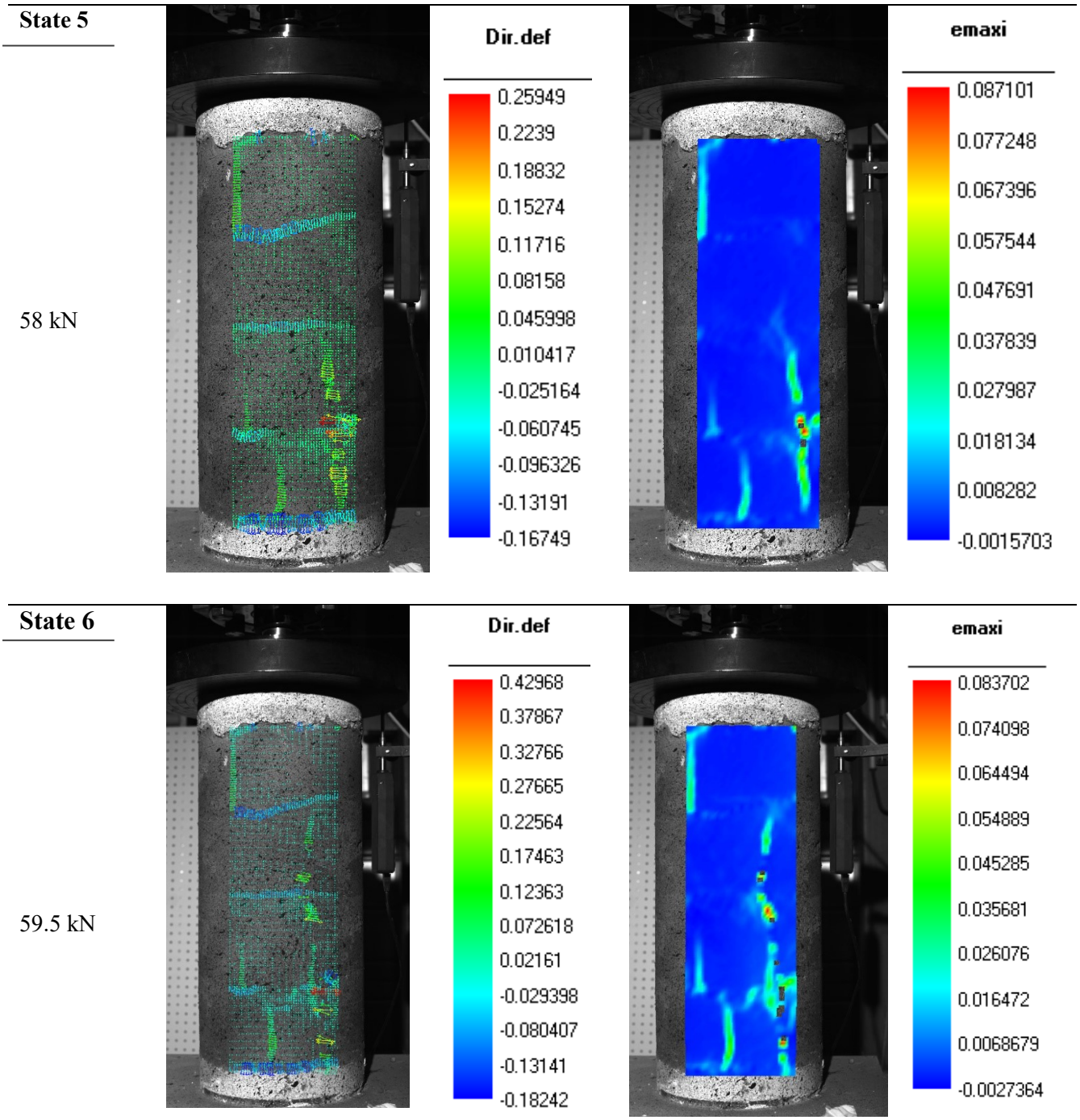

Figure 2.17 The crack pattern and the direction of principal strain vectors showed by the 7D software for one of the cylindrical specimen (C3) in different states of the loading

From the direction of the principal strain vectors shown in Figure 2.17, it had been noticed that the interfaces tend to be squeezed and crush faster under compression comparing to the rest of the points in the material (principal strain in state 1, 2, 3 during the first loading of the compression test near the interface are bigger than the other parts in the specimen), therefore higher deformation is obtained at the interface between the layers, than in the layer itself which is also related to the variation of density in one layer. Indeed during the manufacturing, the bottom of each layer is less compacted when compared to the rest of the upper points in the layer

due to the compaction energy that is greater at the layer top. Since the energy is distributed within the layer, the density at the top of the layer is higher than in the bottom, therefore it is assumed that the density varies linearly inside the layer as shown in Figure 2.18. This subject was addressed in the work of Bui [60] that revealed the heterogenic aspect of the rammed earth due to the variation of the density inside one layer.

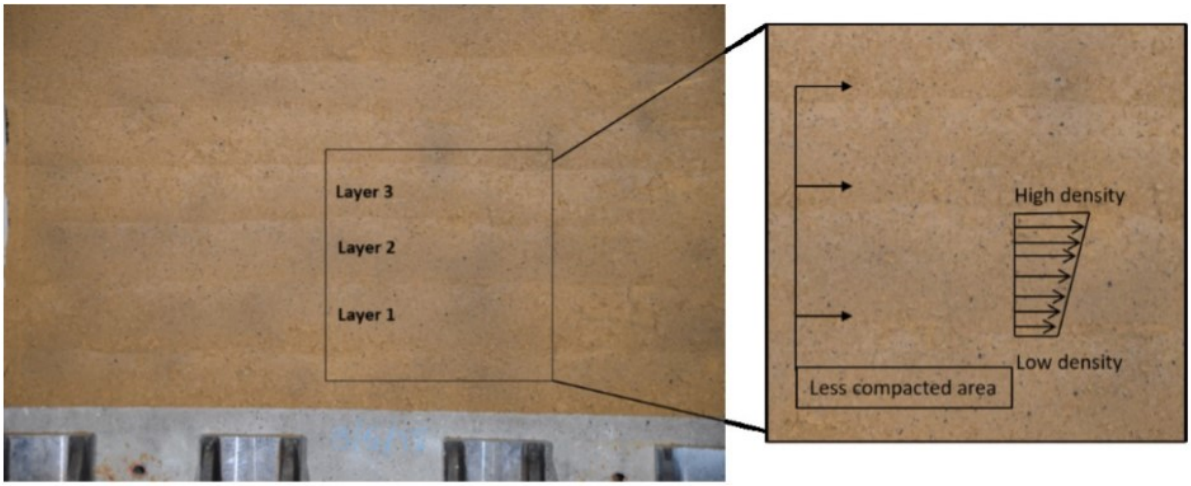

Figure 2.18 Variation of the density within the layer shown on a rammed earth wall

Figure 2.19 shows the DIC results for the vertical strain 'eyy' that reflect more clearly the variation of the deformation in the direction of the loading at a certain point of loading that corresponds to 17 kN. This figure shows undoubtedly the difference in the variation of the deformation between the earthen layer and the interface. Therefore, there is a difference in the correspondent Young modulus of earth layer.

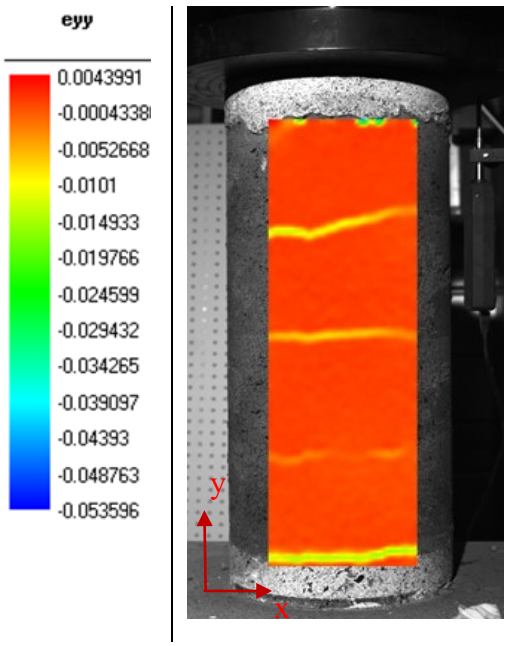

Figure 2.19 The deformation in the direction parallel to the loading for 17 kN state of load for the specimen (C3)

During the compression tests, it was observed that the interface may interfere to initiate the cracking in the sample (as in the case of state 4 in Figure 2.17) where the direction of the principal vector initiate from the interface of the first layer and continue along the height of the specimen. Therefore, the interfaces between the layers can be considered as weak points for this material especially in the case of horizontal loading where the interface is more solicited. At the end of the test, all the cylindrical specimens failed in a similar manner as shown in Figure 2.20.

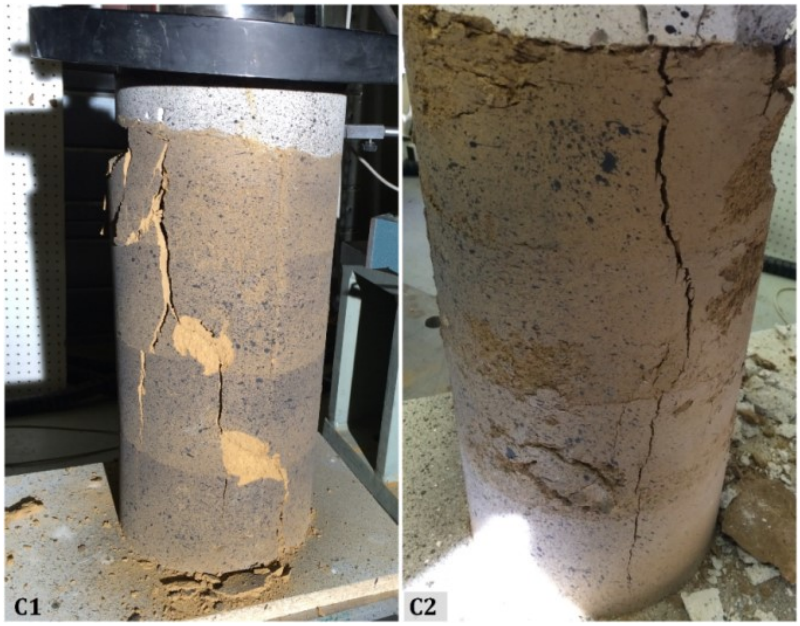

Figure 2.20 Failure pattern of the cylindrical specimens (C1) and (C2)

Vertical cracking was obtained through the full height of each specimen. These cracks crossed the compacted earth layers and tend to align in parallel to the applied compression direction. In the case of the prismatic specimens, cracks mostly appeared in the central part propagating toward the top and bottom edges. Inclined cracks were also obtained at the corners with signs of crumbling from the sides during the loading phase. After reaching the ultimate load, brittle failure occurred and some pieces from the specimens fell out. Figure 2.21 shows the crack pattern at the end of the test for the prismatic specimens.

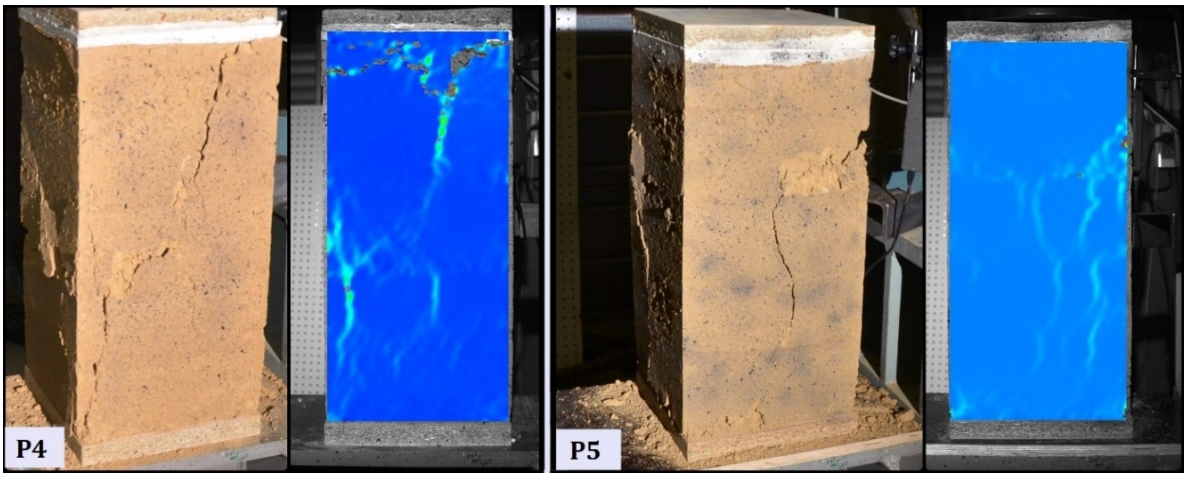

Figure 2.21 Crack pattern in the case of two prismatic specimens (P4) and (P5)

As the failure occurred, the prismatic rammed earth specimens showed cone shaped cracking pattern on one side (Figure 2.22). This can be due to the friction between press plates and sample faces. In fact, in some cases, the system of compression test could generate friction between the steel plate and the end of the surface of the specimen due to a tangential force that is induced between these two. This phenomenon is illustrated in Figure 2.23 by Duffaut [74]. It could be concluded that the friction might have occurred and influenced the failure mode of the prismatic specimens and less for the cylindrical specimens that have small smaller friction area due to smaller section (Table 2.2). The degree of the platen restraint on the rammed earth specimen depends on this friction and on the height of the specimen. To avoid this friction in some cases the addition of a lubricant on the platens is suggested. Hence, it is clear that the geometry of the specimens affected the measured values of the compressive strength and the failure pattern of the rammed earth specimen.

Figure 2.22 Failure of prismatic specimen

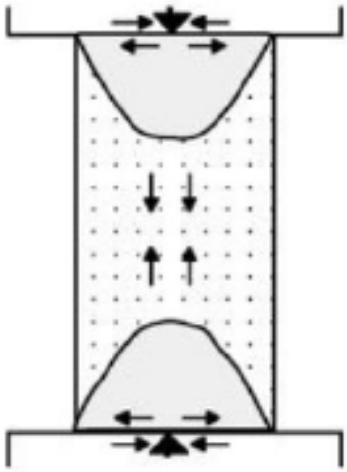

Figure 2.23 Effect of the friction in a uniaxial compression test [74]

2.5 Identification of cohesion and friction angles by direct shear tests on rammed earth used

In order to study the earthquake behavior of an entire rammed earth structure, complex numerical models seems a necessary approach. For the numerical modeling of rammed earth material, two important parameters are the friction angle φ and the cohesion c. Due to the superposition of successive earthen layers during the manufacture of rammed earth walls, two kinds of characteristics should be distinguished: characteristics of the earthen layers and those of the interfaces between earthen layers [75]–[77]. The characterization of the friction angle and the cohesion is the first important step to create robust numerical models for the seismic evaluation of rammed earth buildings. In fact, the experimental data on the shear parameters of rammed earth in the literature are limited; therefore, the first scope of this study is to determine φ and c of the earthen layers through direct shear testing.

This section presents an investigation on the cohesion and friction angle of the rammed earth through shear box tests (within the earthen layer). A larger shear box (0.49 m width × 0.49 m length × 0.45 m height) was specifically designed for this study to reproduce the same manufacturing conditions of the 1-scale rammed earth walls. Two types of tests were conducted inside the layer and at the interface. In another approach, standard shear box test was also performed on the specimens having 10 cm width × 10 cm length × 3.5 cm height. The specimens for this box were directly taken from rammed earth walls. All the obtained experimental values were tested in a numerical model (in Chapter 5) to simulate pushover tests of rammed earth walls.

2.5.1 Bibliography about shear tests applied on rammed earth

Several previous studies in the literature aimed to identify the friction angle and the cohesion but important dispersions in the obtained results were observed and the values recommended for these parameters need to be further investigated.

Cheah et al. [78] performed tri-axial and triplet tests on cement-stabilized rammed earth specimens (3 layers of approximately 70 mm thick). The specimens were also tested with and without fiber reinforcement. From the tri-axial tests, the apparent cohesion and the friction angle for stabilized rammed earth (without fiber reinforcement) was found to be 724 kPa and 48°, respectively. From triplet test, the cohesion and angle of friction of the interface were found to be 328kPa and 45°, respectively. The difference in apparent cohesion results appears because the triplet test measures the shear strength at the interface between rammed earth layers, while the triaxial test measures the shear strength of the material through several rammed earth layers.

Jaquin et al. [79] also carried out triaxial tests on compacted soil specimens but these authors concentrated on the relationship between the suction and the strength of compacted soil material, no results on c or φ were presented.

Nowamooz et al. [80] performed monotonic triaxial tests to determine different characteristics of rammed earth. During these experiments, the cohesion and the friction were determined using the yield surface of the Drucker Prager criterion. An angle of 41° and cohesion of 13.4 kPa, were obtained. Other studies used numerical approaches, by finite elements [76] or discrete elements [77] to reproduce certain experiments and to identify c and φ by calibration. The values identified by those authors were $\varphi = 37\text{-}45^{\circ}$ and $c=0.1\text{-}0.15\ f_c$ (where f_c is the compressive strength).

The friction angle φ and the cohesion c are usually determined because they are classical parameters in soil mechanics. To identify these parameters, two main approaches can be used: experimental or numerical. The experimental technique has the advantage of providing "direct experimental values" with appropriate experiments while for the numerical approach the calibration of the results is needed and the identified values are "indirect". To determine the friction angle and the cohesion, the most well-known tests are tri-axial or direct shear box (Casagrande's box). However, for the experimental approach, the representativeness of the tested specimens should be insured, especially in the case of rammed earth material [60] where a lack of homogeneity in the material is observed.

For that reason, in this present study, we chose to apply the direct shear tests. Indeed, the direct shear test on compacted earth was used in several studies in the literature. Bouchira et al. [81] studied the performance of earth material through the evaluation of the shear strength, the experiments were done on a compacted sandy clay reinforced with barley straw by using a Casagrande box of 60mm x 60mm x 36mm, this study showed an increase of the shear strength in function of the reinforcement.

Corban and Augarde [82] also carried out direct shear tests on rammed earth specimens to evaluate the shear strength parameters within the layer. Rammed earth specimen of 60mm × 60mm × 20mm was used and the effect of the stabilization with wool and cement was discussed. An important variation of the results was observed due to the specimens' representativeness. In general, the cohesion and angle of internal friction of unstabilized rammed earth specimens tested in this study were found to be varying from 55kPa to 80kPa and 23° to 65° respectively.

In the present study, first the direct shear tests were performed in a tailored box (0.49 m width × 0.49 m length × 0.45 m height) which was specifically designed and manufactured to test representative rammed earth specimens and secondly standard direct shear tests were performed on specimens which had been taken from representative rammed earth walls. The identified values are then used as input parameters in a finite element model to verify their relevancy (in Chapter 5).

2.5.2 Principles of the Casagrande shear test

The Casagrande shear test is a classical test in soil mechanics. Figure 2.24 shows the principle of the shear. The soil specimen is placed in a shear box that consists of two independent half boxes. The plane located at the separation of the two half-boxes is called sliding plane and corresponds to the specimen shear plane. The test consists of applying a vertical force (N) that is maintained constant during the test and then applying a horizontal shear force (F) on one of two half-boxes as in (Figure 2.24).

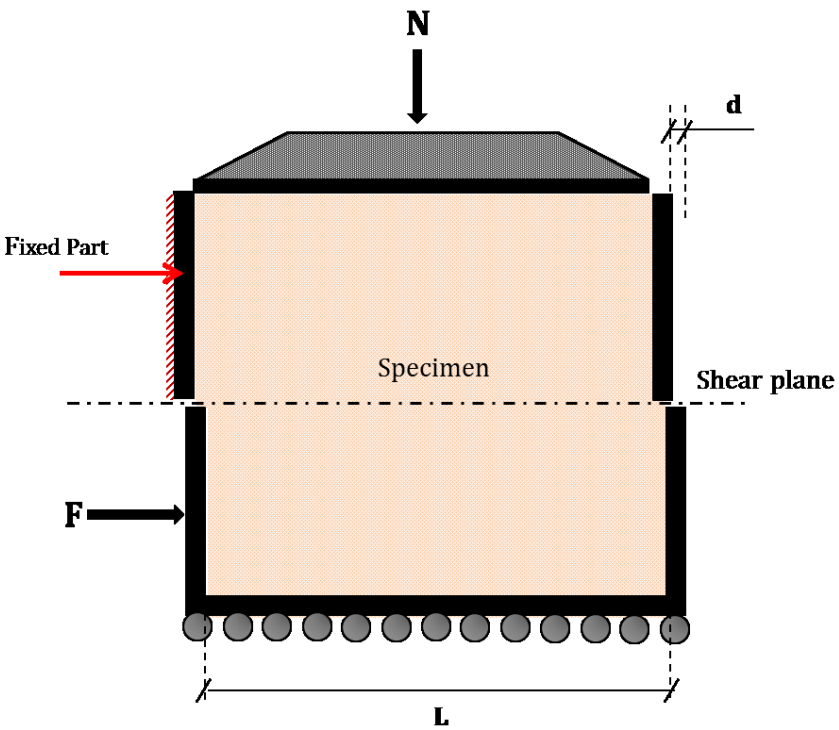

Figure 2.24 Principle of the direct shear test

This test gives the relation (τ) in function of (σ) from which we can deduce a Mohr Coulomb behavior law for this material defined by the following equation:

$$\tau = c + \sigma \tan \varphi \tag{2.2}$$

Where

φ: Soil internal friction angle

c: the apparent cohesion

σ: normal stress on the failure plane

τ: Shear strength

The value of the shear stress must be corrected by the correspondent value of the sheared area by using the displacement values displayed on the lower part of the shear box as followed:

$$\tau = \frac{F}{L(L-d)} \tag{2.3}$$

With

L: the initial length of the shear box

d: the displacement of the lower part of the shear box obtained by the sensors.

Standard requires at least 3 tests to determine c and φ, where each test is carried out at a different vertical stress. By plotting these data on the (τ-σ) diagram, the straight line denoted by the equation $\tau = c + \sigma.\tan(\varphi)$ can be seen in Figure 2.25.

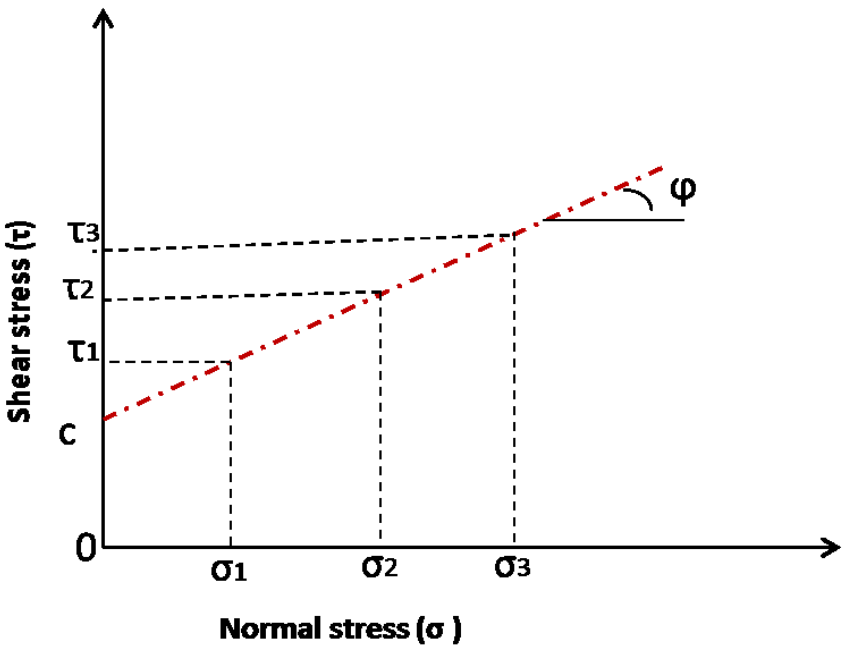

Figure 2.25 Mohr-Coulomb failure envelope

These shear boxes are designed with respect to various conditions set out in the standard NF-P 94-071-1 [83]. This standard should be respected and adapted to the manufacturing process of the large box. In fact, there are several constraints on the elements of the shear box. The frame must be dimensionally stable even under the application of different stresses on the shear box; a tolerance of +/- 1 ° is accepted for the horizontal retention of the box. The application of the vertical load on the specimen must follow a vertical direction with a tolerance +/- 2°. The force applied must be kept constant. Therefore, the large shear box must be dimensioned following these constraints.

2.5.3 Tests on the full-scale shear box

Test device:

The big shear box has the following dimensions: 0.49 m width × 0.49 m length × 0.45 m height, it was specially designed and manufactured to test big specimen having similar characteristics of that of a real rammed earth wall and therefore the same process of manufacturing can be engaged.

The 0.49 m-width takes into account the current thickness of rammed earth walls in France and Europe. The 0.45 m-height enables the manufacturing of three earthen layers in the box where the horizontal shear plan is in the middle of the second layer. It is important to note that the last layer (upper layer) is less representative than the other layers since it receives only one compaction being the last one to be compacted (while other layers receive compaction several times), so the last layer should not be tested in shear.

The tailored shear box is made of two steel boxes as shown in Figure 2.26 where the dimension of each box is 0.49 m × 0.49 m × 0.225 m. These boxes are composed of 4 welded UPN 220 steel profiles as seen in Figure 2.26.

The horizontal displacement of the lower shear box is enabled by cylindrical rolls of 4 cm diameter and 20 cm in length. These rolls were placed under the box; into 2 parallel rows. The whole system was placed on a steel base of I shape which is fixed to the steel loading frame. The inside surface and the interface of the box is covered with Teflon plates of 5 mm thickness; these surfaces are very smooth due to the low coefficient of friction of the Teflon material. As for the loading plate, a rigid plate is normally used in direct shear tests (for example as in [84] and [85]). For this reason, a special metallic plate was designed that is composed of several beveled profiles.

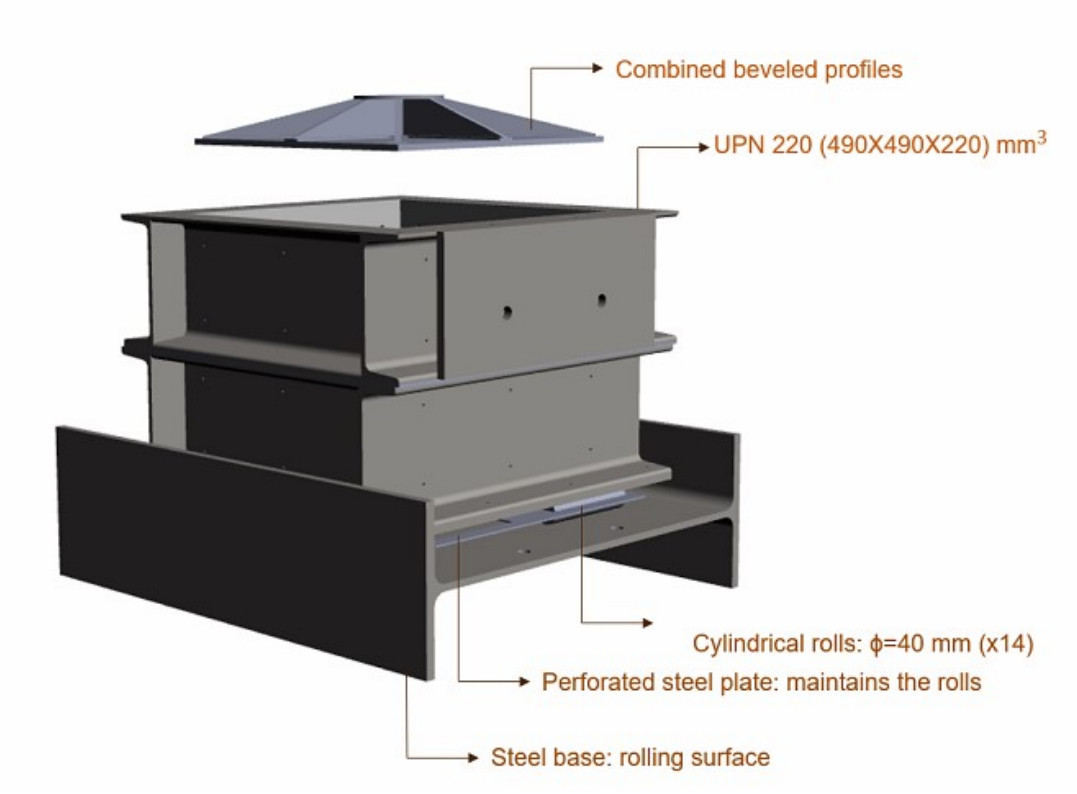

Figure 2.26 The model of the large-scale designed shear box

Specimen manufacturing:

The manufacturing process consisted of ramming the earth (with moisture content equal to 12 %) in three layers directly into the shear box using a pneumatic rammer (Figure 2.27). Three different specimens were manufactured. The center of the intermediate layer corresponds to the median plane of the shear box; therefore, the mechanical properties obtained will correspond to a rammed earth layer similar to the layers of the walls.

Then, the rammed earth specimen was turned 90° and kept in the metal box in a vertical position during the curing period (Figure 2.27 (b)). Two sides (0.5m x 0.5m) were opened to facilitate the moisture evaporation as in Figure 2.27 (b). The temperature around the specimen was maintained about 50°C to accelerate the drying. Samples were tested 1 month after construction.

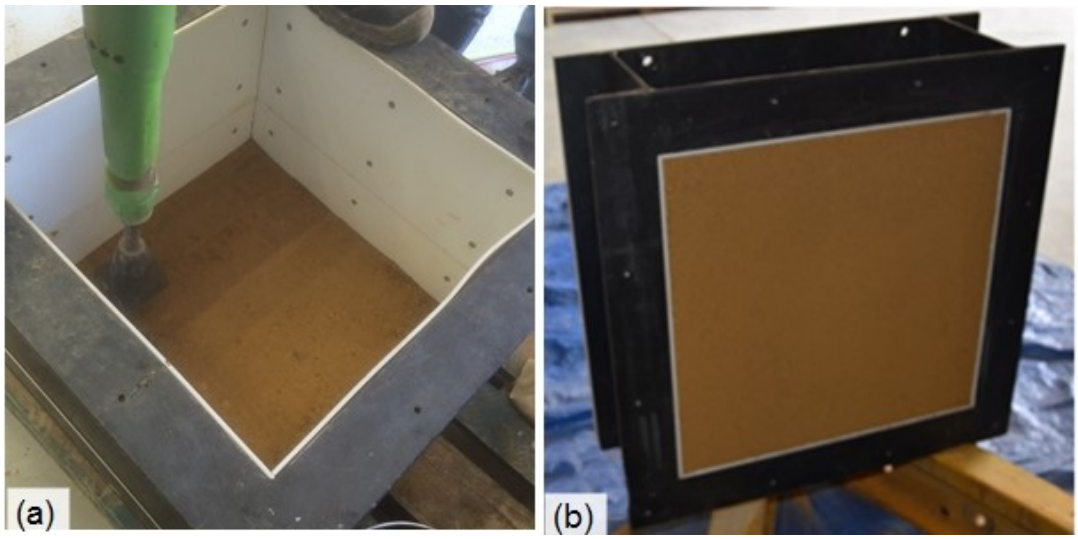

Figure 2.27 (a) Manufacturing rammed earth directly in the shear box; (b) Opening two sides of the shear box for evaporation

Shear test on the one-scale shear box:

An electrical actuator VE was used to apply the vertical load as shown in Figure 2.28. This load was applied at a rate of 1 kN/s. The values for the vertical load chosen for three different tests are 0.1, 0.2 and 0.3 MPa. Sand was spread on the upper part of the rammed earth top layer that is in contact with the metallic plate to assure surface leveling during the distribution of the vertical stress. To avoid the sand filling any gap between the earth and the Teflon plates a plastic film was used (Figure 2.29).

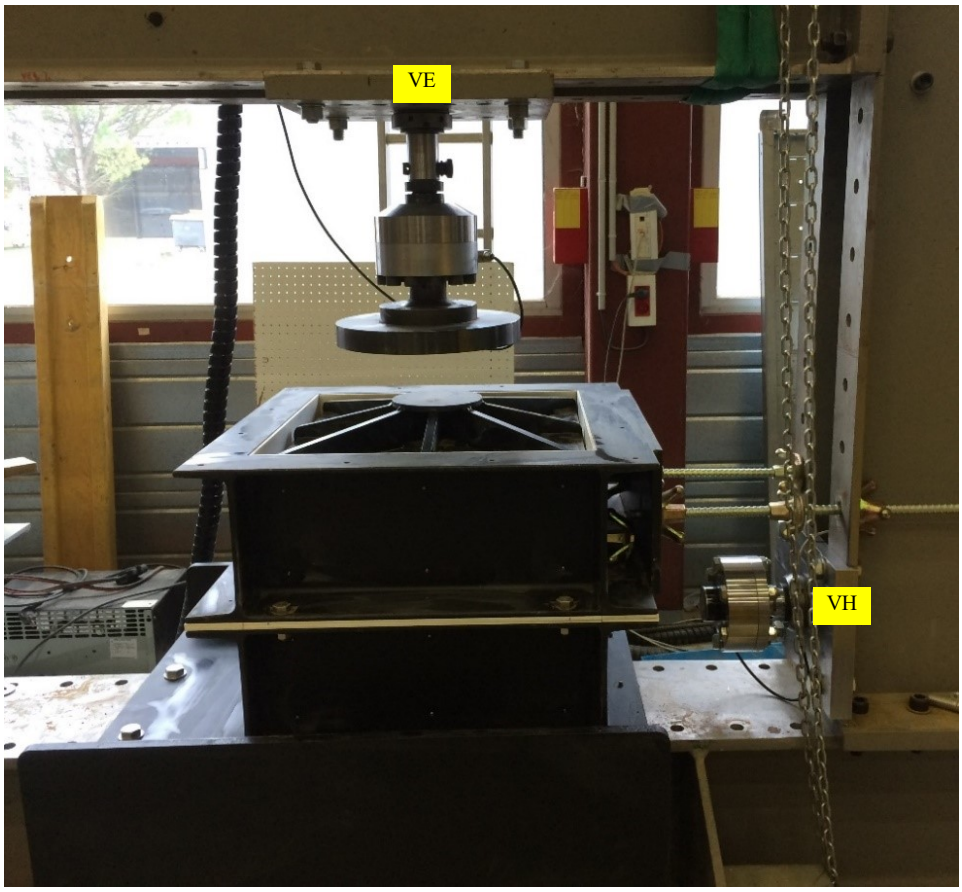

Figure 2.28 The shear box installed on the loading frame

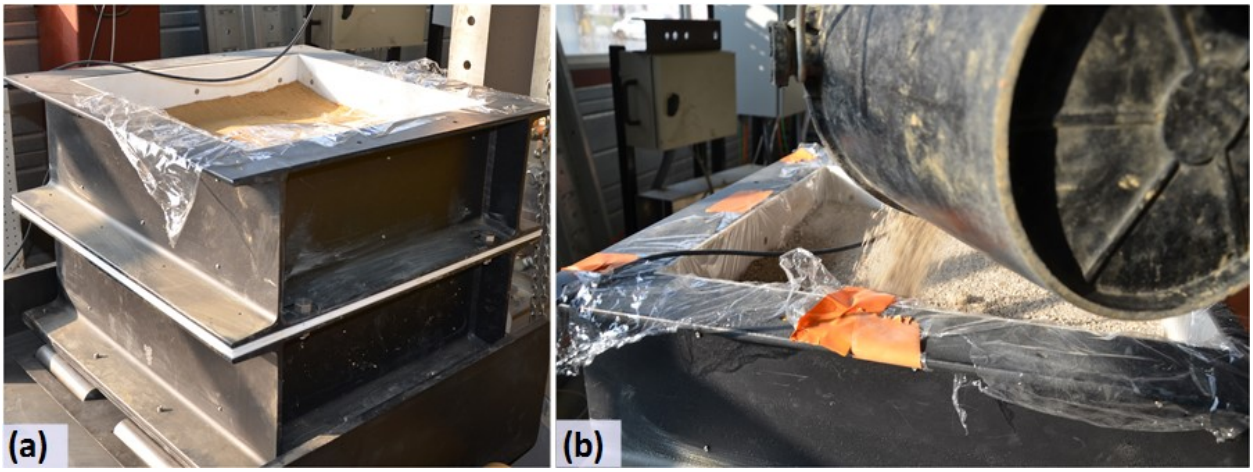

Figure 2.29 (a) Plastic film on top of the rammed earth layer; (b) Adding sand on top of the specimen for the surface leveling

The horizontal shear force was carried out by a horizontal actuator (VH) as shown in Figure 2.28, of a maximal capacity of 300 kN. The shear force was applied with displacement control, 1 mm/min, up to failure. The upper part of the shear box was fixed during the test to a vertical column of the steel frame by using tie rods. A displacement sensor M4 was placed on the

fixed part of the shear box to verify if it has any displacement during the test. Displacement sensors M1, M2, and M3 (vertical) were used to check the movement of the upper face of the specimen (an average displacement was noted during the tested shear boxes about 6.3 mm). M5, M6 were placed on the lower part of the box to obtain the horizontal displacement of the shear box. Figure 2.30 (a) and (b) shows the placement of these sensors.

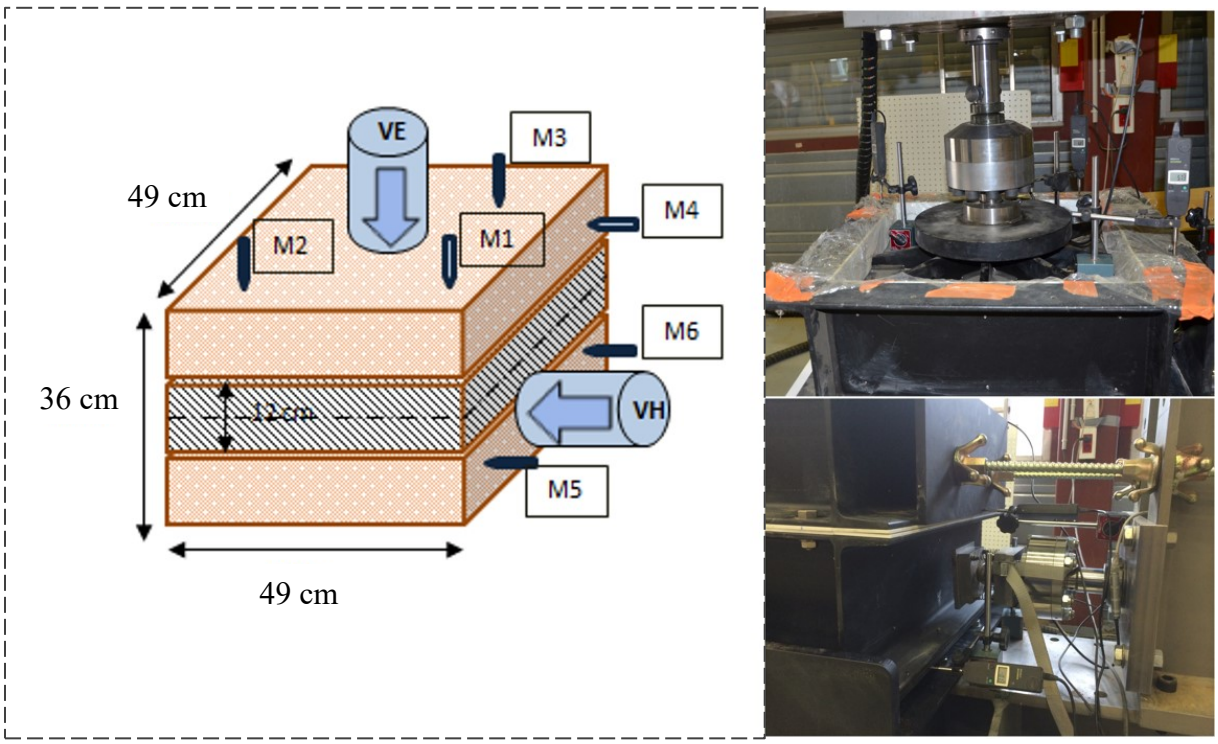

(a) (b)

Figure 2.30 (a) The configuration of the test setup; (b) Positions of the displacement sensors

Results of the Large shear box (inside the layer):

Figure 2.31 displays the horizontal displacement in function of the horizontal force of the hydraulic actuator for the three samples. It is interesting to note that for the case of 0.1 MPa-vertical stresses, a peak was observed while this was not the case for the 0.2 and 0.3 MPa-vertical stresses. It is well known in soil mechanics that the peak corresponds to the behavior of "dense sand" where the soil grains are in an interlocking phase and the shear strength reaches the maximum value when there is a "jump" of the soil grains under the shear stress. When the vertical load increases (the case of 0.2 and 0.3 MPa), the confinement increases, this phenomenon could not be produced.

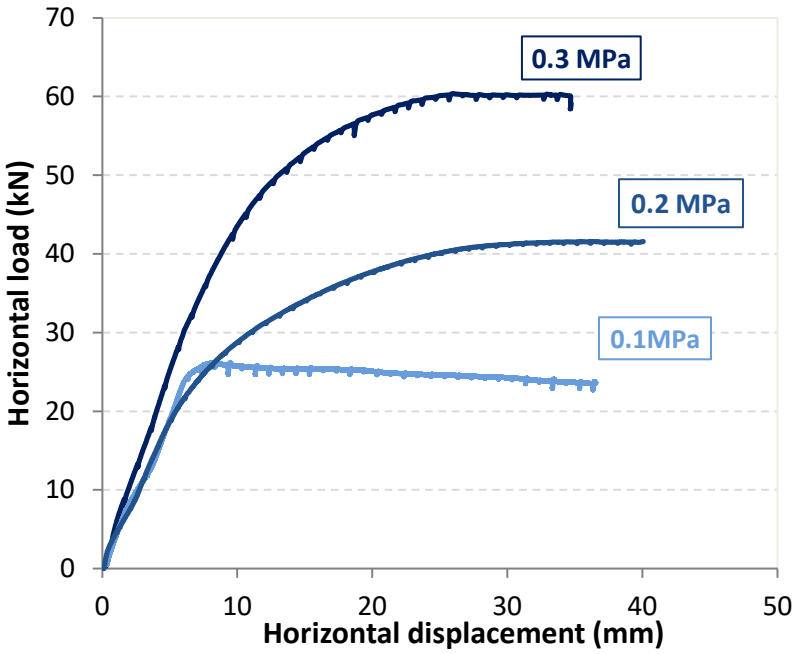

Figure 2.31 The horizontal shear force in function of the horizontal displacement of the horizontal actuator

Figure 2.32 exhibits the shear box when removing the upper part of the shear box to examine the sheared area of each specimen after the test. After removing this part; the rammed earth layer was sheared in the middle of the layer, the lower part of the layer was horizontally displaced. The value of the shear stress was corrected by the correspondent value of the sheared area by using the displacement values displayed by the sensors set on the lower part of the shear box. The displacements sensor M4 assured that the upper part of the shear box was well fixed during the test.

Figure 2.32 Unmolding of the upper part of the shear box after the test

Figure 2.33 shows the three samples after each test for each vertical stress applied. For the three samples, the cracks were spread in the middle of the layer. These cracks were diffused on the longitudinal median plane of the box as in the small typical shear tests.

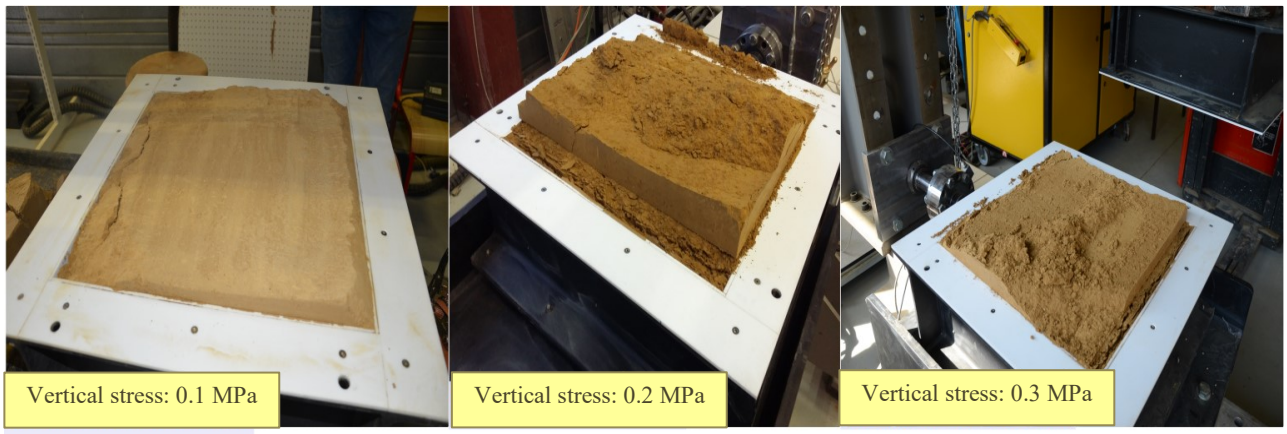

Figure 2.33 The sheared surface of each specimen with the corresponding value of vertical stress

From the Mohr-Coulomb regression line obtained by the three tests, the cohesion and angle of friction are determined as shown in Figure 2.34. The values obtained for the big shear box are c=30.3 kPa and φ=35.3°.

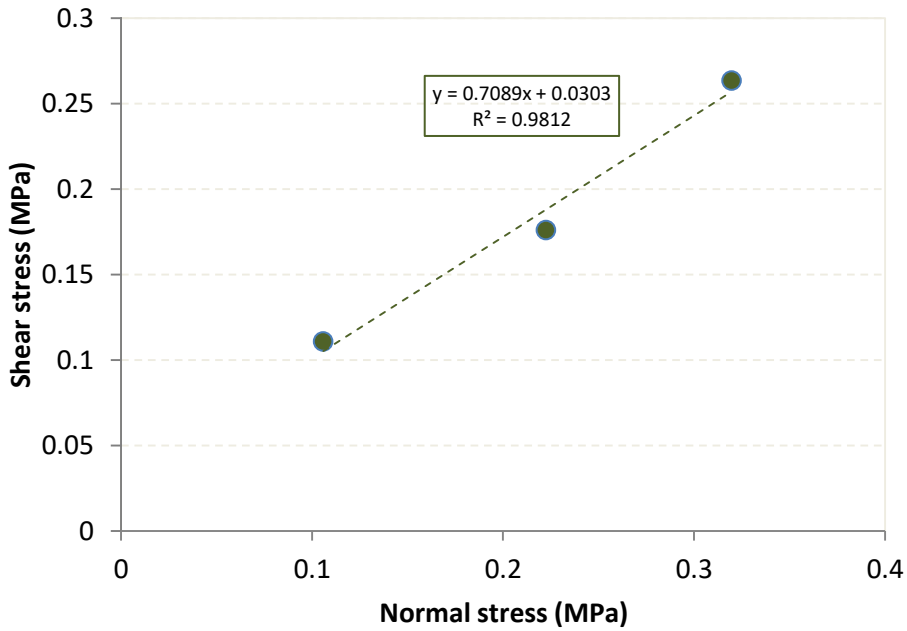

Figure 2.34 Plot of the determination of *c* and *φ* for the large shear box inside one layer

Results of the large shear box at the interface:

It was previously shown that the interface between the layers can be influenced as these parts are more solicited than the upper part of the layers. Hence the shear box was also used to test rammed earth at the interface between the layers and to characterize their mechanical properties.

In this case, the manufacturing process consisted of ramming the earth (with moisture content equal to 12 %) in four layers. The same process of manufacturing was adapted to these specimens but only two different specimens were manufactured (due to the lack of time in this thesis and waiting period for drying of each specimen). The interface of the second layer corresponds to the median plane of the shear box; therefore, the mechanical properties obtained will correspond to a rammed earth at the interface.

Figure 2.35 displays the horizontal displacement in function of the horizontal force of the hydraulic actuator for the two samples for two loading stress 0.1 MPa and 0.3 MPa. The graph shows that, at a same vertical stress, the specimens tested inside one layer had a greater shear strength than that of the interface. This is not surprising because inside the layer - that is better compacted during the manufacturing – it exists a greater density and therefore a greater strength than at the interface. Thus, comparing to the results obtained previously inside the layer, the maximum shear force was equal to 76-83 % of the one obtained inside one layer.

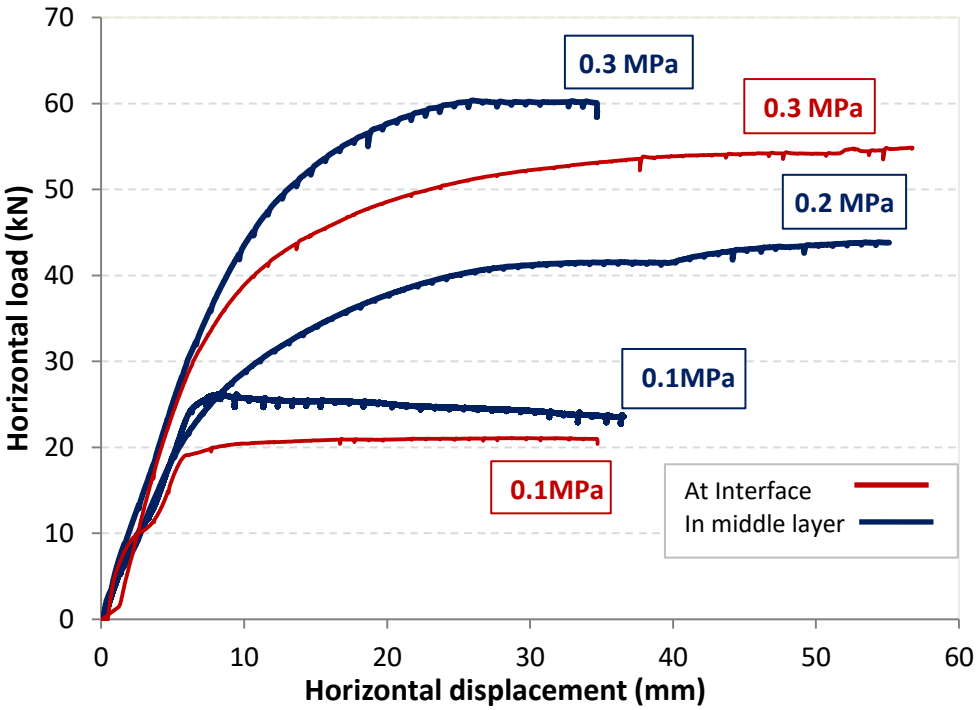

Figure 2.35 The horizontal shear force in function of the horizontal displacement of the horizontal actuator for the two case tests

With only two points we can obtain an approximation for the cohesion and the friction angle at the interface from the Mohr-Coulomb regression line as shown in Figure 2.36. The values obtained for the big shear box are c=24.7kPa and φ=32.9° (Figure 2.36). The cohesion obtained at the interface was lower (24.7kPa) than in the intermediate layer (30 kPa). As for the friction angle the value (φ=32.9°) obtained was in the same range with the one obtained from the test inside the layer (φ=35.3°).

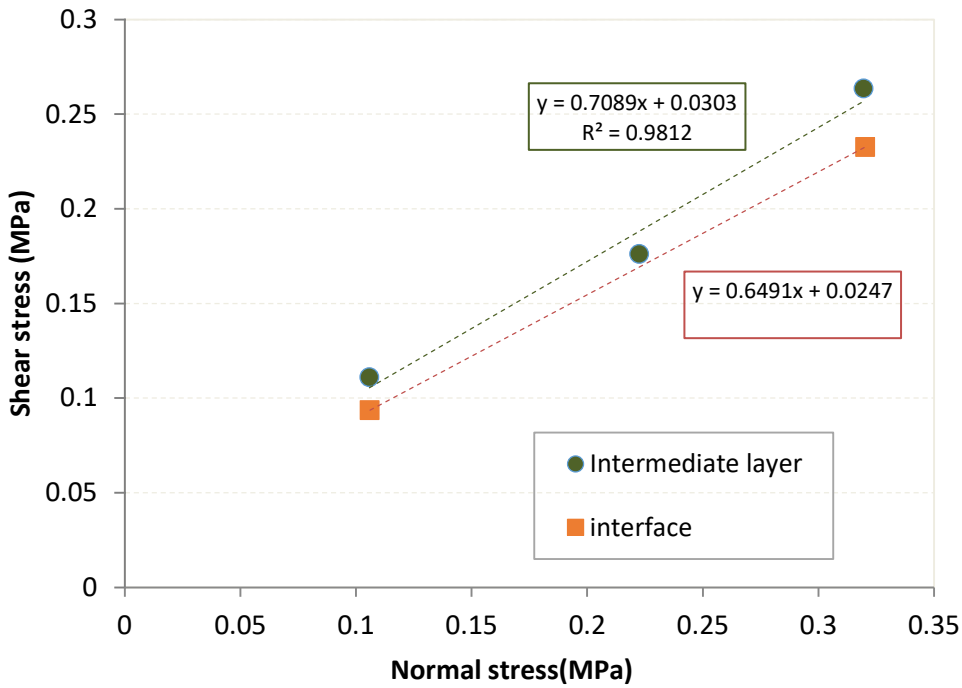

Figure 2.36 Plot of the determination of *c* and *φ* for the large shear box for the two cases

2.5.4 Analysis of the results

For both tests (at the interface and in the layer) the cohesion values were found to be relatively low. To conclude on the accuracy of these values, many aspects which may have influenced the results are discussed in this section as the effect of moisture content and the consolidation time.

Effect of moisture content on the obtained results:

A strong influence of the moisture content on the mechanical behavior was discussed by many authors. Champiré et al. [86] studied the mechanical parameters of the compressed earth with respect to the relative humidity on cylindrical specimens. The author has made several analyses on the mechanical parameters such as variation of compressive strength, Young's modulus with respect to change in moisture content of the specimen due to an alteration in relative humidity. From this analysis, the author concludes that the unstabilized earthen building materials face a reduction in strength parameters with an increase in moisture content. This subject was approached by several authors Bui et al. [63] and Jaquin et al.[79]. In fact, the strength in the unstabilized rammed earth is associated with the level of pore pressures (suction) between the soil particles. As the material dries, the suction increases inducing higher cohesion in the wall ([79] and [78)] therefore conferring to the material higher strength.

The suction values of "Dagneux" soil is represented according to the calibration of Soudani [87], ENTPE in Figure 2.37. It can be seen that the soil suction increases when the water content of the soil decreases which is in agreement with the suction measurements done in the studies of Bui et al. [63], Jaquin et al. [77], Nowamooz and Chazallon [78] on unstabilized rammed earth.

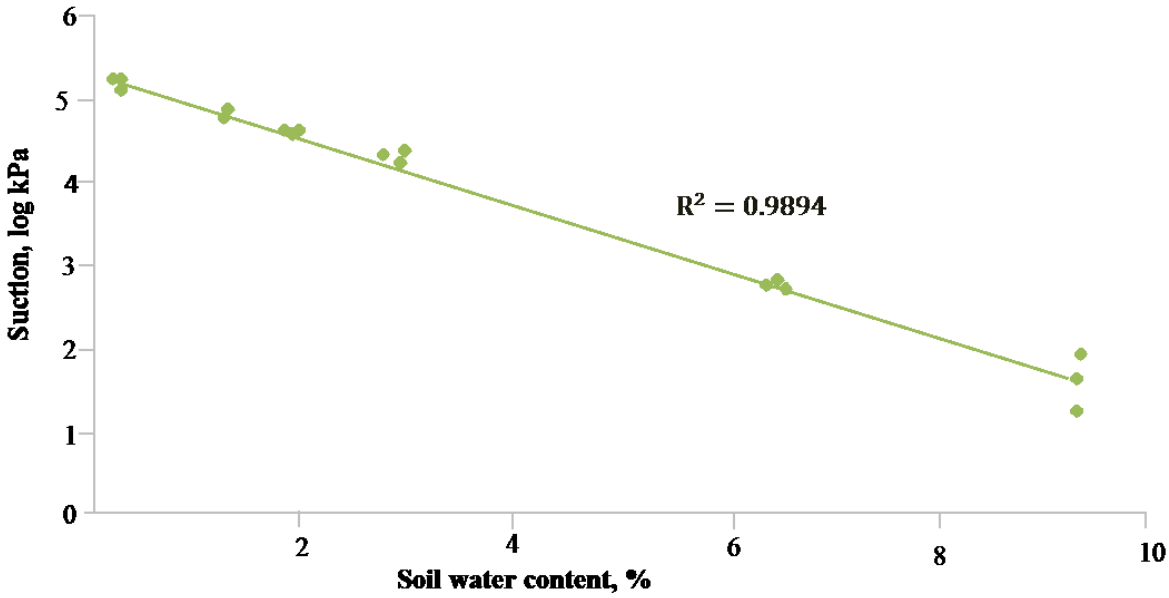

Figure 2.37 Variation of the suction in function of soil water content with respect to ENTPE calibration values [87]

In a study conducted by [88] within the Project of Primaterre, the same material that originates from "Dagneux" was used to investigate the shear strength at interface of several specimens at different condition's: oven dry (0% moisture at test); ambient state (w=1-2%) and moist state (water content >4%). The experimental procedure is performed using the uniaxial press and inclined metallic wedges that can help inducing shear stress and normal stress on the specimen interface. Figure 2.38 shows the variation of the shear strength of the rammed earth interface with the variation in moisture state at the testing time for specimens tested at an inclination of 30°. The results conducted in this study showed that the specimen at the dry state had the higher mechanical strength. The shear strength (at the interface) was lower in the case of the specimen with higher moisture content at the testing time.

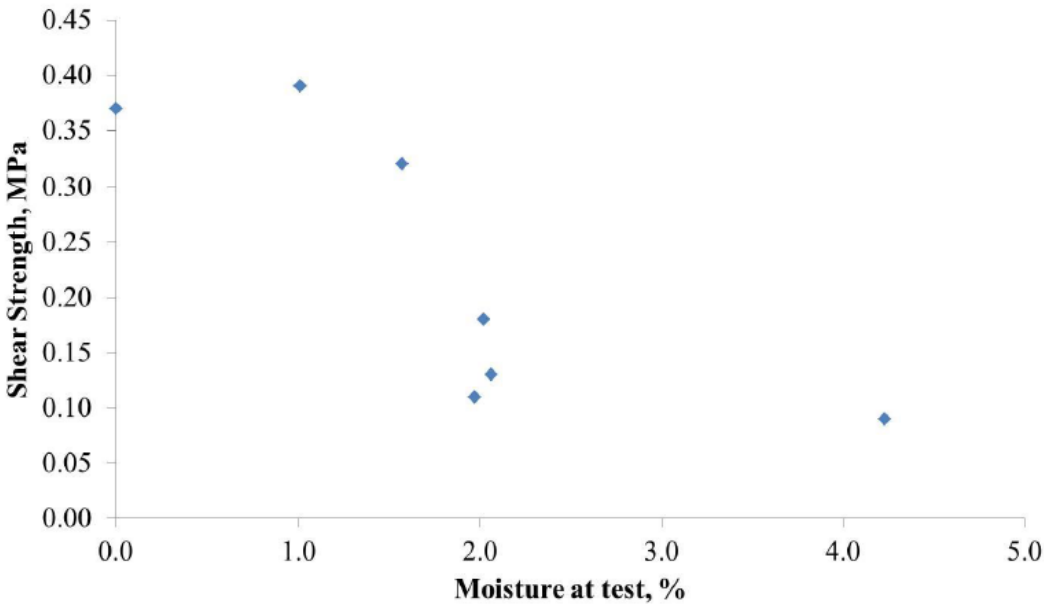

Figure 2.38 Variation of shear strength with moisture state at test – 30° inclination [88]

Based on the results obtained by Holur, 2016 with the same soil, the impact of the moisture content has a great significance on the shear strength in the case of our large shear box. As the shear strength is related to the cohesion by the Mohr-Coulomb criteria, the cohesion will also face a severe decrease when the shear strength decreases.

The water content in each layer of the large box specimen varied significantly from the center of each layer to the borders (4% at borders and 6 % at the center). Hence the fact that the earth layers had, in general, more than 4% of water content at the testing time adds a lot of uncertainties for the characterization of the cohesion of the material.

Table 2.5 indicates the time for curing in the case for the different specimens conducted in this thesis (walls in chapter 3, and large shear box). The table shows that for the walls that had 25 cm thickness, the time of curing was 2 months to finally attain moisture content about (2-3 %). With a greater thickness (the case of the large shear box), the specimens' drying was slower due to the bigger thickness of these specimens, therefore, the earth specimen wasn't dry enough for testing. In this case, the curing time should be more than 2 months since the thickness was greater than the one of the walls. Hence, the mechanical parameters are directly influenced by the fact that the specimen had more than 4% of water content. As for the friction angle studies conducted on a direct shear test of sandy clayey mixture doesn't show a great impact from the moisture content at test.

To conclude the accuracy of the values of the cohesion conducted in this test is still questionable. These values will be incorporated into a numerical model in chapter 4 to test its reliability.

Table 2.5 Moisture content at the testing time depending on the curing time for different type of tests conducted in this thesis

Type of test	Specimen dimension	Curing time	Water content at test (%)
Large shear box	0.49 m x 0.49 m x 0.36 m	1 month	>4-6
Walls under pushover	1.5 m x 1.5 m x 0.25 m	2 months	<2-3

Effect of time and consolidation of rammed earth wall:

In general, the final goal is the determination of the parameters (cohesion and friction angle) of the walls tested under pushover test (in Chapter 3). It is worth to mention that the walls have been submitted to consolidation for more than two/three months, indeed the wall's high weight (approximately 1 tons) and the weight of the concrete beam (300 kg) that have been placed on the wall (see Chapter 3) contribute to the consolidation effect and could have an impact on the parameters that we aim to determine.

In geotechnical investigation on normally consolidated clay, it has been shown that for measurement of the undrained cohesion, the consolidation pressure has to be taken into account for the interpretation of the results [89].

Skempton [90] have proposed the following relationship between the undrained cohesion and the consolidation pressure for a saturated soil:

$$\frac{C_u}{\sigma_c'} = 0.11 + 0.0037\,PI \tag{2.4}$$

Where

PI: plasticity index (in %)

C_u: undrained cohesion

σ_c': consolidation pressure

This leads to the graph shown in Figure 2.39 for a normally consolidated soil. The cohesion increases with the depth as well as the consolidation pressure, with a ratio depending on the plasticity of the soil.

For the rammed earth of the walls, the material is not saturated but presents residual moisture content. According to [91] consolidation is the process in which reduction in volume takes place by the expulsion of water under static loads. Consequences are a reduction of the voids index and simultaneously increasing of internal friction angle [92]. Furthermore, in the case of the walls, higher values of cohesion and friction angle are to be expected.

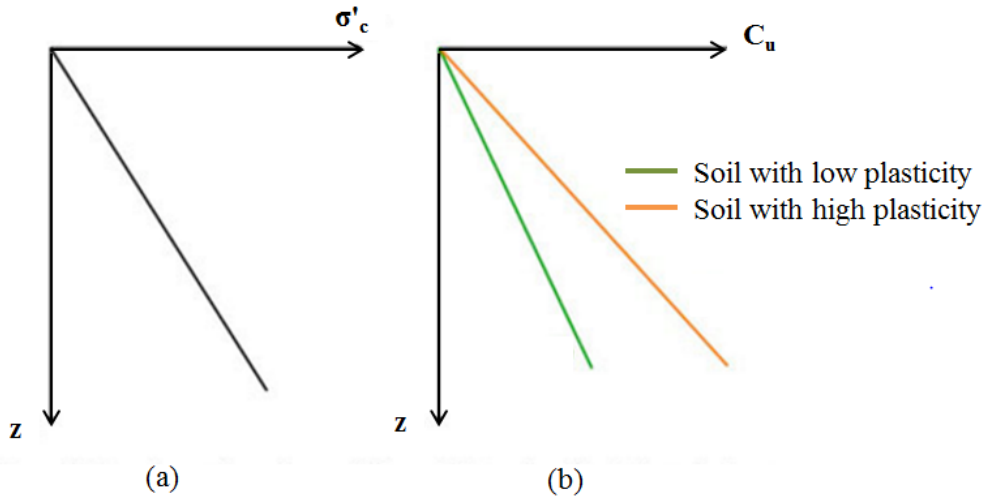

Figure 2.39 Properties in function of depth for soil normally consolidated: (a) consolidation pressure; (b) undrained cohesion

Hence the soil that was explored in the case of the large shear box was not submitted to the same conditions as in the case of earth wall (that are tested under pushover test), as a consequence it is interesting to analyze the parameters of specimens extracted directly from the wall at the same conditions: same water content – same consolidation effect. Therefore, in parallel with the experimental process of the large shear box, the small specimen was taken directly from the walls to test under direct Casagrande shear test which is a practical test and easy to perform. It is worth mentioning that since the wall had 1.5 m width × 1.5 m height × 0.25 m thickness, it was infeasible to have a specimen with the dimension of the large shear box (0.49 m x 0.49 m), as a consequence the samples were cut and tested under typical small shear boxes. The next section explains more in details the process of the direct shear test on these specimens and the results obtained.

2.5.5 Tests on standard Casagrande box

The standard Casagrande's shear box (10cm × 10cm × 4 cm) was used (Figure 2.40 (a)) to test the rammed earth specimens. The standard shear box with these dimensions is currently used in geotechnical measurements to identify the friction angle and the cohesion of the sand or soil. A confining stress is applied vertically to the specimen, and the upper half-boxes is pulled laterally (speed of 1.5 mm/min) until the specimen fails.

Conventionally, specimens are directly fabricated in the shear box. However, in the case of rammed earth material, a preliminary study showed that the specimens manufactured directly in the box could not be representative for a rammed earth wall. Indeed, several factors influence the representativeness of small specimens compared to in-situ walls: for small specimens, the confinement effect is higher during the compaction; the friction effects between the rammed earth and the formwork is also higher; the compaction energy is also higher when the thickness is smaller (energy transmission). Furthermore, manufacturing a representative rammed earth specimen by a pneumatic rammer in a small box (10 cm × 10 cm × 4 cm) is not easy. For this

reason, we decided to take specimens directly from a 1.5 m width × 1.5 m height × 0.25 m thickness rammed earth wall.

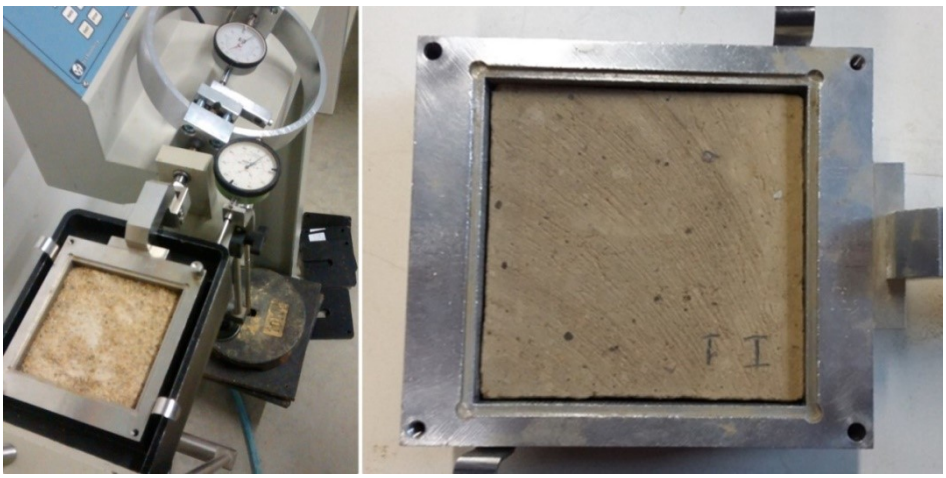

(a) (b)

Figure 2.40 (a) A standard direct shear test; (b) the rammed earth specimen inside the box

The specimens for direct shear tests were taken after two months, and at a quasi-dry state (less than 3% of moisture content, by weight). To extract the specimens from the wall, firstly big earthen blocks (of irregular dimensions but the size were about of 36 cm × 36 cm × 25 cm) were taken by using a manual hammer. Then, a specific saw was used to reshape the big blocks into earthen blocks which consisted of one rammed earthen layer (12 cm of thickness, Figure. 2.41). Finally, the specimens were cut into accurate dimensions (10 cm × 10 cm × 3.5 cm) to fit the shear box (Figure 2.41).

As mentioned before, the density of a rammed earth layer (12 cm) decrease from the top to the bottom. That was why specimens for the shear tests were taken at different positions in an earthen layer: four specimens (Figure 2.42 (a)) were taken at 1 cm from the top, where the compaction was the most important and three specimens (Figure 2.42 (b)) were taken in the middle of the layer. The samples at the bottom of the layer could not be taken because they were too brittle. The specimens at the bottom, closed to the interface, could not be extracted because they were too brittle.

.

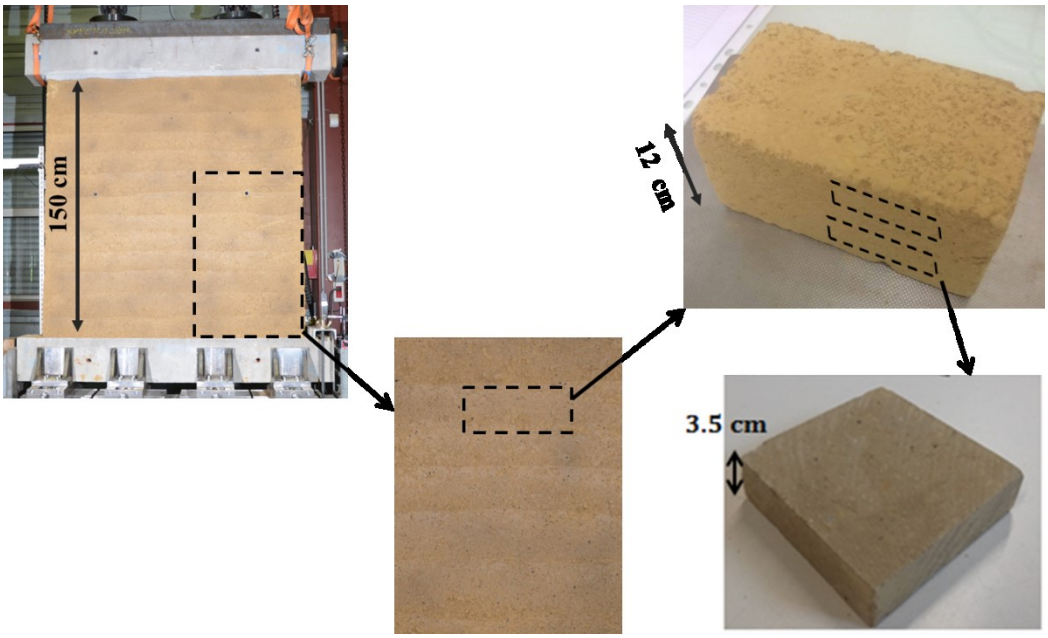

Figure 2.41 Location of the collected samples inside one layer (upper and middle part of earthen layer)

(a) (b)

Figure 2.42 (a) specimen taken from the upper part; (b) specimen taken from the middle part of an earth layer

Test Results:

For each direct shear test, the maximum shear stress was noted and the experimental results giving the relationship between the shear stress τ and the normal stress σ are summarized in Figure.2.43 for all tests. Firstly, note that the tests are consistent with Mohr Coulomb's theory since the experimental results are on the same straight line (i.e. a correlation coefficient greater than 95%). Furthermore, the graph shows that, at a same vertical stress, the specimens from the upper part had a shear resistance greater than that of the lower part. This result is not surprising because the upper part - which was better compacted during the manufacturing - had a greater density and therefore a strength greater than that of the lower part.

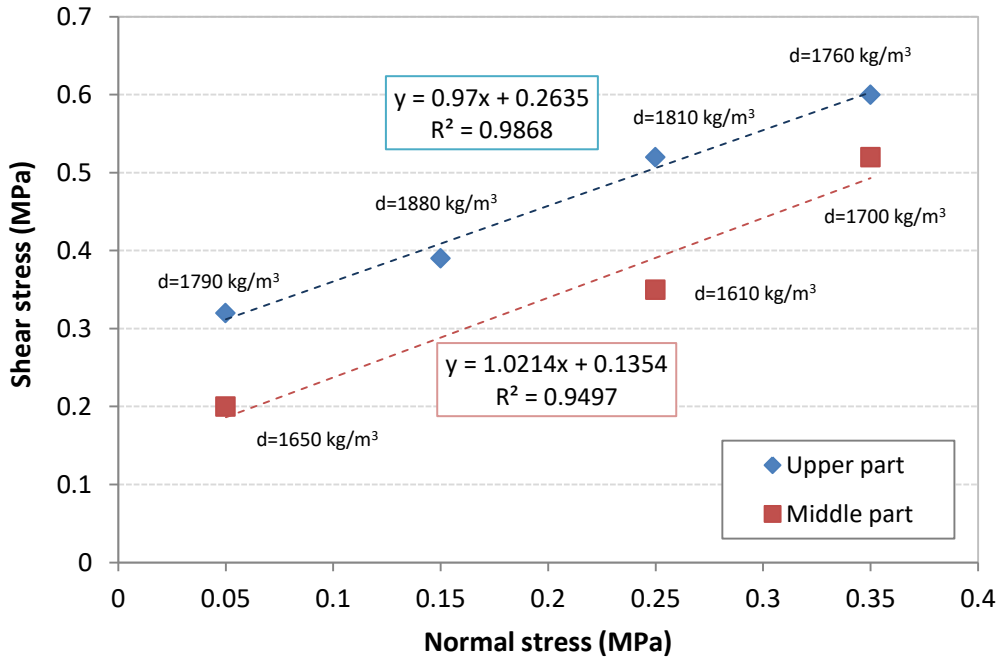

Figure 2.43 Plot of the determination of *c* and *φ* for the standard shear box with the density of each specimen

Following the Mohr-Coulomb's theory, the friction angle and the apparent cohesion can be determined from Figure 2.42, giving respectively 44.1° and 263 kPa for the specimens taken from the layer's upper parts, whereas φ = 45.6° and c = 135 kPa for specimens taken for the layers' middle parts. It is interesting to note that the friction angles obtained were similar for the upper and lower parts of an earthen layer (about 45°). This resemblance could come from the similar roughness of earth grains, between the upper and middle parts. The main difference was the cohesion: the upper part had a more important cohesion (263kPa), comparing to the lower part (135kPa). The upper part of a layer is denser (density (d) between 1750 kg/m^3 and 1880 kg/m^3) since it receives directly the compaction during the ramming process. Oppositely, the lower part is weaker, especially on the bottom of some layers (density between 1600 kg/m^3 and 1700 kg/m^3). It is suggested that with a higher compactness, the dimensions of the micropores in the upper part were smaller than that of the lower part; the smaller micropores gave a higher suction which provides higher cohesion and mechanical strength [79],[63].

Otherwise, the quality of the samples that were close to the bottom layer was not as good as the samples that come from the upper part. Figure 2.43 shows the visual difference between a specimen taken from the upper part and the one taken from the middle part of a layer. This variation highlights again the heterogeneous characteristic in one layer.

2.6 Discussion

Table 2.6 recalls all the results obtained from the small shear box and the large shear box. A big difference is obtained regarding the cohesion values between the one-scale shear box and the small standard shear box inside one layer.

Table 2.6 Results of the parameters: large shear box and small shear box

Type of test	Specimen size (cm)	Friction angle (◦)		Cohesion (kPa)		Water content at test (%)
Large shear box	49 x 49 x 36	layer	interface	layer	Interface	4-6
		35.3	32.9	30.3	24.7	
Small shear box	10 x 10 x 3.5	Upper layer	Middle layer	Upper layer	Middle layer	2-2.5
		44.1	45.6	263	135	

Indeed, the difference of the water content at the testing time between the two specimens is significant. This supports the previous idea mentioned in section (2.5.4) in which the impact of water content (in fact suction) was discussed. The small specimens were left to cure in enough time to achieve (2-2.5%), moreover they had small dimensions that ease a greater evaporation, which could explain the difference. On the other hand, the large specimen had more than 4% of water content at the testing time hence their mechanical parameters were directly influenced and the cohesion had drastically decreased. The small shear box shows that the mechanical properties of the rammed earth wall can improve in function of time and that the cohesion and the friction angle for the rammed earth walls are higher than the one obtained by the large shear box.

Furthermore, it is worth pointing out that the specimen size effect could also have influenced the results as it is a well-known issue in classical mechanics. This phenomenon has already been observed on shear box tests with different size and it has been reported in the literature by [93] and [94] on a different type of materials. In general, these studies showed by increasing the specimen size, the mechanical characteristics decrease.

Comparison with existing results:

Table 2.7 presents a synthesis of the results of friction angles and cohesions obtained for rammed earth from different sources mentioned previously.

Table 2.7 Synthesis of friction angle and cohesion.

Sources	Friction angle (°)	Cohesion (kPa)	Type of test
[77]	48	100	Assumed values for numerical analyses
[78] *	48	724	Tri-axial
[80]	41	13.4	Triaxial
[76]	36.8	560	Assumed values for numerical analyses
[82]	23-65	55-80	Shear box
Current study	35.3	30.3	Large shear box
	44-45	135-260	Small shear box

*Stabilized rammed earth

The results show important variations of the friction angle and cohesion in function of each study (difference of material used, of the approach used). Globally friction angle varied between 35-45° but great dispersion was noted for the cohesion which proves the sensibility of this parameter (suction effect). Yet, more investigation for these parameters at the interface and in the layer is still needed as these parameters should be included in the design principles.

2.7 Summary and Conclusions

The soil used in this study was assessed by achieving compression test on rammed earth specimens. It was found that there was a significant variation in the material performance depending on the selected geometries of the specimen (cylindrical or prismatic specimens). The compressive strength was greater in the case of the cylindrical specimen. These results are similar to other results found in the literature.

Through the DIC, the Young modulus was calculated and the crack pattern of the specimen under compression was revealed. The DIC also highlighted the influence of the interface on the general behavior of each specimen (higher strain obtained by the 7D on the interface). It can be clearly admitted that these interfaces can have an impact on the behavior of the structure and on the crack propagation and should be taken into account in the mechanical behavior of rammed earth.

The shear parameters of rammed earth were also investigated by means of experimental tests inside one layer and at the interface. Mechanical characterization as the shear parameters was obtained through experimentation of large-scale shear box tests of 0.49 m x 0.49 m x 0.36 m in height at two positions: inside the layer and at the interface between two layers. Standard direct shear tests were also used on two types of specimens: specimens taken at the upper part of an earthen layer and specimens taken at the middle part of an earthen layer.

For the large shear box, the results show that the interface between layers has lower mechanical properties than in the layer itself. The results also show that suction is a source of strength in unstabilized rammed earth and that the strength increases as water content reduce.

For the direct small shear tests, two types of specimens were tested: specimens taken at the upper parts of an earthen layer and specimens taken in the middle parts. The results obtained for the upper part were $\varphi_{layer} = 44.1^{\circ}$, $c_{layer} = 263$kPa; and for the lower part were $\varphi_{layer} = 45.6^{\circ}$, $c_{layer} = 135$kPa. Experimental results showed quantitatively the influences of the compaction on the dry densities of the earthen layer and consequently influences on the shear parameters. The interesting finding was that the friction angles obtained for the upper and middle parts of an earthen layer were similar because of the similar roughness of earth grains; and that the upper part had higher cohesion than the middle part due to a higher suction.

When comparing to the results of the large shear box, results show that mechanical properties of the rammed earth are higher than the one obtained from the large shear box (Table 2.7). Hence, the cohesion and the friction angle are expected to be higher on rammed earth wall.

From the point of view of Unsaturated-Soil Mechanics, the cohesion and friction angle were determined in this study using the total mean stress with no measurement of the suction effect. Therefore, the experimental parameters are apparent, and they may be different from one test to another. Thereafter, numerical simulations (in chapter 4) are interpreted in total stresses and discussions are carried out on apparent parameters.

Chapter 3. In-plane behavior of rammed earth walls under static loading: experimental testing

3.1 Introduction

In the matter of the behavior of rammed earth walls, the comprehension of the shear behavior of the walls are fundamental and are rarely found in the literature. Several studies were conducted dealing with rammed earth under vertical loading [14], [60], [95]. Yet only a few studies investigate the behavior of rammed earth walls subjected to horizontal loading. In fact, examining the failure modes is essential for the structural design and the assessment of the mechanical performance of rammed earth buildings by predicting the force or deformation where the failure will occur.

The main objective of this experimental study is to analyze the shear behavior of a non-stabilized rammed earth wall when subjected to lateral forces in its plane. The in-plane failures occur in walls parallel to the direction of earthquake shaking. The application of monotonic loading is considered as an adequate static approach for estimating capabilities under dynamic loading [96], [97]. The evaluation can, therefore, be achieved by performing detailed experiments of static pushover tests [98].

Therefore, several walls with different height/length ratios were built and tested to obtain nonlinear shear force–displacement curves. The image correlation was used to visualize the cracking during the test and to identify the general damage and failure modes.

Moreover, these tests provide data for the assessment of the mechanical behavior in terms of damage and base shear-displacement envelope. The results on the integration of these data in the seismic evaluation are reported in Chapter 5, using the static nonlinear pushover method.

3.2 Experimental laboratory tests found in literature

This part intends to discuss some of the few experimental campaigns that have been conducted on rammed earth walls under in plane loading for a better understanding of the crack pattern and failure modes of structures and to explore the type of experimental test that has been adopted by these authors.

Silva et al. [99] performed a diagonal shear test on 0.55 m x 0.55 m x 0,2 m rammed earth walls (Figure 3.1(a)) which allowed the elaboration of knowledge of the shear behavior of unstabilized rammed earth. Results of these tests are shown in Figure 3.2. The average shear strength of unstabilized rammed earth was found to be 0.15MPa and shear modulus of about 640MPa. As for the crack pattern, the failure of these walls was characterized by a set of cracks with diagonal orientation as illustrated in Figure 3.1(b). Silva observed that cracks also appeared between the interfaces and that they can behave as weakness surfaces for the overall behavior of the wall.

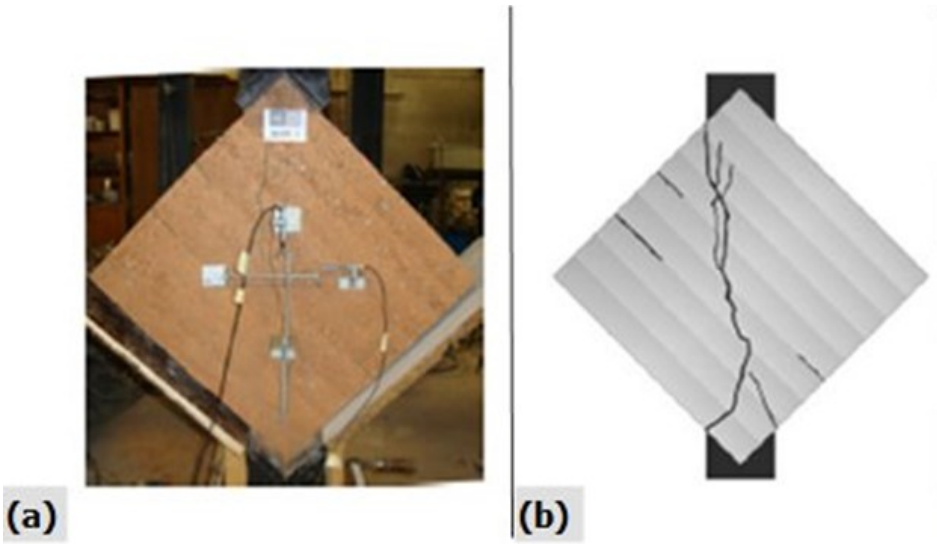

Figure 3.1 (a) Experimental setup of diagonal shear test; (b) Crack pattern at failure of one of the walls, [99]

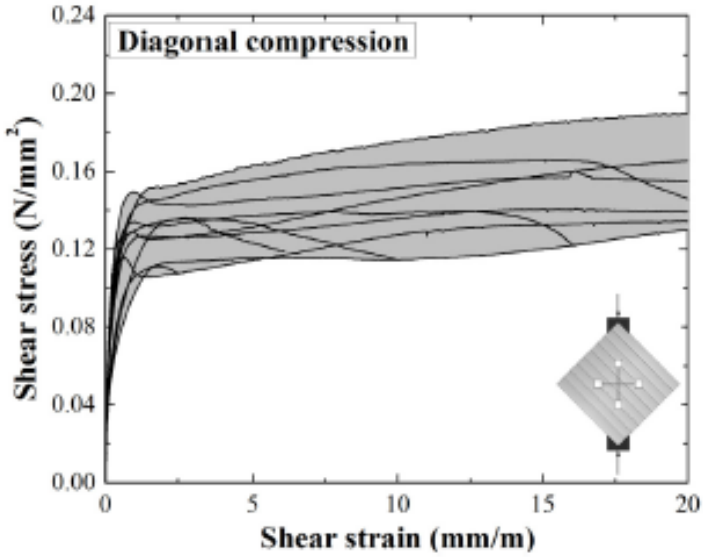

Figure 3.2 Stress-strain curves of the unreinforced rammed earth wallets tested under diagonal compression [99]

In a recent study, Miccoli et al. [75] tested rammed earth walls of size 1.3 m x 1.05 m x 0.25 m for cyclic shear-compression tests. The walls were first pre-loaded with three hydraulic actuators by a steel capping beam on top of each wall (Figure 3.3). The vertical stress was equal to 0.56 N/mm^2 (this value corresponds to 15% of the mean value of f_c measured by uniaxial compression tests where f_c represents the compressive strength of the material) and it was kept constant during the horizontal loading. The results of this study discussed the failure modes and the displacement capacity of experimented walls. The crack pattern for the first and the third wall showed two diagonal lines (Figure 3.4(a) and Figure 3.4(c)) and for the second wall, only one diagonal crack appeared.

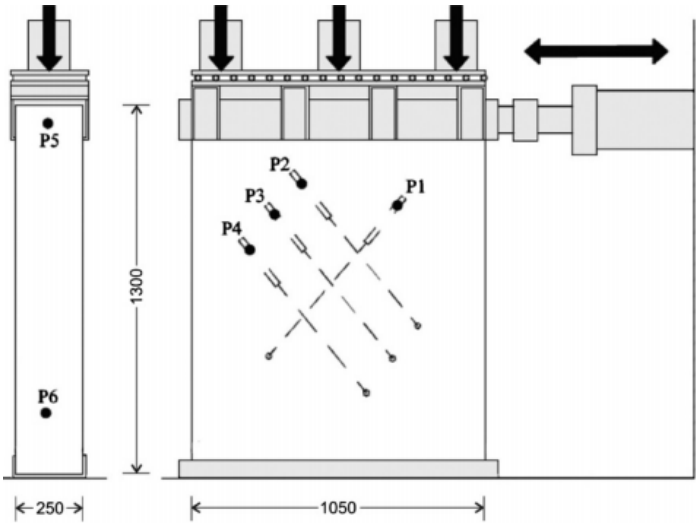

Figure 3.3 Scheme of the cyclic in-plane shear-compression test [75]

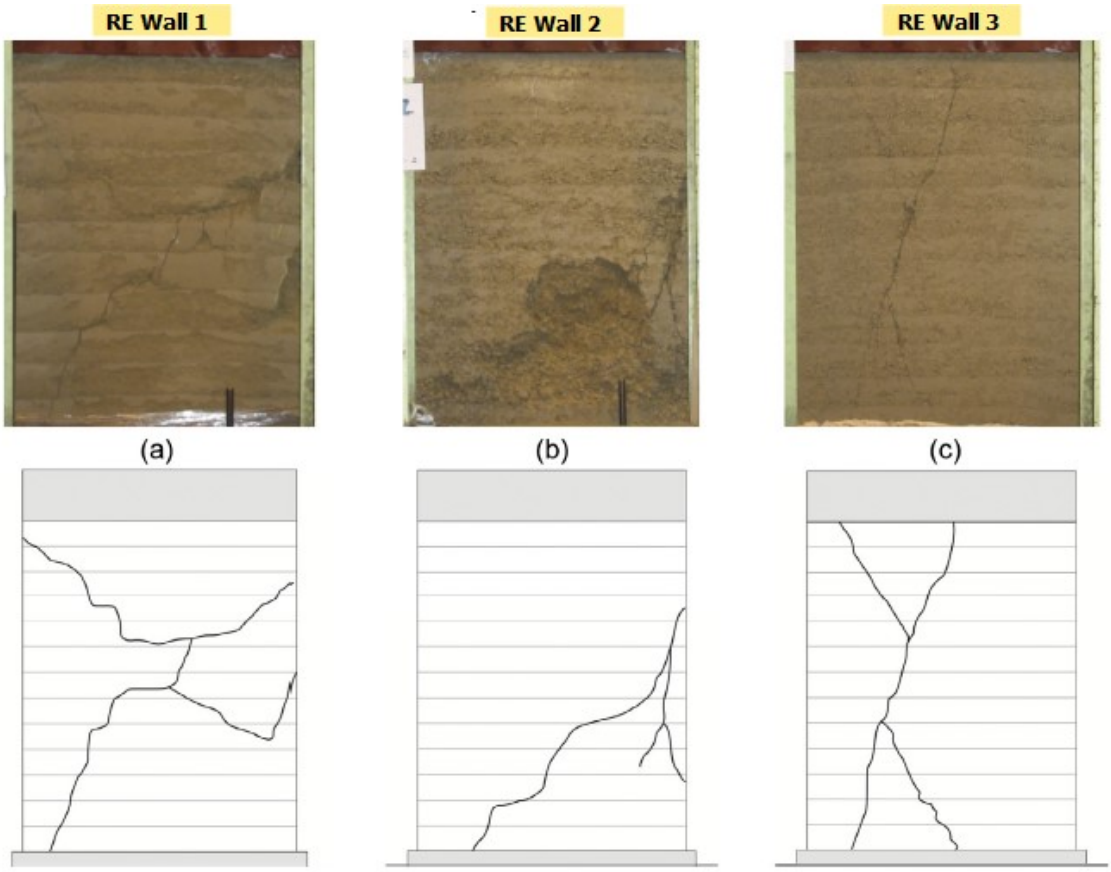

Figure 3.4 Crack pattern under a combination of vertical compression and cyclic shear: (a) RE Wall 1, (b) RE Wall 2, (c) and RE Wall3, [75]

Liu et al. [100] also conducted monotonic lateral loading for rammed earth to validate a new retrofitting technique. This retrofitting technique was validated through a set of experimental test for rammed earth walls under monotonic lateral loading (details about the retrofitting technique

is explained in appendix A, Figure A.5). Figure 3.5 illustrates the experimental setup. The dimensions of the wall were 2.4 m x 2.1 m x 0.6 m and they were cast on a concrete footing. The failure for the unreinforced rammed earth was governed by a shear failure mechanism as shown in Figure 3.6 and the ultimate force reached was about 73 kN. A comparison of the test results for the wall specimens before and after reinforcement was conducted (Figure 3.7) showing higher ultimate load and maximum horizontal displacement for the reinforced structure. Thus, this proposed method was validated by the authors as an effective retrofitting technique. However, the relevancy of these reinforcement techniques in the case of the real structure is still questionable especially due to their influence on the other important aspect of the rammed earth.

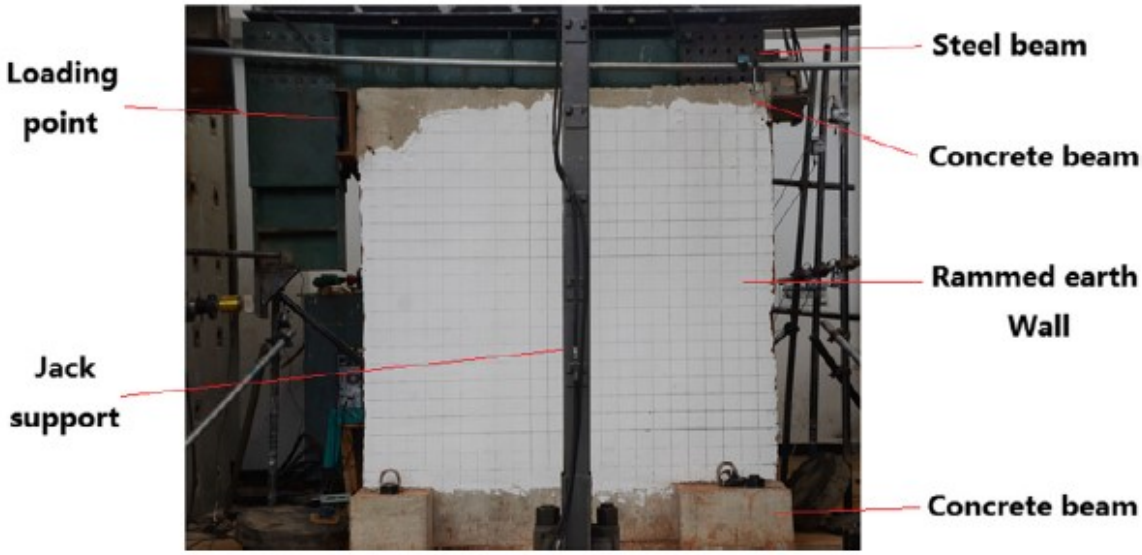

Figure 3.5 Experimental setup, from the study of [100]

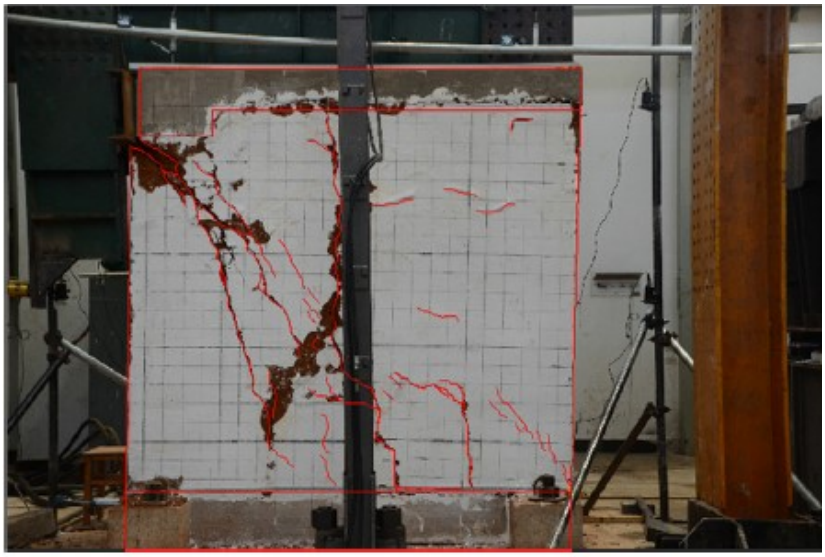

Figure 3.6 Failure of unreinforced rammed earth, from the study of [100]

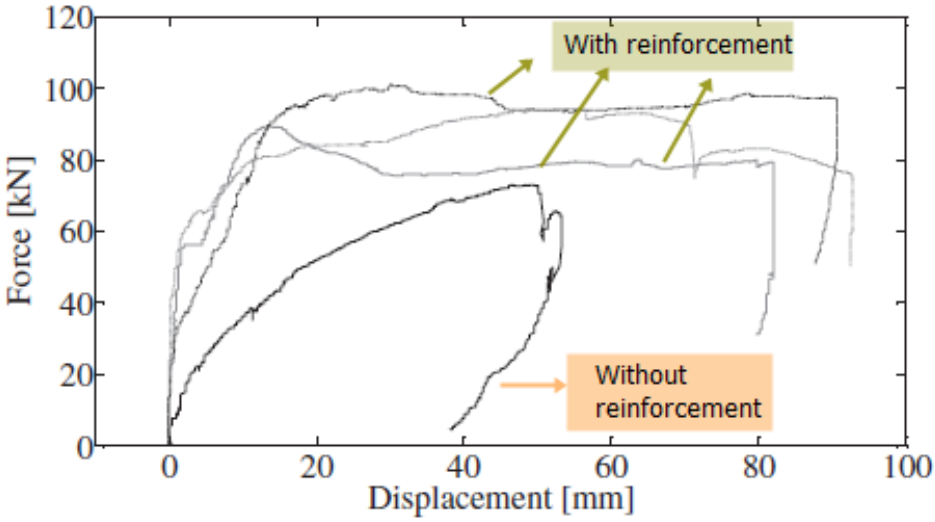

Figure 3.7 Horizontal load–displacement response for the wall specimens before and after reinforcement (solid line) [100]

It's noteworthy to mention that the studies conducted to investigate the shear behavior of rammed earth on the scale of walls are so few and recent. Table 3.1 summarizes the maximum load obtained in the mentioned studies.

Table 3.1 A comparison of test results for the wall specimens under in-plane loading from the literature

Wall dimensions Height (mm) x width (mm) x thickness (mm)	Type earth	Ultimate lateral load (kN)	Failure mode	Reference
1300 x 1050 x 250	Unstabilized	60-78	Shear failure	[75]
2400 x 2100 x 600	Unstabilized without retrofitting	72.94	Shear failure	[100]
2400 x 2100 x 600	Unstabilized with retrofitting technique *	94.25	Shear failure	[100]

* This technique is mentioned more in details in Appendix A

In most of these studies that investigated walls subjected to an in-plane loading, the diagonal shear were observed, this is theoretically predictable. Besides that, some of these tested specimens suffered also from localized horizontal cracks that were located at the interface of earth layers. Hence, similar failure modes are to be expected in our experimental tests under horizontal loading.

3.3 In-plane failure modes: Referring to masonry walls

In-plane failure modes dominate structures where the ratio between the height and the wall thickness is relatively small. When the walls are slenderer, the out-of-plane failure mode can be dominated.

Studying the failure mechanism of masonry wall could be very useful for the study of rammed earth walls. The masonry wall has some similarity with rammed earth in the sense of having joints between the masonry block that create a sort of discontinuity in the wall.

In the case of rammed earth, the interface between the earth layers create a heterogeneous aspect for the wall and consequently can be influenced by an analogous mechanism of failure of those of masonry walls. Therefore, the study of a masonry wall under shear behavior can provide valuable information for our study especially that numerous experimental campaigns have been conducted in the literature [101]–[103]. This section intends to show the type of tests that could be conducted, the parameters that can influence the shear test and the mechanism of failure for the case of masonry walls.

Firstly and according to [101], the behavior of masonry is complex as a result of weakness plans along the vertical and horizontal joints. In addition, the application of a horizontal force on a previously loaded wall causes the contributions of flexural and shear stresses. When the masonry wall is subject to flexure, horizontal cracks appear at the interface brick-mortar due to the low tensile strength of masonry joint plans. According to the author, these are only local cracks and the overall rupture of the wall does not occur in these conditions. These cracks reduce the resistant section subjected to the compression, causing a concentration of compressive stresses and rupture of the wall by compression that affects the bottom corner (Figure 3.8). A similar feature can be found for the rammed earth specimens as in the previous section. Horizontal local cracks were located in the interface between the rammed earth layers for lack of cohesion and friction, therefore cracking can propagate following these interfaces (Figure 3.8).

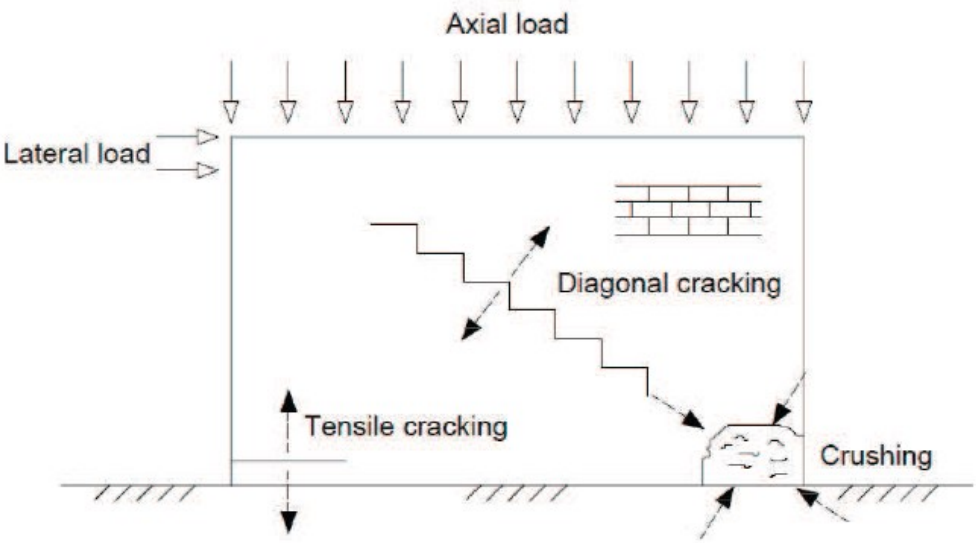

Figure 3.8 Failure modes of walls subjected to shear [101]

Some tests carried out by [102] correspond to tests under constant vertical load and cyclic lateral loading on brick walls. According to [102] if the vertical compressive stresses in the wall are low and the quality of mortar is poor, sliding of a part of the wall along one of the bed-joints can occur under lateral loading (Figure 3.9 (a)). This type of failure is generally observed in the upper part of masonry buildings, this phenomenon is rarely observed in the lower part where generally, the diagonal cracking predominates (Figure 3.9 (b)). These cracks are caused by principal tensile stresses developed in the wall under the combination of vertical and shear load.

Thus, many authors investigated the parameters influencing these failure modes in order to obtain a diagonal shear crack, consistent with the mode of failure related to horizontal actions.

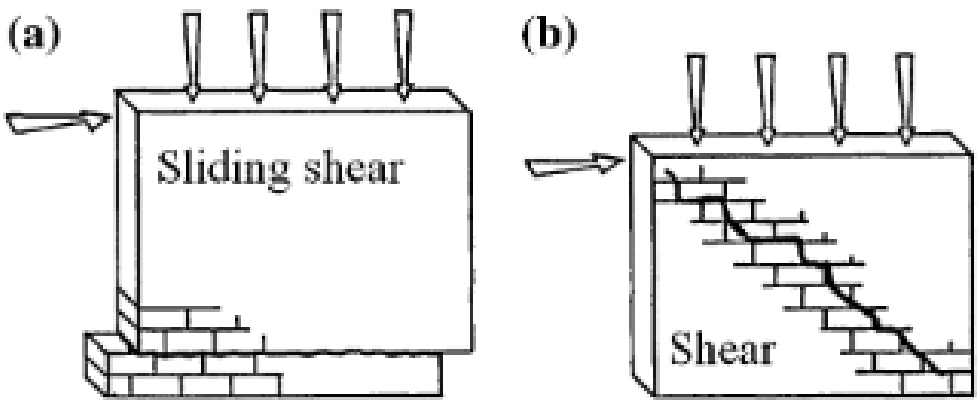

Figure 3.9 Failure mechanism: (a) Sliding on bed joint; (b) Diagonal cracks formation, [102]

In the case of rammed earth, similar failure mechanism to those of masonry can occur. The heterogeneous aspect of rammed earth can induce a mechanism of failure due to the sliding between two earth layers. On the other hand, this type of failure could be avoided by controlling the confinement of the wall.

Tomaževič and Weiss [103] studied the influence of the level of pre-compression that turned out to be the predominant parameter. The authors tested different levels of vertical loads, ranging from 15% to 30% of the characteristic resistance of the masonry. The behavior became more brittle when increasing vertical loading. They concluded on the increase in the shear strength of the walls with the increase of the pre-compression stress. They also observed a greater rigidity (beginning test during the elastic phase). Results also showed that the walls tested with lower levels of pre-compression allowed for larger displacements, with greater ductility. According to [102], the shear strength of masonry also depends on its geometry (length/height ratio), the mechanical characteristics of the masonry and the boundary conditions. He recommends a ratio (h / l) equal to 1.5 for the study of masonry shear.

Three type of tests are recommended for the design of masonry structures by [104] to assess the design of masonry structure. In-plane loading tests of symmetrically fixed, cantilever walls at constant vertical load [103]and diagonal compression test as in Figure 3.10.

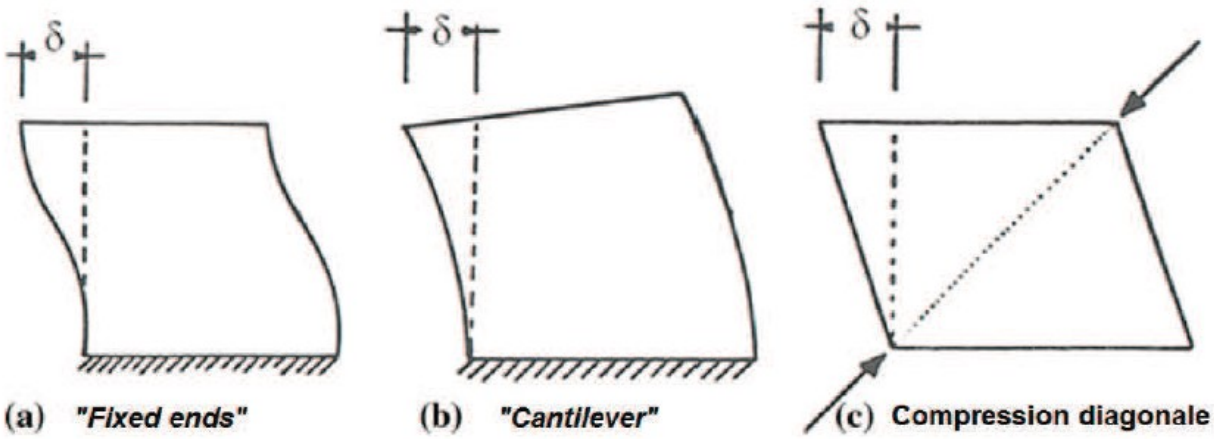

Figure 3.10 Schematic presentation of different types of tests suitable for evaluation of parameters of seismic resistance of masonry wall [104]

As mentioned before the pre-loading is an important parameter that can have a direct effect on the behavior of the masonry during the test. The literature has shown that the test type "cantilever" is widely referenced and used to represent the different failures modes that may occur, depending mainly on the vertical preload applied ([102] and [103], for example). Thus, the cantilever type of test is more adapted because it allows the control of the vertical force applied throughout the test, and therefore the failure mode that wishes to be characterized.

The experimental testing of the rammed earth walls in this study was conducted using the cantilever type of test. With the analogy of the failure modes of masonry walls, different failure modes can result from rammed earth walls carrying lateral loads: diagonal shear failure, sliding shear failure at the interface, in-plane bending failure.

3.4 Experimental Program of Pushover tests

This section explains the experimental campaigns that were carried out in the laboratory to test four rammed earth walls under static loading. Detailed explanation about the specimen manufacturing and test setup are provided. The failure modes of rammed earth walls are also exposed and analyzed.

3.4.1 Specimen manufacturing

Rammed earth walls were constructed in the laboratory, with two different height/width ratios. Two walls were 1.5-m-high × 1.5-m wide × 0.25-m-thick, representing at the 0.5-scale a 3-m-high × 3-m-wide × 0.5-m-thick wall, which is the current configuration of rammed earth walls in France. Two other walls had the same width and thickness but were 1.0 m high, to study the influence of the height/width ratio on the in-plane performance of rammed earth walls. Walls were built on a 0.25-m × 0.25-m × 1.8-m concrete beam (Figure 3.11).

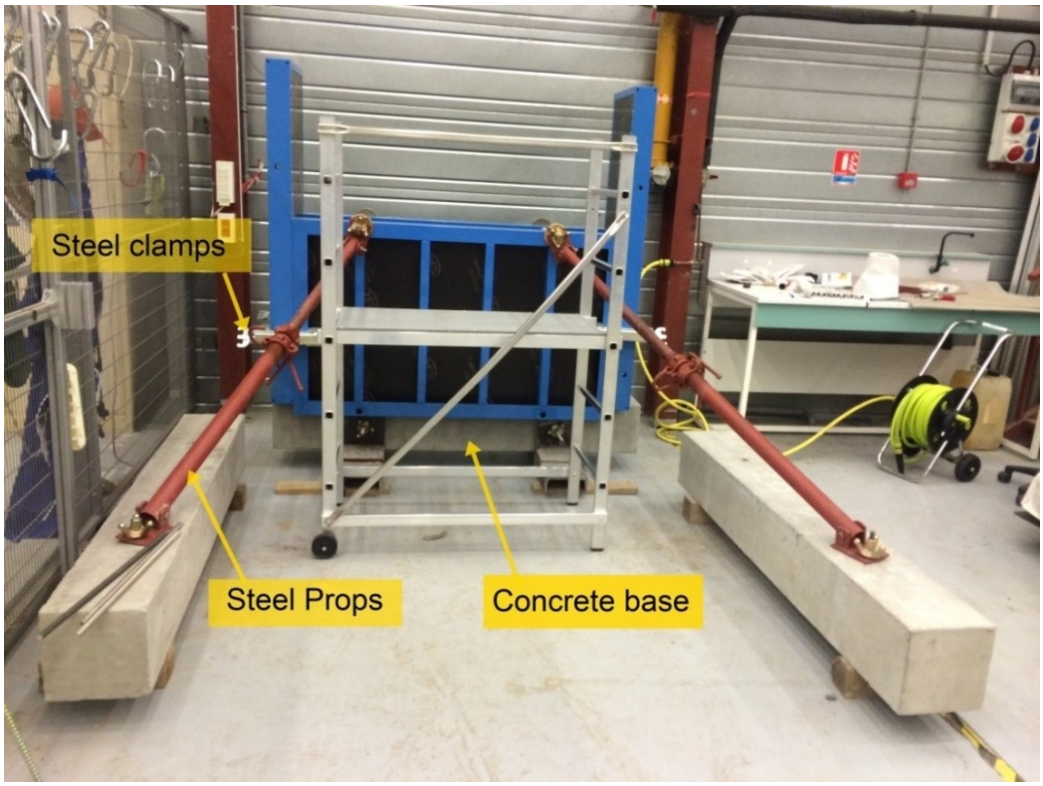

Figure 3.11 Metallic formwork fixed to the ground before the manufacturing

The preparation of the soil mixture was carried out manually for each specimen in the laboratory. Figure 3.12 (a) illustrates the preparation of the walls in the lab. The soil was spread on the ground and then water was distributed by means of a water pipe. The mixture of earth with water was done manually using hand shovels. At the beginning, a cement mixing tank was used for the homogenization of the soil with the water, but the method wasn't very accurate as the machine tends to transform the earth into small circular balls while rotating. Mixing with hand shovels proved to be more effective in this case.

Figure 3.12 Manufacture of the wallet-specimens: (a) preparation of the soil; (b) compaction by the means of a pneumatic rammer; (c) demolding the frameworks; (d) placing the concrete beam on top of the wall

Water was added to the earth to obtain the optimum manufacturing water content (following the optimum proctor done in Chapter 2), approximately 12% by weight in this case. The characteristics of each wall are given in Table 3.2. Specimens were sampled to check the water content repeatedly and the drop test was used along the preparation to control the water addition. The manual method assured the best homogenization of the earth.

The mixture was then poured into a formwork and compacted in layers using a pneumatic rammer (Figure 3.12 (b)). The formwork panels were reinforced and stiffened by means of two props fixed to two concrete beams that were placed on the ground as in Figure 3.11. Steel clamps were also used to tighten the formwork. This was essential because the formwork risk to displace under the vibration of the pneumatic rammed.

At the end, the disassembling of the formwork was carefully done after the manufacturing by sliding each shutter to avoid any damage to the specimen (Figure 3.12 (c)).

The walls were then cured at laboratory ambient conditions (20°C and 60% relative humidity, RH) for two months. This is the time necessary to quasi-dry the specimens. In two months, the moisture content of the walls was about 3% (determined after the pushover tests). After the wall was erected, another 0.25-m × 0.25-m × 1.8-m concrete beam was placed on top of the wall (Figure 3.12 (d)). This beam made it possible to apply a horizontal load on the top of the wall during the pushover test. Before installing the concrete beam, a thin lime mortar layer was added on the top surface of the wall to increase the bonding between the wall and the beam, after that the beam was carefully placed. The four walls are represented in Figure 3.13.

Table 3.2 Characteristics of the wall specimens

Wall number	Wall dimensions Height (m) x width (m) x thickness (m)	Manufacturing water content (%)	Water content at test (%)
1	1 x 1.5 x 0.25	13	3
2	1.5 x 1.5 x 0.25	12	4
3	1.5 x 1.5 x 0.25	11	3
4	1 x 1.5 x 0.25	13	3

Figure 3.13 The four rammed earth specimens before the pushover test

3.4.2 Experimental Setup

The experimental device consists of a steel loading frame where the beams and columns have an HEB400 cross section. The bottom concrete beam was fixed to the steel frame using four steel brackets that can be mechanically adjusted for satisfactory embedment (Figure 3.14). A steel prop (B on Figure 3.14) was used as a support to prevent the beam from sliding when the top

horizontal displacement was applied. The bottom concrete beam was also maintained by vertical tie rods to prevent the beam from rocking (T on Figure 3.14).

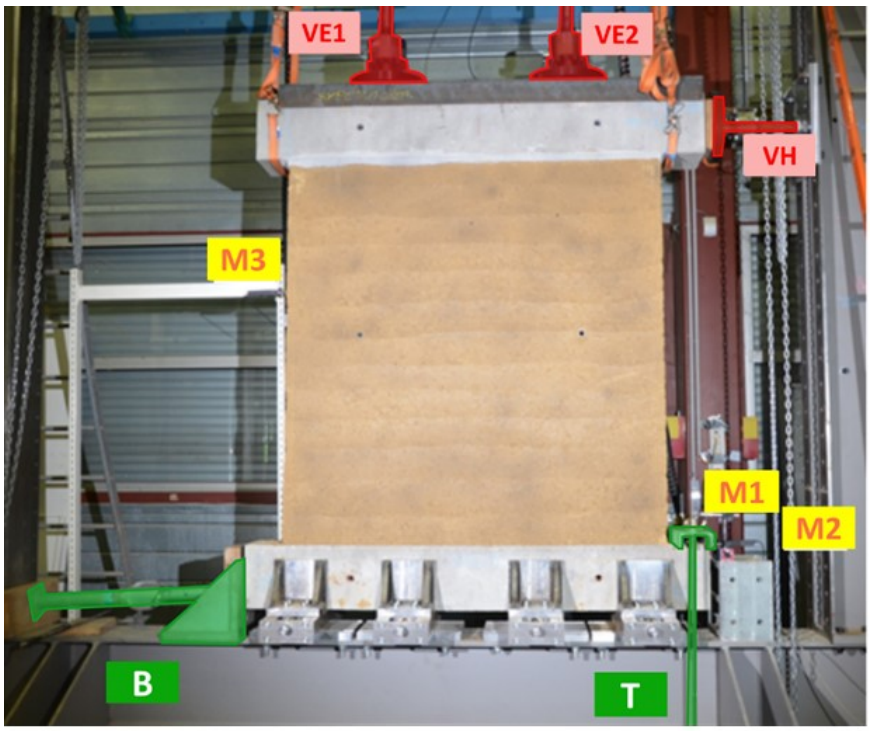

Figure 3.14 Test setup on a rammed earth wall (1.5 m × 1.5 m × 0.25 m)

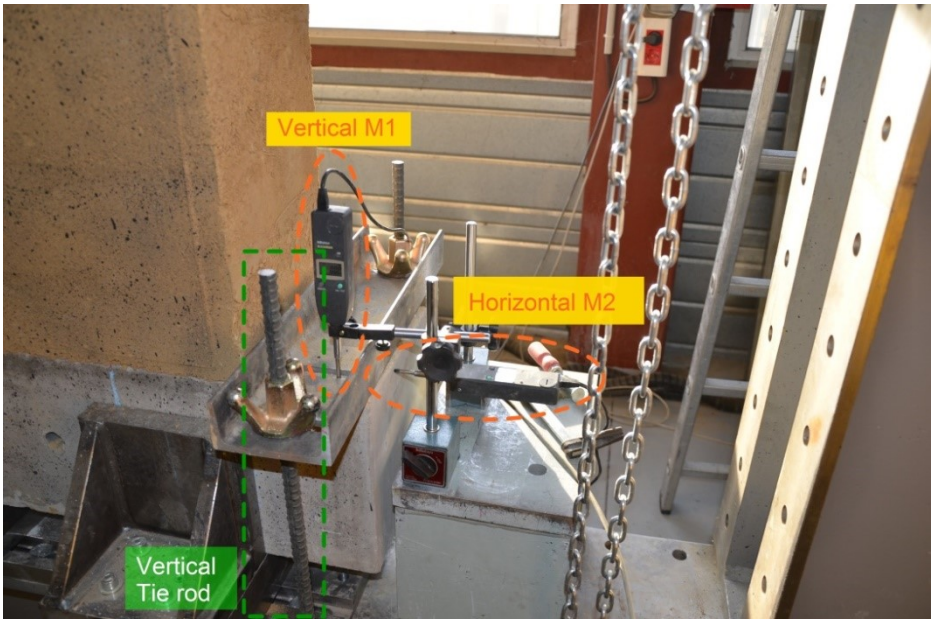

Figure 3.15 Vertical tie rod to prevent the beam from rocking

Displacement sensors M1 (vertical) and M2 (horizontal) were used to check if there was any movement of the bottom concrete beam during the test (Figure 3.15). The displacements measured by the horizontal sensor M3 were used to verify the accuracy of the results obtained from the digital image correlation.

DIC Setup and synchronization of the results:

The DIC was used as a measurement technique to capture the failure process of the rammed earth walls and to provide all the needed information about the displacement field for the corresponding structure.

During the tests, the two projectors installed were the only two light sources present. Thus, it is possible to guarantee a constant illumination for the specimen. Both projectors were installed on each side of the camera but sufficiently far so that the camera is not disturbed by the heat emitted by these projectors. To facilitate the processing of the results, a specific box allows the synchronization of all the measurement recorded during the test (the force and displacement of all three actuators and the three displacement sensors) and the images captured with the camera. The acquisition frequency was 1 image per second. The DIC setup is illustrated in Figure 3.16.

Figure 3.16 (a) The position of spot lights and camera; (b) Close-up of a camera and adjustment apparatus

Loading steps:

For the pushover test, first vertical loads were applied to the top of the wall to simulate the vertical loads in a building (dead and live loads). Two electrical actuators VE1 and VE2 were used to apply these vertical loads (Figure 3.14). These loads were applied at a rate of 1 kN/s to 60 kN in each actuator. These vertical loads were maintained constant during the horizontal pushover. They represent a normal stress of 0.3 MPa, as in current rammed earth walls in a two-storey house. These loads were distributed on the top concrete beam through a system that includes a UPN 300 steel profile and cylindrical rolls placed at the top surface of the upper

concrete beam (Figure 3.17). This system allows a horizontal displacement of the beam during the horizontal loading without friction.

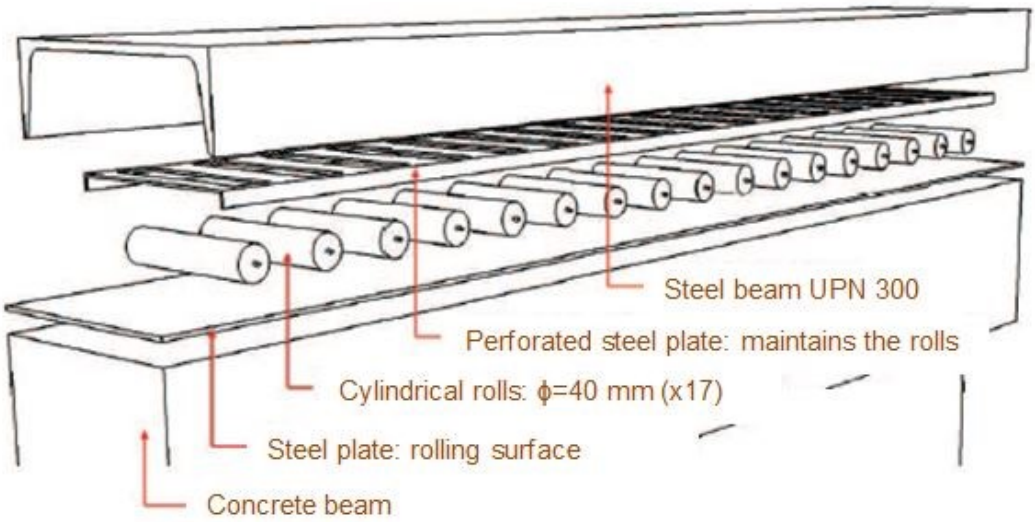

Figure 3.17 System placed on top of the beam

Then the horizontal pushover was carried out by a hydraulic actuator (VH) with displacement control (VH on Figure 3.14). The loading rate was 1 mm/min until failure. The DIC was also used to measure the displacements and inspect the evolution of the cracking in the walls during the test. A summary of the parameters of the test is shown in Table 3.3.

Table 3.3 Summary of loading system parameters

System	Characteristics
Hydraulic actuator (VH)	Loading rate:1mm/min Horizontal displacement
Electrical actuator (VE)	Loading rate: 1kN/s Applied vertical load: 120 kN

3.4.3 Process of an experiment

The accomplished tests showed primarily good stability. First, the vertical force VE1 and VE2 applied remained constant during the test throughout the application of the horizontal force (Figure 3.18 for wall 1). The same procedure is adopted for each wall and similar graphs as for wall 1 are obtained for the other walls 2, 3 and 4.

In addition, displacement sensors M1 and M2 showed a low vertical movement of the lower beam, M1 showed (relative average value: 0.26 mm) and low horizontal movement (0.22 mm),

respectively. These are average values found for the walls. Given these results, the beam is considered to be well supported by the frame, thus validating the boundary conditions that have been set before the experiment.

The force-displacement curves for each wall provided by the hydraulic jack allowed us to obtain the following curves in Figure 3.19.

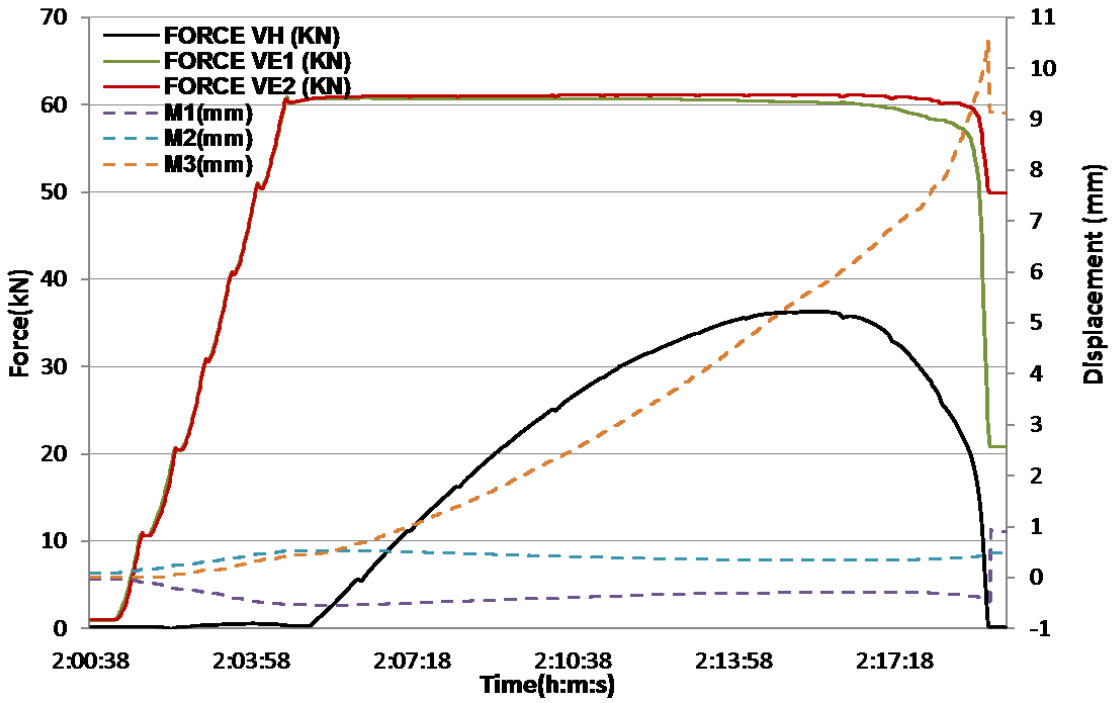

Figure 3.18 Evolution of the forces applied by the actuators VE1, VE2 and VH and measurement of the sensors M1, M2 and M3 in a function of time for the case of test wall 1

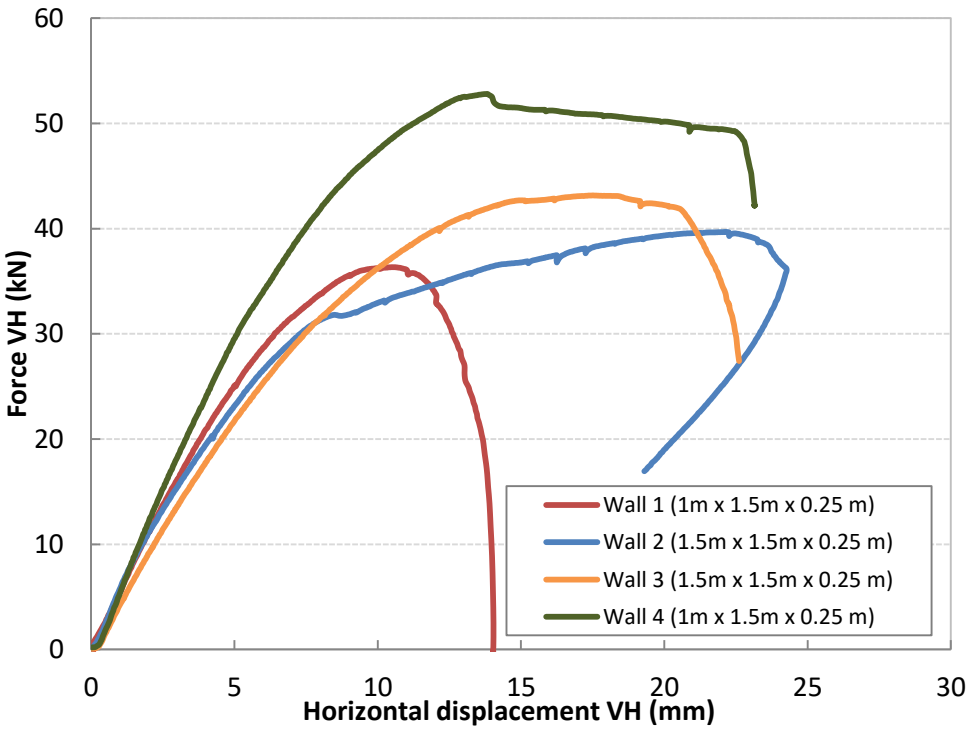

Figure 3.19 Horizontal force in function horizontal displacement provided by the hydraulic actuator VH for each of the tested walls

Through these results, the first thing to be observed is the net difference between wall 4 and wall 1 (possessing the same hight) which was relatively surprising. Concerning walls 2 and 3, they presented similar behavior in terms of ultimate strength and initial stiffness. These results will be discussed more in details in the next section.

3.4.4 Comparison of measurement with M3

To validate the relevance of the measurements performed by the image correlation, a comparison was made between these results of the displacement provided by the 7D software and those measured by the M3 displacement sensor depending on the horizontal force applied by VH. Pixels close to the placement of M3 were chosen as in Figure 3.20.

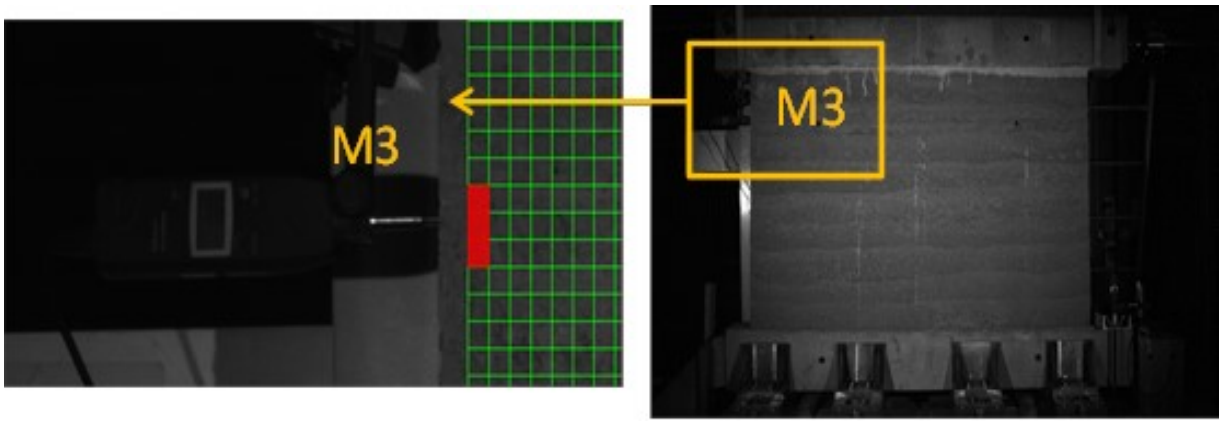

Figure 3.20 Pixels close to the placement of M3

Figure 3.21 illustrates this comparison for wall 1 (1 m height) where a good correspondence between the two measurements was observed (Figure 3.21). This proves the precision of the apparatus used and assures the accuracy of the results provided by the software 7D. The same comparison is done with the other walls (refer to Appendix C). In general, we can neglect the lag difference for some walls (for example in Figure C.3) because it is mainly due to an error from the experimental setup of the placement of sensors. We can certainly proceed to use the results provided by the DIC.

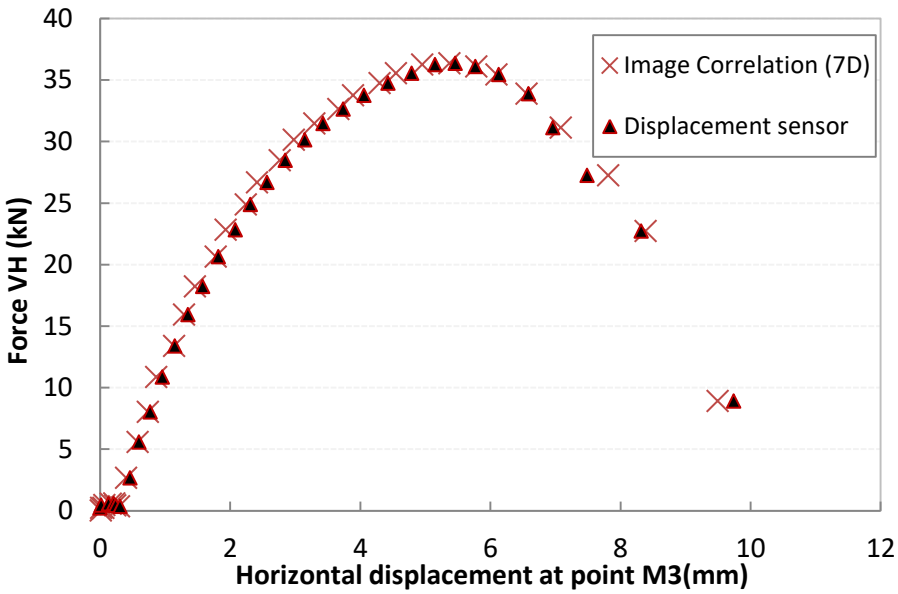

Figure 3.21 Comparison between the displacement given by the image correlation and the displacement sensor in function of the horizontal force VH for wall 1

3.4.5 Results of the walls tested

Phase 1: vertical loading

During the first step of the pushover test, the vertical loading, the wall suffered from only uniaxial compression loading. The displacements during this phase were recorded using DIC (Figure 3.22). The vectors on top of the wall assure a uniform distribution with small variation between the two extremities of the walls (average 0.5mm). This difference is also observed for wall 2, 3 and 4.

Through the DIC, we were also able to visualize the vertical displacement and calculate the vertical strain 'eyy' at the local scale (an example on wall 3 is given in Figure 3.23) during the preloading phase. The same outcome was observed for the other walls (Appendix C). It can be seen that the interface between layers is highlighted by higher deformation in the wall. This was also observed on the cylindrical and prismatic specimens tested under compression (in chapter 2). This point out a specific behavior for rammed earth walls where these interfaces seem to be solicited where the strain is accumulated more than the other parts of the wall. The phenomenon was visible at the local scale for all the walls. Therefore, between 2 successive layers it is assumed that it exist a significant change in stiffness.

From the displacements of the middle part (following the height) of the wall, the Young modulus was calculated (Figure 3.22). Two points are chosen in this area and Young's modulus is calculated by the following formula:

$$E_{wall} = \frac{\Delta F . H}{S . \Delta H} \tag{3.1}$$

Where ΔF is the difference between two pre-loading points, H is the distance between two points in the middle area chosen for the calculation of the displacements, S the surface of application of the vertical stress and ΔH is the difference between the two displacements measured at two levels of loading.The zone for calculation is given in Figure 3.22. This calculation was done using only the displacement fields which was more precise than the strain fields given by the DIC. It should be noted that the effect of the spatial heterogeneity on the calculation of the Young's Modulus wasn't taken into account due to the difficulty of having accurate results of the strain measurement inside one layer of rammed earth through the DIC. That is why an area in the middle part of the wall was chosen for this calculation which corresponds to a global calculation of Young's Modulus.

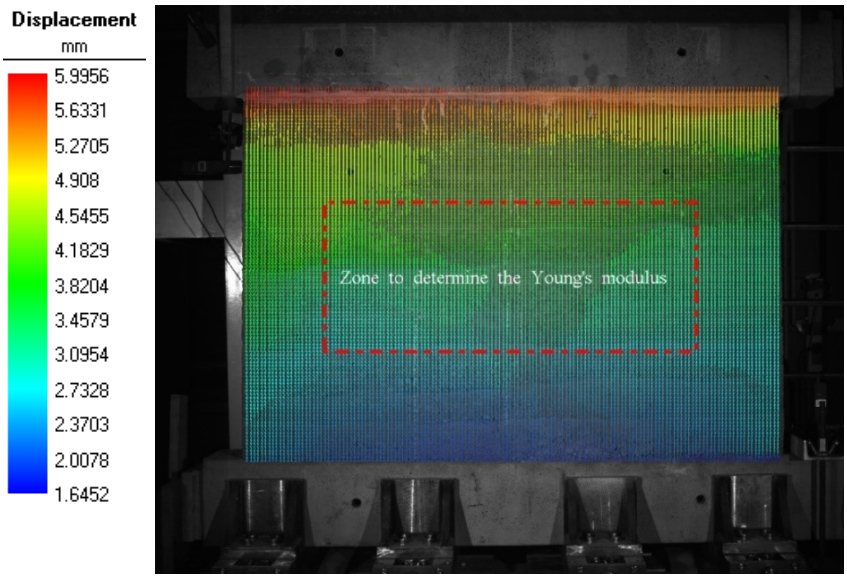

Figure 3.22 Displacement vectors of wall 1 during the vertical loading phase

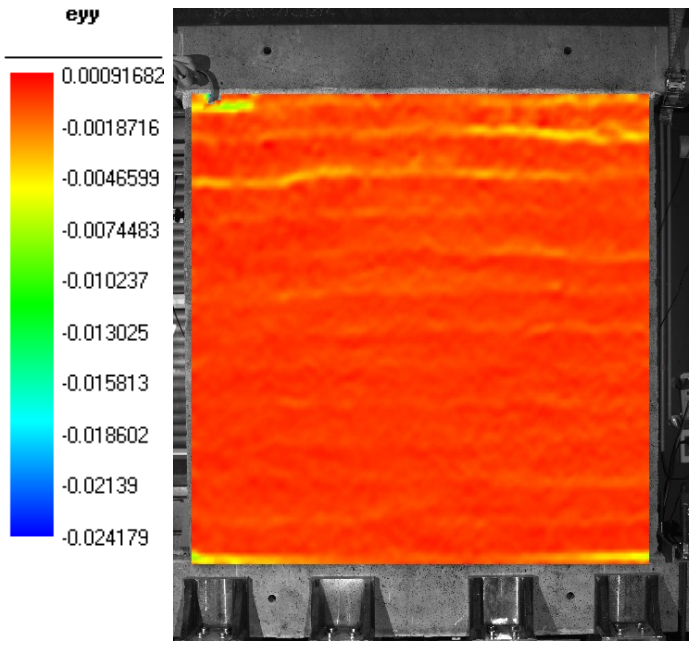

Figure 3.23 Vertical strain at the end of the preloading phase (case of wall 3)

The results are summarized in Table 3.4. The average Young's modulus obtained of the tested walls was approximately 400 MPa. This value is slightly higher than that of the prismatic specimens but lower than that of the cylindrical specimens, presented in the previous chapter. As mentioned in the previous chapter values of densities obtained on the cylindrical specimens was also higher than the prismatic ones which are why better results are obtained. In this case, it is suggested that the compressive strength of the walls is closer to that of the prismatic specimens than that of the cylindrical specimens. The difference in the results obtained in our study between the cylindrical specimens and that of the walls confirms the results observed in the literature.

Table 3.4 Young's modulus of the walls.

Wall number	E (MPa)
1	375 ± 20
2	391 ± 30
3	435 ± 25
4	440 ± 15

Phase 2: Horizontal loading

Figure 3.24 shows the horizontal loads in relation to the horizontal displacements on top of the four walls. These displacements were obtained from the DIC that is more accurate than the displacements given by the horizontal actuator (which was relatively influenced by the stiffness of the loading system). A pixel on the top to the left of the wall was chosen for the calculation of this displacement as shown in Figure 3.25.

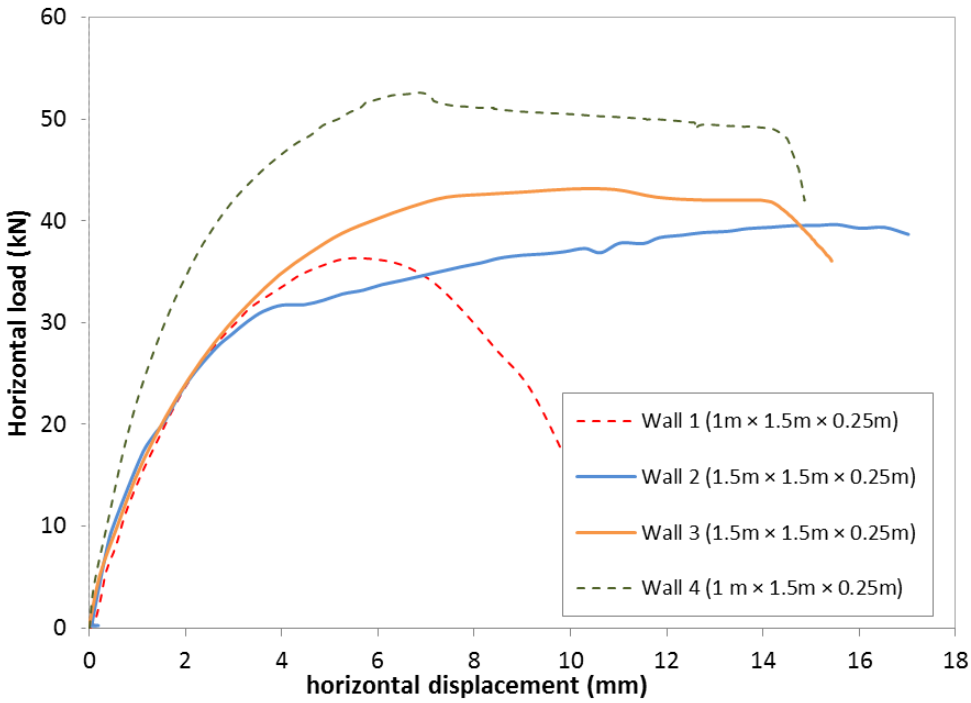

Figure 3.24 Horizontal loads on top of the walls in relation to the top horizontal displacements

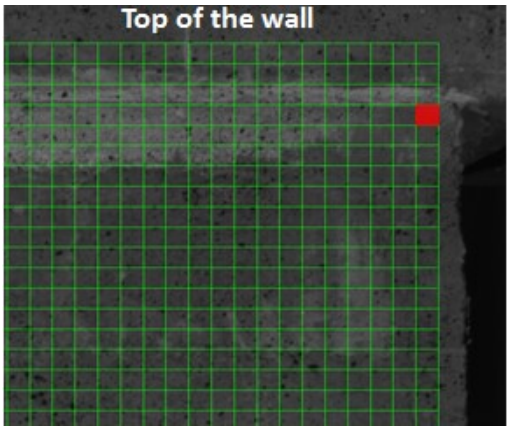

Figure 3.25 Point chosen for the calculation of the top displacement

The results shown in Figure 3.24 demonstrate that the four walls had similar initial slopes of the horizontal load – horizontal displacement curves (up to a certain limit 10 kN, which was about 20% of the maximum loads), and then the behavior differed after this limit due to the damage of each wall (by losing significant earth pieces) that caused the stiffness degradation. It was observed that the walls did not exhibit any early rupture that could have occurred due to sliding between earthen layers. Walls 2 and 3, sharing the same height (1.5 m), exhibited nonlinear behavior and similar maximum horizontal load about 40 kN. The stiffness degradation resulted from the occurrence of micro-cracks inducing important displacement ductility and returning globally a mechanical behavior less brittle and more predictable. A summary of walls results is given in Table 3.5.

Table 3.5 Summary of walls results

Wall number	Wall dimensions Height (m) x width (m) x thickness (m)	Maximum load (kN)	Displacement at max. load (mm)
1	1 x 1.5 x 0.25	36.33	6.6
2	1.5 x 1.5 x 0.25	43.1	11.5
3	1.5 x 1.5 x 0.25	39.7	15.5
4	1 x 1.5 x 0.25	52.6	6.3

As for the walls 1 and 4 that have a height of 1m, a different behavior compared to walls 2 and 3 is to be expected due to their lower height (lower flexural moment at the bottom section) inducing a better strength capacity. Nevertheless, this was observed only for wall 4 that achieved a maximum horizontal load which was greater than the other walls (53 kN) with important ductility. On the contrary, the structural behavior of wall 1 was the most fragile with a global

resistance significantly lower than wall 4. The maximum horizontal load was close to that of walls 2 and 3 but no ductile behavior was observed. In fact, the wall was damaged by high local compressive strains to the left side after reaching the ultimate load. Figure 3.26 exhibit the aspect of the wall with the appearance of severe damage to the left side of the wall. DIC in the next section shows more clearly the propagation of the crack.

Figure 3.26 Damage of wall 1 after reaching the ultimate load

Hence it could be suggested that the wall 1 had an inferior quality compared to other walls when observing the exterior aspect of the layers. Figure 3.27 shows the wall aspect directly after manufacturing. This wall was the first wall to be constructed and we assume that it could be less well controlled by the laboratory staff. In fact, the manufacturing process plays an important role, any changes in the manufacturing of these layer due to either excessive water content or not enough compaction in some of the layers can impose a lower density, therefore reducing the total capacity of the wall. By visualizing the exterior aspect of the wall (Figure 3.28), the layers appear to be in some areas less dense than the ones for other walls, we can therefore assume that this wall could correspond to walls having a lower density in real practice.

Figure 3.27 Wall 1 just after the manufacturing

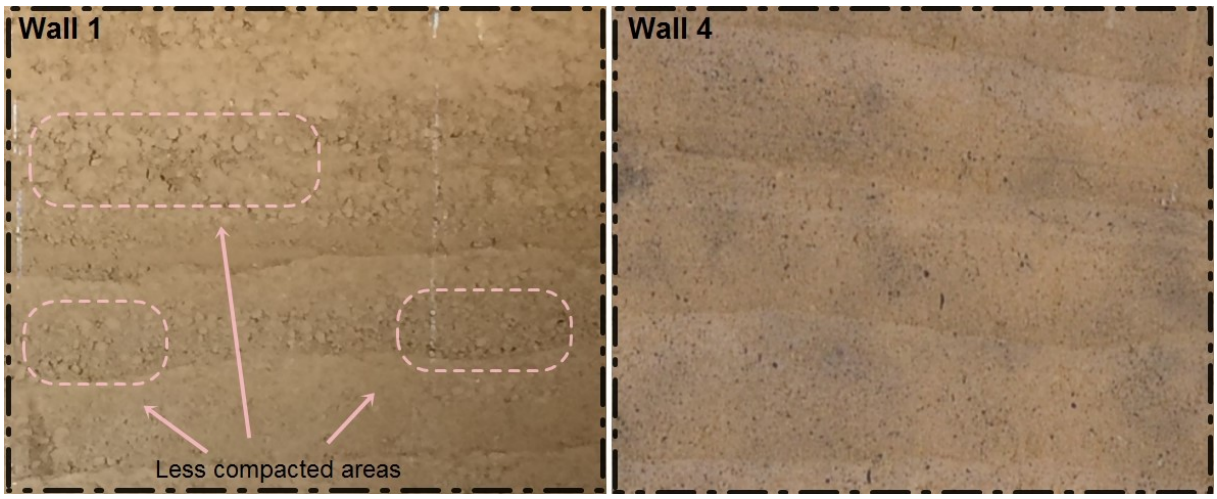

Figure 3.28 Visualizing less compacted areas in the exterior surface of wall 1 comparing to wall 4

3.4.6 Visualizing the crack propagation

Failure modes mechanism:

As mentioned earlier, three main failure modes (diagonal shear failure, in-plane bending failure, sliding shear failure) may occur when a wall is submitted to an in-plane horizontal load [105]. Apart from sliding shear that can occur between two earth layers, the rammed earth wall can experience both flexural and shearing deformation. This behavior can be modeled by two models [106]:

- The strut-and-tie model [106]: for this type of model, the wall exhibit diagonal shear failure. Based on plasticity theory the model can reproduce diagonal cracks and rocking failures. The approach of the strut-and-tie method is illustrated in Figure 3.29 where the force transfer to the wall is done through compressive strut and tension tie. Following strut-and-tie theory, when a wall suffers from a horizontal load F, a diagonal compression strut and a vertical tensile tie are developed in the wall as seen through the deformation of the walls. The failure of the wall is in the diagonal strut or in the vertical tie, depending on the stresses in these zones and the strength of the material.

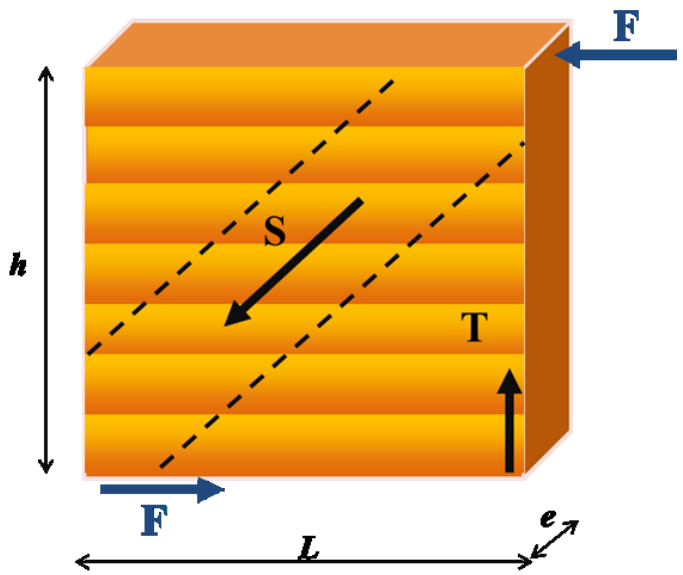

Figure 3.29 Strut and tie model: force transfer mechanism from which diagonal shear failure occurs

- A cantilever beam: for this type of failure, the wall exhibit bending about an axis perpendicular to the wall, which causes compression stresses at one end of the wall and tensile stresses at the other. This approach uses beam theory, a simple way in engineering, but it is not the best-adapted approach for walls (where shell theory would be better adapted). Indeed, following the flexure approach, diagonal cracks will not be assessed. The in-plane bending failure can take place when walls are very high and in the case of low vertical loads.

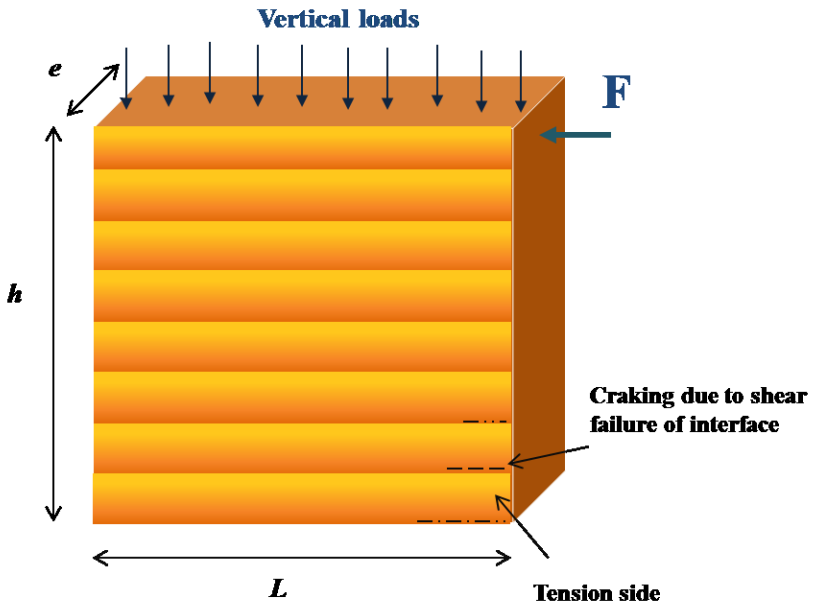

Figure 3.30 In-plane bending failure in a wall

The general failure of the walls:

It is, of course, difficult to compare the strength walls with different slenderness that has not experienced the same failure mode. But we have realized that most walls exhibit a shear failure with diagonal crack and in some cases the crack propagated along the horizontal following the interface between the layers in a form of stair stepping.

In general, for all the walls crushing occurred on one side of the wall as the strain accumulated between the two first layers without visible signs of cracks on the other side (Figure 3.31). Further details through DIC images are provided in this section where this phenomenon is clarified.

Figure 3.31 Crushing on the left side for different walls during the test

Analysis of walls with 1 m height (walls of number 1 and 4):

Case of Wall 1:

Figure 3.33 illustrates the direction of deformation through the principal vectors for wall 1. This allows the monitoring of the propagation of the diagonal crack. In general, for the tested walls, quasi-diagonal cracks were generally observed. Indeed, a diagonal compressive strut was formed in the diagonal zone during the pushover test, which created an extension in the direction perpendicular to the strut (Figure 3.32).

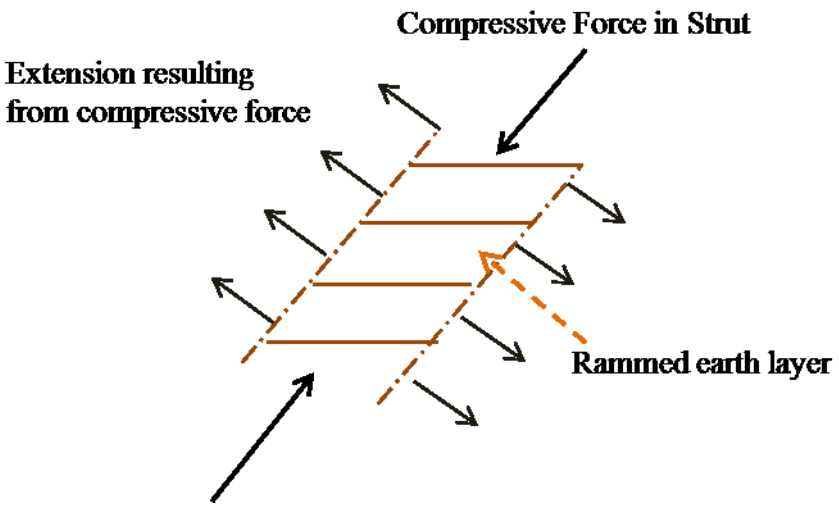

Figure 3.32 Tensile stresses resulting from compressive strut

In the case of wall 1 the cracking was initiated by crushing at the left side followed by the propagation of a diagonal crack that reached the third layer (see Figure 3.33 and Figure 3.35). Figure 3.34 allows perceiving the strut direction through the displacement fields. The cracking followed the interface of the third layer and then continued propagating to the right side of the wall in a diagonal shape as seen through the maximal principal strain 'emaxi' given by the 7D software as seen in Figure 3.36. As the value of the horizontal forces was increased, the width of the cracks increases very fast especially after reaching the ultimate strength of the wall (Figure 3.35). Minor vertical cracks were also observed due to some local tensile stress.

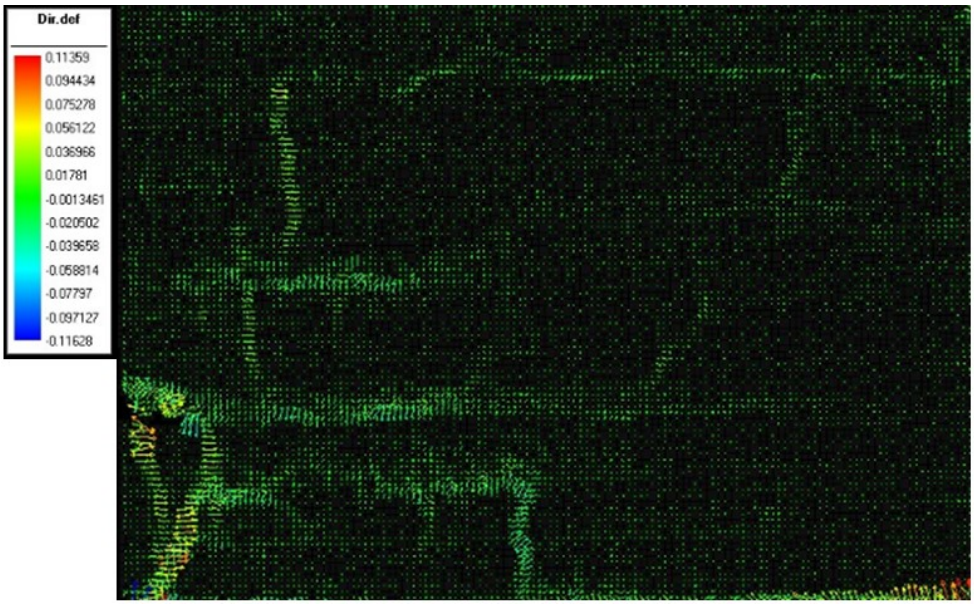

Figure 3.33 Direction of principal strain vectors that highlight the deformation on the left side of the wall 1 for the ultimate strength

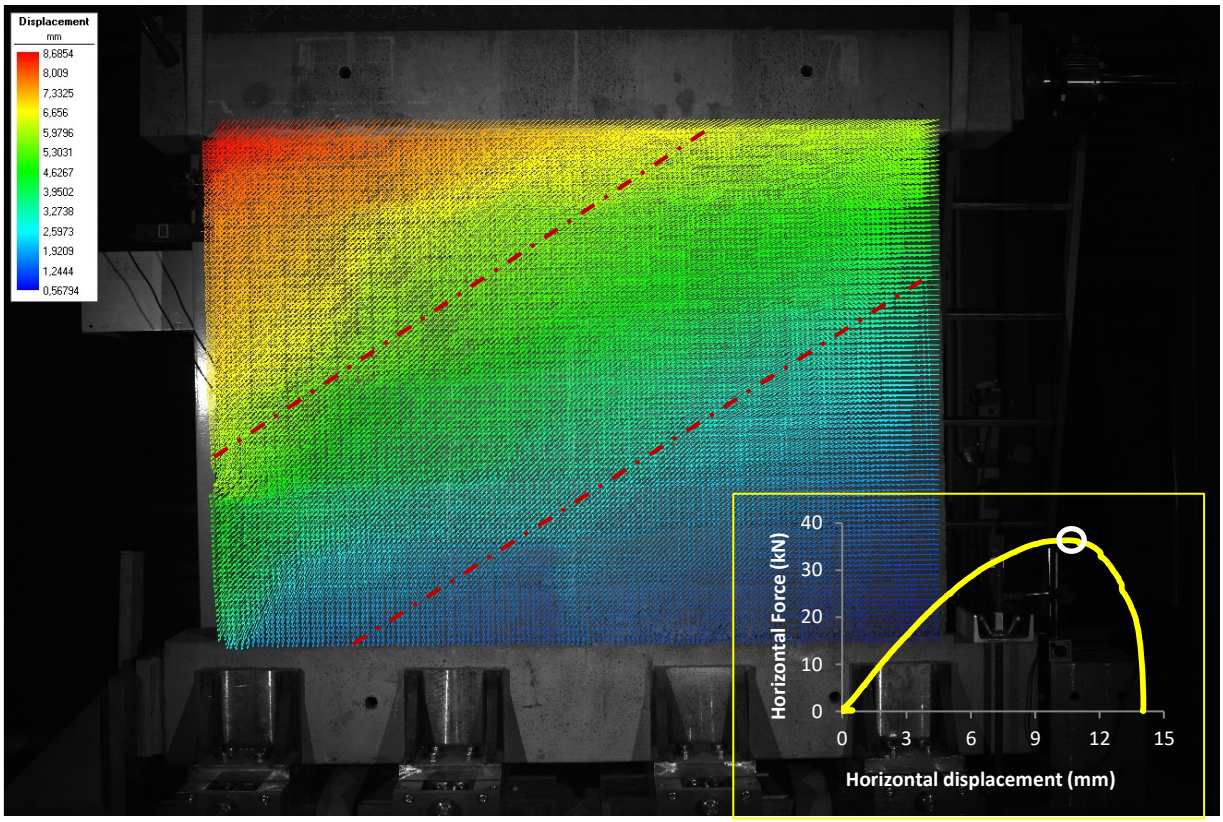

Figure 3.34 Visualizing the strut direction through the displacement vector for wall 1

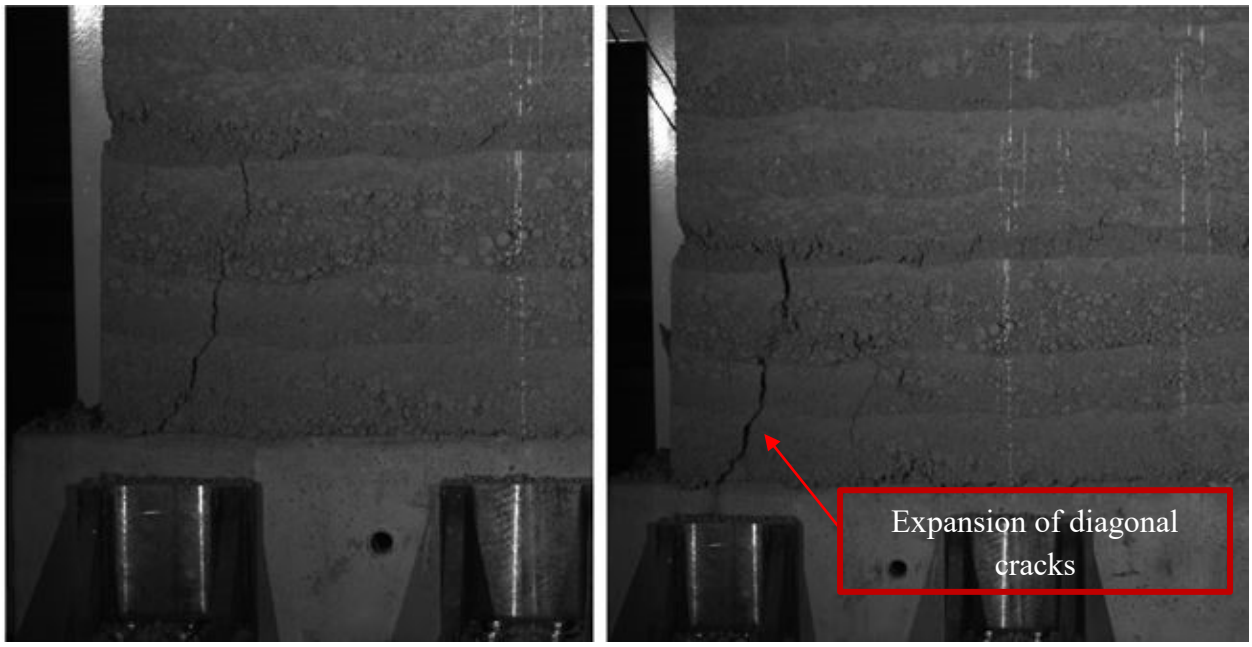

Figure 3.35 Expansion of cracking width for wall 1 after attaining the ultimate strength

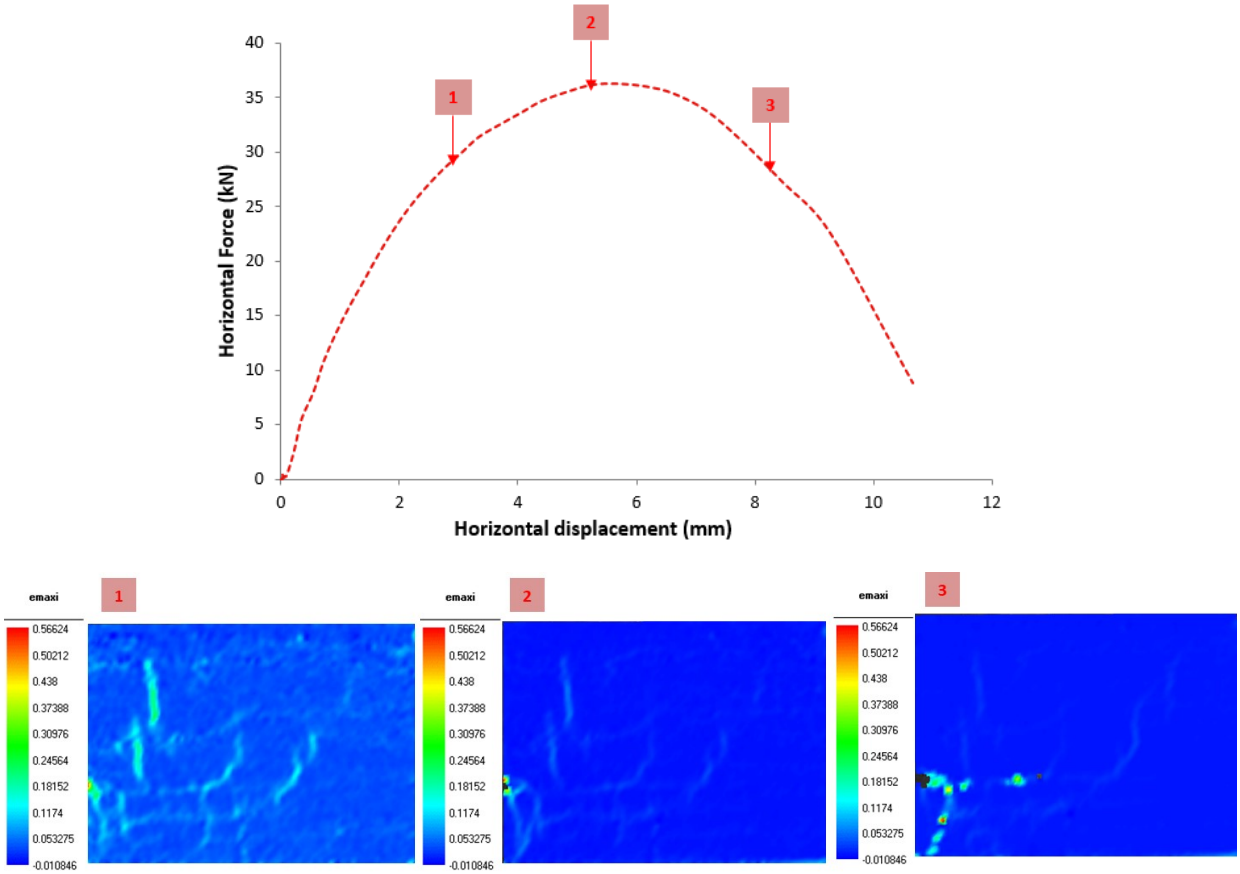

Figure 3.36 Cracking evolution of the wall 1, in function of horizontal displacement

Case of Wall 4:

For wall 4 we distinguish 2 phases during the vertical loading and the horizontal loading. In fact, signs of cracks before the test were noted (some of them due to shrinkage, and some of them when dismantling the framework). Therefore, these cracks were solicited in the both cases of loading.

First, in the pre-loading phase of the test, some pre-existing cracks extended as shown in Figure 3.37 through the maximal principal strain, and some other cracks were closed which was clearly linked to compressive forces as in Figure 3.38 through the minimal principal strain 'emini'. We focus on the fact that these are only minor cracks (with low cracking width), the DIC exhibited the deformation on the local scale and therefore can detect them and localize their propagation.

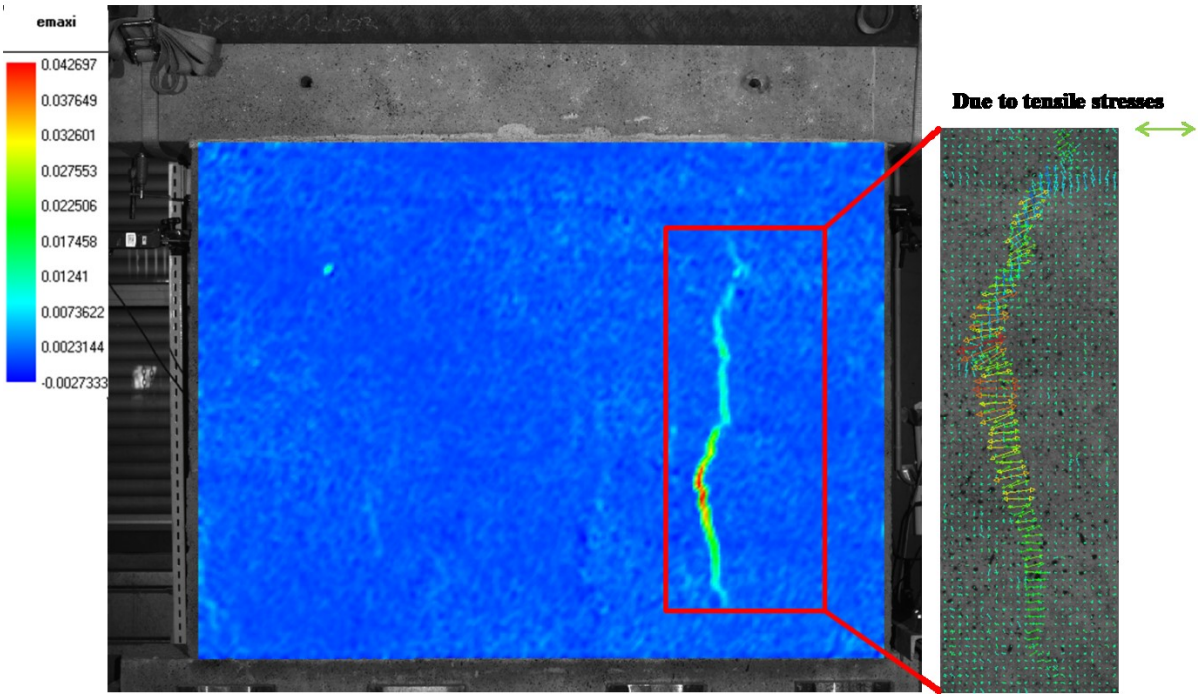

Figure 3.37 Crack growth due to extension during the pre-loading phase for wall 4

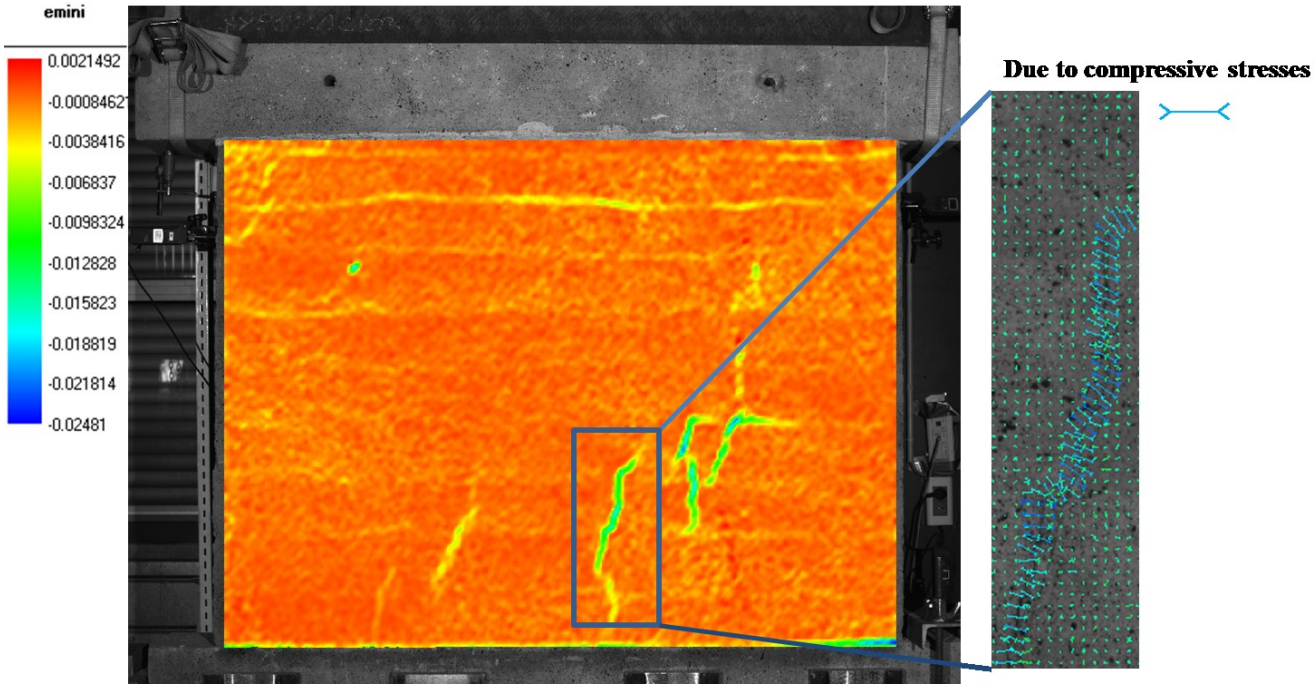

Figure 3.38 Crack closure due to compressive stress during the pre-loading phase for wall 4

In the second phase of the experimental test, during the horizontal loading and before reaching the ultimate strength, one of the cracks expanded to the top of the wall 4 (Figure 3.39) and then took a diagonal orientation following the interface (Figure 3.39 state 2). Another diagonal crack also appeared at the upper right part of the wall (Figure 3.39 state 3). It should be noted that although during the loading new cracks were formed and old ones propagated, no significant

strength loss had occurred. Figure 3.40 permits to distinguish between the type of cracks that are new and the one that already existed before the test.

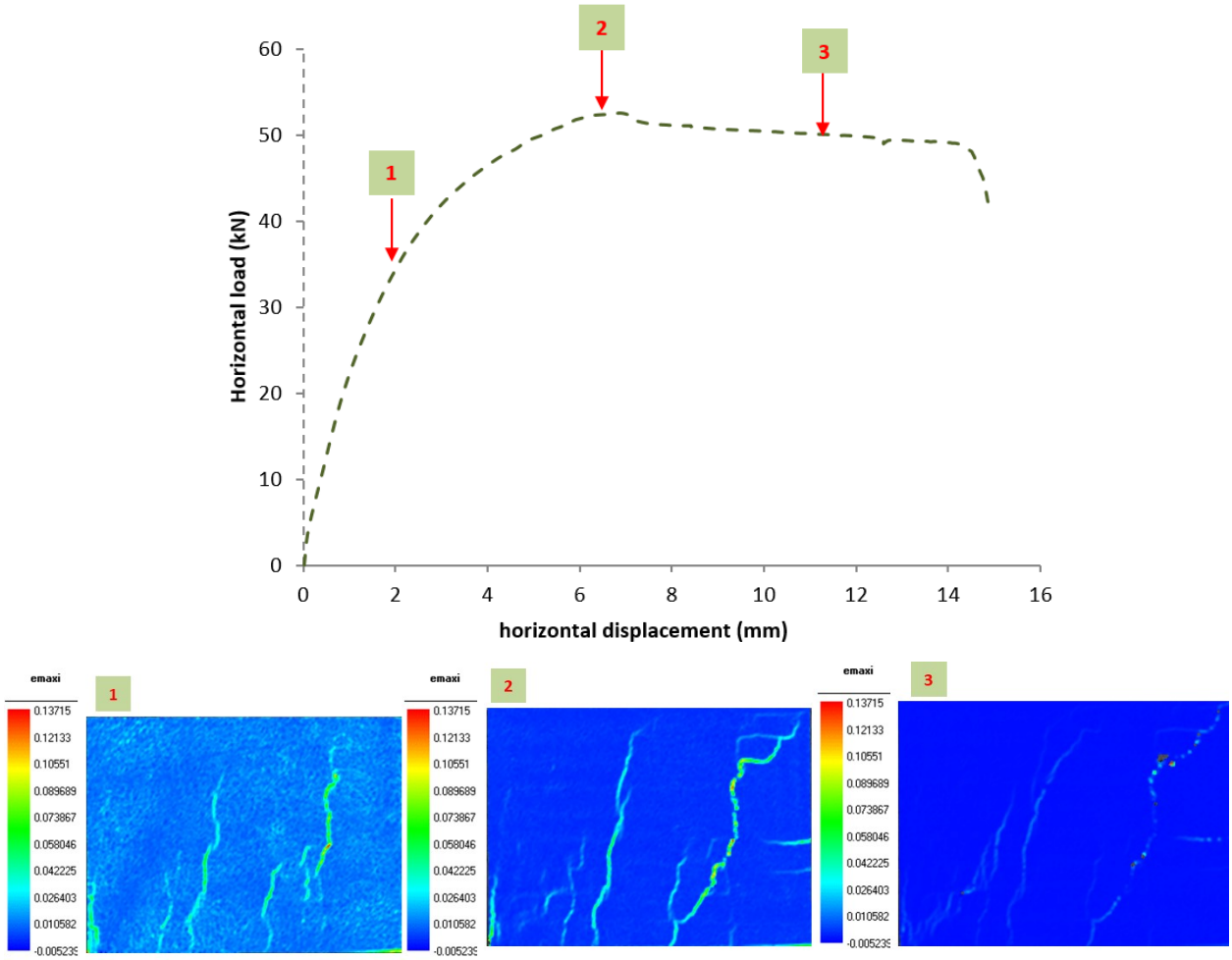

Figure 3.39 Cracking evolution of the wall 4, in function of horizontal displacement

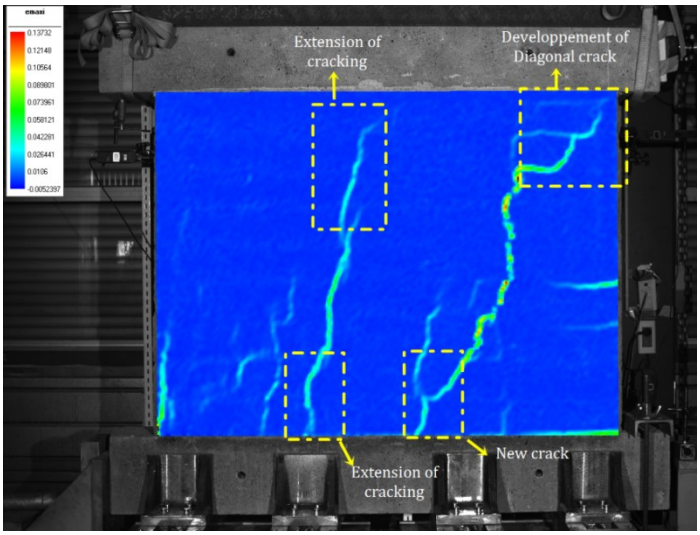

Figure 3.40 Damage of wall 4 during the horizontal loading for 52 kN of horizontal load (state 2 on Figure 3.39)

Analysis of walls of 1.5 m height (walls of number 2 and 3):

Figure 3.41 illustrates the crack propagation of wall 2 and Figure 3.42 for wall 3 through the displaying of the major principal strain in each case. According to these figures, the first deformation to be noticed is the deformation in the left part that is mainly due to compressive forces.

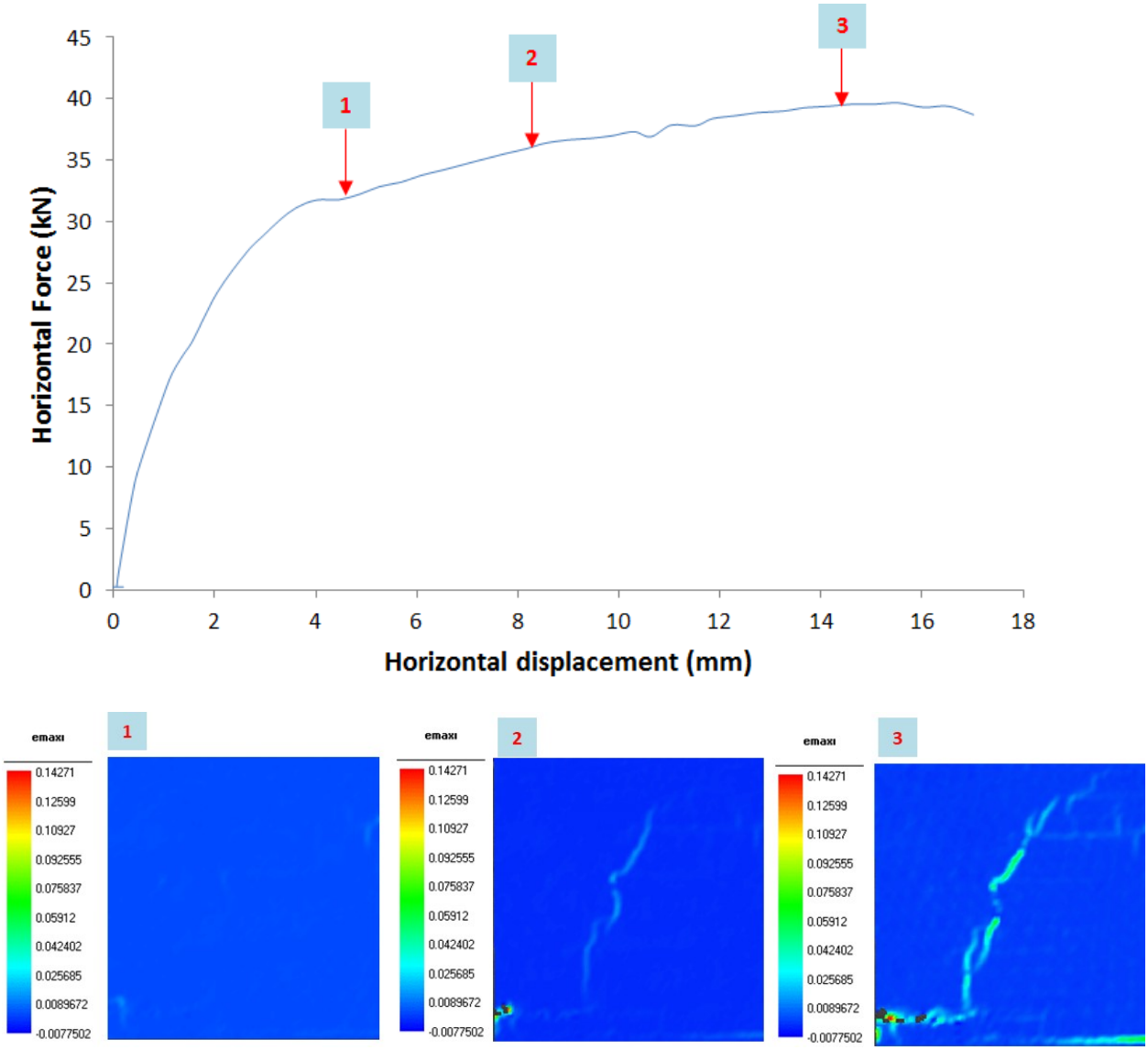

Figure 3.41 Cracking evolution of the wall 2, in function of horizontal displacement

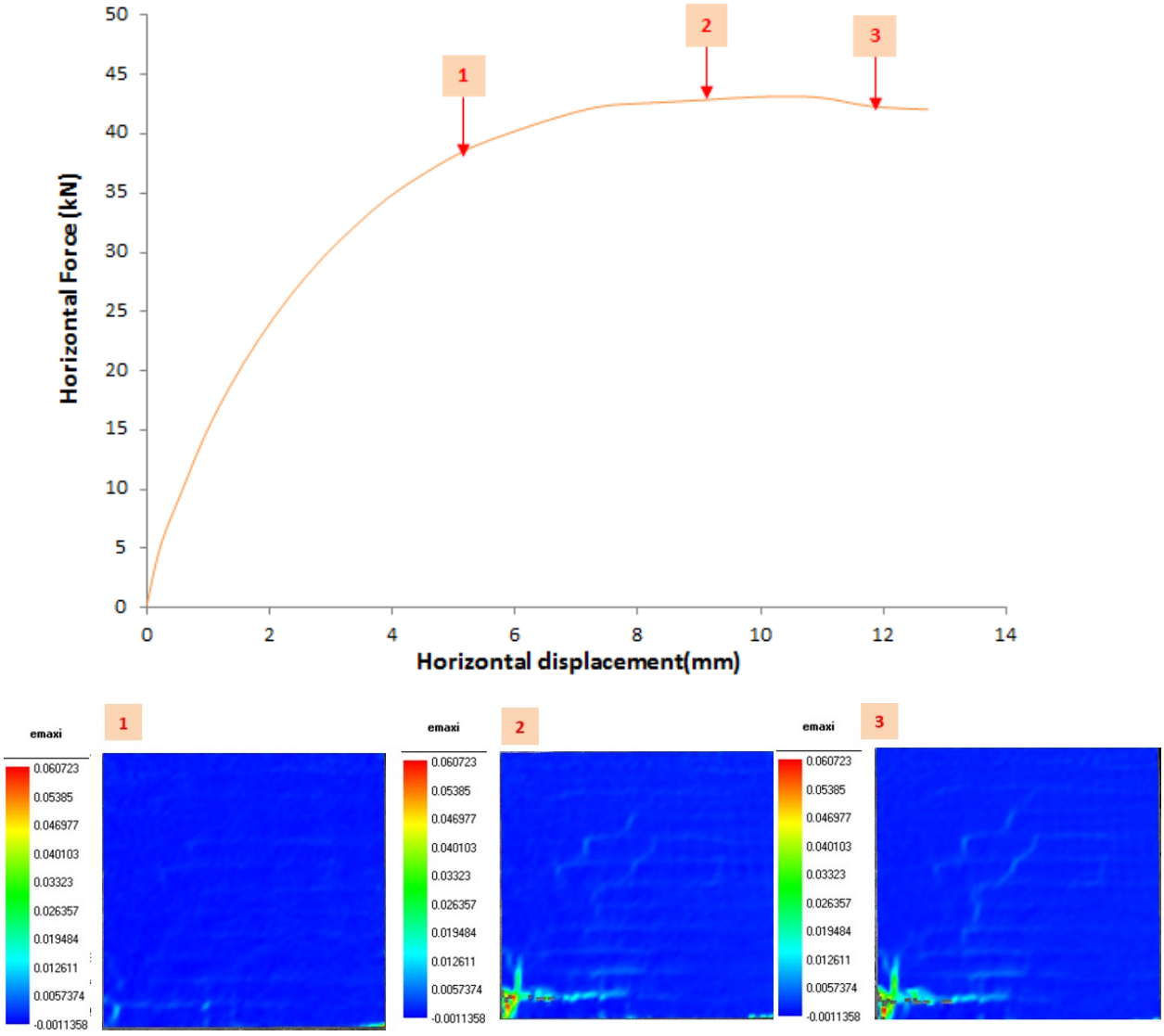

Figure 3.42 Cracking evolution of the wall 3 in function of horizontal displacement

Some pieces from this side felt over due to the crushing, the image correlation was difficult to achieve in these points where pixels have been lost (Figure 3.43). The same event has occurred for wall 2 at also similar stage.

When the loading increased, layer-interface sliding shear occurred by visualizing a horizontal crack, at the lower-left part of the walls, at an interface between two first earthen layers. Figure 3.44 exhibit the principal minor deformation obtained by the 7D software with the direction of deformation for both walls 2 and 3. It was found that both walls exhibit the same type of horizontal crack that was extended to nearly the center of the wall. These cracks influence the resistant section that is subjected to compression, producing a concentration of the compressive stresses and crushing of the bottom corner. Another local vertical crack below this horizontal crack was also formed in the two walls.

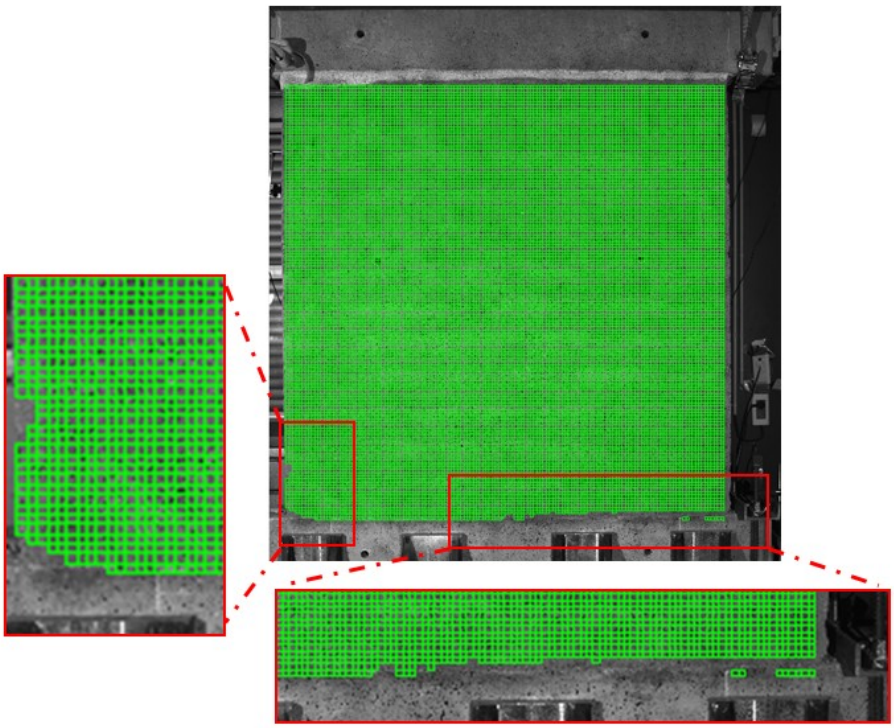

Figure 3.43 Losing pixels due to loss of material observed for wall 3

The horizontal crack appeared when the horizontal force reached about 85% of the maximum load as observed for wall 2 and 3. This is an interesting result because until now, the interfaces between earthen layers have generally been considered as weak points for the overall behavior of rammed earth walls, in particular when the walls were subjected to horizontal loads. So, before this study, one could speculate that the horizontal cracks would appear at an early stage at the interfaces; however the experiments revealed that the interfaces were effectively the weak points of a rammed earth wall subject to horizontal loading, but their behavior is acceptable (failure at 85% of the maximum load). These results also confirm the observations made by Ciancio and Augarde, [107] on stabilized rammed earth subjected to horizontal wind force, where the interface strength was indirectly estimated to 70–80% of the corresponding earthen layer's strength.

The deformation pattern with the horizontal sliding cracks can be seen more clearly in Figure 3.44 (DIC illustration at the local scale). Eventually, the apparition of diagonal cracks for the walls was detected in the hardening phase. In fact, the two walls show diagonal cracking but at a different stage. For wall 2 the diagonal crack was observed when reaching about 34 kN (Figure 3.41). Wall 3 revealed the same type of crack just before reaching the ultimate strength (Figure 3.42). It should be noted that the cracks were in form of staircase following the interface between each layer and are mainly due to tensile forces.

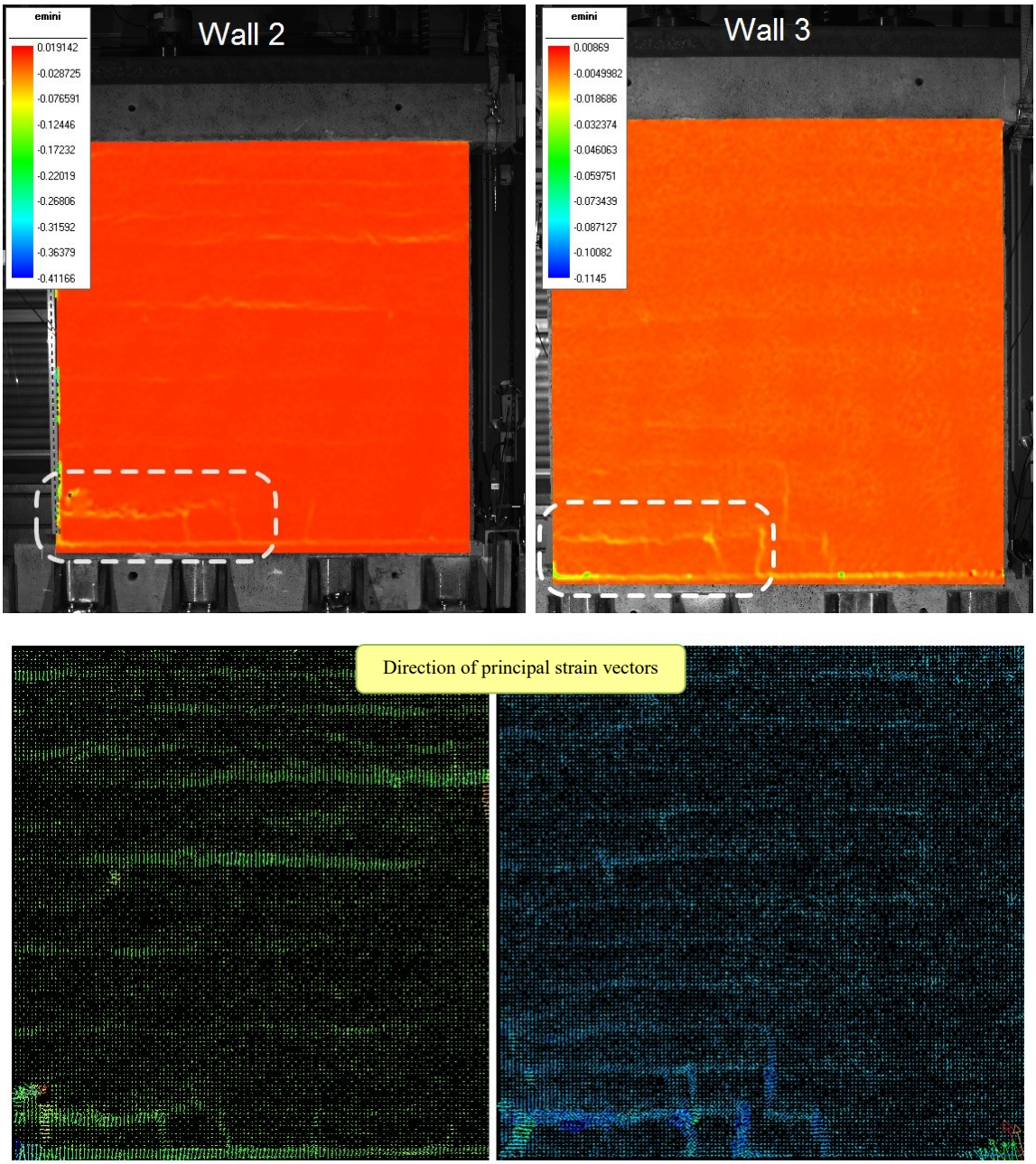

Figure 3.44 Developing of horizontal crack in the first layer and the appearance of local vertical crack near center for wall 2 and 3

The intervention of the flexure mode was also detected for the case of wall 2 and 3 where the rocking of the walls at their base was well noticed (more perspicuous than the other walls and clearly due to a moment greater than 50%). These walls, with a higher slenderness ratio, had greater tensile stresses at the embedment. A zoom on the right low side of the wall 3 describes more clearly the rocking, as in Figure 3.45 where the direction of the principal vectors in the correlated area reveal high values for most of the points in contact with the beam where the uplift had occurred. This figure demonstrates clearly the uplift of the wall on its right side that was equal to 595 mm for wall 3. Hence the failure of these walls was due to the action of bending moment and shear forces. Figure 3.46 shows also similar behavior for wall 2.

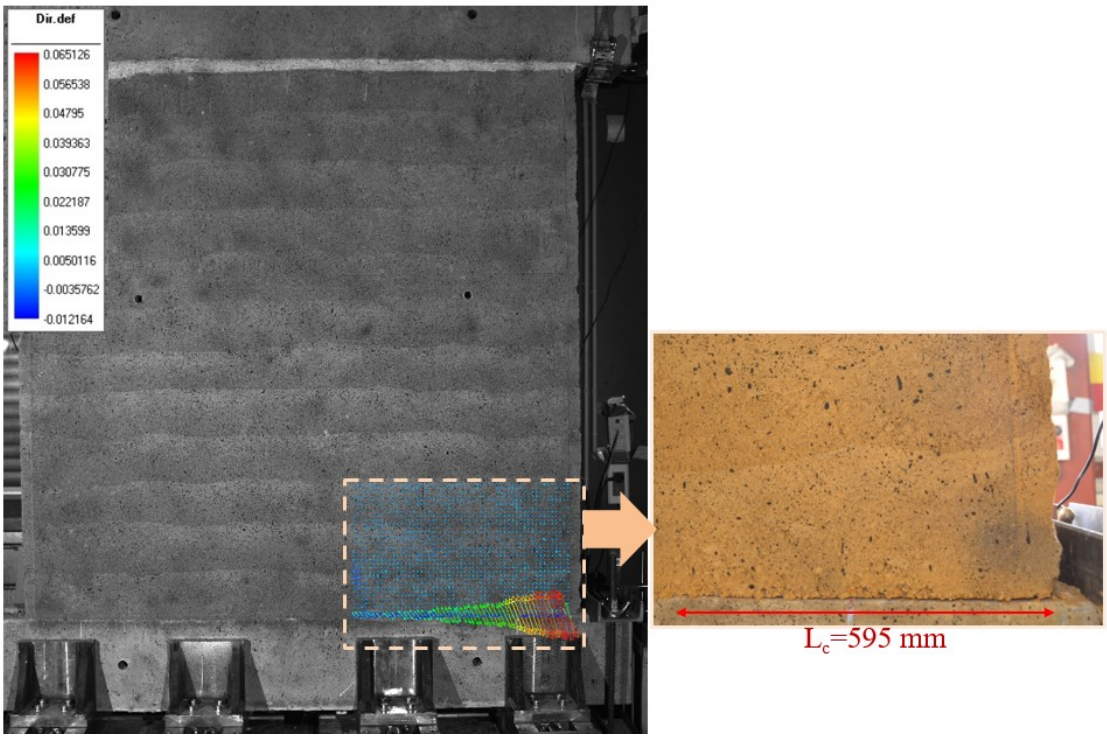

Figure 3.45 Rocking at the base of wall 3 for 2 (corresponding to 36 kN horizontal loading)

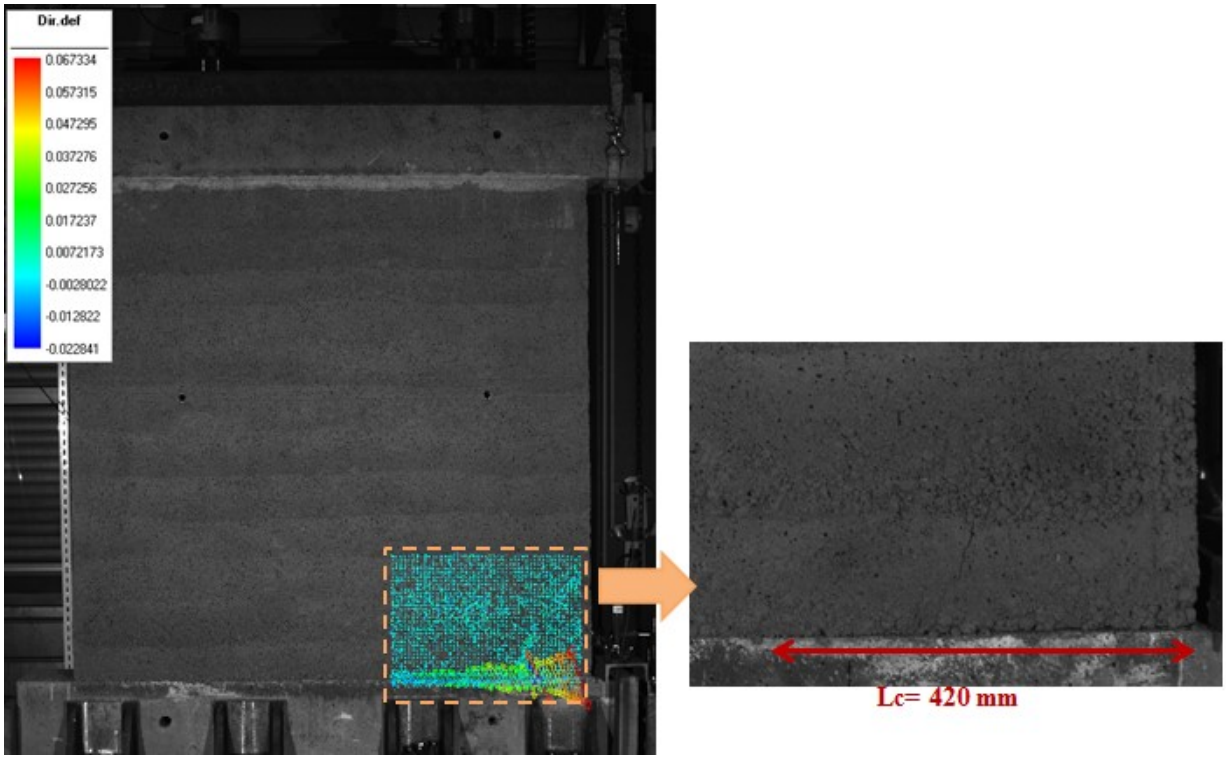

Figure 3.46 Rocking at the base of wall 2 (corresponding to 32 kN horizontal loading)

3.4.7 Summary of the failure modes obtained for rammed earth walls

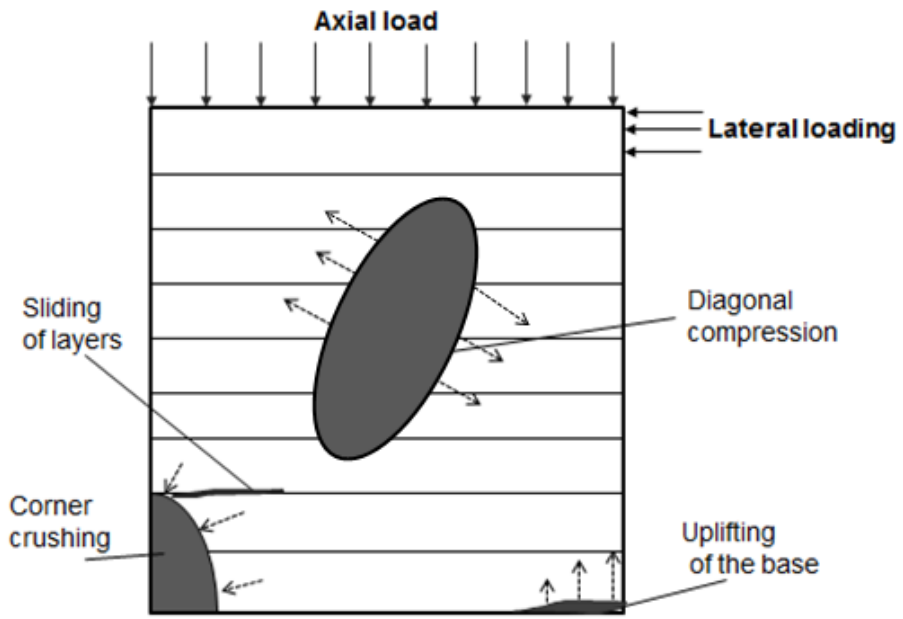

Figure 3.47 Summary of all the failure modes of rammed earth walls subjected to shear

Figure 3.47 sums up all the types of failure mechanism that were observed during the testing under lateral loading that can be summarized by: corner crushing from one side because of the stress concentration in this area, diagonal cracking that is due to diagonal compressive strut failure, sliding of some layers due to interface shear failure and local uplifting from the base due to tensile stresses.

3.4.8 Finale state of the walls

Finally, during the test, it was noted that none of the walls tested had a brittle behavior. Wall 1 was the most damaged. But after the tests, all walls still supported the concrete beam and could be transported by elevator without collapsing (Figure 3.48). The crack pattern at the end of the tests shows the similarity for wall 2, 3 (that had the same height) and that exhibited similar ultimate strength and initial stiffness.

After each experiment, the walls were destroyed for recycling (Figure 3.49). Even when destroying the walls, they behaved as disconnected layers as if they were solid units of earth blocks and in some cases, the cracks tended to track the interface in form of staircase. This behavior reveals once again the effect of the interface on the overall behavior of the wall.

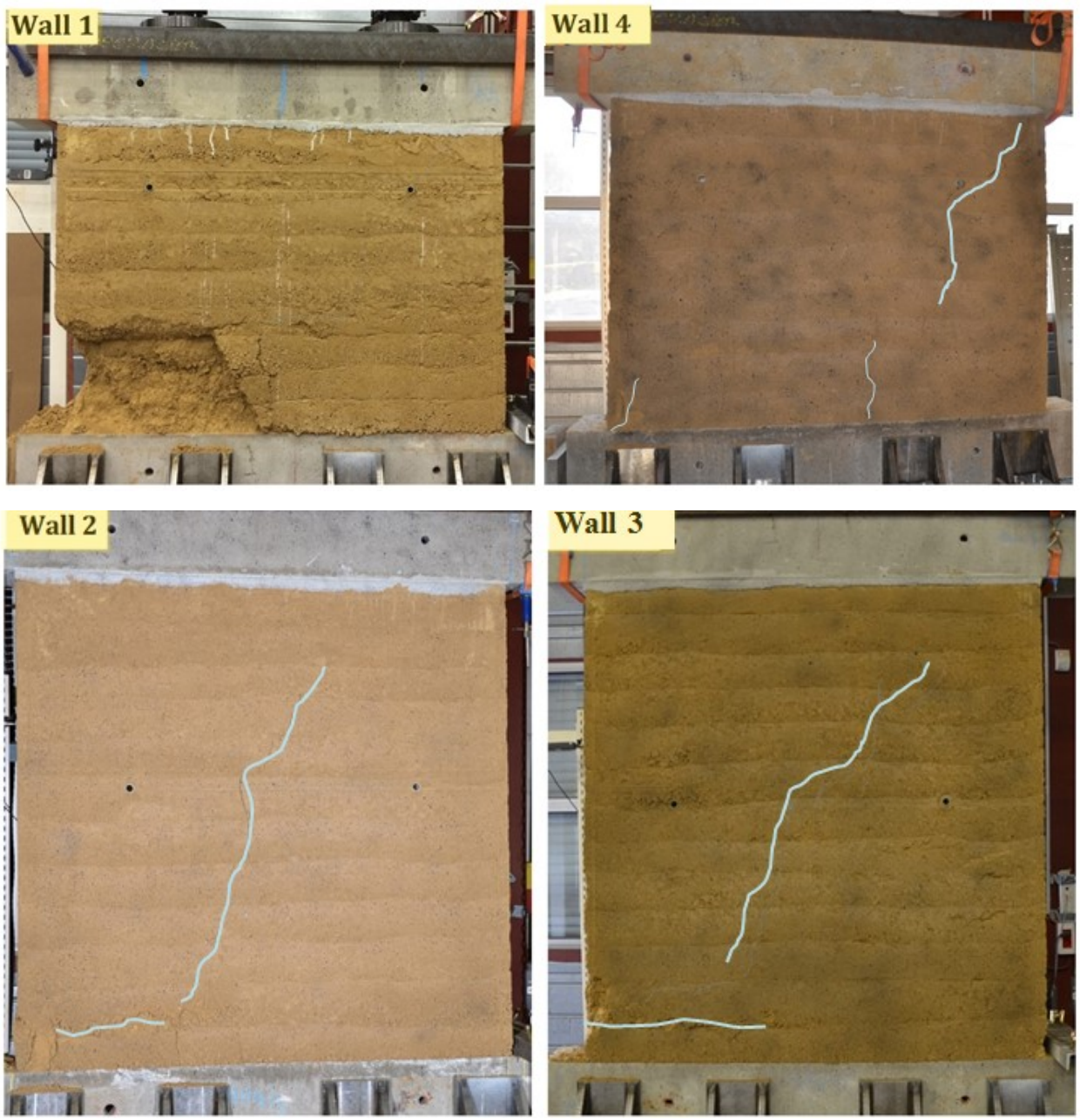

Figure 3.48 The four walls at the end of the test

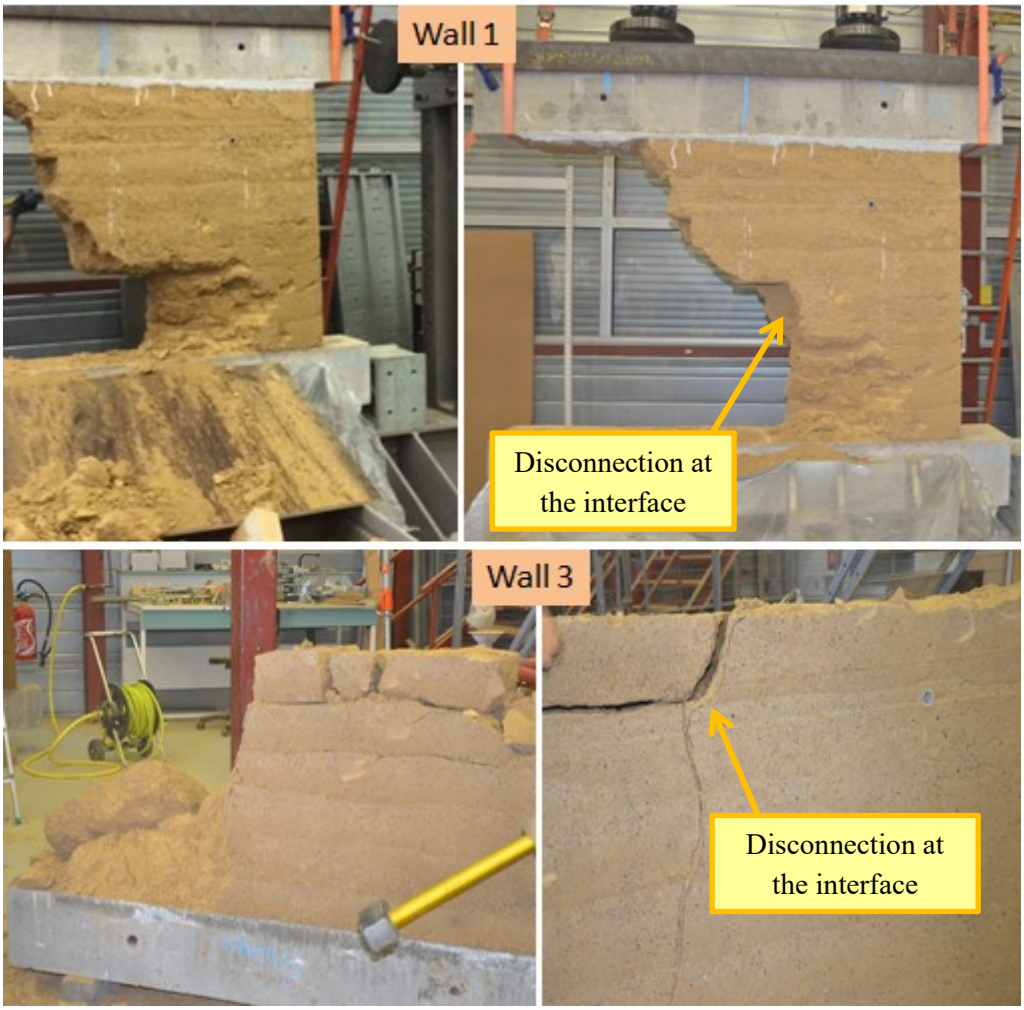

Figure 3.49 Visualizing interface failure when destroying the walls after each test

3.5 Conclusion

Determining the structural failure of rammed earth walls is an important feature that enables the risks assessment associated with earthquakes; on one hand, it contributes to finding suitable and appropriate ways for the conservation and restoration of these building and on another hand it draws new plans for the conception of new buildings.

In this context, this study has investigated the in-plane behavior of rammed earth walls. Four walls with two different heights were constructed in the laboratory and submitted to pushover tests. The DIC was used primarily to verify the data measured by the displacement sensors, to determine the deformability of the walls by revealing the location that corresponds to cracks through the calculation of the strain fields provided by the software 7D. The images recorded by the camera system allowed an accurate analysis. The experimental laboratory tests on rammed earth walls highlighted several important behavioral aspects which are the following:

- In general, diagonal shear and horizontal interface shear failure were dominated. The quasi-diagonal cracking due to strut failure caused by the transversal tension was observed for these walls at a different stage of loading.

- Crushing on the left sides of the walls were also noted. The DIC detected local strain near the interfaces between the layers as observed during the pre-loading phase (local deformation) and during the horizontal loading (global deformation). The interfaces between earthen layers are considered as weak point causing the concentration of strain in these areas and therefore reducing the resistant section of the wall. The same aspect was observed on other shear test on small walls done in the literature, where it was also spotted that the failure of the wall can take place due to delamination of layer interface [76], [78], [99], [108]. This feature is also observed in the case of masonry walls were bed-joints have also shown a critical sliding behavior.

- The different results obtained for walls 1 and 4 (with the same height) showed that the manufacturing process could have a significant influence on the performance of rammed earth walls. We concluded that wall 1 had a lower quality taking into consideration that it was the first wall to be constructed. The lower quality can be attributed to a lower density that was observed through the layer's state that appeared to be less dense comparing to other walls. The density can have a major impact on the shear loading capacity of rammed earth wall. On the other hand, as for wall 4, no loss of stiffness nor capacity occurred even with the presence of pre-existing cracks. These cracks changed the cracking trajectory but the orientation remained in a diagonal band.

- The walls with the higher slenderness ratio (1.5 m height) experienced the interference of a flexural rocking behavior; the direction of the principal vectors revealed a remarkable uplifting in the right side of wall mainly due to tensile stresses. Both walls 2 and 3 presented similar behavior in terms of ultimate strength and initial stiffness and they suffered from failure due to the action of shear forces and the intervention of bending moment as well.

- The results indicated that shear load can be transmitted through the interface between layers. As observed many specimens that revealed horizontal cracks. The interface shear mechanical properties i.e. cohesion and friction coefficient are important parameters to be determined. A criterion that takes into account the cohesion and the friction that is able to characterize these failure surfaces in the numerical modeling is proposed. It is also suggested to consider the heterogeneous aspect of the rammed earth by representing the earth layers and the interface as different elements in the finite elements modeling.

- The behavior of the material was linear up to a certain limit and then progressive cracking results through a nonlinear response. The response of the rammed earth is therefore characterized by significant non-linear behavior response with a remarkable ductility.

- From the numerical modeling point of view, it is unquestionably challenging to find a suitable behavior law to represent rammed earth. Many limitations persist like the

heterogeneous aspect, the complexities of the cracking paths and the inelastic response of rammed earth. Nevertheless, the law of behavior that can be adopted for the numerical modeling should take into account the nonlinear behavior. Ductile behavior must be also attributed by including the hardening phase in order to accurately predict the load-deformation behavior.

In the next Chapter, numerical modeling to simulate the experiments on the walls under static loading will be explored based on the experimental data resulting from materials tests.

Chapter 4. Identifying the parameters for numerical modeling of rammed earth walls

4.1 A review from the literature

Few studies on rammed earth are trying to simulate its behavior using Finite Element Method (FEM) or Discrete Element Method (DEM). Previous studies have first adopted simple behavior laws and more recent studies search to reproduce the failure mechanism of earth walls under a different type of experimental tests. In this section, we refer to some of these few studies found in the literature for modeling rammed earth.

Bui et al. [75] used FEM to simulate walls of (1m x 1m x 0.3 m) under concentrated compression loads, with a classical model for concrete (Mazard's model). In that study, the cracking and failure loads were correctly reproduced but the stiffness degradation and the crack propagation should be improved. Nowamooz and Chazallon [80] applied a complex FEM of unsaturated soil mechanics (Basic Barcelona Model), however, the comparison with experimental results on rammed earth specimens was lacking in their study, so the model's relevance could not be confirmed.

Gomes et al. [21] evaluated the seismic behavior of rammed earth structures in Portugal through FEM. The study presents several limitations where the seismic assessment was conducted with the classical elastic linear equivalent approach, without any detail of the behavior of the material.

On the other hand, other studies search to simulate the shear behavior of rammed earth. A study was reported by [76] in which the authors used a specific non-linear stress-strain model to simulate the behavior of the rammed earth walls under diagonal compression tests by FEM. This model integrates several possible non-linear stress-strain relationships according to the type of stress involved, namely compression and tension as in Figure 4.1. The interface between layers was also simulated using Mohr-Coulomb interface model. The parameters applied in this model were not obtained by experiments and not available in the literature. They were only estimated. Therefore, the used model could not automatically reproduce the experimental results but needed a calibration. The results (Figure 4.2 (b)) showed a good agreement with the experimental envelope of the shear stress-shear strain curves after calibration of the parameters.

After validating this model, the authors simulated the deformability and shear behavior of rammed earth walls under static lateral loading in another recent study [75]. This is the only study found in the literature which simulates rammed earth walls under in lateral loading. With this model, the authors could reproduce the diagonal crack obtained experimentally. Nevertheless, a large sensitivity analysis was performed to assess different input parameters. It was found that the sliding failure was influenced by the parameters of the interface elements (mainly the friction angle). Indeed, more experimental testing to define the parameters of the interface between layers is required.

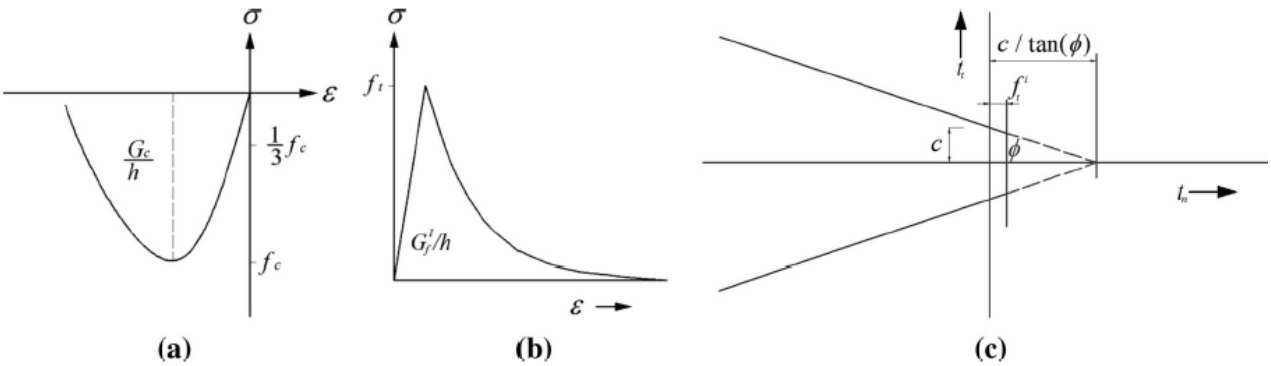

Figure 4.1 Material models adopted in the numerical modeling: (a) stress-strain relationship in compression; (b) stress-strain relationship in tension; (c) Coulomb friction model used in the interfaces, [76]

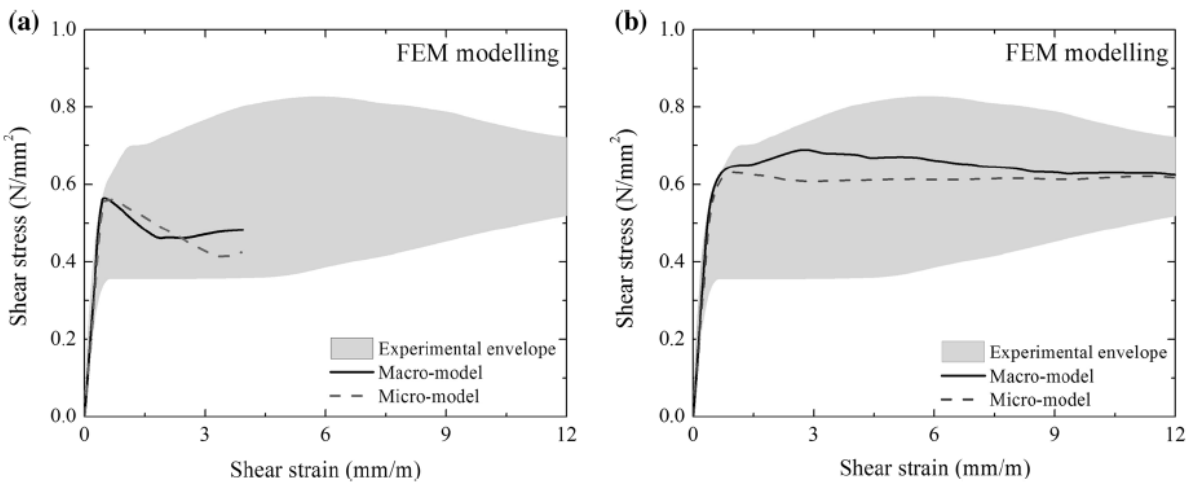

Figure 4.2 Behaviour of the macro- and micro-model: (a) using the initial parameters; (b) after calibration [76]

Bui et al. [77] used the discrete element method with Mohr-Coulomb failure criterion for earthen blocks and Mohr-Coulomb interface model for interfaces between earthen layers. The technique of DEM was applied on masonry structures but has not been applied on rammed earth. This is one of the few studies that exist in the literature that uses DEM to model rammed earth walls. The model was tested with several cases: walls' compression test, walls' diagonal compression test where the experimental results of [99] were used and also walls' vibration under light shocks. This study identified 13 parameters needed for the used model. The main parameters were the cohesion and the friction angle. It was admitted that the cohesion of the earthen layer is 7-10% of the compressive strength and the friction angle varied between 45°-56°. The interface's characteristics were assumed to be 80-90% of the earthen layers. The results obtained shows that there is no influence of the interface when compared to a homogeneous model (Figure 4.3) in the case of vertical loads.

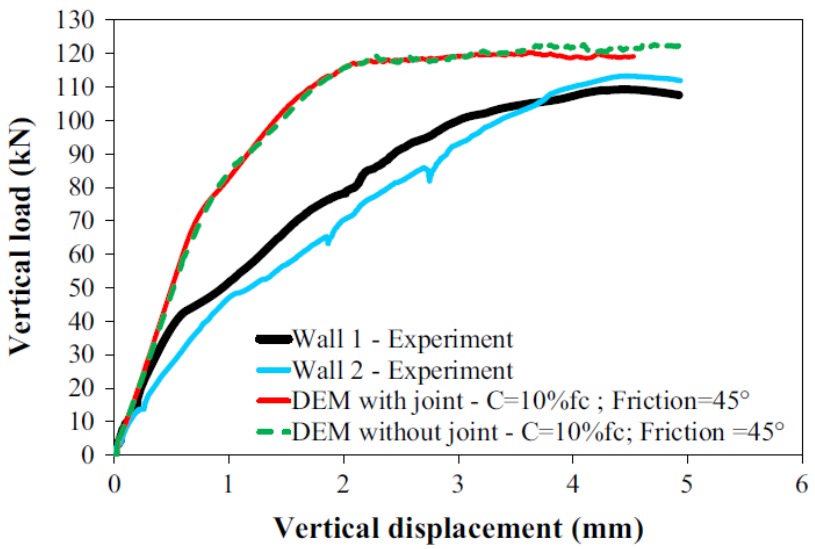

Figure 4.3 Comparison of the numerical and experimental results for vertical loads [77]

For the case of diagonal loading, the model with the interface elements gave better results concerning the ultimate load as demonstrated in Figure 4.4. The case where the interface characteristics varied from 85 to 100% reproduces satisfactory results.

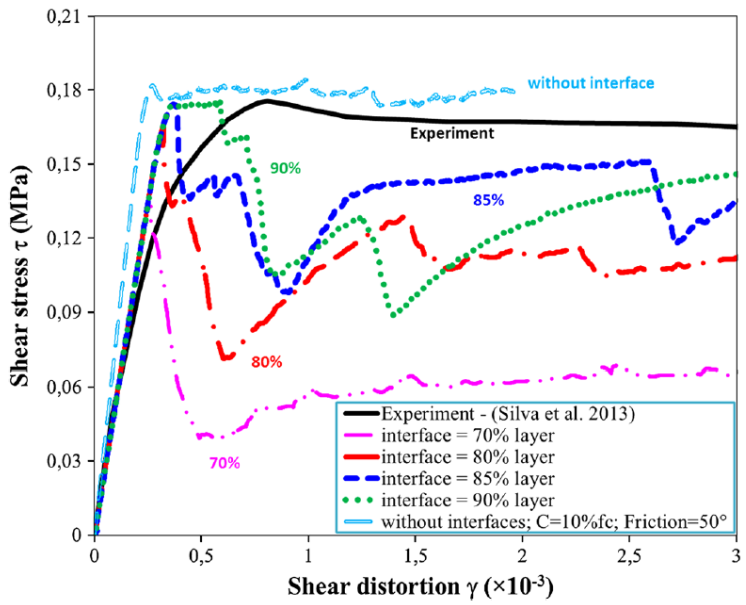

Figure 4.4 Comparison of the numerical results in the case of diagonal loading [77]

Showing the limitation of these studies found in the literature, in this chapter we seek to overcome the difficulties found when modeling rammed earth by adopting simple behavior law that takes into account the non-linear behavior on one hand and the most significant parameters of the rammed earth and their influence on the global behavior, on the other.

4.2 Modeling rammed earth walls by using Drucker-Prager criterion

Complex constitutive laws for the modeling of rammed earth demand detailed information about the material's properties which is not often available due to the lack of experimental tests on this material. Furthermore, many uncertainties exist due to the variability that can be found in the characterization of earth materials which add many complexities to the modeling of this material. An adjustment should, therefore, be found to search for reliable models that can represent rammed earth behavior law avoiding complex constitute laws.

In order to search for a model which can give relevant results and simple enough for practical uses, this chapter presents a numerical study using the Drucker-Prager model as a behavior law for rammed earth.

The objective of the numerical simulation conducted in this chapter is to simulate the behavior of rammed earth walls under in-plane loading by using the advanced Finite Element (FE) Aster code [109] with 3D solid elements. Having a non-negligible thickness for the rammed earth walls compared to the high, the 3D model seems to be a good approach for the modeling of the walls; it provides a compromise between reliability and computational time. This model was first validated through a diagonal shear test from an existent study in the literature (section 4.2.2) considering a homogeneous and continuous rammed earth wall. Then for the pushover tests, interface elements were added to the tested model. The main parameters of Drucker-Prager model are the cohesion and the friction angle of the earthen layers. In a first approach, the outcomes of the shear box done in Chapter 2 (at the large and small scale) were applied. Then these parameters were calibrated in order to obtain the experimental results.

4.2.1 Description of nonlinear constitute law

As most of the experiments carried out in the literature demonstrate an elastoplastic behavior [60], the Drucker-Prager model was selected to simulate the behavior of the rammed earth material. This model was used due to its robustness (as it works in 3D) and its simplicity when compared to other advanced models (see for example [80]). The advantage that represents this model comparing to a more simple model like the Mohr Coulomb criterion is the integration of the hardening phase which is more suitable for the prediction of the behavior of rammed earth as already shown by the experiments.

The Drucker-Prager model [110] is a failure criterion which is currently used in the modeling of soil mechanics (sand, soil, rock) and concrete material. Indeed, the model can give relevant results with a limited number of the parameter used.

The Drucker-Prager behavior law is written:

$$F(\sigma, p) = \sigma_{eq} + \alpha\, I_1 - R(p) = 0 \tag{4.1}$$

Where I_1 = Tr (σ), σ_{eq} the second invariant of stress, and α is a function of the friction angle such as:

$$\alpha = \frac{2\,sin\,\varphi}{3 - sin\varphi} \tag{4.2}$$

R(p) is the value taken by the criterion for tr (σ) = 0, function of the cumulated plastic strain p.

The variation of R with the material plasticization (from R(0)= σ_y à R($p_{ultimate}$)=$\sigma_{y.ultime}$) presents the hardening. The parabolic hardening is chosen for our model; this function is written:

$$\begin{cases} R(p) = \sigma_y \left[1 - \left(1 - \sqrt{\frac{\sigma_{y\,ultime}}{\sigma_y}}\right)\frac{p}{p_{ultime}}\right]^2 & p\epsilon\,[0; p_{ultime}\,] \\ R(p) = \sigma_{yultime} & p > p_{yultime} \end{cases} \tag{4.3}$$

The parameter σ_y is expressed in function of φ and the cohesion:

$$\sigma_y = \frac{6c\,cos\varphi}{3 - sin\varphi} \tag{4.4}$$

4.2.2 Homogenous model: application on a diagonal shear test

To test the reliability of the Drucker-Prager model, we first started by trying to reproduce the experimental results of specimens tested under diagonal compression obtained from the study of Silva et al. [99]. For the numerical simulation a simple model without interface was adopted, so the scope of this section is to verify the use of the FE model (without interface) employing the Drucker-Prager criteria.

Experimental data:

The wall GSRE_7.5 mentioned in the study of Silva et al. [99] was selected for this study, i.e., granitic stabilized rammed earth with 7.5% of fly ash (by weight). This stabilization technique consists of the alkaline activation of fly ash (to create a geopolymeric binder). The experimental results obtained in that study were: compressive strength f_c=1.09MPa; shear strength τ =0.18MPa, and shear modulus G= 620MPa. This wall was chosen because its compressive and shear strengths were similar to that of currently unstabilized rammed earth although its Young's modulus (1500MPa) was higher than the current values obtained for unstabilised rammed earth (see [63], for example). This was probably due to the geopolymer stabilization. The walls of (55 x 55x 20) cm^3 were tested, by applying a monotonic displacement and using supports of 10 cm in length. The test procedure was similar to that of ASTM E519 [111]. Figure 4.5 exhibits the specimen from the study of [99].

Figure 4.5 Experimental setup of a diagonal compression test [99]

Numerical Model:

Figure 4.6 shows the corresponding numerical model of the present study that was constituted from 4049 tetrahedrons elements.

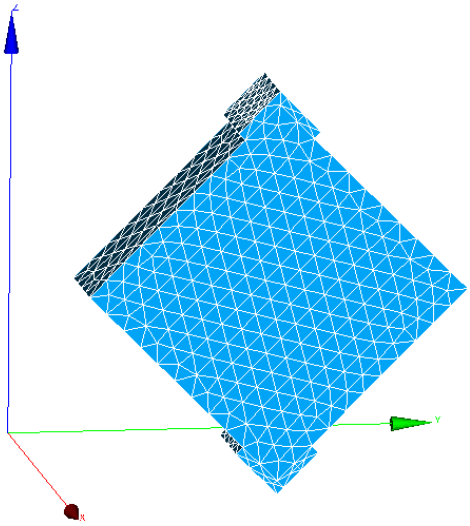

Figure 4.6 Numerical model

Following the ASTM standard, the shear stress τ of the specimens is calculated as follows:

$$\tau = \frac{0.707.P}{A_n} \tag{4.5}$$

Where P is applied load and A_n is the net area of the specimen. The shear strain (or shear distortion) γ is obtained by:

$$\gamma = \frac{\Delta v}{g_v} + \frac{\Delta h}{g_v} \tag{4.6}$$

where Δv is the vertical shortening of the panel, Δh is the horizontal extension of the panel, and g_v and g_h are the vertical and horizontal gage lengths. In this FEM model, Δv and Δh were measured on two diagonal lines of the specimen.

In this section, the relationship proposed by [77] for the cohesion was used ($c = 0.1\ f_c$) and the friction angle varied between 36˚ to 41˚ which seems appropriate for a first approach. The results are presented in Figure 4.7. The models could reproduce the initial slope of the experiment. The friction angle of 41˚ could reproduce the ultimate shear stress and the transition phase from linear to non-linear (Figure 4.7(b)). Although the typical "shear peak" was not reproduced with the numerical model due to the limited number of parameters, however, the last one could reproduce the post-peak softening phase of the material. Hence it reproduced the elastoplastic behavior of rammed earth in this case. This model is adopted in the following for the simulation of the experiments on the scale of the wall.

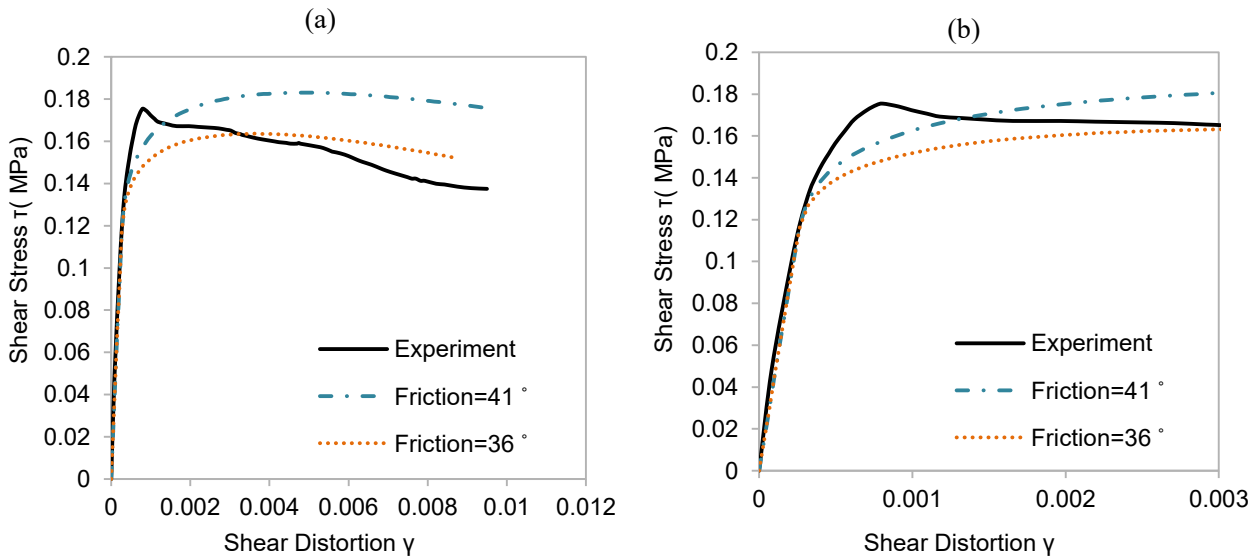

Figure 4.7 (a) Numerical and experimental results of the diagonal compression test; (b) and a zoom at the initial behavior

4.3 Validation of Drucker-Prager on Pushover tests

4.3.1 Presentation of the model:

The following numerical modeling was used to reproduce the tests performed on the rammed earth wall series (Chapter 3). In the experimental study, the walls that had an overall size of 1.50 x 1.50 x 0.25 m^3 (wall 2 and wall 3) gave similar results in terms of maximum capacity. The numerical simulation of the pushover tests is therefore carried out for this case (H=1.5 m). The

tests on the large shear box and small one are used as a reference to calibrate the various parameters (c and φ).

Geometry, boundary and loading conditions:

Figure 4.8 illustrates the geometry and meshing of the rammed earth wall with two concrete beams. The boundary conditions applied to the lower beam allowed complete blocking of this beam on the frame in accordance with the experimental measurements (Chapter 3, Section 3.3). The top beam is used for the application and distribution of the loading conditions within the wall. A first condition allows the application of a uniformly distributed vertical load, force controlled until the application of the experimental preload of 120 kN (vertical stress 0.3 MPa). This loading was then kept constant throughout the duration of the simulation, in accordance with the experimental study. The second condition concerns the application of a progressive horizontal displacement at the head of the wall. In order to guarantee a good distribution of the forces within the beam, and therefore the wall, the upper beam was first considered (Figure 4.8). Then, a rigid plate (E_{pla} = 210 GPa) was modeled, according to the experimental study. The displacement is applied punctually at the level of this plate.

The wall was modeled with 12 layers of 11.4 cm each (named “earthen layer”) and thin layers of 1 cm (named “interface”) between the earthen layers. Indeed, the role of the interfaces may not be important in the case of vertical loads, but important in the cases where the interfaces are more solicited [77]. In the present study where the walls are subjected to horizontal loads, the effect of “interface” layers in the model might have a significant impact on the results. In fact, the “interface” layers represent the bottom part of an earthen layer where the soil was less compacted than the upper part and consequently, its mechanical properties are lower. The thickness of the "interface" layers was decided upon observations by DIC during uniaxial compression tests where the thickness of the weak layers was approximately about 1 cm. Therefore modeling the alternating between these two layers with different properties is a simple way to take into account the periodic layers of the rammed earth wall. This modeling enables to consider each layer and each interface layer with different parameters. Each layer and interface are considered as homogeneous and isotropic.

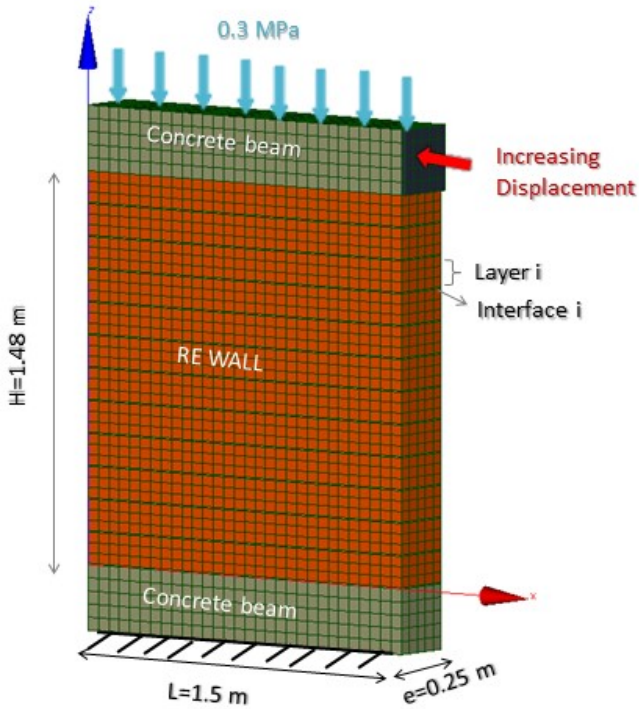

Figure 4.8 Geometry and boundary conditions of the numerical model

The layers and the interface elements are considered as rectangular solid hexahedrons, meshed with cubic elements, the same thing was applied to the two concrete beams. The mesh used consist of the most regular and homogeneous elements possible. The finite element mesh of the model used to simulate the tests was constituted by 8575 hexahedrons elements (Figure 4.8). Each simulation takes between 7-15 hours of estimating time.

Table 4.1 lists all the parameters used for this modeling.

Table 4.1 Lists of the different parameters required for the different material

Element	Parameters
Concrete (Elastic)	E= 30 GPa ; ν= 0.2
Earth Layer (Elasto-plastic, Drucker Prager)	E=400 MPa ; ν= 0.3 cohesion: c_{lay} (kPa) ; friction angle: φ_{lay} (°)
Earth interface (Elasto-plastic, Drucker Prager)	E=400 MPa ; ν= 0.3 cohesion: c_{int} (kPa); friction angle: φ_{int} (°)

The concrete corresponds to the load transfer elements (upper and lower beams). It is considered to be elastic with Young's modulus E = 30 GPa and a Poisson coefficient ν = 0.2. The Drucker-Prager criterion was chosen for the earth and interface layers.

4.3.2 Influence of the parameters: cohesion and friction angle

In the modeling of the pushover test, Young's modulus for the rammed earth walls was equal to 400 MPa, this value is obtained through the experimental study on the tested walls from the DIC as shown in Chapter 3. The Poisson's ratio is equal to 0.23 as reported in [86], [112].

Reference: Large shear box

In order to check the relevancy of the values obtained from the one-scale shear box. The experimental values were introduced as input parameters in the model as seen in Table 4.2. Based on the experimental results, the friction angle and the cohesion were tried, respectively of φ_{lay}= 35.2°; c_{lay} = 30.7 kPa and for the interface φ_{int} = 32.9°; c_{int} = 24.7kPa (obtained from the results of two direct shear tests at the interface, presented previously). The results showed that the couples obtained from the one-scale shear box, give very low numerical results and could not reproduce the maximum force obtained from the experiments (Figure 4.9). The maximum horizontal load is mainly influenced by the cohesion and the friction angle. More particular the low value of the cohesion obtained experimentally has a major influence on the results. The reason comes from the difference of the moisture content between these specimens and the walls tested as mentioned before. As discussed previously in Chapter 2, the water content at the testing time has a direct impact on the mechanical parameters (compression and shear behavior) and could have introduced a lot of uncertainties for the characterization of the cohesion and the friction angle of the material. In order to check the influence of the cohesion and the friction angle other parameters are tested based on the ratio layer over interface called Ratio φ and Ratio c calculated for the large shear box as shown in Table 4.2. These parameters allowed us to link the interface and the layer parameters and to estimate the interface parameters once the layer parameters are fixed.

Table 4.2 Numerical values chosen for the numerical model of rammed earth wall based on the large shear box data

Reference test: Large shear box	Friction angle φ_{lay} (°)	Cohesion c_{lay}(kPa)	Friction angle φ_{int} (°)	Cohesion c_{int}(kPa)	Ratio φ φ_{lay}/ φ_{int}	Ratio c c_{lay}/c_{int}
Middle layer	35.3	30.3			1.07	1.22
Interface between layer			32.9	24.7		

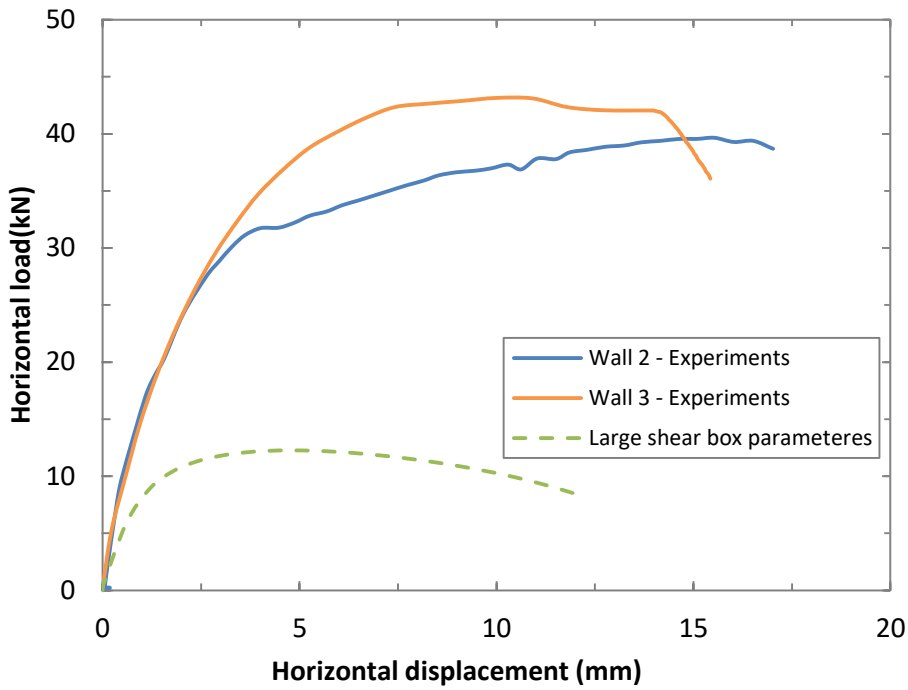

Figure 4.9 Results of the numerical model with the input parameters of large shear box

Reference: Small shear box

In another approach, the model was tested for different couples of (cohesion, friction angle) based on the experimental values obtained from the small shear box as a reference. The output parameters from these tests were higher than the one obtained with the large shear box and therefore better results are to be expected.

In this approach the values obtained from the upper layer and bottom layer are used, these values are incorporated into the model for the layers. As for the interface, since no test has been conducted, the values are estimated using the ratio layer over the interface (*Ratio φ* and *Ratio c*) obtained from the large shear box (Table 4.2). Therefore, the values of the friction angle and cohesion introduced for the interface of the model that correspond to the upper and middle layer are calculated as follow:

$$\varphi_{int} = \frac{\varphi_{lay}}{(Ratio\ \varphi)_{large\ shear\ box}} \tag{4.7}$$

$$c_{int} = \frac{c_{lay}}{(Ratio\ c)_{large\ shear\ box}} \tag{4.8}$$

Where *Ratio φ* and *Ratio c* are calculated in Table 4.2.

The numerical values proposed for the model are indicated in Table 4.3 for both the layers and interface.

Table 4.3 Numerical values chosen for the numerical model of rammed earth wall based on the small shear box data

Reference Test: Small shear box	**Layer** (known)		**Interface** (calculated)		**Ratio:** Calculated from the large shear box parameters	
	Friction Angle	Cohesion	Friction Angle	Cohesion		
	φ_{lay}(◦)	c_{int} (kPa)	φ_{int} (◦)	c_{int}(kPa)	Ratio φ	Ratio c
Upper layer	44.1	263	41	215	1.07	1.22
Middle layer	45.6	135	42.6	110	1.07	1.22

Results of the numerical simulation based on the data of Table 4.3 are shown in the Figure 4.10. From these results, we can clearly observe a great influence of the values of the cohesion and the friction angle on the peak capacity.

The results based on the upper layer data overestimated the maximal horizontal load (H_{num}=90 kPa) comparing to the experiments (H_{exp}=39-42 kN). This is not surprising as the cohesion value adopted in the numerical input for the earth layer (close to 263 kPa) is very high and therefore results of the horizontal capacity are important as well. This value for the cohesion does not seem reliable for the earth layer since it was only measured on a specimen that was taken from very well compacted areas and it doesn't consider the whole aspect of the layer.

As for the input parameters obtained from the middle layer, the maximum load for the numerical model was greater than that of the experimental model (H_{num}=53 kN) for about 25%. This variation may be due to the used parameters which are not yet optimized. In this case, the difference could be adjusted through a parametrical study by calibrating the parameters. It should be mentioned that in this case the cohesion of 135 kPa for earthen layers which was used is similar to other values found in the literature for unstabilised rammed earth based on the hypothesis of [41], [77] that showed that the cohesion was about 0.07-0.1 × f_c .

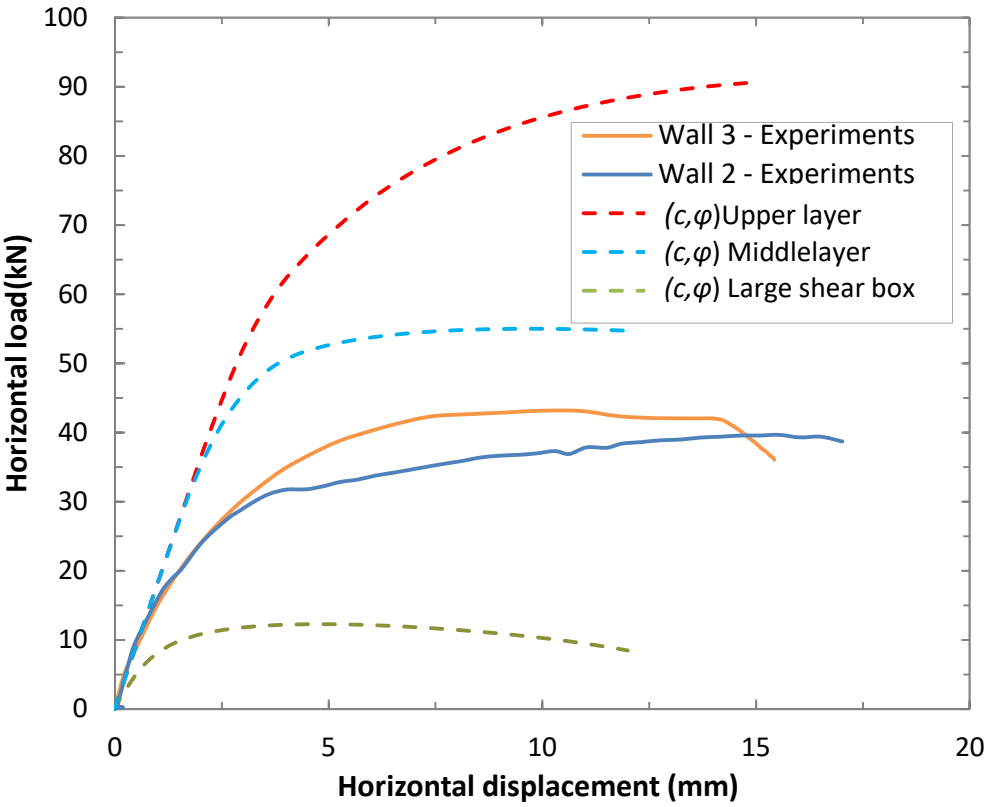

Figure 4.10 Comparison of the numerical and experimental results

Hence, we decided to choose the parameters of the middle layer that correspond to the following values: φ_{layer}= 45.6°, φ_{int}= 42.6°, c_{layer}= 135 kPa, c_{int}= 110 kPa which gave the closest results in terms of maximum load. In the next section, the adjustment of the parameters (layer and interface) are investigated by proceeding with these initial values in order to approach the experimental curves.

4.4 Parametric study

Based on the initial numerical results obtained on the middle layer that was the closest to the experimental curves (in terms of horizontal capacity), a parametric study is carried out. This analysis focuses on the variation of either the friction angle (both for interface and layer) or the cohesion (both for interface and layer) using the Ratio φ and Ratio c calculated from the large shear box data.

The following simulations were adopted:

-1st simulation: the cohesion values respectively of c_{layer} = 135 kPa and for the interface $c_{interface}$ = 110 kPa were fixed and a set of values of friction angle was tested φ_{layer} = (30°, 35°, 40°, 45°). As for the values of the friction angle for the interface, they are calculated using the relation Ratio φ.

-2nd simulation: the friction angle respectively of φ_{layer} = 45.6° and for the interface $\varphi_{interface}$ = 42.6°) were fixed and a set of values of cohesion was tested c_{layer} = (80, 100, 120, 140) kPa. As

for the values of the friction angle for the interface, they were calculated using the relation of Ratio *c*. Table 4.4 summarizes all the input parameters for this parametric study.

Table 4.4 Parameters considered in the parametric study

Simulation	**Set values for layer**		**Corresponding values for interface**		**Ratio used for calculation**
	Friction angle φ_{lay}(°)	Cohesion c_{lay}(kPa)	Friction angle φ_{int}(°)	Cohesion c_{int}(kPa)	
1st *simulation*	30	*135*	28	*110*	Ratio φ =1.07
	35	*135*	32.7	*110*	
	40	*135*	37.4	*110*	
	45	*135*	42	*110*	
2nd *simulation*	*45.6*	80	*42.6*	65	Ratio *c* =1.22
	45.6	100	*42.6*	82	
	45.6	120	*42.6*	98	
	45.6	140	*42.6*	114	

Results of this analysis where the effect of the parameters variation on the horizontal load capacity of the rammed earth wall are reported in Figure 4.11 and Figure 4.12 based on the different sets of layer and interface values obtained by the parametric study in Table 4.4. It is evident that the values of the parameters of the interface have an influence on the ultimate load obtained which justifies the use of a model with an interface.

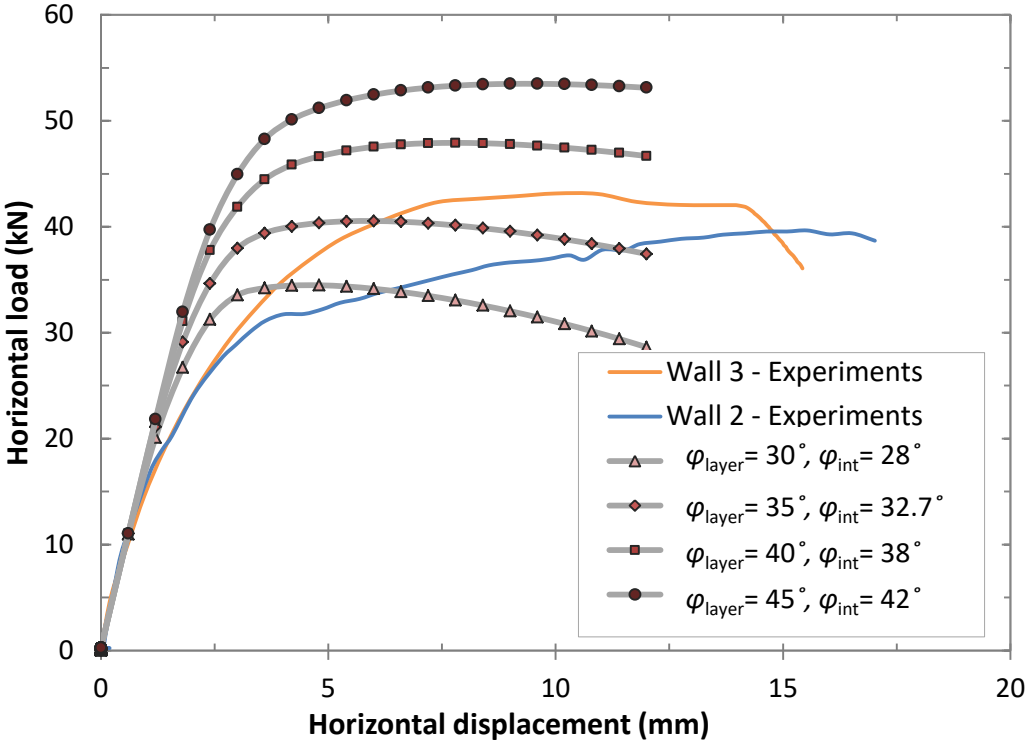

Figure 4.11 Comparison of the numerical and experimental results according to the 1st simulation

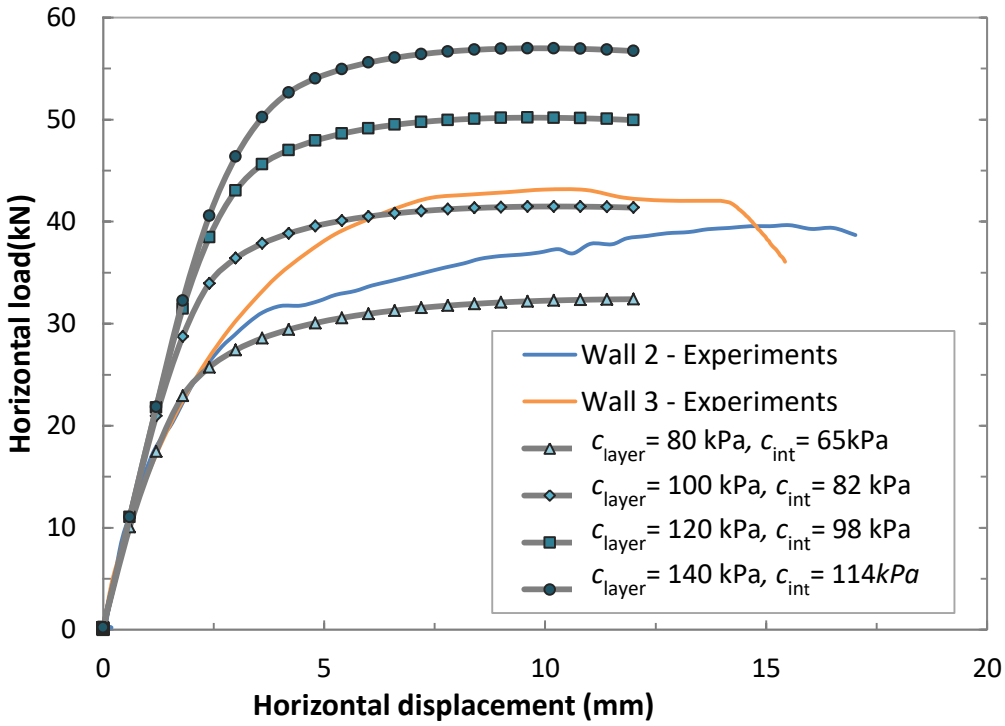

Figure 4.12 Comparison of the numerical and experimental results according to the 2nd simulation

For the 1st simulation (where the cohesion of the layer and interface are fixed), the numerical simulations in Figure 4.11 shows that among the values tested, when the friction of the layer is between φ_{lay} =35° - 40° and φ_{int} =32° -38° for the interface, the maximum load is near the experimental one (H_{num} between 34 and 41 kN). Nevertheless, the more the friction angle of the layer and the interface decrease to these values, the more we noted a change in the post-peak slope; which was not observed in the case of the experimental tests. Hence from this simulation, it could be concluded that the variation of the friction angle didn't allow us to approach the experimental curves properly. From here, we can choose to fix the friction angle of the layer and interface to the values (φ_{lay} =45.6° and φ_{int} = 42.6°) where the results gave a stable post peak and examine the second simulation where only the values of the cohesion were varied.

Therefore in the second simulation, Figure 4.12 shows that when the friction angle is fixed for both the layer and interface to these values (φ_{lay} =45.6° and φ_{int} =42.6°), and the cohesion decrease, the results tend to approach the experimental one. From the results in Figure 4.12 the best pair for layer cohesion was c_{lay}= 80-100 kPa and for the interface $c_{int=}$ = 65-82 kPa that could reproduce the maximum horizontal load (H_{num} between 32 and 41 kN). For these values, the numerical model could also reproduce the experimental initial stiffness and global elastoplastic behavior. Moreover, due to the attribution of the hardening phase, the ductile behavior was observed in the prediction of the load-deformation behavior. However, the numerical results could not allow having the experimental second slope before the maximal load.

Based on the experimental data and the numerical results that were established on the variation of the cohesion, it could be concluded that this parameter is the most critical and proper experimental test to evaluate this parameter must be attained.

4.5 Conclusion and recommendation

Modeling rammed earth demand detailed information about the material's properties which is limited due to the lack of experiments tests on this material. Many uncertainties exist because of the variability that can be found in the characterization of earth materials. In this chapter, the experiments done on two rammed earth walls subjected to pushover tests are modeled.

The Drucker-Prager model that takes into account the nonlinear behavior of the material was adopted where the main parameters are the cohesion and the friction angle of the earthen layers. The "interface" layers of 1cm-thick were introduced.

In general, the numerical results (after calibration from the direct shear test) showed a good agreement with the experimental results in terms of initial stiffness and the displacement at the beginning of the plasticity. The attribution of the hardening phase induced the ductile behavior that was observed in the prediction of the load-deformation behavior. On the other hand, the behavior showed a less gradual transition between the elastic and plastic behavior.

The key parameters for this study where the cohesion and friction angle that had a strong influence on the results. A great dispersion was noted from the direct shear tests on the values of the cohesion that differ significantly but not for the case of the friction angle that was between

(35° and 45°). Therefore additional testing is required to define the parameter of the cohesion which seems to be crucial for this study, plus including the measurement of suction in order to obtain the effective parameters.

Regarding the parameters at the interface, the values of these parameters need to be determined, hence further experimental investigation should also address the mechanical behavior of rammed earth at the interface.

Concerning the parametric study, we could propose an effective base to perform reliable FEM of rammed earth walls that consist on a variation of friction angle between 35°- 45° and cohesion between 100-135 kPa while employing Ratio φ and Ratio c for the corresponding interface value. It is interesting to note that these values are in the same order of magnitude with the results obtained in a previous study using numerical modeling ([75], [77]). Nevertheless, further experimental data to refine the recommended values should be achieved.

Chapter 5. Assessing the seismic performance of rammed earth walls by pushover tests

5.1 Introduction

Buildings with rammed earth have shown a great significance in the world, from the simplest shelter of humans to the amazing temples, these structures represent many important heritage sites. Modern rammed earth building is also taking place in the constructions sector by retrieving many important priorities in the building material.

Despite the attractive aspects of this construction material, some countries where the population still lives in earthen buildings have been influenced by severe and damaging earthquakes causing many earth buildings to collapse. Moreover, it was found that it exists a high agglomeration of earth buildings which coincides with the map of high seismic risk areas in the world (Figure 5.1). Rammed earth structures are considered to be vulnerable due to their poor mechanical characteristics (compressive strength, tensile strength as shown in the previous chapters) and heavyweight because of the thickness of the walls required for the resumption of the permanent and live loads. These combined aspects make rammed earth walls particularly sensitive to dynamic effects that can cause brittle failures without any prevention. It's an important detail in case of evacuation of the building and eventually in case of high damage, material loss and death.

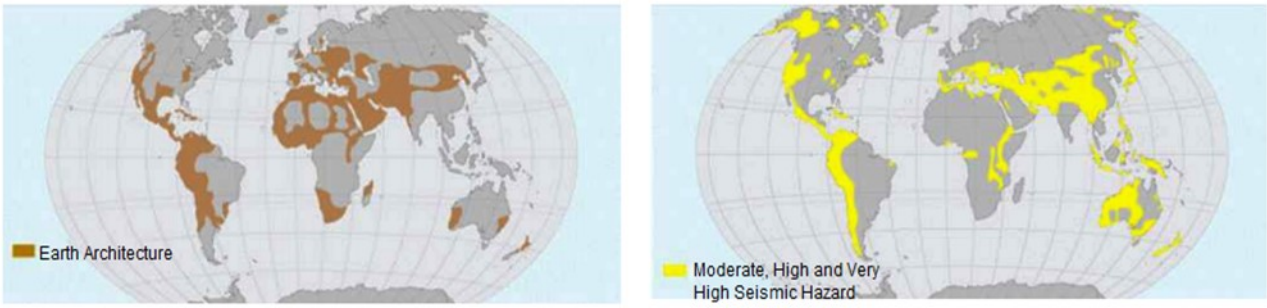

Figure 5.1 Distribution of earth construction and high seismic areas in the world [113]

In the case of rammed earth buildings in France where they are found to be spread mainly in the Rhône alpine region, these structures can be prone to moderate seismicity as shown by seismic zone map in France (Figure 5.2). It is, therefore, necessary to take into account the seismic design in this region.

Moreover, it exist a large number of heritage sites that are built from earth and that need preservation in the context of sustainable development. However, the conservation of rammed earth structures necessitates a profound knowledge of the materials properties and failure mechanisms [114].

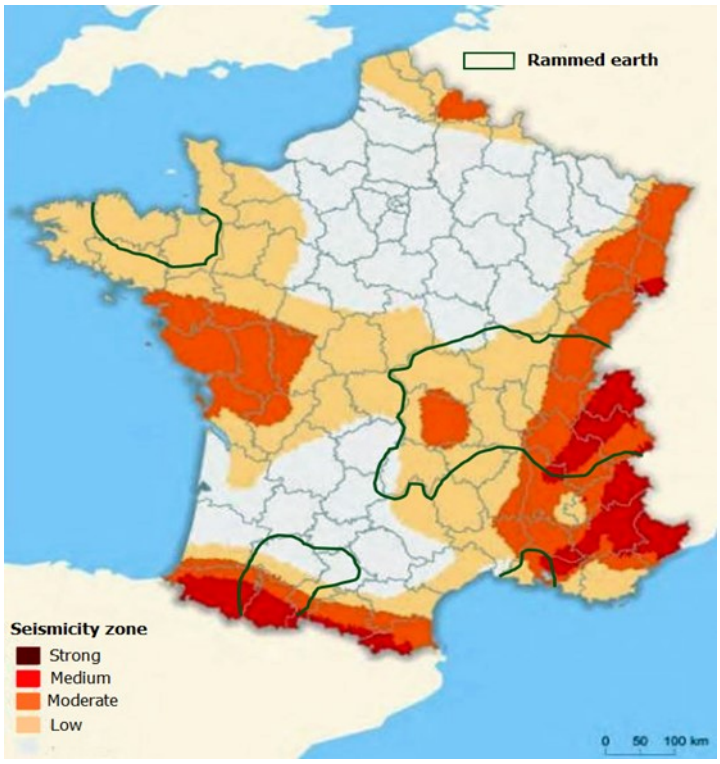

Figure 5.2 Earth building map and seismic zones in France [11]

In fact, the performance of rammed earth walls in buildings under dynamic loading is a major concern (especially in the regions that can be subjected to high seismicity). When exposed to these loading conditions (combination of horizontal and vertical loading) walls are subjected to in-plane shear and/or out of plane lateral force. This requires experimental testing of the shear response and capacity of rammed earth walls. Therefore, important parameters can be assessed by the experimental tests under static lateral load like obtaining the ultimate drift as well as the ultimate load which enhances for the assessment of the mechanical performance of rammed earth buildings.

With respect to the seismic behavior of rammed earth walls, the understanding of the shear behavior of the walls is fundamental and is rarely found in the literature.

5.1.1 Vulnerability of earth buildings to earthquakes

Earthquakes are characterized by acceleration movements of the soil. This acceleration produces large inertial forces on the structure that is related to the mass of each element of the structure. The seismic loads can act in two ways “in-plane” and “out of plane”. In the case where acceleration is “in plane”, shear forces are generated and diagonal crack normally occurs, then the wall tends to lose the stiffness and strength. For the “out of plane” acceleration, the seismic forces act perpendicularly to the walls and in this case cracking starts at the lateral corners of the walls and then the walls are prone to collapse due to flexural effects [115].

In the case of earth buildings, earthquakes appear to be the major causes of structural instability. The high seismic vulnerability of earthen buildings is due to the wall’s high weight that can

develop high levels of inertial forces during earthquakes and the low mechanical properties that lower the ability of the structure to withstand earthquakes.

Many deadly earthquakes have occurred in different regions where many rammed earth houses are found.

In China, Lundian suffered enormously from an earthquake on the 3rd of August 2014. Most of the houses were a two-story building made of rammed earth that was exposed to severe damage or collapse [100].

In 2003 in Bam, Iran, the Bam citadel (UNESCO world heritage) one of the largest adobe heritage of the world that persisted over two millennia, was severely damaged by a 6.5 Richter scale earthquake [116]. Similarly, the Erzincan earthquake in 1992, that hit eastern Turkey, caused the damage of 1200 building, and the earthquake in Peru, Pisco 2007 where most of the earth structures were highly damaged [75].

The damage of these buildings can be attributed to the low quality of traditional earth building due to the absence of basic engineering practice, since these houses are often built in low socio-economic societies where there is no compliance with the seismic codes and lack of knowledge on the properties of earth construction. On the other hand, a different parameter plays an important role like the soil type, seismicity zone, the structural dynamic characteristics (natural frequencies, damping ratio). It is therefore important to understand the different factors that affect the response of the structure.

Nevertheless, we can find some historical earth structures that resisted rather well to many seismic attacks. For example, the Hakka rammed earth houses (Figure 5.3) in the Fujian Province of China that withstood since the 17th century seven earthquakes of magnitude 5 or higher on Richter scale [117]. No structural damage had been recorded for the structures in this region. Figure 5.3(b) shows the Huanji Tulou wall crack due to a strong earthquake in 1918. Many recent types of research have been conducted on the Hakka structures demonstrating the durability the advancement and the innovation in the design and performance of these structures in the engineering of rammed earth construction as in [118].

Another example is found in New Zealand following the February 2011 Christchurch earthquake (6.3 on the Richter magnitude scale) and the September 2010 Darfield Earthquake (7.1 on the Richter magnitude scale) [19].Observation of the performance of earth building was inspected by a survey on twenty-six building among them adobe, rammed earth and cob done by Morris and Walker [119] after the Christchurch earthquake. Table 5.1 presents a summary of some of the assessed earth buildings including their damage state. The survey shows that many old unreinforced rammed earth building (constructed between 1950 and 1980) survived with only minor cracks [119]. It should be noted that among these structures, some of them had reinforced concrete foundations and bond beams.

As for the Darfield earthquake, it was the first major earthquake where modern reinforced earth buildings have been tested. Nevertheless, the damage was minor in most of the modern buildings surveyed. For the unreinforced rammed earth, the damage was recorded on a historical building constructed in 1977 with unstabilized rammed as shown Figure 5.4. The wall shows sliding

cracks at the base and diagonal in-plane cracks (similar cracks were obtained in our experimental study as seen in Chapter 3). Damage surveys were also performed where some earth building performed poorly and some other performed well.

The number of rammed earth building that had performed well under several seismic events mean that if rammed earth buildings are well executed they can have a satisfactory performance.

Table 5.1 Summary of some of the earth buildings inspected after the February 2011 Christchurch Earthquake

Earth wall material	Construction date	Damage state
Rammed earth (RC frame)	1965	B1-Slight damage
Reinforced rammed earth	1980	B1-Slight damage
Unreinforced rammed earth	1955	A-None
Unreinforced rammed earth	1953	B1-B2 Slight damage
Unreinforced adobe	1854	C2-Moderate with cracking damage
Unreinforced Cob	1982	C2-Moderate with cracking damage

Damage State: A–None, B–Slight, C-Moderate with cracking damage throughout the building, D-Extensive crack damage throughout, E-Very extensive damage with collapse or partial collapse of the structure. The digit indicates where in the scale eg B1 low within the B category, B2 mid B category, B3 borderline to C

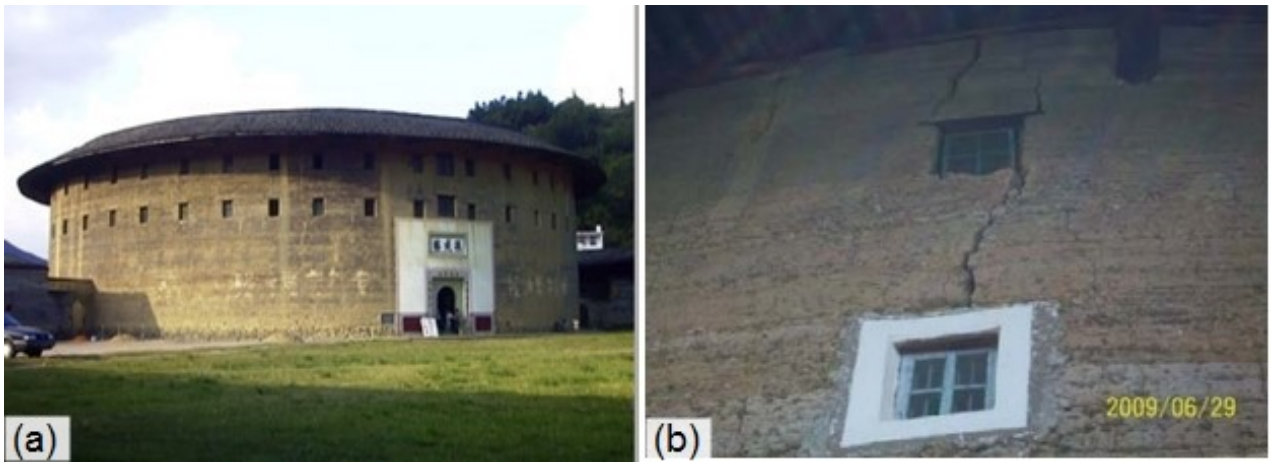

Figure 5.3 (a) Fujian Tulou (Hakka rammed earth building) cluster, Fujian province, Southern China; (b) Huanji Tulou wall crack after earthquake, [117]

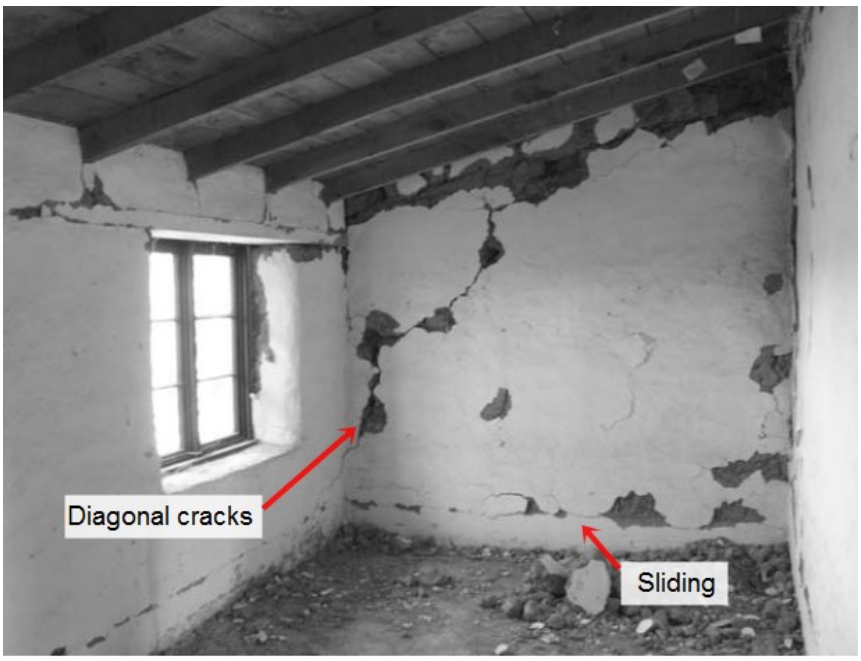

Figure 5.4 Damage of an unreinforced and unstabilised rammed earth building in New Zealand near to Darfield in 2010 [119]

5.1.2 Objective of this chapter

Research on the seismic capability of earth buildings in general and on rammed earth in particular is rarely found in the literature. Some studies are mainly conducted on adobes, maybe because this technique is more popular in seismic zones than other earth building techniques. However, the failures mechanism of rammed earth materials needs to be fully developed with further investigation on the strengthening solutions.

This chapter intends to evaluate the seismic performance of rammed earth using the experimental tests conducted in Chapter 3.

The nonlinear static (pushover) analysis is used for the evaluation of the seismic response of the buildings following the European regulation EN 1998-1 [120]. From the experimental tests on several walls nonlinear shear force–displacement curves had been achieved. The capacity curve is then obtained by transposing these shear force-displacement curves to an acceleration–displacement system. Then by using the standard spectra of an equivalent single degree of freedom system, the displacement demands (performance points) are determined to permit to the assessment of the seismic performance of the walls studied in different conditions (seismicity zones and soil types). The second objective was to determine limit states for the case of rammed earth walls that associate local damage limit states (LS) to specific points of the global force-displacement response of the rammed earth walls. In fact, to evaluate the displacement demands and the state of damage in the wall, these states must be well defined. Hence, based on the findings by other researchers for the case of masonry walls, limit states are proposed based on the measurement of crack propagation evaluated from the static wall tests obtained in chapter 3.

5.2 Definition of Limit state of rammed earth walls

Two approaches are usually used to assess the seismic performance of a structure: the classical force-based approach and the more recent displacement-based approach [120], [121]. The second approach is well known as being better adapted to earthquake design [122], which was the reason for adopting the displacement-based approach was used in this study to assess the seismic performance of the walls studied.

In order to evaluate the building, once the displacement capacity of the wall is defined, limit states (LS) need to be developed and linked the local deformation measurements such as the cracks width or strains. These limit states must differentiate several phases for the wall behaviour to describe the state damage and when local failure mechanism can occur. Hereafter in this section limit states are being defined based on the crack pattern observed for the rammed earth walls. Until now no limit state has been suggested for earth type of structures.

In order to well define the limit states, the calculation of the drift must be done. In fact, for the case of wall structure elements, the capacity under horizontal in-plane loading is normally expressed in terms of story drift. The inter-storey drift (short: drift) is defined by the total lateral displacement at the top of the wall divided by the storey height h. It can be calculated as following:

$$Drift = \frac{u_h}{h} \tag{5.1}$$

Where u_h is the relative horizontal displacement between the top and base of the storey high wall. In our case, the storey height h is equal to the height of the wall. As mentioned in the previous section, once the target displacement is determined this will allow us to reach the drift ratio.

As for the limit states, many researchers have defined these states for the case of masonry structures (Calvi [121] , Abrams [123], ATC [124], Bosiljko [125], Petry and Beyer [123]–[128], Tomagevic [128]). This limit states either describe the whole structures or individual elements. The one defined by Calvi [126] on the damage stated of masonry walls were used in order to define the limit states for our own results which are linked to the appearance of new cracks and the change in the kinematics of the walls. In this analysis on rammed earth walls, the general definition of each state established by Calvi was well respected.

Based on the findings of [121] to assess the damage state from the drifts, the limits proposed by masonry structures are the following:

- LS1: no damage
- LS2 (minor structural damage and/or moderate non-structural damage): the structure can be utilized after the earthquake, with no need for significant strengthening and repair to structural elements. The suggestif drift limit is 0.1%.
- LS3 (significant structural damage and extensive non-structural damage): the building

cannot be used after the earthquake without significant repair. The suggestif drift limit is 0.3%.

– LS4 (collapse): repairing the building is neither possible nor economically feasible. The structure will have to be demolished after the earthquake. Beyond this LS, global collapse with danger for human life has to be expected. The suggestif drift limit is 0.5%. Figure 5.5 show these limit states.

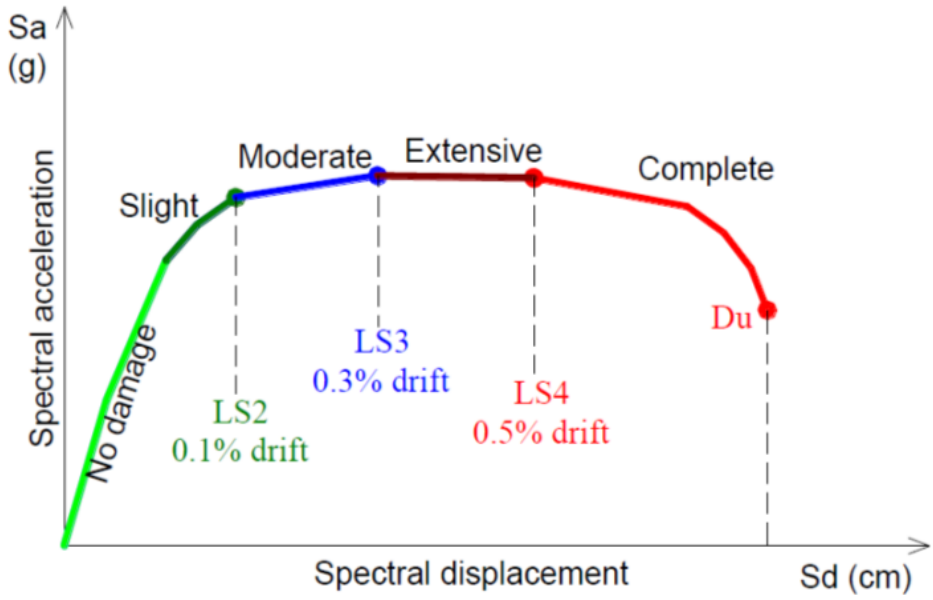

Figure 5.5 Damage limit states following drifts proposed by Calvi [126]

According to Calvi for the LS1 and LS2 limit, no damage concentration is yet observed, nevertheless when the structure attains the LS3 limit a damage concentration is assumed at the ground story level.

Based on the observation of the behavior of the rammed earth walls, the occurrence of the limit states is proposed based on the behavior of the wall and the occurrence of the local crack pattern which follows the definition of each one suggested by Calvi. Table 5.2 describes these limit states for the rammed earth walls and the corresponding one for the case of masonry walls.

Table 5.2 Local deformation measures for characterizing different limit states

LS	Local crack pattern	Damage state: Calvi, [126]
LS1	At this stage, no cracks are observed	No damage
LS2	-Appearance of the first crack at bed joint - First appearance of inclined cracks	Slight
LS3	-Concentration of deformation in the diagonal part or at the compressed corner due to crushing on the left side -First observation of fall of earth particles -Loss of some parts of the toe region due to uplifting	Moderate
LS4	-Extension of the diagonal cracks, or extensive crushing of the compressed zone -Extensive falling of earth particles	Extensive

We first note that for the LS1 no visible cracks are obtained. For LS2 we distinguish the first reduction of wall stiffness associated with the first appearance of cracks. LS3 indicate the damage concentration through the deformation in the diagonal part or at the compressed corner with a remarkable loss of earth particles. This limit state is typically associated with the maximum shear capacity of the global force-displacement curve. As for LS4 significance loss of earth can be observed along with the extension of these cracks.

Quantifying the damage states:

In order to quantify these deformations and specify the beginning and the end of each limit state, the cracks widths were identified using the DIC. The results of wall 2 and 3 that had (1.5 m height and 1.5 widths) are used since results were similar in term of load deformation and crack pattern. For the other two walls that had 1 m height, the crack pattern was disturbed by the pre-existing cracks hence the analysis would be misleading. For that reason, we pursue the analysis with only two walls. Each of the three different states was distinguished based on the visibility of the crack and the general behavior of the wall. As we observe the crack width of the two walls during the loading, the wall pass through the different state, and for all the loading case the width of the cracks starts expanding from 0.1 mm at an early stage of loading to reach 1.5 mm after the peak load. Hereafter, the state of the walls was differentiate depending on the crack width and the material loss for the following states: cracks between 0.5 mm and 1 mm, cracks bigger than 1mm and the first observation of material loss and finally to crack exceeding 1.5 mm and heavy material loss. Figure 5.6 summarizes these limits along with the associated drift and loading in a general manner.

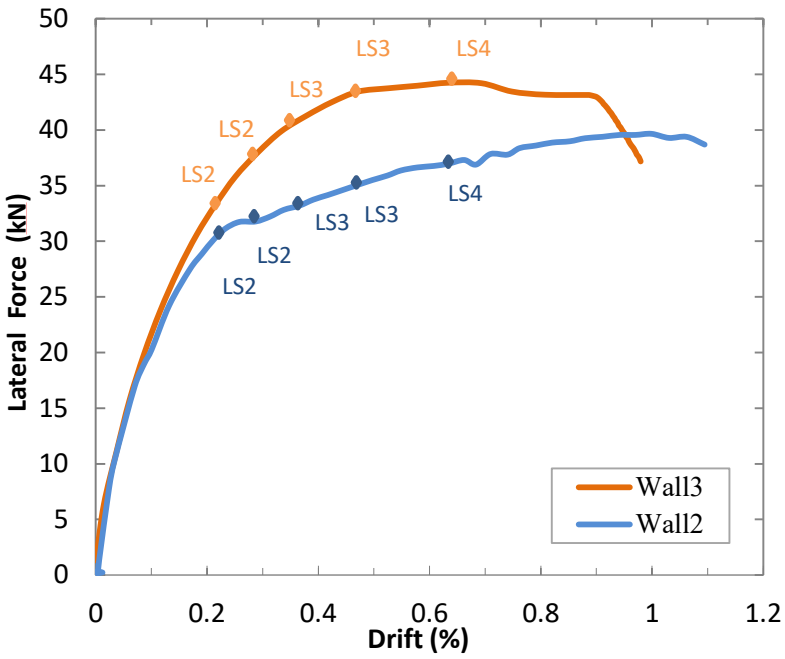

Damage due to:

LS2: First sign of cracks of :

0.5 mm <width of cracks < 1mm

LS3: Cracks become more visible concentrated at one of these positions: corner, diagonal or at bed layers: Width of cracks bigger than 1 mm, first signs of losing earth particles, signs of uplifting of the wall

LS4: Expansion of cracks width to more than 1.5 mm: Loss of compressed zone by visualizing loss of the material, uplifting become significant

Figure 5.6 The force-drift ratio for wall 2 and 3 with the evolution of the limit states

Figure 5.7 shows the location of the cracks and the associated width in order to define the limit states.The first signs of cracks that were associated to LS2 (slight) were the one that has between 0.5 and 1 mm as seen in Figure 5.7 (case of wall 2 associated to drift 0.23%). These cracks start to appear in the first non-linear part of the load-deformation curve of the wall. The cracks corresponding to LS2 were not easily visible directly on the wall, they were only explored through the DIC that revealed their location.This is why in the region where the drift exceeded 0.1 % the behavior was associated with slight damage.

After this stage, the cracks become more conspicuous (more than 1mm width) where they can be slightly observed on the wall and some small particles began to fall (this case is observed through Figure 5.8 for 0.32% and 0.4% of drift). For this case, the damage is considerate to be moderate.When the earth particles became prone to falling in heavier portions and the crack exceed 1.5 mm, the damage starts to be associated to extensive (as shown in Figure 5.8 for 0.6% drift). Hereafter the LS3 was limited to 0.6 % of drift that corresponds to the beginning of LS4 (extensive). As for the end of the limit state of LS4 (extensive), it was not suggested since no total collapse was observed for any of the walls.

LS	Through DIC	Observation of the crack	Drift
LS2	Observation on Wall 2 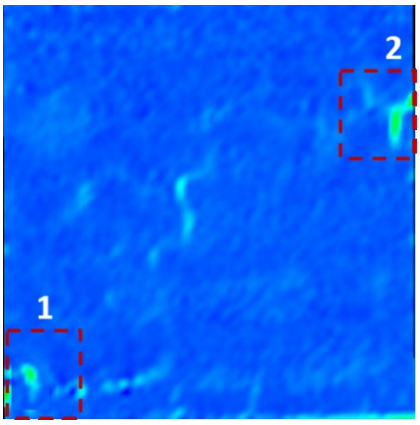 	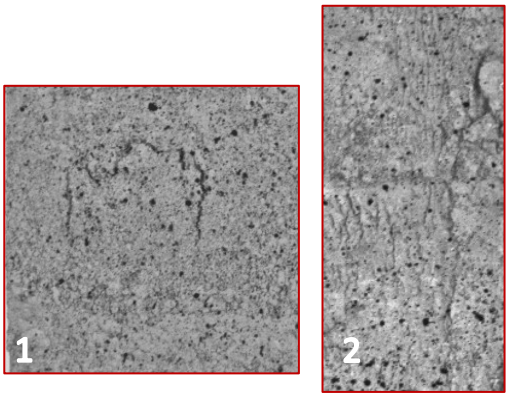 • 0.5 mm < Crack width < 1mm • Appearance of diagonal crack <0.5 mm	0.23%
LS3	Observation on Wall 2 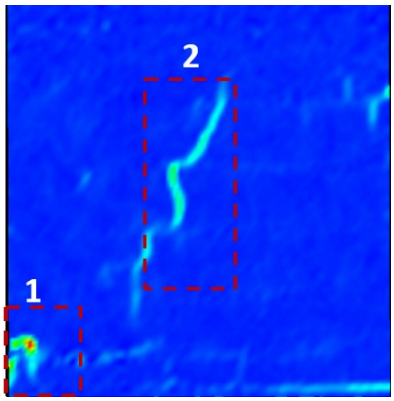 	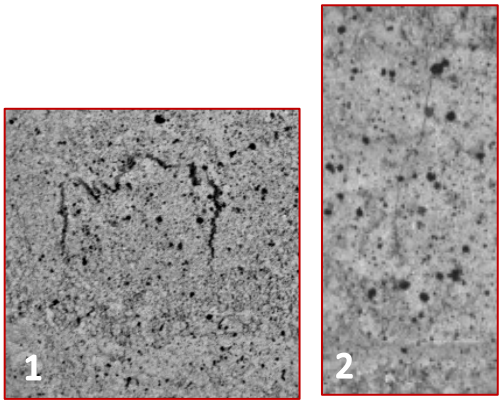 • Crack width on the right > 1mm • 0.5 mm < Diagonal crack < 1 mm	0.32 %
LS3	Observation on wall 2 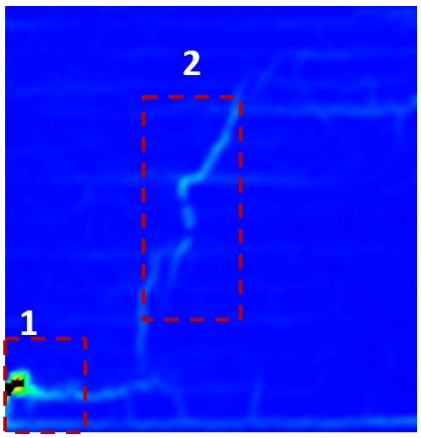 	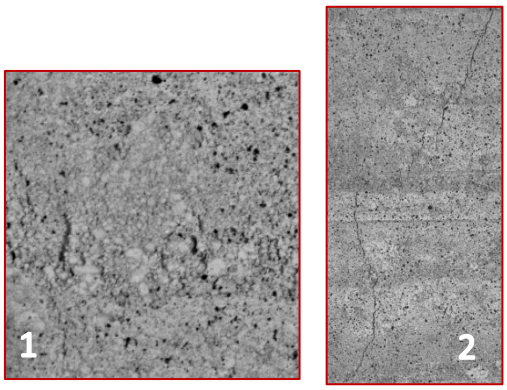 • Crack width on the right > 1mm • loss of earth particles	0.4%

LS3	Observation on wall 3 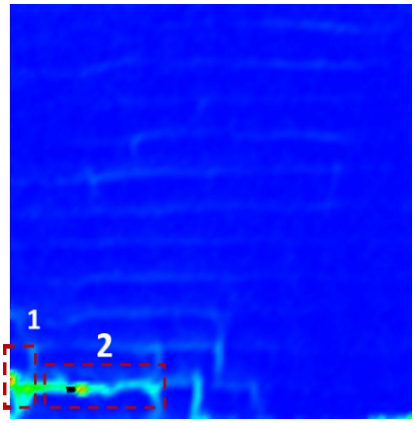 	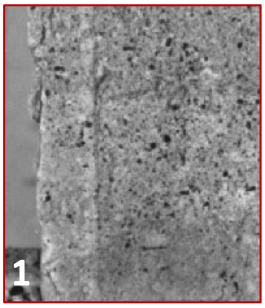 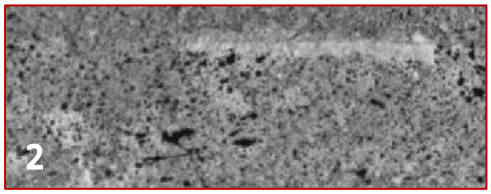 • Loss of earth particles	0.43%
LS4	Observation on wall 2 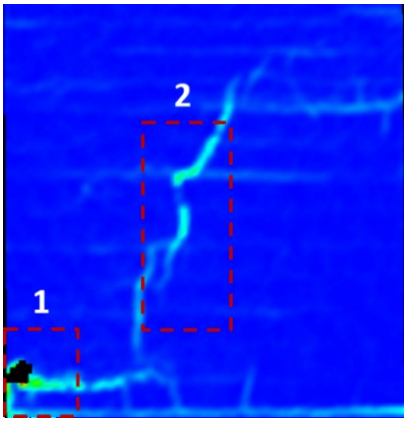 	 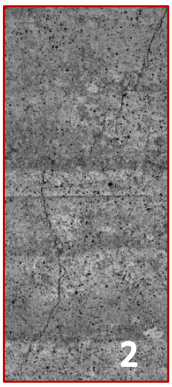 • Crack width on the right > 1.5mm • Diagonal crack > 1 mm • Significant loss of particles	0.6 %
LS4	Observation on wall 3 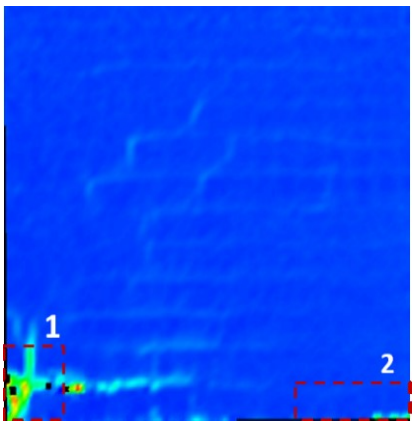 	 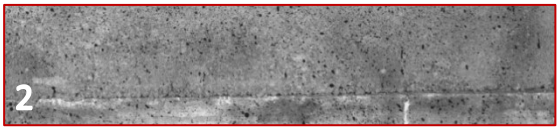 • Crack width on the right > 1.5mm • Significant uplifting	0.6%

Figure 5.7 Quantifying the crack width and location with the corresponding limit state

Figure 5.8 summarizes the suggested limit states for rammed earth walls through the association of the drift ratio. Only the value of the LS4 seems to be underestimated in the adaptation of the method. Hereafter, the method proposed by Calvi can be adjusted for the case of rammed earth wall as conducted in this study and the values to be retained for the drift are that of Figure 5.8. Therefore these limits will be used in order to analyses the results of the pushover test in the next section.

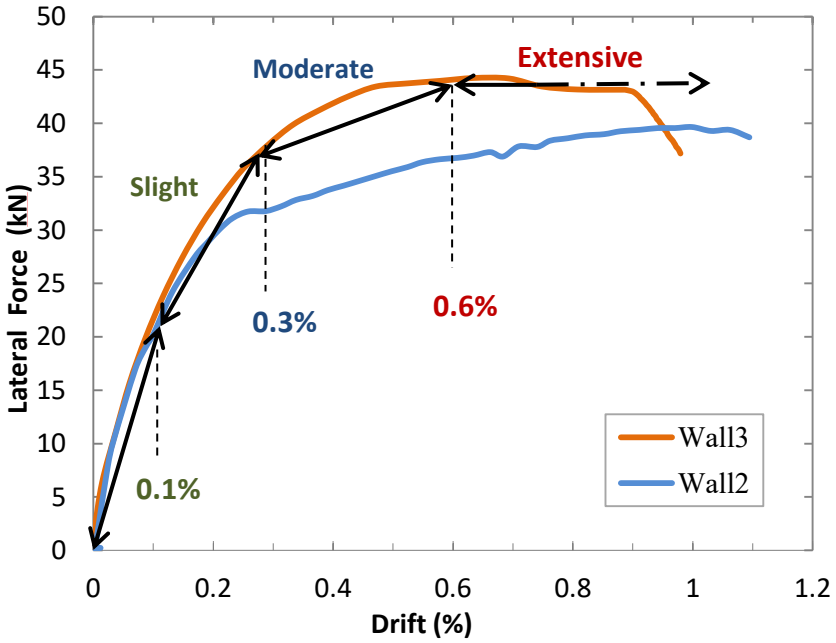

Figure 5.8 Suggested limit states for rammed earth walls

It should be noted that limit states are not defined for the case of rammed earth in the literature and this finding can serve future inspection on the behavior of rammed earth walls.

5.3 Pushover analysis in the seismic assessment: explanation of the method

Two essential and critical components must be determined to assess the seismic performance which is the seismic capacity and the seismic demand. The seismic capacity is the capability of the building to resist the seismic effects while the seismic demand is the specification of the earthquake effects on a building. Therefore, the performance is being evaluated in a way that the capacity is greater than the demand [129] by performing either inelastic time history analyses or using nonlinear static pushover analysis.

The static nonlinear methods despite their simplicity are considered to be accurate enough for practical application in building evaluation and design.

There are many nonlinear static procedures that have been officially introduced in the design codes worldwide. They started to be implemented in the framework of the engineering based on the seismic performance [129], [130]. In Europe, the N2 method proposed by [131] was implemented in Eurocode 8 [120]. This method has been formulated in the acceleration-displacement format [132].

The steps of this method consist of first determining the elastic response spectra. This spectrum could be transformed to inelastic spectra by using the reduction factor R_μ. The second step is to perform the pushover analysis to achieve the capacity curve of an equivalent single degree of freedom (SDOF) system and finally reaching the seismic demand of this system.

Each step of this method will be elaborated in more detail in this section.

5.3.1 The Eurocode elastic response spectra

Input earthquake ground motion is defined by a response spectrum. To analyze the performance of the structure, the response spectra are the main data that must be provided; these spectra are called "elastic response spectra" that depends on many parameters like the type of soil, the zone of seismicity of the corresponding structures. The values of the periods T_B, T_C et T_D and the soil parameter S that describes the response spectra depends on the type of the soil. Figure 5.9 shows the elastic spectrum from Eurocode 8.

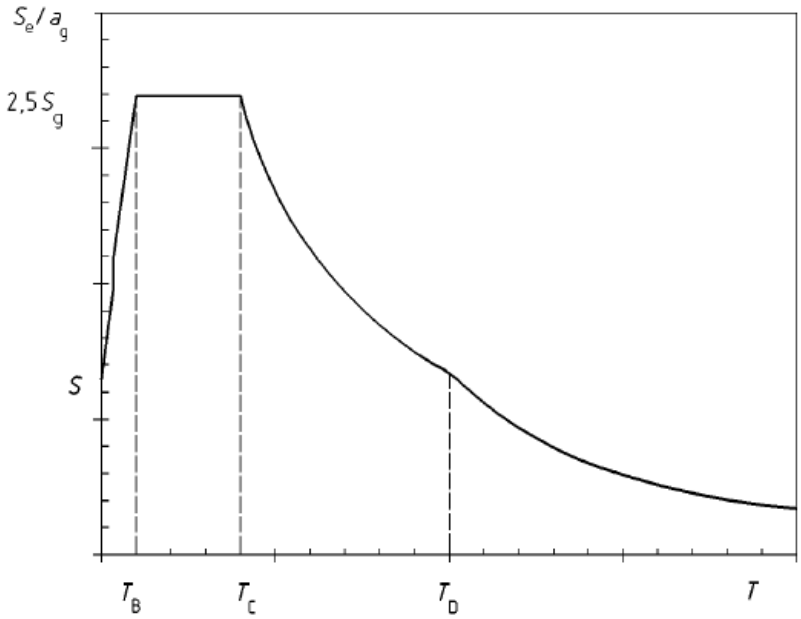

Figure 5.9 Elastic spectrum from Eurocode 8

5.3.2 Nonlinear Static Analysis Procedure

The pushover analysis is a static nonlinear analysis with constant vertical load and gradually increasing lateral loads distribution until a predetermined target displacement is reached. Both

the force distribution and target displacement are based on the assumption that the response of the structure is controlled by the first mode of vibration and that the mode shape remains constant after the structure yields. The method consists on assuming a displacement shape, and the load pattern is related to this displacement shape.

Moreover, the response of a Multi-degree of freedom (MDOF) structure must be transformed to the response of an equivalent SDOF system. This concept is illustrated in Figure 5.10.

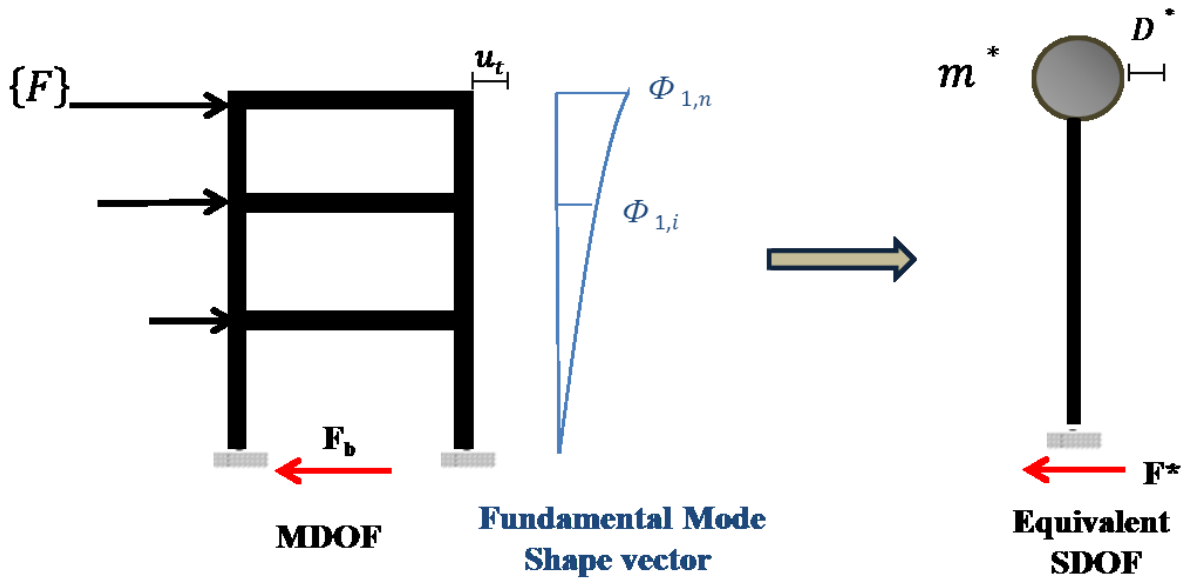

Figure 5.10 Conceptual explanations for transformation of MDOF to SDOF system

Starting from the differential equation of MDOF model submitted to horizontal ground earthquake motion $\ddot{u}_g$:

$$[M]\{\ddot{U}\} + \{F\} = [M]\{1\}\ddot{u}_g \tag{5.2}$$

Where [M] is the mass matrix, {F} is the storey force vector. The displacement shape {Φ} is assumed to be constant i.e (not a function of time). This is a basic assumption in this procedure. U is relative displacement vector defined as:

$$\{U\}=\{\Phi\}u_t \tag{5.3}$$

Where u_t denotes the top displacement.

In the pushover analysis, an increasing pattern of forces needs to be applied for each mass points of the system, it is determined as follow:

$$\{F\} = [M]\{\Phi\} \tag{5.4}$$

From this equation, it follows that:

$$F_i = m_i\Phi_i \tag{5.5}$$

Where mi is the weight of the 'i' storey, and Φ_i is the i_{th} element of the mode shape vector corresponding to the 'i' storey.

By multiplying the left-hand side of the equation (5.2) by $\{\Phi\}^T M \{1\}$ the equation that describes the SDOF system can be written:

$$m^*\ddot{D} + F^* = -m^*\ddot{u}_g \tag{5.6}$$

Where $m*$ is the equivalent mass of the SDOF system:

$$m^* = \{\Phi^T\}[M]\{1\} = \sum m_i \ \Phi_i \tag{5.7}$$

D^* and F^* the equivalent displacement and force of the equivalent SDOF:

$$D^* = \frac{u_t}{\Gamma} \tag{5.8}$$

$$F^* = \frac{F_b}{\Gamma} \tag{5.9}$$

Where F_b is the base shear and u_t top displacement for MDOF

$$F_b = \sum F_i = [M]\{\Phi\}^T\{1\} = \sum m_i \, \Phi_i \tag{5.10}$$

The constant Γ controls the transformation from MDOF to SDOF

$$\Gamma = \frac{\{\Phi^T\}[M]\,\{1\}}{\{\Phi^T\}[M]\,\{\Phi\}} = \frac{\sum m_i \Phi_i}{\sum m_i \Phi_i^2} \tag{5.11}$$

It should be noted that the constant Γ is used for the transformation of both displacement and force.

From the analysis of the MDOF structure a base shear, F_b- top displacement u_t, diagram is obtained that correspond to the capacity curve of the Figure 5.11. It should be noted that the constant Γ is used for the transformation of both displacement and force for the (F^*- D^*) diagram.

For simplicity, a bilinear idealization (Figure 5.11) of the pushover curve is applied from which the yield strength F^*_y and displacement D^*_y are determined. From the bilinear capacity pushover diagram the elastic period T^* is determined for the SDOF system as follows:

$$T^* = 2\pi\sqrt{\frac{m^* D_y^*}{F_y^*}} \tag{5.12}$$

By dividing the Force-deformation (F^*-D^*) diagram by the equivalent mass m* the capacity curve in acceleration–displacement (S_a-S_d) format can be obtained by applying:

$$S_a = \frac{F^*}{m^*} \tag{5.13}$$

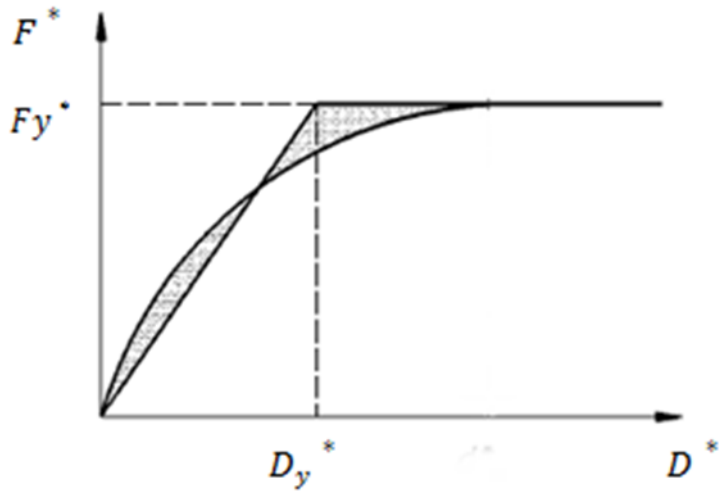

Figure 5.11 Bilinear idealization for the equivalent SDOF system [120]

5.3.3 Seismic Demand in acceleration–displacement (S_a-S_d) format

The correlation between the standard acceleration S_{ae} and the natural period T is plotted in acceleration vs. displacement domain to obtain the demand diagram (the following calculation comes from Eurocode 8). S_{de} is the elastic response spectrum in displacement, expressed as:

$$S_{de} = \frac{T^2}{4\pi^2} S_{ae} \tag{5.14}$$

The inelastic spectra can be also computed in terms of the ductility reduction factor Rμ (due to the energy dissipation of ductile structures), and ductility factor μ. The acceleration ordinate S_a and the displacement spectrum S_d of an inelastic SDOF system can be calculated from an elastic design spectrum as follows, [133]:

$$S_a = \frac{S_{ae}}{R_\mu} \tag{5.15}$$

$$S_d = \frac{\mu}{R_\mu} S_{de} = \mu \frac{T^2}{4\pi^2} S_{ae} \tag{5.16}$$

The reduction factor R_μ is usually expressed in terms of ductility μ and period T as defined below:

$$R_\mu = (\mu - 1)\frac{T}{T_C} + 1 \qquad T < T_C \tag{5.17}$$

$$R_\mu = \mu \qquad T \geq T_C \tag{5.18}$$

Where T_C is the characteristic period of the ground motion, defined as the transition period from the constant acceleration segment to the constant velocity domain of the spectrum

Therefore, the inelastic demand spectra for a certain ductility factor μ can be obtained in the Sa-S_d format as in Figure 5.12.

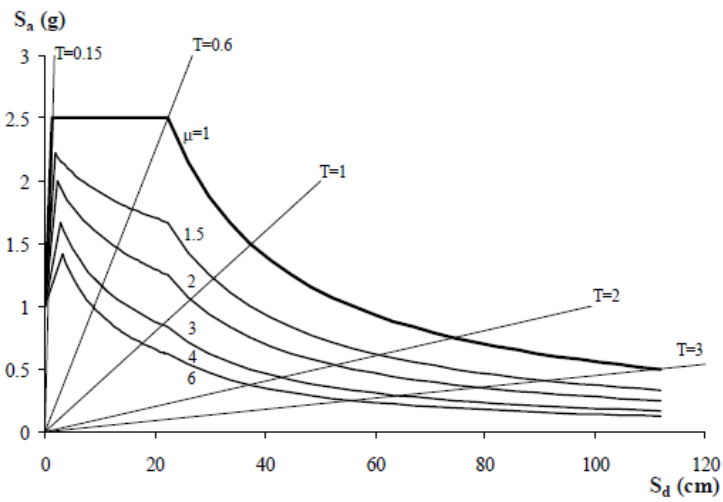

Figure 5.12 Demand spectra in S_a-S_d format for constant ductility [132]

5.3.4 Superposition of the capacity spectrum with the demand spectrum

The processing is briefly summarized in Figure 5.13 where the studied structure is converted to an equivalent single degree of freedom system.

The capacity curve – presented by the relationship between the base shear force F_b and roof displacement u_t (Figure 5.13 (b) is plotted in S_a-S_d) format where the shear force F_b is converted to the maximum acceleration S_a and the displacement on top of the wall is converted to the spectral displacement S_d by diving on the equivalent mass and by the transformation factor. As mentioned before, the standard acceleration spectrum S_a is transformed into an acceleration–displacement (S_a-S_d) format to obtain the demand spectrum.

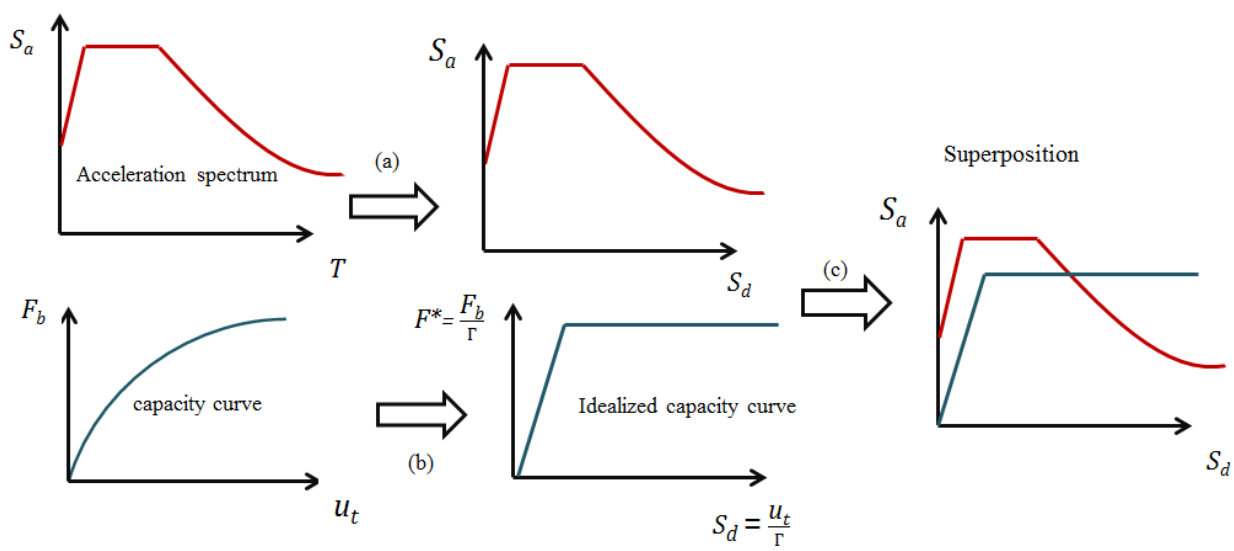

Figure 5.13 Pushover analysis processing

Once the capacity spectrum and the demand spectrum are plotted together in the S_a-S_d format, (Figure 5.13(c)) the seismic demand can be calculated between the capacity curve and the demand spectrum following Figure 5.14 and Figure 5.15 (shown below).

From the performance point, the seismic performance of the studied structure can be assessed. This method is efficient when the first mode is predominant [121], as in the case of rammed earth constructions [120], [134].

Seismic demand for the SDOF system:

The displacement demand S_d of the equivalent SDOF system can be determined by using the following equations:

$$S_d = \frac{S_{de}}{R_\mu}\left(1 + (R_\mu - 1)\frac{T_C}{T^*}\right) \qquad T^* < T_C \tag{5.19}$$

$$S_d = S_{de} \qquad T^* \geq T_C \tag{5.20}$$

Where R_μ is the ratio between the acceleration of the elastic system (S_{ae})and the acceleration of the system (S_{ay}) :

$$R_\mu = \frac{S_{ae}}{S_{ay}} \tag{5.21}$$

$$S_{ay} = \frac{F_y}{m*} \tag{5.22}$$

The graphical procedure is shown in Figure 5.14 (for medium and long period structures, and Figure 5.15 for short- period structures). The elastic period of the idealized bilinear system T* is represented by the radial line.

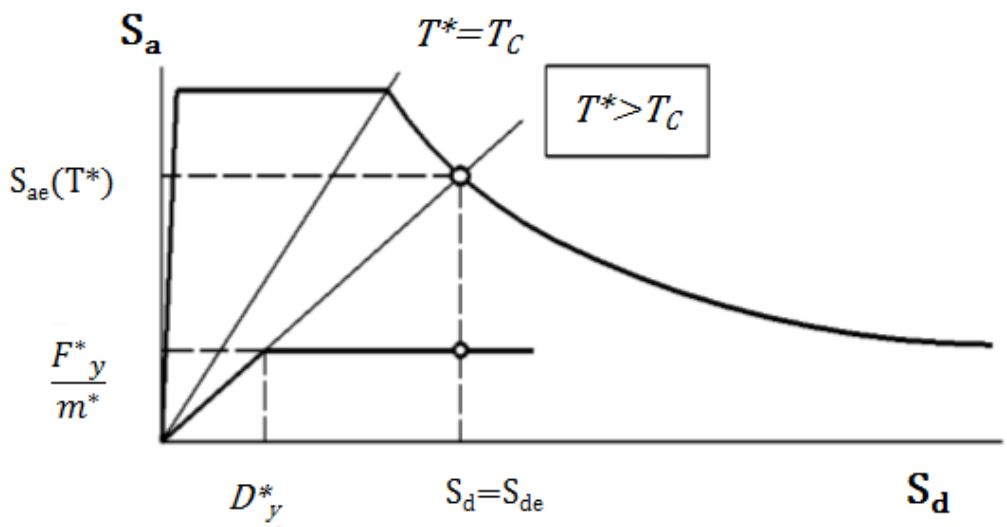

Figure 5.14 Estimation of target displacement from Eurocode method for T* > T

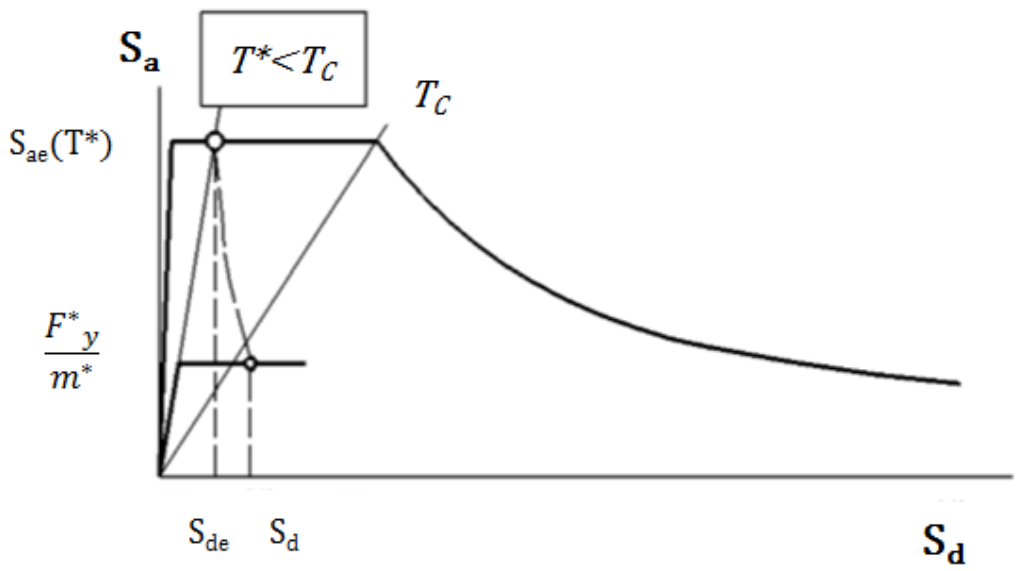

Figure 5.15 Estimation of target displacement from Eurocode method for $T^* < T_c$

Seismic Demand for MDOF Model:

After finding the SDOF displacement demand, this displacement must be transformed back to the top displacement of the MDOF model using:

$$u_t = \Gamma\, S_d \tag{5.23}$$

Local Seismic Demand for MDOF model:

Local quantities of interest such as rotations, storey drifts, corresponding to u_t, can then be determined.

5.4 Seismic evaluation of rammed earth house

For the test example, the response of a two-storey rammed earth building with a simplified plan (Figure 5.16) subjected to different ground motion was analyzed. The plan was inspired by a rammed earth house in Bourg en Bresse, France. A linear displacement shape is assumed Φ^T= [0.5; 1]. Rammed earth buildings in France currently have one or two stories and the wall thickness is about 0.5 m (Bui and Morel, [62]). The storey height is about 3 m; the length of rammed earth walls is about 2.5- 3 m. The spans between the load-bearing rammed earth walls is about 5 m. The vertical loads on each floor (which is important for the calculation of the equivalent mass) depends on the architecture of each building (spans between load-bearing rammed earth walls, materials of the floor, materials of the walls in the upper stories, …). The vertical elements between the walls and on the facades, are light elements (wooden and glass infill, in order to benefit the thermal insulation or natural lighting from those materials). The vertical loads at the top of the rammed earth walls include the dead loads (self-weights of the floors, roof, walls) and the live loads (which comprises, following Eurocode: 1.5 kN/m² for imposed loads of residential floors; and 0.5 kN/m² for light non-load-bearing walls). In order to calculate the equivalent masses, the internal wall was chosen, and the loads are calculated for a

5m span of the floor. The transfer of the loading for each equivalent mass to the wall is illustrated following Figure 5.17. Following this calculation, the mass of each equivalent system obtained was m_1= 15 tons and m_2 =7.73 tons.

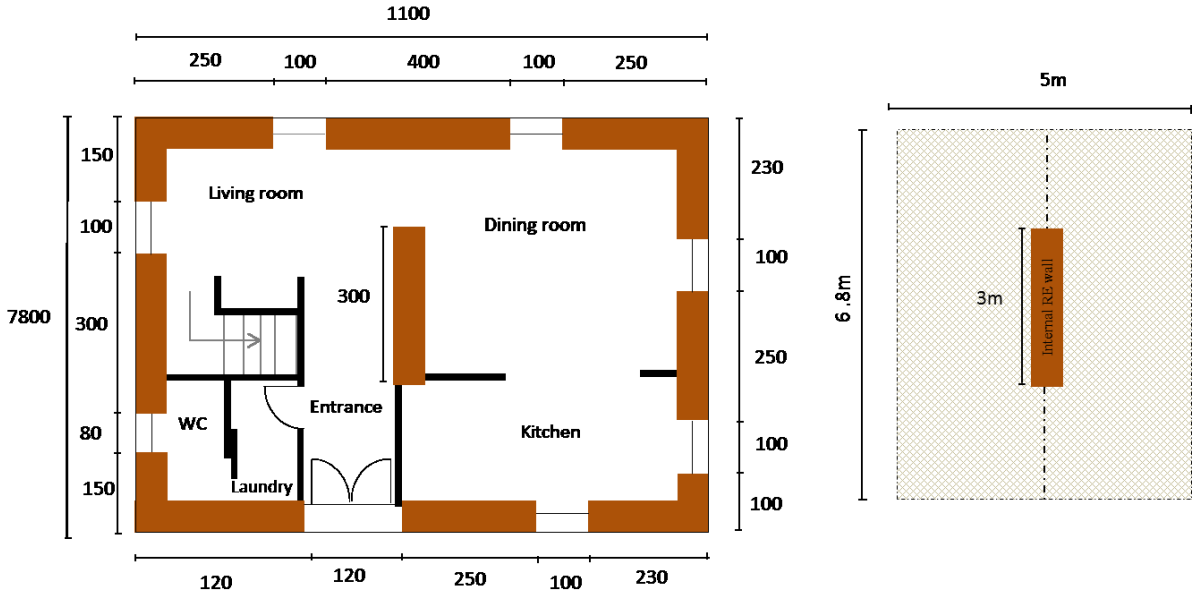

(a) (b)

Figure 5.16 (a) Example of a simple plan of a rammed earth house inspired from (www.architecte-interieur-lyon);(b) The surface of loading calculation corresponding to the internal wall

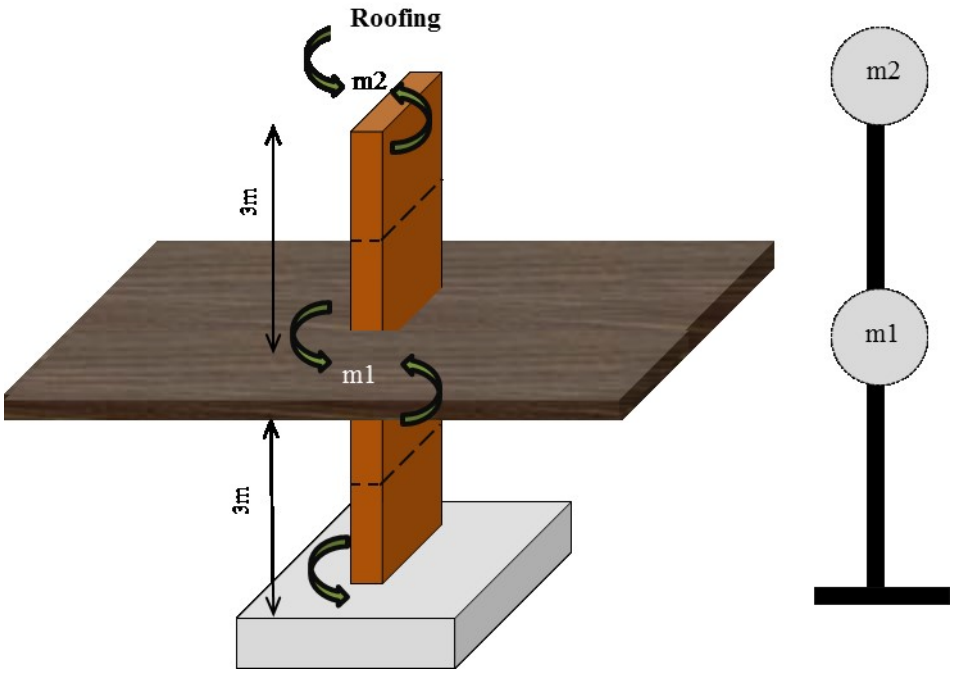

Figure 5.17 The transfer of the loading corresponding to each wall and the equivalent mass of each wall

After calculating each mass, the total equivalent mass of the system can be calculated using (equation 5.7) which gives m^*= 15.23 tons. Finally, the MDOF system is transformed to an equivalent SDOF system using the equation 5.8 and 5.9 along with the transformation constant which is Γ= 1.3 in this case (equation 5.11).

5.4.1 Scale effects

This section aims to use the pushover tests to assess the seismic performance of rammed earth buildings. To transpose the results obtained from the laboratory pushover tests, the scale effects should be determined. In order to reach the top displacement, the wall at the second floor at 6m height should be considered (that correspond to the top of the building).

As mentioned before three main failure modes may occur when a wall is submitted to an in-plane horizontal load diagonal cracks, uplift cracks ("rocking") and sliding cracks [105]. This behavior can be modeled by the flexure beam model or shear model.

Giving that the diagonal failure was dominated for these walls, the analytical model of a shear beam is adopted to study the influence of the scale effect. Hereafter, to transform the experimental capacity curves to real scale curves, both the horizontal force and the displacement must be converted to the one that corresponds to a real scale wall at a 6m height. The calculation below explains the factors that should be used to take into consideration the influence of the scale effects:

a. *From a tested wall A (L_1=1.5 m × h_1=1.5 m × e_1=0.25 m) to a real scale wall B (L_2=3 m × h_2=6 m × e_2=0.5 m):*

We consider that a rammed earth wall has: A as section area, G the shear modulus, τ_{max} the maximum shear stress. The rest of the components (maximum shear force, top displacement and shear of the real scale wall are calculated in function of the experimental results as shown in Table 5.3).

Following the shear model, with $L_2 = 2.L_1$, $h_2=4.h_1$, $e_2=2.e_1$, it is simple to obtain:

$$F_2 = 4\,.\,F_1 \tag{5.24}$$

Where F_1 and F_2 are, the maximum horizontal loads supported by walls A and B.

As for the rigidity, we can have:

$$k_2 = k_1 \tag{5.25}$$

b. *From a tested wall C (L_3=1.5 m × h_3=1.0 m × e_3=0.25 m) to a real scale wall D (L_4=3 m × h_4=6 m × e_4=0.5 m):*

In this case: $l_4 = 2l_3$, $h_4=6h_3$ but $e_4=2e_3$, in the same way, we can be obtained:

$$F_4 = 4\,.\,F_3 \tag{5.26}$$

$$k_4 = \frac{2}{3} \, . \, k_3 \tag{5.27}$$

Table 5.3 Scale effect parameters from experiments to the scale of rammed earth wall building

Parameters	**Tested wall A** (1.5m x 1.5m x 0.25)	**Real scale wall B** (3m x 6m x 0.5)	**Tested wall C** (1 m x 1.5 m x 0.25m)	**Real scale wall D** (3m x 6 m x 0. 5m)
Shear stiffness	$k_1 = \frac{\mathrm{G\,A_1}}{\mathrm{h_1}}$	$k_2 = k_1$	$k_3 = \frac{\mathrm{G\,A_3}}{\mathrm{h_3}}$	$k_4 = \frac{2}{3} \, . \, k_3$
Maximum force due to shear	$F_1 = A_1 \, . \, \tau_{max}$	$F_2 = 4 \, . \, F_1$	$F_3 = A_3 \, . \, \tau_{max}$	$F_4 = 4 \, . \, F_3$
Top displacement resulted from shear model	D_1	$D_2 = 4 \, . \, D_1$	D_3	$D_4 = \frac{2}{3} \, . \, D_3$

After applying these parameters conversion to the initial experimental curves, the base shear F_b in function of the top displacement u_t is obtained. Next, the load is divided by the transformation factor and the equivalent mass, as explained previously to obtain the S_a, and the displacement is divided by the transformation factor in order to have S_d.

The final step implies a bilinear idealization of each pushover curve where the yield strength and the displacement amount are calculated. Once the curves are superposed the drift is then calculated for the first level for a wall of (3 m x 3 m x 0.5 m) where the damage will be most intense.

5.4.2 Seismic assessment of 1-scale walls:

The demand spectrum was built for class II buildings (current buildings) and for two types of foundation soil: types A and B. Following Eurocode 8 [120], the A-type soil corresponds to a rock or very stiff soil (shear wave velocity v_s > 800 m/s) and the B-type soil corresponds to a good soil (shear wave velocity v_s = 360–800 m/s). The demand spectrum used was based on the normalized accelerations mentioned in the French Annex of Eurocode 8.

Step 1: Transformation to acceleration-displacement curve

The procedure adopted for the transformations from the force-displacement curve to the acceleration displacement curve is given in Figure 5.18 for each wall. The acceleration is calculated for each corresponding experimental horizontal force by dividing with the equivalent corresponding mass. Nevertheless, the mass applied on the experiments correspond to higher vertical stress, in order to reach the same order of magnitude the equivalent mass m* was

multiplied with a correction coefficient to reach the same order of vertical stress of the one applied on the experimental walls (0.3 MPa stress).

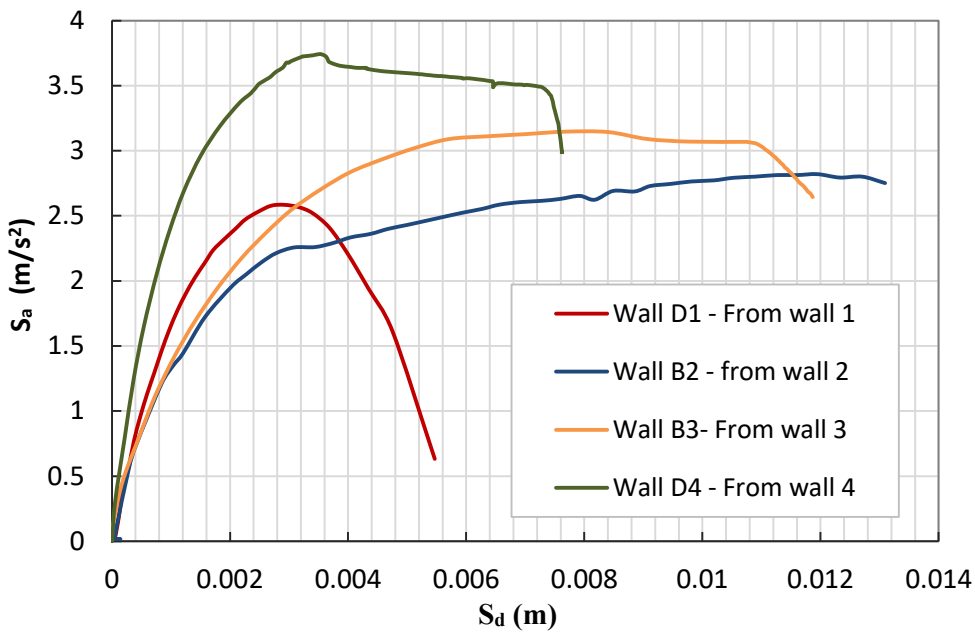

Figure 5.18 Transformation from force-displacement curve to acceleration-displacement curve for case of wall 1

Step 2: Idealization of the capacity curves

The second step imposes a bilinear idealization of each pushover curve where the yield strength and the displacement amount are calculated as shown in Figure 5.19 and Figure 5.20. This procedure is repeated for every wall and the obtained capacity curves are plotted with the spectrum of different seismicity on the same graph in order to search for the target displacement in step 3.

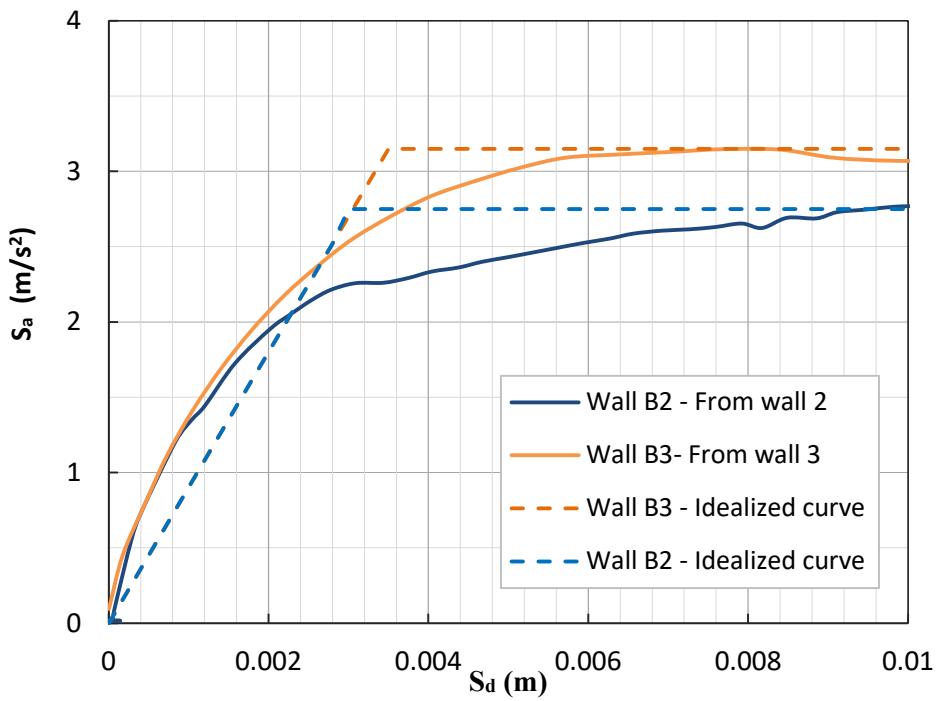

Figure 5.19 Idealization of the capacity curves for wall B2 and B3

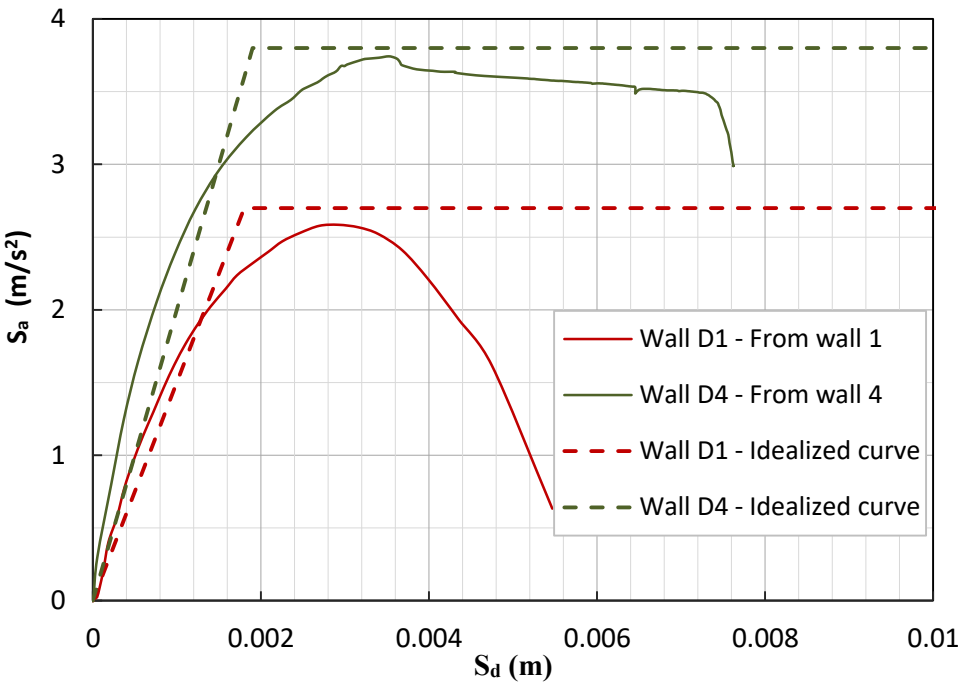

Figure 5.20 Idealization of the capacity curves for wall D1 and D4

Step 3: Superposition with the elastic spectrum and calculation of the drift

The superposition of the capacity curved with the elastic spectrum is shown in Figure 5.21 for zone A and Figure 5.22 for zone B. Once the curves are superposed the displacement demand is then calculated for the first level for a wall of (3m x 3m x 0.5 m) where the damage will be

mostly concentrated.Therefore to obtain the drift ratio the displacement demand will be divided by 3 m heigh using (5.1).

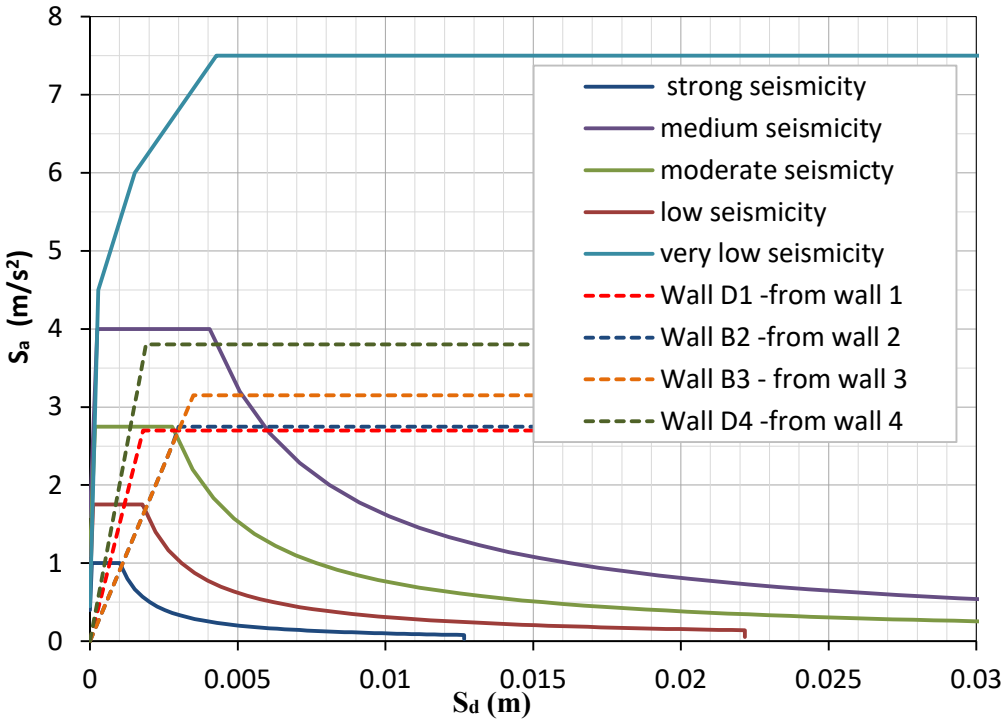

Figure 5.21 Capacity spectrum for different seismicity zones, soil A

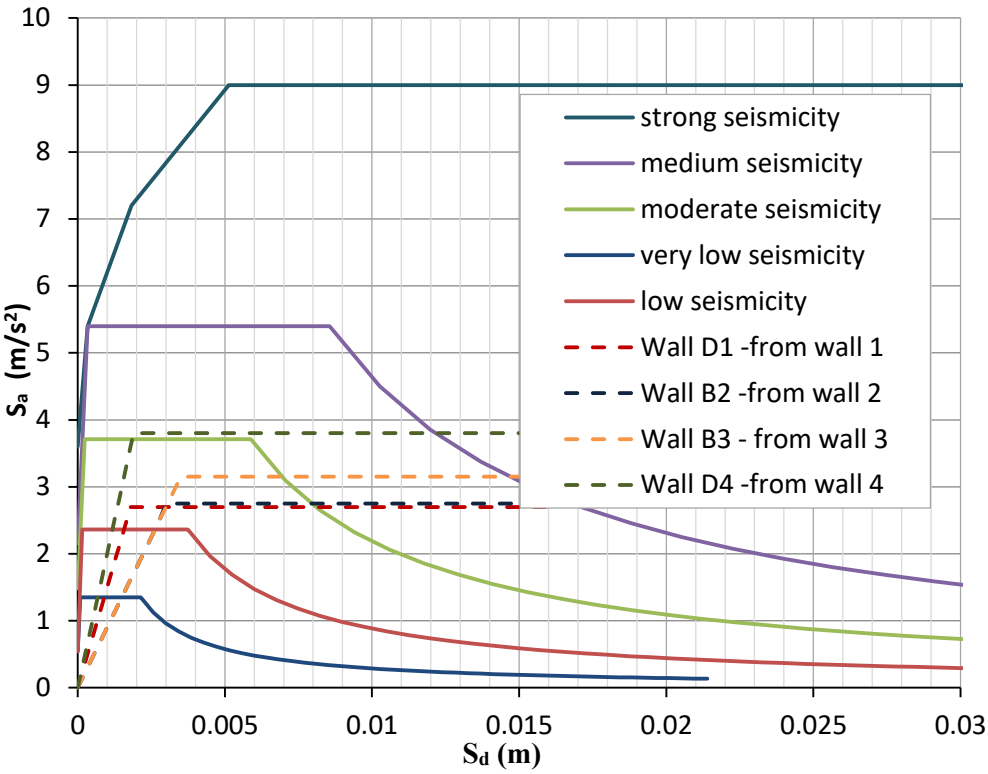

Figure 5.22 Capacity spectrum for different seismicity zones, soil B

The target displacement is calculated depending on the corresponding T^* of the equivalent structure and respecting to the conditions ($T^* > T_c$ or $T^* < T_c$) for each spectrum as shown in Figure 5.14 and Figure 5.15. Then, each displacement is multiplied with the transformation factor to reach back the MDOF.

An example of this calculation for wall 2 and 3 for the case of medium seismicity is shown below:

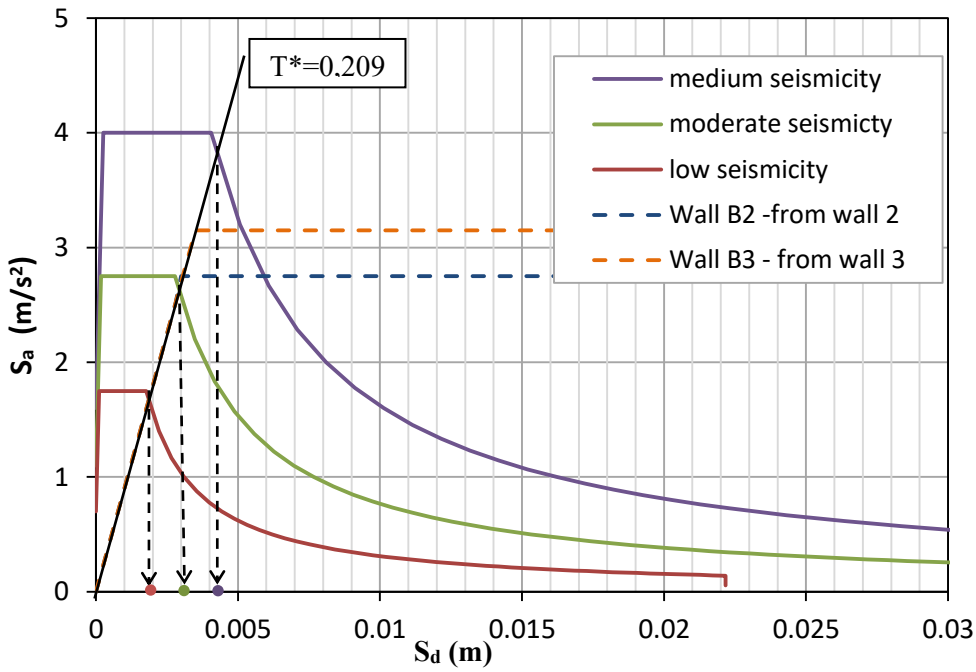

Figure 5.23 Visualizing the intersection points between the elastic spectrum and the capacity curves

1-Determination of the displacement demand S_d

After the calculation of the equivalent period (applying equation 5.12), we can obtain T^*=0.209. Having $T^*>T_c$, the displacement demand is directly obtained as seen in Figure 5.23 (intersection of the dotted line with the spectrum). We can easily obtain S_d =0.0045 m in case of medium seismicity.

2-Transformation of SDOF displacement demand to the top displacement of the MDOF model:

Once the displacement demand is obtained as seen previously, it should be transformed back to the MDOF model by multiplying with the transformation factor (equation 5.23). We can therefore obtain:

$$u_t = \Gamma . S_d = 1{,}3 . 4{,}5\ 10^{-3} = 5{,}85.10^{-3} m$$

3-Drift

Once reaching the target displacement of top the MDOF system, finally the drift can be calculated by dividing the value of the displacement demand over the height which is 3m in this case:

$$Drift = \frac{5{,}85.10^{-3}}{3}.100 = 0.195\ \%$$

This procedure was repeated for each wall respecting the conditions ($T^* > T_c$ or $T^* < T_c$).

Step 4: Evaluation of each wall

The limit states of the walls studied for the type-A soil is summarized in Table 5.4 and for the type-B soil in Table 5.5.

Table 5.4 Inter-storey drifts calculated for soil A

Seismicity zone	Wall 1		Wall 2		Wall 3		Wall 4	
	Drift (%)	Damage state	Drift (%)	Damage state	Drift (%)	Damage state	Drift (%)	Damage state
Very low	0.039	No damage	0.043	No damage	0.043	No damage	0.039	No damage
Low	0.078	No damage	0.085	No damage	0.086	No damage	0.052	No damage
Moderate	0.133	Slight	0.13	Slight	0.13	Slight	0.052	No damage
Medium	0.132	Slight	0.195	Slight	0.195	Slight	0.128	Slight
Strong	0.42	Moderate	0.53	Moderate	0.55	Moderate	0.3	Moderate

Table 5.5 Inter-storey drifts calculated for soil B

Seismicity zone	Wall 1		Wall 2		Wall 3		Wall 4	
	Drift (%)	Damage state	Drift (%)	Damage state	Drift (%)	Damage state	Drift (%)	Damage state
Very low	0.063	No damage	0.078	No damage	0.078	No damage	0.043	No damage
Low	0.01	Slight	0.12	Slight	0.12	Slight	0.15	Slight
Moderate	0.133	Slight	0.17	Slight	0.17	Slight	0.086	No Damage
Medium	0.22	Slight	0.3	Moderate	0.3	Moderate	0.17	Slight
Strong	0.72	Collapse	0.82	Collapse	0.85	Collapse	0.48	Moderate

Following the criteria used, the studied walls can have a satisfactory performance on the seismicity zones, ranging from "very low" to "medium" for the soil of type A. As for type-B soil, the walls studied can have an acceptable performance on the seismicity zones, yet ranging from "very low" to "moderate". For the case of "medium seismicity," the walls become prone to moderate damage.

It is important to mention that the walls presented in this manuscript were tested under a 0.3MPa vertical stress (corresponding to the dead and live loads of the floor and roof), which is a heavy load to support for a rammed earth wall. This means that the results obtained correspond to an unfavorable case in practice. For the case where these dead and live loads are smaller (e.g. a one-storey rammed earth house or the ground floor from rammed earth and second floor in wood, which is the current trend in France, to take advantage of the good thermal inertia of the walls and good insulation from the wooden structure), the seismic performance obtained would be better.

Discussions:

The results show that, for the configurations studied in this paper, from "very low" to "moderate" seismicity zones, unreinforced rammed earth buildings can be constructed on type-A and B soils. For the "medium" seismicity zone, only type-A soil is acceptable.

In Eurocode 8, a condition is imposed for unreinforced masonry:

$$a_g . S < 2m/s^2 \tag{5.28}$$

Where a_g is the design horizontal acceleration (which is a function of the seismicity zones) and S depends on the soil types (more details can be found in Eurocode 8). So, we can verify if the conditions imposed for unreinforced masonry can be applied for the case of rammed earth structures.

Indeed, following equation (5.28) and information about seismicity zones and soil types detailed in Eurocode 8, unreinforced masonry buildings can be constructed on type-A and B soils for seismicity zones from "very low" to "moderate". For "medium" seismicity zones, only soil A is appropriate. This condition is similar to the results obtained in this study. Therefore, this condition in Eurocode 8 for unreinforced masonry seems applicable also for rammed earth buildings studied in this paper. This verification is important for the engineering application because the condition proposed in Eurocode 8 is a simplified formula which can be easily used by engineers.

5.5 Conclusion

Earthquakes appear to be the major causes of structural instability for earth buildings. A large number of rammed earth houses exists in the world and should be preserved in the context of sustainable development and conserve our heritage sites. Furthermore, for the construction of new rammed earth walls in seismic regions, a seismic-resistant design should be adopted to

assure safety issues. The seismic assessment maintained in our study is a step towards a better understanding of the performance of these structures in case of a seismic event.

In this context, the capacity curves were established for the studied walls and the damage states were determined for different seismicity zones and soil types. However, in order to develop such models, local deformation measures that characterize the different limit states must be determined. Therefore, the limit states have been suggested for rammed earth walls of 1.5m height and they were used in the evaluation of the performance of one scale walls.

Following the damage limits that were proposed, the rammed earth walls studied can have a satisfactory performance on seismicity zones ranging from “very low” to “medium” with type-A soil. It is important to note that the most important seismicity zone in Metropolitan France is “medium”. For type-B soil, the acceptable results were only found for seismicity zones from “very low” to “moderate”. Other soil types (C and D) were not studied because the demand spectrum is higher for these soil types as per Eurocode 8 but the performance would be lower than for the type-B soil. A condition in Eurocode 8 for unreinforced masonry was also verified for the case of rammed earth structures. The results showed that this condition seemed applicable also for rammed earth buildings. This point is important because the condition proposed in Eurocode 8 is a simplified formula which can be easily implemented by engineers.

It is also important to assert that the walls presented in this paper were tested under a 0.3MPa vertical stress, which is a heavy load to support for a rammed earth wall. This means that the results obtained correspond to an unfavorable case in practice. Indeed, when the vertical compressive stress increases, this can prevent the rocking phenomenon; however, an increase of vertical compressive stress accompanies also an increase of mass, so the seismic load increases too. A preliminary study showed that the mass increase is more unfavorable than its benefit. That is why in practice, for the case where these dead and live loads are smaller (e.g. a one-storey rammed earth house or the ground floor in rammed earth and second floor in wood, which is the current trend in France, to take advantage of the good thermal inertia of earth walls and good insulation from the wooden structure), the seismic performance obtained would be better.

General Conclusion

The understanding of rammed earth from the mechanical structural point of view is essential in order to pursue studies that permit the protection of the earth heritage and on the other hand for the conception of future modern sustainable construction. The work in this thesis contributes to the knowledge of the in-plane response of unstabilized rammed earth walls. The behavior of these structures under this type of loading is a major concern which can enhance the assessment of their mechanical performance in case of seismic action. The comprehension of the shear behavior of the rammed earth walls is fundamental and rarely found in the literature. Therefore an experimental program was conducted in this thesis that consists of testing several unstabilized rammed earth walls subjected to lateral loading and determining their structural failure. In this study, correlation of images was a major tool for the treatment of the results to measure the deformations and detecting the occurrence of cracks.

The mechanical characterization of the chosen soil was first conducted using compression tests on a cylindrical and prismatic specimen. These specimens were representative with the same thickness of the layer's wall. The results showed the influence of the geometry on the obtained compressive strength of rammed earth specimens (higher values for cylindrical specimen comparing to prismatic ones). The DIC on these specimens highlighted higher deformation at the interface between the layers and in some cases cracks' initiation from these areas. Therefore, the first aspect to be pointed out is that interfaces between the layers can be considered as weak points for this material especially in the case of horizontal loading where the interface is more solicited.

The shear parameters of rammed earth material were also investigated by experimental direct shear test on two scales: large shear box and the standards one. From the large shear box, the results showed that interface between layers have lower mechanical properties than in the layer itself which is related to the lower density in this area as the earth is less compacted.

Experimental results of the small shear test showed quantitatively the influences of the compaction on the dry densities of the earthen layer and consequently influences on the shear parameters. The interesting finding was that the friction angles obtained for the upper and middle parts of an earthen layer were similar because of the similar roughness of earth grains; and that the upper part had higher cohesion than the middle part due to a higher suction. The experimental parameters obtained from these tests are apparent and they can differ from one test to another. Henceforth, a strong variation of these two parameters with suction can be expected, especially because rammed earth material is a heterogeneous fine-grained soil with water content. Identifying those parameters using an effective mean stress should be investigated in further studies.

At the scale of a wall, experiments were carried out on rammed walls at different scales tested under static lateral loading. The shear response and the capacity of each rammed earth wall were determined. The results of the analysis showed a linear behavior of the walls up to a certain limit

and then progressive cracking results through in nonlinear response. The response of the rammed earth was therefore characterized by significant non-linear behavior response and a remarkable ductility. Another aspect was noticed during this analysis which was a divergence in results obtained for walls 1 and 4 (with the same height) which points out that the manufacturing process could have a significant influence on the performance of rammed earth walls.

Eventually, different types of failure mechanism were detected during the testing under lateral loading which can be summarized by: corner crushing from one side because of the stress concentration in this area, diagonal cracking that is due to diagonal compressive strut failure, sliding of some layers due to interface shear failure and local uplifting from the base due to tensile stresses. Moreover, the failure patterns that were observed for walls indicate a preponderance of the shear phenomenon with no brittle behavior. Some of these cracks passed through the interface between layers hence showing again the importance of the determining the mechanical properties at the interface. This aspect is in agreement with other shear tests on small walls conducted in the literature where it was also observed that the failure of the wall can take place due to delamination of layer interface ([76], [78], [99], [108]). Therefore, more advanced studies to characterize the properties on the interface should be conducted in the future.

In a second part, the behavior of rammed earth walls tested under in-plane loading was modeled resorting to the finite element method (FEM). The experimental results derived from the direct shear tests were used for the numerical parameters. The “interface” layers of 1cm-thick were introduced. The analysis showed that the key parameters of this study were the cohesion and the friction angle (in earth layers and at the interface). A parametric study was performed by varying the cohesion and the friction angle at the interface and inside the layer in order to reproduce the experimental results. The results showed the necessity of having additional testing to define the parameter of the cohesion which seems to be crucial for this study. Nevertheless, despite the simple criterion of plasticity used, this model allows the reproduction of the experimental initial stiffness and the global elastoplastic behavior.

In the final part of the thesis, the assessment of the experimental results (at the wall scale) was completed using the pushover methodology according to Eurocode 8. The evaluation of each wall was achieved based on a proposition of the limit states. Based on the observation of Calvi on masonry walls, we defined a set of local limit states which are based on the occurrence of cracks in the wall and the evolutions of it state during the loading. Hereafter, these limit states were quantified by observing the behavior of each tested wall and the evolution of the width of cracking and then it was identified through the association of the drift ratio depending on the cracking width and the material loss. It should be noted that limit states are not defined for the case of rammed earth in the literature and this finding can serve future inspection on the behavior of rammed earth walls. Based on these data, the performance of a 1 scale wall was examined on different ground acceleration. In this analysis, the demand spectrum was built for two types of foundation soil: types A and B. The results showed that the rammed earth walls studied demonstrated a satisfactory performance in seismicity zones ranging from “very low” to “medium” with type-A soil which is the most important seismicity zone in Metropolitan France. For type-B soil, the acceptable results were only found for seismicity zones from “very low” to

“moderate”. Other soil types (C and D) were not studied, but the performance would be lower than for the type-B soil.

Finally, it should be indicated that the study conducted in this thesis was limited to the in-plane performance of rammed earth walls by using horizontal loading tests, however performing cyclic loading tests would be more close to reality. The out-of-plane behavior and the effects of openings (door and windows) for the case of the rammed earth should also be assessed. These features may have a strong influence on the behavior of rammed earth constructions and should be investigated in further studies.

Appendix

Appendix A. Strengthening rammed earth: old and new techniques

To improve the performance of earth material many studies have been conducted in the literature using different reinforcement techniques and materials. This paragraph intends to show some of these methods that are found in the literature.

In fact, due to its low cost, the rammed earth will continue to be used in many regions where most of these regions are situated in seismic areas. Therefore, to assure the safety of the occupants in case of seismic risk, the application of effective low-cost techniques can be applied and eventually the behavior of the walls could be more resisting if appropriate techniques that are compatible with the earth are used.

In a study of [6], it was suggested to reinforce rammed earth walls with vertical reinforcement like vertical rods or bamboo (Figure A.1) inside the wall, these bars should be connecting the foundation and a ring beam above the wall. [6] also mentioned the disadvantages of using horizontal reinforcement. This is mainly because the shear force cannot be transferred by the rods due the low bonding between these elements and earth material. On the second hand the presence of these elements can initiate the propagation of horizontal cracks and therefore damage the wall, and eventually, it is practically difficult to ram the wall in the presence of horizontal bars inside the framework.

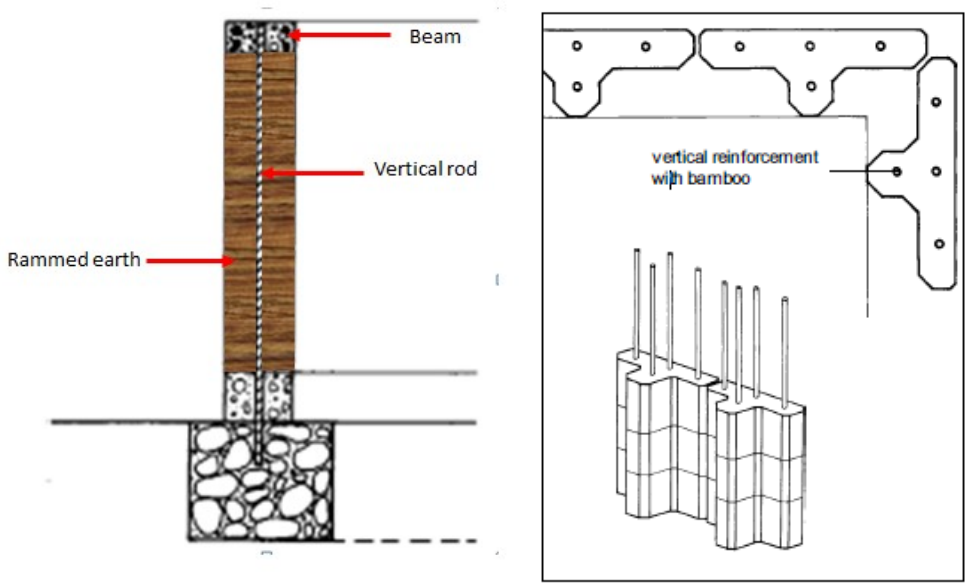

Figure A.1 The use of vertical rods as reinforcement for rammed earth walls proposed by Minke, 2001

In New Zealand, many construction details for the reinforcement of earth walls have been included in the standard. Specific details from the standard are shown in Figure A.1 where the rammed earth walls are reinforced using steel reinforcement and dowel connection. To resist out

of plane loading for longer walls the standard suggests using additional vertical reinforcing. Specific details from the standard are shown in Figure A.2

It is essential to mention that most of these proposed reinforcement techniques must be validated by further laboratory tests in order to adopt them as solutions for real house building and to test their effectiveness.

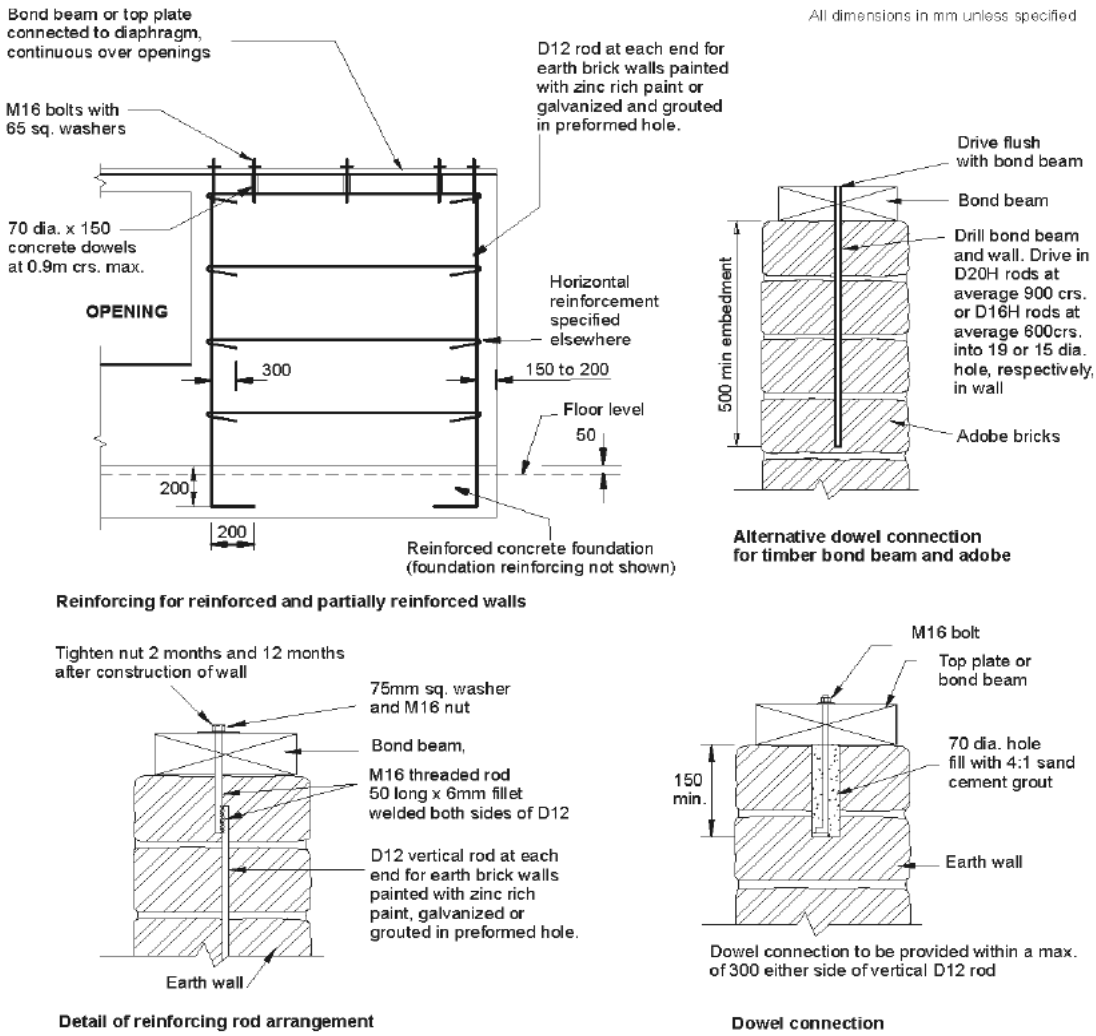

Figure A.2 Typical reinforced wall detail proposed by NZS 2499 Code

A.1. Laboratory testing of retrofitting techniques:

Some other researchers conducted experimental laboratory tests to prove the effectiveness of the reinforcement techniques. [135] proposed the post-tensioning rods as a technique of vertical reinforcement as shown in (Figure A.3). This method can be applied for new rammed earth building and can be considered easy to apply when compared to other techniques presented.

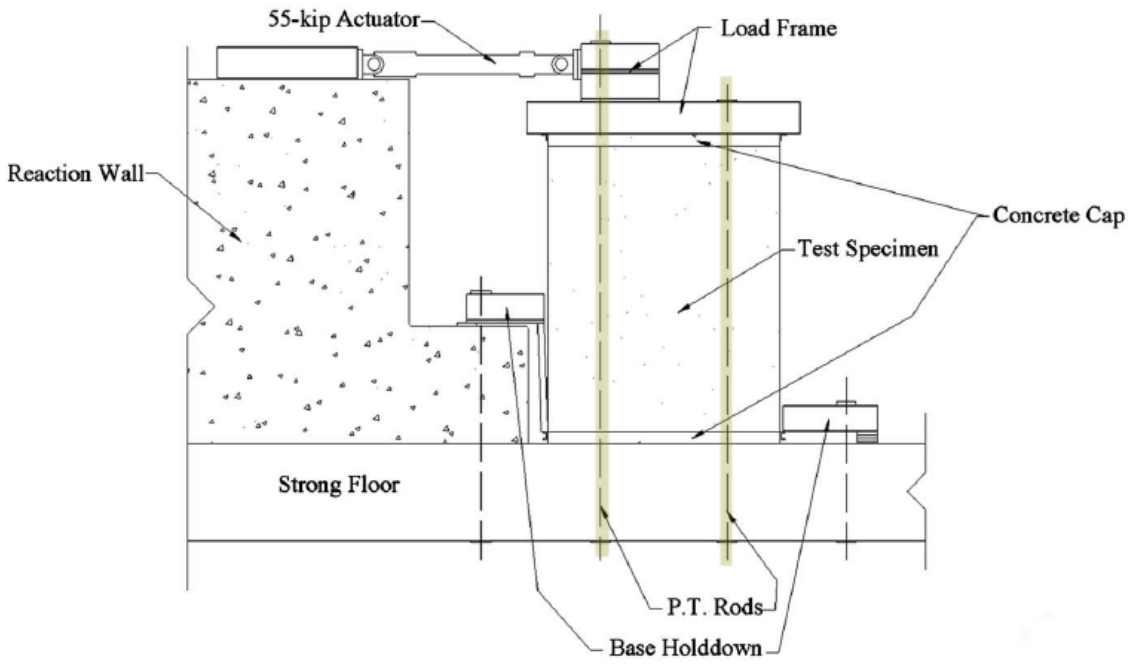

Figure A.3 Test setup and placement of post-tensioned rods [135]

Other researchers search for new methods that are applicable in the rural poor area and that can be used on existing and new building houses. For example in the study of [136] that showed the efficiency of the reinforcement with horizontal and vertical wire mesh strips on improving the mechanical capacity of the rammed earth wall panels to withstand seismic events. The mesh was covered with cement and sand mortar (Figure A.4).

In his study, the panels were tested under dynamic excitation using shake table (to simulate the seismic excitations). Results demonstrate that the specimen that was reinforced had fewer cracks and performed better in terms of load levels. However, the relevancy of these reinforcement techniques in the case of the real structure is still questionable.

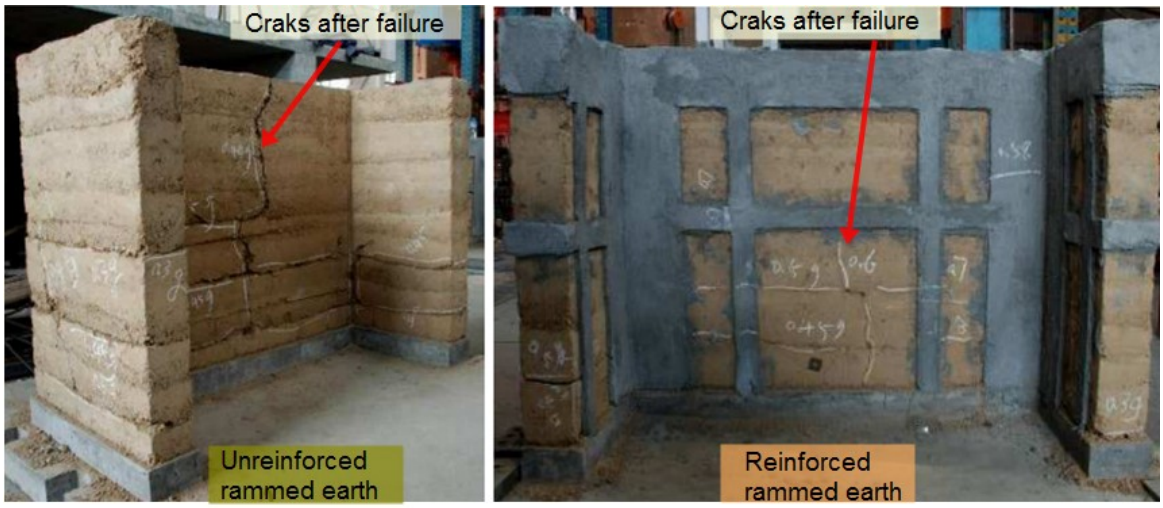

Figure A.4 Rammed earth panel without and with reinforcement after the test

Other methods intended to increase the soil strength by adding reinforcement material which has a high tensile strength as in [100]. In this study, they proposed a new retrofitting technique using externally bonded fiber materials to improve the mechanical behavior of the structure. First, they seek to find a suitable fiber material that is cost-effective and that is compatible with the rammed earth. Three type of fiber material was proposed (canvas, bamboo, and tarpaulin), these Fiber materials were chosen based on important features: the strength, workability, ductility, availability, and cost. Finally, the tarpaulin selected for this study after many laboratory tests. This retrofitting technique was validated through a set of experimental test for rammed earth walls under monotonic lateral loading. The walls were strengthened by bonding tarpaulin strips around the walls using different strengthening schemes, as in Figure A.5.

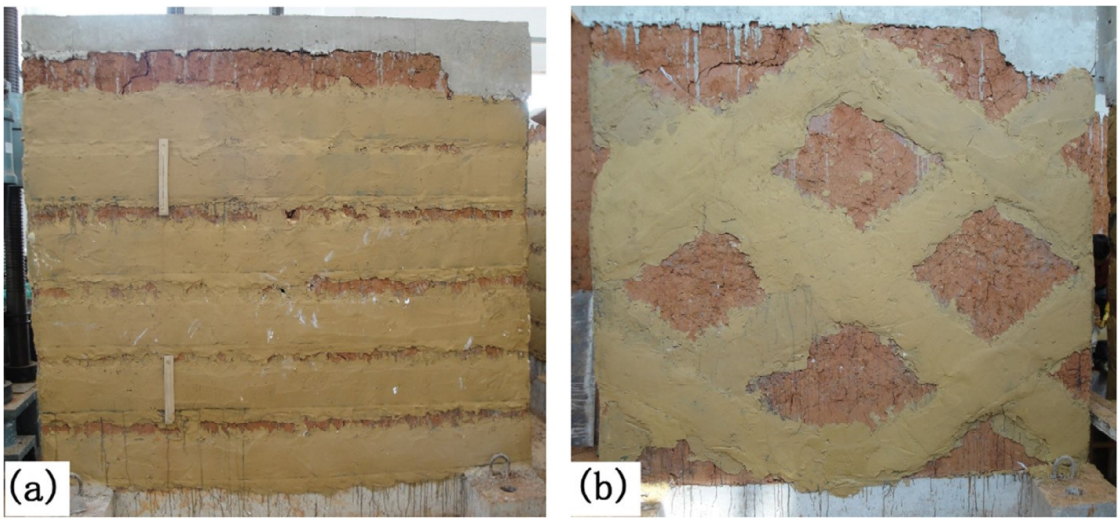

Figure A.5 Retrofitting scheme of the rammed earth wall: (a) horizontal direction; (b) diagonal direction

In a second recent study done by these authors [137], this technique was applied on a larger scale that consists of two rammed-earth model structures with and without reinforcement tested with the shaking table tests to simulate the dynamic response (Figure A.6).The results confirm that the proposed method can improve the dynamic behavior (seismic performance) of rammed earth structures by improving the load-bearing capability.

Figure A.6 Comparison of the damage between two models: (a) unreinforced model; (b)reinforced model

As for the crack pattern of the two models, significant improvement was obtained (Figure A.6). For the unreinforced model, diagonal cracks appeared that developed from the right of the lintel to the bottom of the cantilever beam along with some horizontal cracks parallel to the wooden lintel and other vertical cracks while the retrofitted model remained intact without visible cracks only a few roof tiles that fell. Furthermore, this technique can be used in rural areas where rammed earth structures are not designed to resist seismic forces.

Earth structures are also exposed to physical degradation and cracking development through time. These problems can be controlled by some strengthen techniques that can be applied to a group of elements that suffer from structural deficiencies. The most basic technique is filling the cracks using grout injection as shown by [138] that used this method on rammed earth walls. However, some problems can appear if the filling was not compatible with the earth and if the bonding properties were not adequate to the initial material.

Appendix B. Principal of the 7D

The DIC was used as a measurement technique to capture the failure process of rammed earth walls and specimens and to provide all the needed information about the displacement field for the corresponding structure.

Digital image correlation (DIC) is a method capable of measuring the deformation at a surface element. It allows, during solicitations, the measurement of the displacement field at the surface of a specimen by comparing a deformed image to a reference image [72]. The method consists in tracking a random speckle pattern on top of the surface using the recorded images. Different techniques are used to have a random speckle-like: spray painting or air brush.

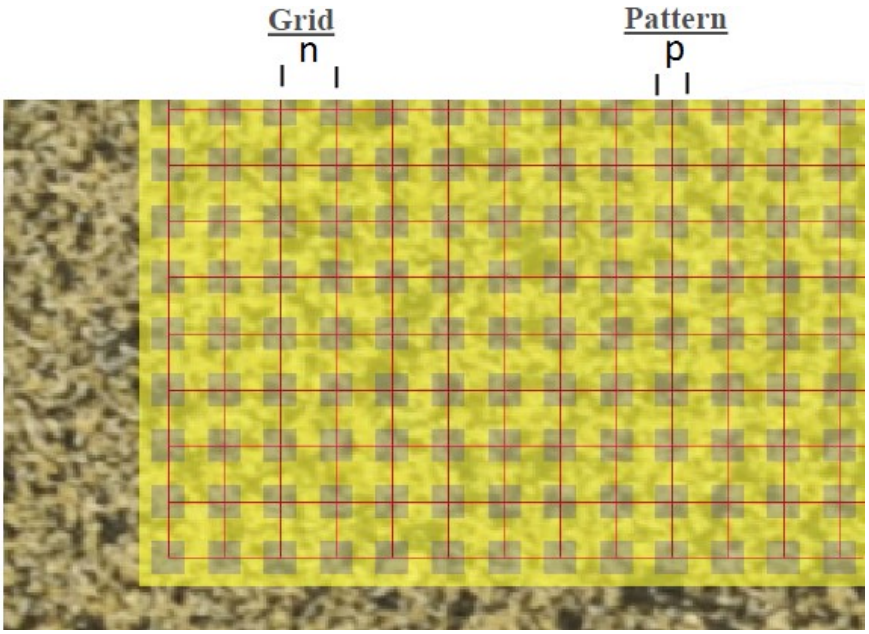

Figure B.1 Definition of the grid element and of correlation pattern [139]

We describe in this section the principle of the image correlation technique, including the specificities of the 7D software. This software is used to analyze the images recorded in our case.

On the reference image, the user defines an analysis area which is discretized into square elements whose side has a length adjustable by the user (as shown on Figure B.1). Therefore, a square grid element of side n is obtained (Figure B.1). This grid mesh allows locating the points where displacement fields will be calculated as shown in Figure B.2. Then the user defines a correlation pattern (squares analysis area of length p that is centered on each point of a grid element as shown in Figure B.2). The objective is to locate every point of the grid on the deformed image based on the comparison with the gray level. A correlation parameter is used as an indicator of the similarity degree between two patterns on the initial and final image. The gray

levels in the deformed image are obtained with bilinear or bi-cubic interpolations. An iterative procedure is adopted in the software to determine the field displacement. For the first iteration, an initial solution of each grid point A,B,C,D is estimated without changing the shape of the correlation pattern. These squares A,B,C,D will then become quadrilateral A_0,B_0,C_0,D_0 on the image that will be correlated. For the rest of iterations, the pattern is deformed in order to minimize the correlation parameter. This operation is repeated for each point in the grid. So the displacement field is determined at every point of the final image as in Figure B.2.

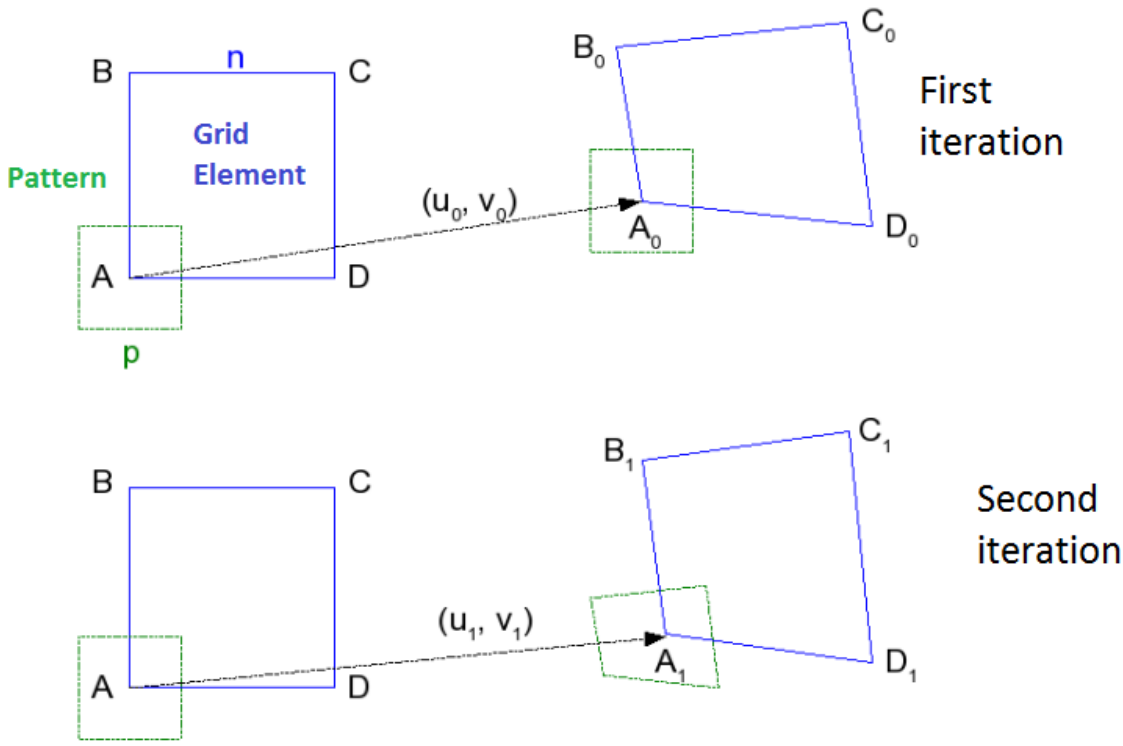

Figure B.2 Iterative process used by the 7D software to obtain the displacement field, according to [72]

Appendix C. Complementary results for the walls

C.1. Comparison of measurement with M3

Figure C.1 illustrates the comparison of the comparator M3 with image correlation for wall 2 (1.5m height), Figure C.2 for wall 3 (1.5m height) and Figure C.3 wall 3 (1m height). A good correspondence between the two measurements was observed. This proves the precision of the apparatus used and assures the accuracy of the results provided by the software 7D.

In general, we can neglect this difference (for example in Figure C.3) because it is mainly due to an error from the experimental setup of the placement of sensors. We can certainly proceed to use the results provided by the DIC.

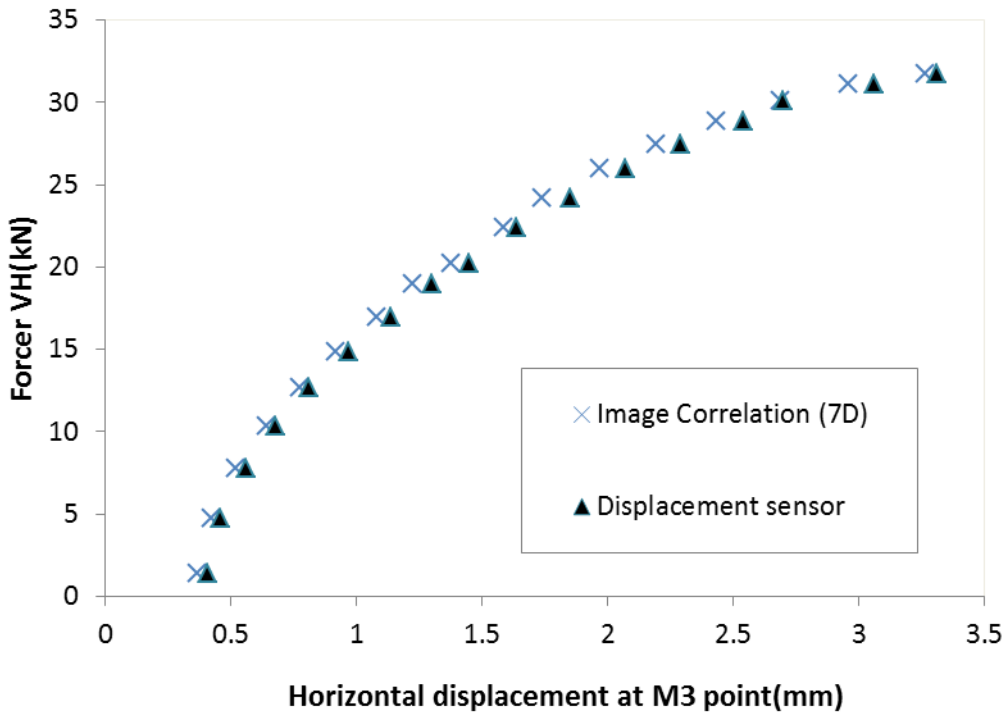

Figure C.4 Comparison between the displacement given by the image correlation and the displacement sensor in function of the horizontal force VH for wall 2

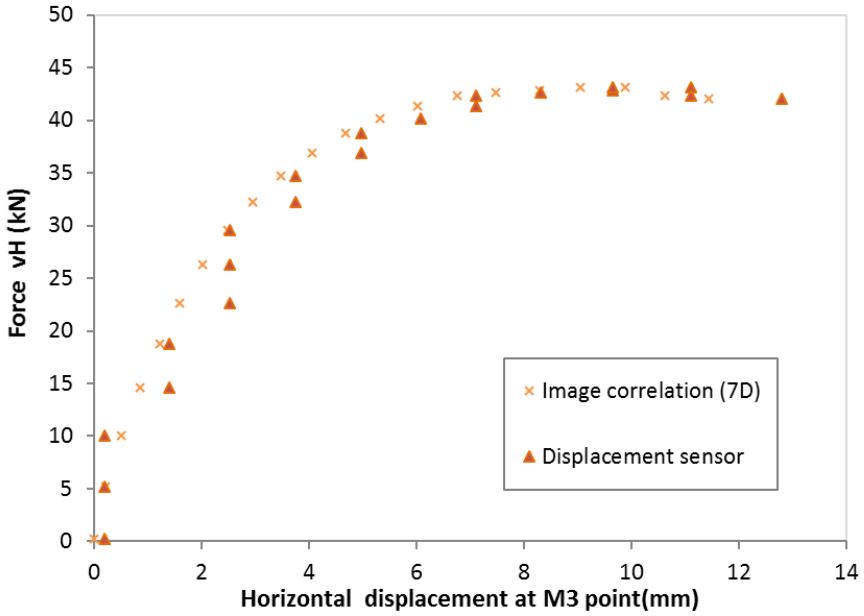

Figure C.5 Comparison between the displacement given by the image correlation and the displacement sensor in function of the horizontal force VH for wall 3

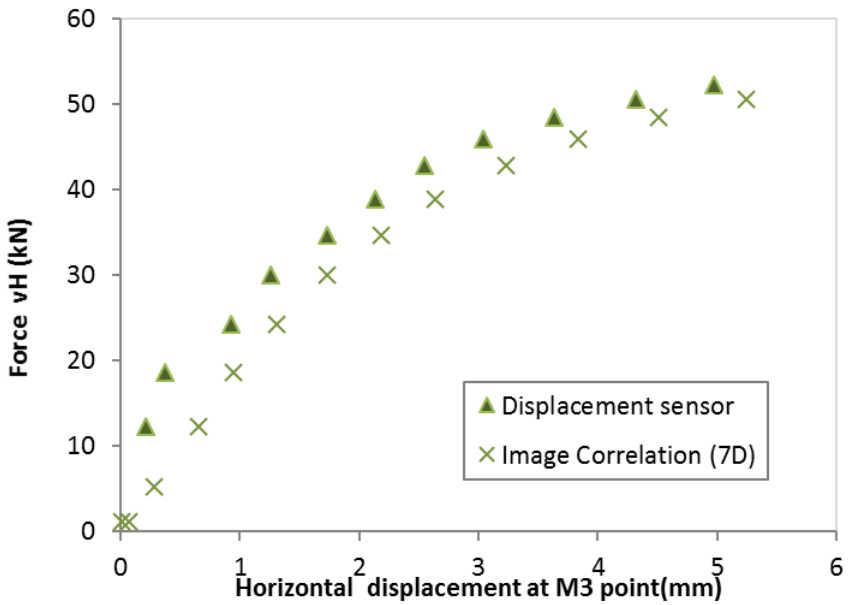

Figure C.6 Comparison between the displacement given by the image correlation and the displacement sensor in function of the horizontal force VH for wall 4

C.2. Vertical deformation during preloading phase

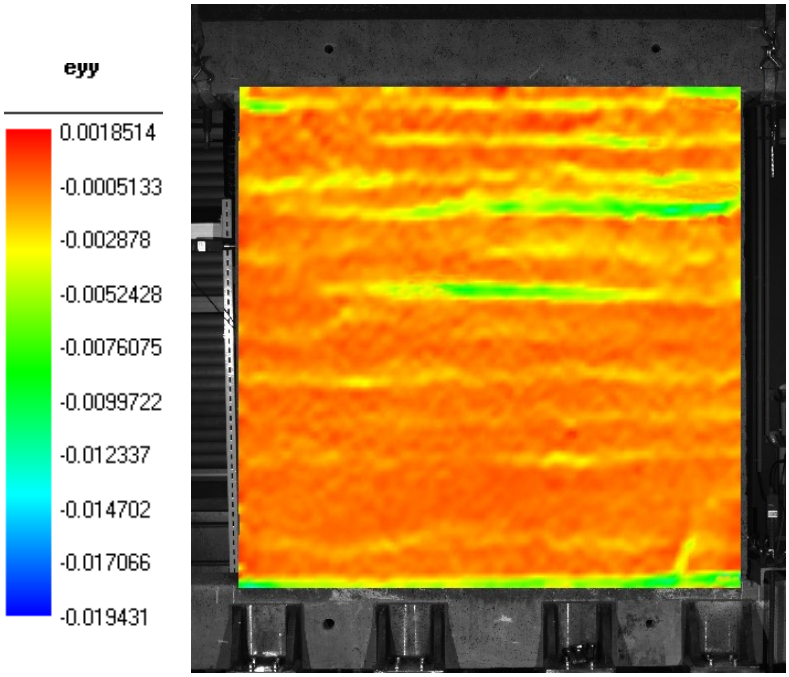

Figure C.7 Vertical deformation for wall 2 at the end of the preloading phase

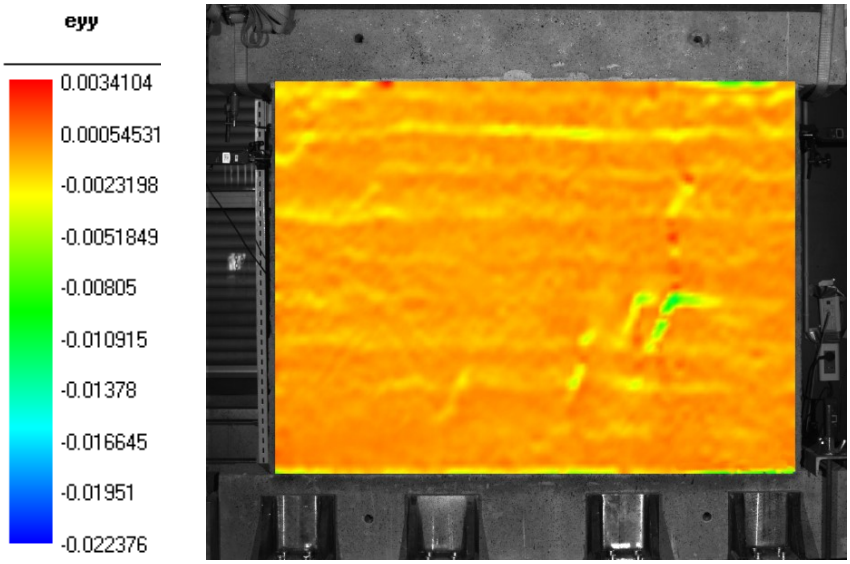

Figure C.8 Vertical deformation for wall 4 at the end of the preloading phase

Synthèse

Dans le contexte mondial de limitation du réchauffement climatique à moins de 2°C en dessous des températures préindustrielles, un enjeu majeur dans le développement est la réduction rapide des émissions de gaz à effet de serre, par le biais notamment d'une baisse de consommation énergétique. Or le secteur du bâtiment est l'un des plus énergivores avec, d'une part, une consommation courante liée à l'habitat qui représente environ 40% des dépenses énergétiques pour les pays européens et d'autre part, une énergie grise de construction très importante. Par ailleurs, la construction classique à base de béton fait face à une pénurie croissante de sable et de granulats, dont la demande explose mondialement (plus de 15 milliards de tonnes par an) en causant des situations à risque pour les populations (trafics, érosions accélérées des côtes, etc.). De ce fait, il devient nécessaire de se tourner vers des choix constructifs alternatifs permettant d'assurer un développement durable en limitant l'énergie grise de construction, en garantissant de bonnes performances énergétiques et en permettant au maximum le recyclage des matières premières.

La construction en pisé, technique ancienne selon laquelle de la terre crue est mise en place par damage de couches successives entre des banches semble pouvoir répondre à cette problématique. Bien qu'abandonné en France depuis le développement de l'utilisation du béton, ce procédé connait ainsi un regain d'intérêt. En effet, son coût en énergie grise est faible au cours de son cycle de vie et le matériau est entièrement et simplement recyclable [28]. De plus, les structures en pisé présentent l'avantage d'une bonne inertie thermique liée d'une part à une épaisseur généralement conséquente des murs monolithiques et d'autre part à l'hygroscopie du matériau terre où se condense et s'évapore successivement l'eau en fonction des variations de conditions extérieures [33].

Cependant, cette spécificité du matériau, notamment sa sensibilité à l'eau, ainsi que sa structure en couches de l'ordre de 15 cm, implique de bien comprendre le comportement mécanique de l'ensemble de la construction pour pouvoir établir les limites de résistance de l'ouvrage sous différentes sollicitations. La performance de ces structures a déjà été analysée en termes de durabilité sous des conditions climatiques [49] et de résistance en compression ([14], [60]). Cependant la réponse sous des sollicitations de cisaillement reste à étudier.

Le travail de cette thèse concerne les aspects mécaniques, liés aux comportements des structures en pisé. Un intérêt particulier a été donné au mécanisme de rupture et aux propriétés mécaniques du matériau.

L'objectif est principalement de déterminer le comportement d'un mur en pisé ; à l'échelle semi réelle, sous une poussée progressive horizontale, cette direction de sollicitions étant caractéristique d'un chargement sismique. L'étude se limite à des conditions statiques. Le principal objectif de cette étude expérimental est alors d'analyser le comportement d'un mur en pisé lorsqu' il est soumis à des efforts de cisaillement dans son plan. Les analyses par corrélation d'images numériques ont, de manière générale, été utilisé pour analyser les modes de ruptures.

Sous quelle forme la rupture a-t-elle lieu dans les murs sous un chargement horizontal ? La mise en œuvre par couche successive horizontale réduit-t-elle la résistance globale de la structure ? Quels sont les paramètres principaux qui contrôlent les comportements mécaniques ? Est-il possible de modéliser simplement de tels comportements mécaniques à l'échelle d'un mur ? Somme nous capable d'estimer, à partir des essais, le comportement sismique de ce type de structure selon l'Eurocode 8 ?

C'est à ces questions que ces travaux proposent de répondre grâce à une approche expérimentale et numérique.

Etude à l'échelle du matériau

Le but des expériences faites dans la première partie de cette thèse est d'acquérir une connaissance sur le comportement mécanique du matériau pisé à travers des essais de compression simple et des essais de cisaillement direct.

La terre utilisée dans cette thèse a été fournie par un artisan professionnel, et provient de "Dagneux", (village situé dans la région Rhône-Alpes dans le sud-est de la France) après la démolition d'une ancienne ferme.

La terre utilisée est composée de :

- 15% de sable (2 - 0,06 mm)

- 65% de limon (60 à 2 µm)

- 20% d'argile (<2 µm)

Dans cette première étude, le sol utilisé a été évalué d'abord en réalisant un essai de compression sur des échantillons cylindriques et prismatiques (Figure 2.11 et Figure 2.12). Les échantillons cylindriques ont un diamètre de 20 cm et une hauteur de 40 cm et les échantillons prismatiques mesurent 25 cm x 25 cm x 50 cm. Les dimensions de ces échantillons ont été choisies pour reproduire l'énergie de compaction appliquée sur les murs pendant la fabrication A partir des résultats des tests de compression (Table 2.2), on a constaté qu'il existait une variation significative de la performance du matériau en fonction des géométries sélectionnées de l'échantillon (éprouvettes cylindriques ou prismatiques). La résistance à la compression était supérieure dans le cas de l'éprouvette cylindrique.

Tableau 6 Résultats des tests de compression non confinés

Géométrie	Dimensions de l'échantillon (cm)	Résistance en compression (MPa)
Prismatique	25 × 25 × 50	1.15
Cylindrique	d=20, h= 40	2

Ces résultats sont similaires à d'autres résultats trouvés dans la littérature. L'analyse de la corrélation d'image a mis en évidence une plus grande déformation à l'interface entre les couches et, dans certains cas, l'initiation de fissures dans cette zone.

Dans un deuxième temps les paramètres de cisaillement (cohésion et angle de frottement) du sol utilisé ont également été étudiés au moyen de tests expérimentaux à l'intérieur d'une couche du pisé et à l'interface. La caractérisation mécanique des paramètres de cisaillement a été obtenue par expérimentations à la boite de Casagrande à grande échelle de 0,49 m x 0,49 m x 0,45 m de hauteur et pour deux états du matériau (à l'interface entre deux couches et au milieu d'une couche). Trois spécimens différents ont été fabriqués dans cette boite de cisaillement puis testés avec un chargement vertical différent. Les dimensions de cette boite ont été choisies pour reproduire l'énergie de compactage appliquée sur les murs pendant la fabrication.

Des essais standard de cisaillement direct (boite de Casagrande classique) ont également été réalisés sur deux types d'échantillons : des prélèvements effectués à la partie supérieure d'une couche de terre (proche de l'interface) et des échantillons prélevés dans la partie médiane (milieu d'une couche).

A partir de la grande boite de cisaillement, les résultats montrent que l'interface entre les couches a des propriétés mécaniques plus faibles liées à la plus faible densité dans cette zone. Les résultats montrent aussi, que ce matériau de construction se comporte comme un sol non saturé pour lequel la succion est un paramètre d'état.

Concernant les petites boites de cisaillement, les résultats montrent que les propriétés mécaniques du pisé évoluent au cours du temps, de telle sorte que la cohésion et le frottement sont plus élevés sur des murs plus anciens (Tableau 2).

Tableau 7 Résultat de petite et grande boite

Type d'essai	**Dimension (cm)**	**Angle de frottement (◦)**		**Cohésion (kPa)**		**Teneur en eau test (%)**
Grande boite de cisaillement	49 x 49 x 36	Couche	Intérface	Couche	Intérface	4-6
		35.3	32.9	30.3	24.7	
Petite boite de cisaillement	10 x 10 x 3.5	Haut de Couche	Milieu de couche	Haut de Couche	Milieu de couche	2-2.5
		44.1	45.6	263	135	

Etude à l'échelle du Mur

L'objectif de cette partie est principalement de déterminer le comportement d'un mur en pisé, à échelle réelle, sous une poussée progressive horizontale, cette direction de sollicitation étant caractéristique d'un chargement sismique selon l'Eurocode 8.

Analyse Expérimentale

Procédure

Quatre murs en pisé ont été construits successivement en laboratoire (les numéros 1 à 4 correspondent à l'ordre de réalisation) selon 2 géométries :

2 murs (n°2 et 3) avec : H=1.5 m (hauteur), L=1.5 m (longueur) et e=0.25 m (épaisseur)

2 murs (n°1 et 4) avec : H= 1 m, L=1.5 m et e=0.25 m.

Les dimensions ont été choisies telles qu'elles soient représentatives de murs à l'échelle ½ de bâtiment à 1 niveau (hauteur autour 3 m et épaisseur de 50 cm). L'influence de l'élancement H/L vise à être testée par le choix de ces 2 géométries. Chacun de ces murs est construit au-dessus d'une poutre en béton H=0.25m, e=0,25m et L= 1,8m. La mise en place est faite par des couches de terre d'une hauteur moyenne de 15cm, damées grâce à une dameuse pneumatique. Les banches sont ensuite retirées et les murs laissés à sécher pendant 2 mois en laboratoire (20°C et HR=60%). La teneur en eau des murs au moment des tests était de 3%. Une deuxième poutre en béton surmonte chaque mur, une couche de mortier de chaux étant disposée entre le mur et la poutre pour améliorer la liaison terre-béton (Figure 3.14)

Le test consiste à appliquer, sous une charge verticale représentant la descente de charges des planchers et de la toiture, une poussée horizontale progressive en tête du mur. La charge verticale est appliquée dans un premier temps avec un taux de 1kN/s par 2 vérins hydrauliques (VE1 et VE2 sur la Figure 3.14). Ceux-ci sont appliqués sur une poutre acier UPN séparée de la poutre béton au sommet du mur par un système de roulement (Figure 3.14), ce qui autorise un déplacement horizontal de la poutre en béton pendant la poussée horizontale. La charge verticale de 60kN étant atteinte (équivalent à une contrainte verticale de 0.3MPa), elle est maintenue constante pendant qu'un vérin horizontal applique la poussée horizontale progressive sur la poutre béton en sommet de mur (VH sur la Figure 3.14). Un contrôle en déplacement est choisi avec une vitesse de 1mm/min appliquée jusqu'à la rupture. La poutre en béton en base du mur est mise en butée (en bas à gauche) pour éviter le glissement et maintenue par des tirants (en bas à droite) pour éviter le soulèvement de la poutre. Des capteurs de déplacement verticaux et horizontaux (M1 et M2 sur la Figure 3.14) sont installés pour vérifier s'il y a un soulèvement de la poutre BA à la base. Le déplacement horizontal global est mesuré pendant l'essai par un capteur placé sur le mur (M3 sur Figure 3.14). En parallèle, l'une des faces du mur est filmée avec une caméra (précision : 16 million pixels) afin de suivre l'évolution du champ de déplacement en surface de la structure par corrélation d'images. Les bases théoriques de cette méthode ainsi que le logiciel utilisé sont présentés par Vacher et al. [73].

Résultats et analyse

La Figure 3.24 présente pour les 4 murs l'évolution de la force horizontale appliquée en fonction du déplacement horizontal mesuré par corrélation d'image entre la première et la dernière image. Les déplacements fournis par le capteur intégré dans un vérin horizontal sont similaires mais moins précis dû aux jeux du piston et à la rigidité du système de chargement. Ce graphe (Figure 3.24) fait apparaître pour les 4 murs un comportement non fragile post-rupture. Il est important de noter qu'aucun des murs ne s'est effondré après la rupture et notamment que tous ont pu être déplacés hors du portique de chargement sans dommage.

La rigidité initiale est similaire pour les murs n°2 et 3 (H=1.5m). Cependant, alors qu'une rigidité supérieure est attendue pour les murs n°1 et 4 (H=1m) du fait d'un bras de levier plus faible de la force horizontale, seul le mur n°4 vérifie ce comportement, le mur n°1 ayant une raideur similaire aux murs de 1.5 m. De même, les murs n° 2 et 3 (H=1.5m) présentent des réponses similaires en termes d'effort horizontal à la rupture et de comportement ductile post-pic, mais pour H=1m (c'est-à-dire pour un moment de flexion plus faible), seul le mur 4 présente un effort maximal supérieur, alors que la valeur maximale du mur 1 est équivalente à celles des murs de 1.5m de hauteur. Le mur n°1 ayant été le premier construit et testé, il est possible que les conditions de fabrication ou de test aient été moins bien maitrisés que les autres murs. Ce résultat montre aussi l'influence des conditions de fabrication du pisé - qui n'est pas un matériau industriel – sur sa performance vis-à-vis des sollicitations horizontales.

La Figure 3.41 et Figure 3.42 présente, pour le mur n°2 et n°3 (H=1.5m), l'évolution du déplacement au sommet latéral droit du mur au cours de l'essai de poussée progressive, ainsi que l'évolution des fissures identifiée par la corrélation d'images. Les valeurs maximales de déplacement correspondant ici à de la fissuration, il apparaît 2 orientations privilégiées de fissures, pour ces murs ainsi que pour les 2 autres murs. La fissuration diagonale du mur correspondant à la bielle de compression de la structure chargée et une autre qui est la direction horizontale à l'interface entre les couches damées. Cette fissuration montre une résistance légèrement moindre des interfaces. Cependant, la fissuration entre les couches apparaissant pour 85% du chargement maximal, cette résistance peut être considéré comme acceptable.

Analyse numérique

L'objectif de cette partie est de réaliser un modèle numérique préliminaire d'un mur de pisé sous poussée progressive.

Présentation du modèle

L'expérience de poussée progressive vise à être modélisée, grâce au Code_Aster, pour le cas H=1,5m. La Figure 4.8 rappelle la géométrie de la structure testée avec le mur en pisée et les 2 poutres béton, ainsi que les conditions de chargement (contrainte verticale de 0.3MPa et poussée progressive en tête). Un encastrement est considéré à la base. Le mur est modélisé par 12 couches de pisé de 12cm chacune et par une fine couche de matière d'un centimètre (prénommée par la suite 'interface') entre les différentes couches. Bien que l'introduction d'un gradient progressif de densité par couche soit la manière la plus réaliste de représenter le mur en pisé la

modélisation de l'alternance entre 2 couches de propriétés différentes est la manière la plus simple de prendre en compte le caractère périodique du mur en pisé. L'épaisseur de la couche « interface » a été choisi après des observations et suite à l'analyse d'images Cette modélisation, permet de pouvoir considérer chaque couche et chaque interface avec des paramètres différents.

Le comportement du béton est considéré élastique ; celui du pisé est considéré élasto-plastique avec une loi associée de type Drucker-Prager dont les paramètres les plus importants restent la cohésion et l'angle de frottement. Dans cette partie l'influence de la cohésion et du frottement a été étudié. Ces paramètres ont été adaptés pour le pisé (après analyse des essais de cisaillement) en comparant les résultats expérimentaux et numériques des murs. En général, les résultats numériques (après calibration des paramètres) montrent un bon accord avec les résultats expérimentaux en termes de rigidité initiale et de déplacement au début de la plasticité. Au-delà de la phase élastique, l'étude montre les limites du modèle en particulier dans la production d'une évolution moins progressive entre le comportement élastique et le comportement plastique

Evaluation parasismique

Dans la partie finale de la thèse, l'évaluation des résultats expérimentaux (à l'échelle muret) a été réalisée en utilisant la méthodologie *pushover* selon l'Eurocode 8. L'évaluation de chaque mur a été réalisée sur la base d'une proposition des états limites d'endommagement.

Sur la base de l'observation de Calvi sur des murs de maçonnerie, nous avons défini un ensemble d'états limites locaux basés sur l'apparition de la fissuration. Ces états limites ont ensuite été quantifiés (Figure 5.8) en observant le comportement de chaque murs testée et l'évolution de la largeur de fissuration, Sur la base de ces données, on a examiné la performance d'un mur à 1'échelle 1 sous différentes accélérations du sol. Les résultats ont montré que les murs en pisé étudiés présentent une performance mécanique satisfaisante pour des zones de séismicité basse à moyenne avec un sol de type A (sol rocheux). Pour les sols de type B (Bon sol) les résultats acceptables n'ont été trouvés que pour des zones de sismicité très faibles à modérés.

Pour conclure, le travail de thèse regroupe une mise en évidence expérimentale du comportement du matériau, à plusieurs échelles. Cette compréhension du pisé du point de vue mécanique est essentielle pour assurer la conservation du patrimoine bâti mais aussi des constructions neuves. Le travail dans cette thèse contribue alors à la connaissance de la réponse des murs de pisé non stabilisées. Le comportement de ces structures sous ce type de chargement est une préoccupation majeure qui peut améliorer l'évaluation de leur performance mécanique en cas d'action sismique. Enfin, il convient de noter que l'étude menée dans cette thèse est limitée aux performances en plan et utilise des chargements horizontaux. Il n'a pas été tenu compte d'un comportement hors plan ou d'un quelconque effet des ouvertures (fenêtres et portes) sur le comportement mécanique.

Ces éléments ont une forte influence sur le comportement des constructions en pisé et devraient être pris en compte dans une prochaine étude.

List of publications

International Journal

El-Nabouch, R., Bui, Q. B., Plé, O. and Perrotin, P., Assessing the in-plane seismic performance of rammed earth walls by using horizontal loading tests. *Engineering Structures*, vol.*145*, pp.153-161, 2017

Publication in Proceedings of International Conferences

El Nabouch, R., Bui, Q. B., Plé, O. Perrotin, P. and Plassiard, J.P., Numerical modeling of rammed earth constructions: Analysis and recommendations. In 1st International Conference on Bio-based Building Materials, pp. 21-24, 2015

El Nabouch, R., Bui, Q. B., Plé, O., Perrotin, P., Poinard, C., Goldin, T. and Plassiard J.P., Seismic assessment of rammed earth walls using pushover tests. *Procedia Engineering*, vol.*145*, pp.1185-1192, 2016

El-Nabouch, R., Bui, Q. B., Perrotin, P. and Plé, O., Experimental and Numerical Studies on Cohesion and Friction Angle of Rammed Earth Material. In *Poromechanics VI*, pp. 864-872, 2017

National Conferences

El Nabouch, R., Bui, Q. B., Perrotin, P., Plé, O. and Plassiard, J. P., "Modélisation numérique de structures en pisé: analyses et recommandations." In *Rencontres Universitaires de Génie Civil,* 2015

El Nabouch, R., Bui, Q. B., Prime. N., Perrotin P, Plé, O., and Plassiard, J. P., Evaluation de la performance parasismique dans le plan de murs en pisé,". In Constructions en terre crue: avancées scientifiques, LOCIE, Université Savoie mont blanc, Chambéry, 17th-18th March 2016

El Nabouch R., Bui Q. B., Prime N., Perrotin P., Plé O., Poinard C., Goldin T., Plassiard J. P., Jaffre M., Teytu L., Comportement de murs en pisé sous poussée progressive : études expérimentales et numériques, RUGC16, 25-27 mai 2016

References

[1] H. Schroeder, "Modern earth building codes, standards and normative development," Germany: Bauhaus University Weimar, 2012.

[2] E. Avrami, H. Guillaud, and M. Hardy, *Terra literature review. An overview of research in earthen architecture conservation.* Los Angeles: The Getty Conservation Institute, 2008.

[3] H. Houben and H. Guillaud, *Earth Construction: A Comprehensive Guide.* London, United Kingdom: CRATerre – EAG, Intermediate Technology Publication, 2008.

[4] E. Hamard, B. Cazacliu, A. Razakamanantsoa, and J. C. Morel, "Cob, a vernacular earth construction process in the context of modern sustainable building," *Build. Environ.*, vol. 106, pp. 103–119, Sep. 2016.

[5] T. Graham, "Wattle and daub: craft, conservation and Wiltshire case study," Master thesis, University of Bath, United Kingdom, 2004.

[6] G. Minke, "Construction manual for earthquake-resistant houses built of earth." GATE - BASIN (Building Advisory Service and Information Network, 2001.

[7] D. Silveira, H. Varum, A. Costa, T. Martins, H. Pereira, and J. Almeida, "Mechanical properties of adobe bricks in ancient constructions," *Constr. Build. Mater.*, vol. 28, no. 1, pp. 36–44, Mar. 2012.

[8] I. Gomes, "Earthquake-Resistant Construction with Raw Earth.," Msc. Thesis, Instituto Superior Técnico, Lisbon, Portugal. (in Portuguese), 2008.

[9] V. Burlaco, "Earth- A new look for an old material." 2011.

[10] H. Guillaud, *Marrakech 87 Habitat en terre*. Grenoble: CRAterre., 1987.

[11] B. Pignal, *Terre crue - Techniques de construction et de restauration*. Eyrolles, 2005.

[12] M. Hall and Y. Djerbib, "Rammed earth sample production: context, recommendations and consistency," *Constr. Build. Mater.*, vol. 18, no. 4, pp. 281–286, May 2004.

[13] P. Jaquin, "History of earth building techniques," in *Modern Earth Buildings*, Elsevier, 2012, pp. 307–323.

[14] V. Maniatidis and P. Walker, "Structural Capacity of Rammed Earth in Compression," *J. Mater. Civ. Eng.*, vol. 20, no. 3, pp. 230–238, 2008.

[15] A. Lozano, J. M. Lozano, and A. R. Taroncher, "Energy rehabilitation of buildings of earthen construction," in *Rammed Earth Conservation : Proceedings of the first International Conference on Rammed Earth Conservation, Restapia 2012, Valencia, Spain, 21-23 de june 2012, 2012, ISBN 978-0-415-62125-0, págs. 675-680*, 2012, pp. 675–680.

[16] A. Dorothée, "Petit guide des Architectures en pisé à Lyon.," ENSAL, Lyon, Technical report, 2011.

[17] P. Walker, R. Keable, J. Martin, and V. Maniatidis, *Rammed earth : Design and construction guidelines.* BRE Bookshop, 2005.

[18] Collectif FFB, *Règles professionnelles pour la mise en oeuvre des enduits sur supports composés de terre crue.* Recherche et développement métier, 2012.

[19] H. Morris and R. Walker, "Modern and historic earth buildings: Observations of the 4th September 2010 Darfield earthquake," in *Proceedings of the Ninth Pacific Conference on Earthquake Engineering Building an Earthquake-Resilient Society*, Auckland, New Zealand, 2011.

[20] B. V. Venkatarama Reddy and P. Prasanna Kumar, “Embodied energy in cement stabilised rammed earth walls,” *Energy Build.*, vol. 42, no. 3, pp. 380–385, Mar. 2010.
[21] T. T. Bui, Q. B. Bui, A. Limam, and S. Maximilien, “Failure of rammed earth walls: From observations to quantifications,” *Constr. Build. Mater.*, vol. 51, pp. 295–302, Jan. 2014.
[22] M. Rauch, “Earth house with european standard : A review of the project ”rammed earth house” by the company lehm ton erde baukunst gmbh (soil clay earth building art ltd.) in schlins, austria.,” in *International Symposium on Earthen Structures*, Bangalore, India, 2007, pp. 47–52.
[23] H. Niroumand, M. F. M. Zain, and M. Jamil, “A guideline for assessing of critical parameters on Earth architecture and Earth buildings as a sustainable architecture in various countries,” *Renew. Sustain. Energy Rev.*, vol. 28, pp. 130–165, Dec. 2013.
[24] L. Pérez-Lombard, J. Ortiz, and C. Pout, “A review on buildings energy consumption information,” *Energy Build.*, vol. 40, no. 3, pp. 394–398, 2008.
[25] M. K. Dixit, J. L. Fernández-Solís, S. Lavy, and C. H. Culp, “Identification of parameters for embodied energy measurement: A literature review,” *Energy Build.*, vol. 42, no. 8, pp. 1238–1247, Aug. 2010.
[26] F. Pacheco-Torgal and S. Jalali, “Earth construction: Lessons from the past for future eco-efficient construction,” *Constr. Build. Mater.*, vol. 29, pp. 512–519, Apr. 2012.
[27] C. Thormak, “The effect of material choice on the total energy need and recycling potential of a building,” *Build Environ*, vol. 41, p. 1019=102, 2006.
[28] J. C. Morel, A. Mesbah, M. Oggero, and P. Walker, “Building houses with local materials: means to drastically reduce the environmental impact of construction,” *Build. Environ.*, vol. 36, no. 10, pp. 1119–1126, Dec. 2001.
[29] M. Krayenhoff, *Techno-economic analysis and environmental assessment of stabilized insulated rammed earth (SIREWALL) building*. 2012.
[30] U. Röhlen, and C. Ziegert, “Construire en terre crue – Construction – Rénovation – Finition,” Le Moniteur, Paris, 2013.
[31] CSIRO, “Mud walls give poor insulation.,” Technical report, 2000.
[32] P. Taylor and M. B. Luther, “Evaluating rammed earth walls: a case study,” *Sol. Energy*, vol. 76, no. 1–3, pp. 79–84, Jan. 2004.
[33] L. Soudani *et al.*, “Assessment of the validity of some common assumptions in hygrothermal modeling of earth based materials,” *Energy Build.*, vol. 116, pp. 498–511, Mar. 2016.
[34] H. Houben and H. Guillaud, “Traité de construction en terre.” Editions Parenthèses, 2006.
[35] C. Beckett and D. Ciancio, “A review of the contribution of thermal mass to thermal comfort in rammed earth structures,” in *ResearchGate*, 2012.
[36] H. Houben and H. Guillaud, *Earth Construction, A comprehensive Guide.* London, UK: Intermediate Technology Publications, 1994.
[37] P. A. Chabriac, “Pierre-Antoine Chabriac. Mesure du comportement hygrothermique du pisé. PhD thesis,” ENTPE, Université de Lyon, France, 2014.
[38] PassivAct, “Qualité thermique comparées des matériaux, 2012.” 2012.
[39] W. L. Paul and P. A. Taylor, “A comparison of occupant comfort and satisfaction between a green building and a conventional building,” *Build. Environ.*, vol. 43, no. 11, pp. 1858–1870, Nov. 2008.
[40] Standards Australia, *The Australian Earth Building Handbook*. Sydney, Australia: Australia: Standards Australia, 2002.
[41] NZS 4297, “Engineering design and earth buildings –establishes performance criteria for mechanical strength, shrinkage, durability, and thermal insulation and fire resistance,” New Zealand, 1998.

[42] NZS 4298, "Materials and workmanship for earth buildings – defines requirements for materials and workmanship," New Zealand, 1998.
[43] NZS 4299, "Earth buildings not requiring specific design.," New Zealand, 1998.
[44] J. Tibbets, *Emphasis on rammed earth—The rational. Interaméricas Adobe Builder, 2001, 9, 4-33.*, vol. 9. 2001.
[45] Keable, *Rammed earth structures. A code of practice*. London, UK: Intermediate Technology, 1996.
[46] IS 2110, *Code of practice for in situ construction of walls in buildings with soilcement.* New Delhi, India: Bureau of Indian Standards, 2002.
[47] ASTM E2392/E2392M-20, *Standard guide for design of earthen wall building systems*. West Conshohocken (PA), 2010.
[48] D. Ciancio, P. Jaquin, and P. Walker, "Advances in the assessment of soil suitability for rammed earth," *Constr. Build. Mater.*, vol. 42, pp. 40–47, May 2013.
[49] Q. B. Bui, J. C. Morel, B. V. Venkatarama Reddy, and W. Ghayad, "Durability of rammed earth walls exposed for 20 years to natural weathering," *Build. Environ.*, vol. 44, no. 5, pp. 912–919, May 2009.
[50] J. Desrues and B. Duthilleul, "Stereophotogrametric method applied to the determination of plane strain fields.," *Journal de Mecanique Theorique et Appliquee*, vol. 3, p. 79–103., 1984.
[51] P. Walker, *Standards Australia*. Sydney, Australia: The Australian Earth Building Handbook, 2002.
[52] M. Olivier, "Le materiau terre, compactage, comportement, application aux structuresen blocs de terre.," INSA de Lyon, 1994.
[53] J. C. Morel, A. Pkla, and P. Walker, "Compressive strength testing of compressed earth blocks," *Constr. Build. Mater.*, vol. 21, no. 2, pp. 303–309, Feb. 2007.
[54] M. F. Attom, "The effect of compactive energy level on some soil properties," *Appl. Clay Sci.*, vol. 12, no. 1, pp. 61–72, Jun. 1997.
[55] C. H. Kouakou and J. C. Morel, "Strength and elasto-plastic properties of non-industrial building materials manufactured with clay as a natural binder," *Appl. Clay Sci.*, vol. 44, no. 1–2, pp. 27–34, Apr. 2009.
[56] A. Mesbah, J. C. Morel, and M. Olivier, "Clayey soil behaviour under static compaction test," *ResearchGate*, vol. 32, no. 9, pp. 687–694, Nov. 1999.
[57] M. Olivier and A. Mesbah, "Le matériau terre Essai de compactage statique pour la fabrication de briques de terre compressées," *Bull Liaison Lab Ponts Chaussée*, vol. 146, pp. 37–43, 1986.
[58] ASTM Standards, "ASTM C 165 - Standard Test Method for Measuring Compressive Proper- ties of Thermal Insulations .," ASTM, West Conshohocken, United States, 2000.
[59] D. Lilley and J. Robinson, "Ultimate strength of rammed earth walls with opennings," in *Proc ICE: Struct Build*, 1995, vol. 110(3), pp. 278–287.
[60] Q. B. Bui, J. C. Morel, S. Hans, and N. Meunier, "Compression behaviour of non-industrial materials in civil engineering by three scale experiments: the case of rammed earth," *Mater. Struct.*, vol. 42, no. 8, pp. 1101–1116, Oct. 2008.
[61] L. Miccoli, U. Müller, and P. Fontana, "Mechanical behaviour of earthen materials: A comparison between earth block masonry, rammed earth and cob," *Constr. Build. Mater.*, vol. 61, pp. 327–339, Jun. 2014.
[62] Q. B. Bui and J. C. Morel, "First Exploratory Study on the Ageing of Rammed Earth Material," *Materials*, vol. 8, no. 1, pp. 1–15, Dec. 2014.
[63] Q. B. Bui, J. C. Morel, S. Hans, and P. Walker, "Effect of moisture content on the mechanical characteristics of rammed earth," *Constr. Build. Mater.*, vol. 54, pp. 163–169, Mar. 2014.

[64] British Standard BS1377, "BS 1377-2: 1990 soils for civil engineering purposes – part 2: classification." London:BSI, 1990., 1990.
[65] C. A. Schrader, "Rammed Earth Construction: A Re-Emerging Technology," *Proc Annu Meet - Am Sect Int Sol Energy Soc U. S.*, vol. 6, Jan. 1981.
[66] A. Arrigoni *et al.*, "Reduction of rammed earth's hygroscopic performance under stabilisation: an experimental investigation," *Build. Environ.*, vol. 115, pp. 358–367, Apr. 2017.
[67] U.S. Geological Survey, "A Laboratory Manual for X-Ray Powder Diffraction," Open-File Report 01-041, 2001.
[68] W. Wu, T. G. Berhe, and T. Ashour, *Chapter 20: Embankments and dams - Modern Earth Buildings*. University of Natural resources and Applied Life sciences, Austria, 2012.
[69] J. Keable, "Rammed Earth Standards." ODA Final Project Report R 4864C., 1994.
[70] AFNOR, "NF P94-093 - Sols : reconnaissance et essais - Détermination des références de compactage d'un matériau - Essai Proctor Normal - Essai Proctor modifié.," 1999.
[71] AFNOR, "NF P 94-050. Soils: investigation and testing – Determination of the moisture content – Oven drying methoD," 1995.
[72] F. Grennerat, "Hétérogénéités de déformation au cours du fluage transitoire de la glace polycristalline. Ph.D. thesis, Université de Grenoble.," 2006.
[73] P. Vacher, S. Dumoulin, F. Morestin, and S. Mguil-Touchal, "Bidimensional strain measurement using digital images," in *Proceedings of the Institution of Mechanical Engineers, Part C: Journal of Mechanical Engineering Science*, 1999, pp. 811–17.
[74] P. Duffaut, *Manuel de mecanique des roches, vol. 2 of Collection : Sciences de la terre et de l'environnement.* Les Presses - Mines, Paris, 2000.
[75] L. Miccoli, A. Drougkas, and U. Müller, "In-plane behaviour of rammed earth under cyclic loading: Experimental testing and finite element modelling," *Eng. Struct.*, vol. 125, pp. 144–152, Oct. 2016.
[76] L. Miccoli, D. V. Oliveira, R. A. Silva, U. Müller, and L. Schueremans, "Static behaviour of rammed earth: experimental testing and finite element modelling," *Mater. Struct.*, vol. 48, no. 10, pp. 3443–3456, Sep. 2014.
[77] T. T. Bui, Q.-B. Bui, A. Limam, and J.-C. Morel, "Modeling rammed earth wall using discrete element method," *Contin. Mech. Thermodyn.*, vol. 28, no. 1–2, pp. 523–538, Jul. 2015.
[78] J. S. J. Cheah, P. Walker, A. Heath, T. K. K. B. Morgan, and web-support@bath.ac.uk, "Evaluating shear test methods for stabilised rammed earth," *Proc. Inst. Civ. Eng. Constr. Mater.*, vol. 165, no. 6, pp. 325–334, Dec. 2012.
[79] P. A. Jaquin, C. E. Augarde, D. Gallipoli, and D. G. Toll, "The strength of unstabilised rammed earth materials," *ResearchGate*, vol. 59, no. 5, pp. 487–490, Jan. 2009.
[80] H. Nowamooz and C. Chazallon, "Finite element modelling of a rammed earth wall," *Constr. Build. Mater.*, vol. 25, no. 4, pp. 2112–2121, Apr. 2011.
[81] M. Bouhicha, F. Aouissi, and S. Kenai, "Performance of composite soil reinforced with barley straw," *Cem. Concr. Compos.*, vol. 27, no. 5, pp. 617–621, May 2005.
[82] A. C. Corbin and C. E. Augarde, "Investigation into the shear behaviour of rammed earth using shear box tests," presented at the First International Conference on Bio-based Building Materials, Clermont Ferrand (France), 2015, pp. 93–98.
[83] "NF P 94-071-1," in *Norme francaise-Cisaillement Rectiligne Direct*, 1994.
[84] C. Hsieh and M.-W. Hsieh, "Load plate rigidity and scale effects on the frictional behavior of sand/geomembrane interfaces," *Geotext. Geomembr.*, vol. 21, no. 1, pp. 25–47, Feb. 2003.
[85] C. N. Liu, Y.-H. Ho, and J.-W. Huang, "Large scale direct shear tests of soil/PET-yarn geogrid interfaces," *Geotext. Geomembr.*, vol. 27, no. 1, pp. 19–30, Feb. 2009.

[86] F. Champiré, A. Fabbri, J.-C. Morel, H. Wong, and F. McGregor, “Impact of relative humidity on the mechanical behavior of compacted earth as a building material,” *Constr. Build. Mater.*, vol. 110, pp. 70–78, May 2016.
[87] L. Soudani, “Modelling and experimental validation of the hygrothermal performances of earth as a building material,” Universite de Lyon, ENTPE, 2016.
[88] A. Holur, “Mechanical Testing Procedure for Local Building Materials: Rammed Earth and Laterite Building Stones,” L’Ecole Nationale des Travaux Publics de l’Etat, 2016.
[89] A. Cancelli, “The measurement of undrained cohesion in normally consolidated lacustrine clays,” *Bull. Int. Assoc. Eng. Geol. - Bull. Assoc. Int. Géologie Ing.*, vol. 23, no. 1, pp. 117–122, Jun. 1981.
[90] A. W. Skempton, “Discussion: Further data on the c/p ratio in normally consolidated clays.,” in *Proceedings of the Institution of Civil Engineers*, 1957, vol. 7, pp. 305–307.
[91] K. Terzaghi, *Theoretical soil mechanics*. John Wiley&Sons, Inc., 1943.
[92] A. Caquot and L. Kerisel, *Traite de mecanique des sols. Gauthier Villars, Paris.*, Gauthier Villars. Paris, 1948.
[93] A. B. Cerato and A. J. Lutenegger, “Specimen Size and Scale Effects of Direct Shear Box Tests of Sands,” vol. 29, no. 6, pp. 1–10, Sep. 2006.
[94] R. Z. Moayed and A. Amir, “Specimen size effects on direct shear test of silty sands,” *International Journal of Geotechnical Engineering*, Jul. 2016.
[95] Q. B. Bui and J. C. Morel, “Assessing the anisotropy of rammed earth,” *Constr. Build. Mater.*, vol. 23, no. 9, pp. 3005–3011, Sep. 2009.
[96] A. B. Mehrabi, M. P. Schuller, and J. L. Noland, “Performance of masonry-infilled reinforced concrete frames under in-plane lateral load.,” *Structural Engineering and Structural Mechanics Research Series*, 1996.
[97] P. Gulan and M. A. Sozen, “Procedure for determining seismic vulnerability of building structures,” *ACI Struct*, vol. 96, no. 3, pp. 336–342, 1999.
[98] G. Al-Chaar, M. Issa, and S. Sweeney, “Behavior of Masonry-Infilled Nonductile Reinforced Concrete Frames,” *ResearchGate*, vol. 128, no. 8, Aug. 2002.
[99] R. A. Silva, D. V. Oliveira, T. Miranda, N. Cristelo, M. C. Escobar, and E. Soares, “Rammed earth construction with granitic residual soils: The case study of northern Portugal,” *Constr. Build. Mater.*, vol. 47, pp. 181–191, Oct. 2013.
[100] K. Liu, M. Wang, and Y. Wang, “Seismic retrofitting of rural rammed earth buildings using externally bonded fibers,” *Constr. Build. Mater.*, vol. 100, pp. 91–101, Dec. 2015.
[101] V. Haach, “Development od a design method for reinforced masonry subjected to inplane loading based on experimental and numerical analysis.,” Ph.D. thesis, Universidade do Minho - Escola de Engenharia, 2009.
[102] M. Tomaževič, “Shear resistance of masonry walls and Eurocode 6: shear versus tensile strength of masonry,” *Mater. Struct.*, vol. 42, no. 7, pp. 889–907, Sep. 2008.
[103] M. Tomaževič and P. Weiss, “Robustness as a criterion for use of hollow clay masonry units in seismic zones: an attempt to propose the measure,” *Mater. Struct.*, vol. 45, no. 4, pp. 541–559, Oct. 2011.
[104] I.C.B, *International recommendations for design and erection of unreinforced and reinforced masonry structures.* rotterdam.: Tech. rep.,International Council for Buildings., 1987.
[105] M. Tomazevic, *Earthquake-Resistant Design of Masonry Buildings*, vol. 1. Imperial College Press, 1999.
[106] EN 1996-1-1, *Eurocode 6 - design of masonry structures - part 1-1 : general rules for reinforced*. European Committee for Standardization, 2013.

[107] D. Ciancio and C. Augarde, “Capacity of unreinforced rammed earth walls subject to lateral wind force: elastic analysis versus ultimate strength analysis,” *Mater. Struct.*, vol. 46, no. 9, pp. 1569–1585, Jan. 2013.
[108] P. A. Jaquin and C. E. Augarde, “Analysis of historic rammed earth construction,” in *5th international conference on structural analysis of historical constructions*, New Dehli, India, 2006, pp. 1091–1098.
[109] Aster, “Analysis of Structures and Thermomechanics for Studies & Research,” *www. code-aster. org*, 2011. .
[110] D. C. Drucker and W. Prager, “Soil mechanics and plastic analysis or limit design MECHANICS AND PLASTIC ANALYSIS OR LIMIT DESIGN,” *Q. Appl. Math.*, vol. 10, no. 2, pp. 157–165, 1952.
[111] ASTM, “ASTM E519-02, Standard Test Method for Diagonal Tension (Shear) in Masonry Assemblages.,” STM International, West Conshohocken, PA, 2002.
[112] Q. B. Bui, J. C. Morel, S. Hans, and P. Walker, “Effect of moisture content on the mechanical characteristics of rammed earth,” *Constr. Build. Mater.*, vol. 54, pp. 163–169, Mar. 2014.
[113] B. De Sensi, “Terracruda, Dissemination of Earth Architecture.” 2003.
[114] D. V. Oliveira, R. A. Silva, P. . Lourenco, and L. Schueremans, “Rammed earth construction and the earthquakes2010,” presented at the Congresso Nacional de Sismologia e Engenharia. SÍSMICA, Aveiro, Portugal, 2010.
[115] H. W. Morris, “19 - Natural disasters and earth buildings: resistant design and construction,” in *Modern Earth Buildings*, Woodhead Publishing, 2012, pp. 481–537.
[116] T. Bakeer and W. Jäger, “Collapse analysis of reinforced and unreinforced adobe masonry structures under earthquake actions—case study: Bam Citadel,” 2007, vol. I, pp. 577–586.
[117] R. Liang, D. Stanislawski, and G. Hota, “Structural responses of hakka rammed earth buildings under earthuqake loads,” in *International Workshop on Rammed Earth Materials and Sustainable Structures & Hakka Tulou Forum 2011*, Xiamen University, China, 2011.
[118] R. Liang, G. Hota, Y. Lei, Y. Li, D. Stanislawski, and Y. Jiang, “Nondestructive Evaluation of Historic Hakka Rammed Earth Structures,” *Sustainability*, vol. 5, no. 1, pp. 298–315, Jan. 2013.
[119] H. Morris and P. Walker, “Observations of the Performance of Earth Buildings Following the February 2011 Christchurch Earthquake.,” *Bull. N. Z. Soc. Earthq. Eng.*, vol. 44, no. 4, pp. 358–367, 2011.
[120] EN 1998-1:2004, *Eurocode 8: Design of structures for earthquake resistance*. European Committee for Standardization, 2005.
[121] P. Fajfar, “Capacity spectrum method based on inelastic demand spectra,” *Earthq. Eng. Struct. Dyn.*, vol. 28, no. 9, pp. 979–993, Sep. 1999.
[122] A. K. Chopra and R. K. Goel, “A modal pushover analysis procedure for estimating seismic demands for buildings,” *Earthq. Eng. Struct. Dyn.*, vol. 31, no. 3, pp. 561–582, Mar. 2002.
[123] D. Abrams, “Performance-based engineering concepts for unreinforced masonry building structures.,” *Prog Struct Mat Eng*, vol. 16, pp. 48–5, 2001.
[124] ATC, “FEMA-306: evaluation of earthquake damaged concrete and masonry wall buildings.,” Basic Procedures Manual, Applied Technology Council (ATC), Washington, 1998.
[125] V. Bosiljkov, A. Page, V. Bokan-Bosiljkov, and R. Žarnić, “Performance based studies of in-plane loaded unreinforced masonry walls,” vol. 16, 2003.
[126] G. M. Calvi, “A displacement-based approach for vulnerability evaluation of classes of buildings,” *Journal on Earthquake Engineering*, vol. 3, pp. 411–438, 1999.

[127] S. Petry and K. Beyer, “Limit states of modern unreinforced clay brick masonry walls subjected to in-plane loading,” *Bull Earthq. Eng*, 2014.
[128] M. Tomagevic, “Damage as a measure for earthquake-resistant design of masonry structures : Slovenian experience,” *Can. J. Civ. Eng.*, vol. 34, no. 11, pp. 1403–1412, 2007.
[129] ATC -40, “Seismic Evaluation and Retrofit of Concrete Buildings (Report SSC 96-01 of California Seismic Safety Commission,” Redwood City, California, U.S.A., 1996.
[130] FEMA 356, “Prestandard and commentary for the seismic rehabilitation of buildings,” Washington DC: American Society of Civil Engineers (ASCE), 2000.
[131] P. Fajfar and P. Gašperšič, “Fajfar, P., and , P. (1996). ‘The N2 Method for the Seismic Damage Analysis of Rc Buildings.’ , 25(1), 31–46.,” *Earthq. Eng. Struct. Dyn.*, vol. 25, no. 1, pp. 31–46, 1996.
[132] P. Fajfar, “A Nonlinear Analysis Method for Performance-Based Seismic Design,” *Earthq. Spectra*, vol. 16, no. 3, pp. 573–592, 2000.
[133] T. Vidic, P. Fajfar, and M. Fichinger, “Consistent inelastic design spectra: strength and displacement,” *Earthq. Eng. Struct. Dyn.*, vol. 23, pp. 502–521, 1994.
[134] Q.-B. Bui, S. Hans, J.-C. Morel, and A.-P. Do, “First exploratory study on dynamic characteristics of rammed earth buildings,” *Eng. Struct.*, vol. 33, no. 12, pp. 3690–3695, Dec. 2011.
[135] H. R. Hamilton, J. McBride, and J. Grill, “Cyclic Testing of Rammed-Earth Walls Containing Post-tensioned Reinforcement,” *Earthq. Spectra*, vol. 22, no. 4, pp. 937–959, Nov. 2006.
[136] R. Hu and Y. Dong, “Shake Table Test on Rammed Earth Wall Panels,” in *Advanced Materials Research*, 2010, p. pp 795-799.
[137] Y. Wang, M. Wang, K. Liu, W. Pan, and X. Yang, “Shaking table tests on seismic retrofitting of rammed-earth structures,” *Bull. Earthq. Eng.*, pp. 1–19, Sep. 2016.
[138] R. A. Silva, “Repair of Earth Constructions by Means of Grout Injection,” *ResearchGate*, Dec. 2013.
[139] P. Vacher, A. Haddad, and R. Arrieux, “Determination of the Forming Limit Diagrams Using Image Analysis by the Corelation Method,” *CIRP Ann. - Manuf. Technol.*, vol. 48, no. 1, pp. 227–230, Jan. 1999.